UNIVERSITA' DEGLI STUDI DELL'INSUBRIA

DOTTORATO DI RICERCA IN BIOTECNOLOGIE, BIOSCIENZE E TECNOLOGIE CHIRURGICHE

Curriculum Biologia Cellulare e Molecolare

XXXI CICLO

Iron oxide nanoparticles: a platform for biomolecule conjugation

Nanoparticelle di ossido di ferro: una piattaforma per la coniugazione di biomolecole

Docente guida: Prof. **Giovanni Bernardini**
Tutor: Prof. **Rosalba Gornati**

Tesi di dottorato di:
Ilaria Armenia
Matr. 711330

Dip. Biotecnologie e Scienze della Vita - Università degli Studi dell'Insubria

Anno accademico 2017-2018

TABLE OF CONTENTS

SUMMARY

In the last years, nanotechnology has caught the interest of research communities all around the world. Among the nanomaterials, of great interest are iron oxide nanoparticles (IONPs), which possess unique magnetic properties, low toxicity and high biocompatibility. Furthermore, IONPs can be easily produced and coated with various molecules in order to introduce reactive groups that can be used for the conjugation of biomolecules. Considering their characteristics, IONPs are widely used in industrial and biomedical field.

Here, IONPs were synthetized via co-precipitation method and characterized using different techniques, i.e. TEM, DLS, ζ-potential and SQUID magnetometry. The particles synthetized were reproducible in shape and size distribution, moreover, they were chemically stable at the conditions considered.

In the first part of the project, IONPs were used as a platform for the conjugation of two thermophilic enzymes, L-aspartate oxidase from *Solfolobus tokidaii* and amylase from *B. lichieniformis* to obtain an effective biocatalyst. To this aim, they were conjugated with different binding strategies obtaining NP-enzyme systems with different activities. These differences in enzymatic activity were due to the different orientations of the enzymes respect to NP surface and to the different stretching of the proteins. Considering their superparamagnetism, IONPs can be accessed by remote stimuli and this can be exploited to activate other molecules that are not remotely actuable, such as enzymes. Thermophilic L-aspartate oxidase and amylase were activated in a "wireless" fashion by an external alternate magnetic field (AMF) without increasing the "overall" temperature of the solution where the reaction occurred. Remarkably, the nano-systems were successfully reused for at least three consecutive cycles of AMF activation with the loss of only the 40% of the initial activity. Nanoactuation of thermophilic enzymes by AMF has potential applications in different fields. Indeed, multi-enzymatic processes with enzymes with different temperature optima could be carried in the same reaction pot and thermolable products could be efficiently produced by thermophilic enzymes without suffering for the high temperatures.

The second part of the project was focused on the development of a nano-antibiotic system, using IONPs as a platform for the conjugation of the glycopeptide antibiotic teicoplanin. It is known that IONPs have been investigated as potential nanocarriers for antibiotics to be magnetically directed and recovered from infection sites. The antimicrobial efficacy of NP-TEICO, compared to IONPs and amino-modified NPs (NP-APTES), was assessed through classical microbiological methods (i.e. growth kinetic analysis, minimal bacteriostatic and bactericidal concentrations and agar diffusion assay) and through morphological studies. Results clearly indicate that teicoplanin conjugation confers high and prolonged antimicrobial activity to IONPs toward Gram-positive bacteria, while no antimicrobial activity was detectable towards the Gram-negative *Escherichia coli*. Although IONPs and NP-APTES showed an insignificant antimicrobial activity in comparison to NP-TEICO, data indicate that they established diverse interaction patterns at the bacterial surface. Sensitivity of bacteria to NPs varied according to the surface provided by the bacteria and it was species specific. Positively charged NP-APTES tend to establish electrostatic interactions with negatively charged bacteria. Furthermore, NP-TEICO inhibited *S. aureus* biofilm formation conserving the activity of teicoplanin versus planktonic cells and improving it towards adherent cells. Finally, cytotoxicity of NP-TEICO was assessed on a cancer cell line and on a primary culture, SKOV3 and hASC respectively.

To conclude, IONPs were successfully synthetized, functionalized and employed as a platform for biomolecules conjugation. Indeed two effective different nano-biocatalysts and a nano-antibiotic were obtained.

RIASSUNTO

Negli ultimi anni, le nanotecnologie hanno catturato l'attenzione della comunità scientifica di tutto il mondo. Tra i nanomateriali, di grande interesse sono le nanoparticelle di ossido di ferro (IONPs) che possiedono proprietà magnetiche uniche, oltre ad una bassa tossicità ed un'alta biocompatibilità. Inoltre, le IONPs possono essere facilmente prodotte e, successivamente, funzionalizzate con diverse molecole. Queste hanno la funzione non solo di stabilizzare le IONPs, ma anche di introdurre gruppi reattivi che possono essere utilizzati per la coniugazione di molecole biologiche. Grazie alle loro caratteristiche, le IONPs sono ampiamente utilizzate sia in ambito industriale che in ambito biomedico.

In questo progetto, le IONPs sono state sintetizzate tramite un metodo di co-precipitazione per poi essere funzionalizzate con il 3-aminopropiltrietossi silano (APTES), una molecola che permette di stabilizzare le IONPs in soluzione acquosa, introducendo al contempo dei gruppi aminici sulla superficie della nanoparticella (NP) stessa. Le NP così prodotte sono state caratterizzate tramite diverse tecniche, quali microscopia elettronica a trasmissione (TEM), Dynamic Light Scattering (DLS), mobilità elettroforetica e magnetometria SQUID. I risultati ottenuti hanno dimostrato che un'elevata riproducibilità nella produzione delle NP sia in termine di forma che in termine di distribuzione delle loro dimensioni; inoltre, le NPs sono risultate superparamagnetiche e stabili chimicamente nelle condizioni considerate.

Nella prima parte del progetto, le IONPs sono state utilizzate come piattaforma per la coniugazione di due enzimi termofili, L-aspartato ossidasi da *Solfolobus tokidaii* e α-amilasi da *Bacillus lichiniformis* per ottenere un efficiente biocatalizzatore. A questo scopo, i due enzimi sono stati coniugati alle NP utilizzando diverse strategie, che hanno permesso di ottenere nano-sistemi che presentassero attività enzimatiche diverse. Queste ultime sono dovute ai diversi orientamenti della proteina e alla sua diversa deformazione strutturale, dovuta al legame con la NP tramite diversi residui amminoacidici. Le caratteristiche superparamagnetiche delle NP utilizzate sono state, poi, sfruttate per attivare gli enzimi ad esse coniugati, attraverso l'applicazione di un campo magnetico alternato (AMF). I risultati ottenuti hanno confermato la possibilità

di attivare gli enzimi termofili senza aumentare la temperatura totale del sistema. È stato inoltre possibile far lavorare contemporaneamente l'enzima D-amino acido ossidasi (DAAO) che presenta un optimum di temperatura pari a 37°C. Sorprendentemente, i nano-sistemi sono stati riutilizzati con successo per almeno tre cicli consecutivi di attivazione tramite AMF con la perdita di solo il 40% dell'attività iniziale. La nano-attivazione degli enzimi termofili con AMF ha potenziali applicazioni in diversi campi, infatti, processi multi-enzimatici, con enzimi aventi optimum di temperatura diversi, potrebbero essere condotti nello stesso reattore dove i prodotti termolabili potrebbero essere prodotti efficientemente dagli enzimi termofili senza soffrire per le alte temperature.

La seconda parte del progetto è stata incentrata sullo sviluppo di un nano-antibiotico, utilizzando le IONPs come piattaforma per la coniugazione della teicoplanina, un antibiotico glicopeptidico (NP-TEICO). È noto che le IONPs sono ampiamente utilizzate come nano-carriers per gli antibiotici che possono essere diretti magneticamente ai siti di infezione per poi essere recuperati. L'efficacia antimicrobica di NP-TEICO, confrontata sia all'antibiotico libero che alle NP non coniugate, è stata valutata attraverso metodi microbiologici classici (analisi cinetica della crescita, minima concentrazione batteriostatica e battericida e test di diffusione su agar) e studi morfologici, tramite microscopia ottica a fluorescenza e microscopia elettronica a trasmissione. I risultati indicano chiaramente che la coniugazione della teicoplanina conferisce un'attività antimicrobica elevata e prolungata alle IONPs nei confronti dei batteri Gram-positivi, mentre non è stata rilevata alcuna attività antimicrobica nei confronti dei Gram-negativi. Sebbene IONP e NP-APTES non abbiano mostrato attività antimicrobica, i dati ottenuti indicano un'interazione con la superficie batterica. La sensibilità dei batteri alle NP varia in base alla superficie fornita dai batteri ed è specie-specifica. Le NP funzionalizzate con APTES, che presentano una superficie carica positivamente, tendono a stabilire interazioni elettrostatiche con batteri carichi negativamente. Inoltre, il nano-antibiotico ha inibito la formazione del biofilm di *S. aureus* conservando l'attività della teicoplanina rispetto alle cellule planctoniche e migliorandola verso le cellule aderenti. Infine, è stata valutata la citotossicità di NP-TEICO su una linea cellulare immortalizzata e su una coltura

primaria derivata da tessuto adiposo. In generale la presenza della teicoplanina sulla superficie della NP riduce la tossicità intrinseca delle NPs, migliorando la biocompatibilità del sistema.

Per concludere, le IONP sono state sintetizzate, funzionalizzate e impiegate con successo come piattaforma per la coniugazione di biomolecole.

I. INTRODUCTION

NANOTECHNOLOGY, NANOMATERIALS AND NANOPARTICLES

In the last years, nanotechnology is emerging as a field of interest both for research and industry. It includes all the emerging technologies that deals with the manipulation of matter at the atomic and molecular level, the design, the characterization and the synthesis of structures of nanomaterials (NM)[1]. The European Commission defined NM as "natural, incidental or manufactured material containing particles, in an unbound state or as an aggregate or as an agglomerate and where, for 50 % or more of the particles in the number size distribution, one or more external dimensions is in the size range 1 nm - 100 nm"[2]. According to the number of dimensions in the nanoscale, NM can be classified as nanoplates, nanofilm or nanolayers (one dimension), nanofibers or nanotubes (two dimensions), nanoparticles (NP, three dimensions). NPs can be classified by their origin into natural or anthropic: the natural ones are a key component of our ecosystem and are produced by fossil volcanoes, microbial agents and components of aquatic sediments; the anthropic, instead, could be incidental if derived from industrial processes (for example those generated by photochemical processes and combustion), or intentional if they are produced with a well-defined chemical composition[3–5]. The application of NMs is widespread from food safety [6,7], agriculture[8,9] and cosmetics to industrial applications, such as sensors[10] and photovoltaic devices[11] and catalyst[12,] but also to medicine.

The interest in nanostructured materials comes from the fact that they exhibit properties and functions that differ from bulk-sized materials[13]. The different scale structure causes the increase of the surface per unit mass resulting in a higher chemical reactivity, higher resistance to mechanical stress and in an alteration of the electrical properties, such as an increase of the conductivity[14]. Furthermore, the nanoscale affects the optical and magnetic behaviour of the material, because the quantum effects start to dominate the behaviour of matter[15].

It is well known that some non-magnetic elements, such as iron, nickel, manganese, platinum and palladium, acquire magnetic-like properties at a nanoscale level. These magnetic NPs (MNPs) offer abundant possibilities for biotechnology. First, they have

sizes comparable to those of the biomolecules. Second, the MNPs have a well-defined crystalline structure, high solubility, low intrinsic toxicity, high resistance to mechanical stress and unique magnetic properties such as supermagnetism, high coercivity, low Curie temperature and high magnetic susceptibility. MNPs, indeed, obey to the Coulomb law and can be manipulated by the presence of an external magnetic field. Third, the large surface can be properly modified to conjugate biological agents[16].

Thus, magnetic NMs are used in the production of electronic devices to overcome some technical limits like data recording and storage[17–19] and in fine chemicals such as catalysts in hydrogenation reactions or styrene production[20,21]. Magnetic NPs, helped also in the biomedical field to ameliorate diagnosis and therapy as theragnostic agents[22–24] and to increase the sensitivity of biomedical techniques, such as magnetic resonance imaging (MRI) , in which magnetic NPs are used as novel contrast agents[25,26].

Iron oxide NPs

Among MNPs, iron oxide NPs (IONPs) have aroused great interest in research over the last several years. IONPs belong to the class of inorganic particles having an iron oxide core, coated by either inorganic materials (silica, gold) or organic materials (phospholipids, fatty acids, polysaccharides, peptides or other surfactants and polymers)[27,28].

Sixteen different crystalline structure of IONPs are known, among these the most promising are hematite (α-Fe_2O_3), magnetite (Fe_3O_4) and maghemite (γFe_2O_3). Hematite is characterized by a rhombohedral structure in which oxygen ions form a close-packed hexagonal arrangement and the Fe^{+3} ions occupy two-thirds of the octahedral interstices in the crystalline structure (Figure 1a). Magnetite, instead, has an inverse spinel structure in which the Fe^{+2} ions occupy octahedral sites, while Fe^{+3} ions are randomly distributed between octahedral and tetrahedral sites (Figure 1b). Maghemite presents a spinel structure similar to magnetite, but with vacancies in the cation sublattice; moreover, Fe^{+3} ions, that fill two-thirds of sites, are regularly arranged (Figure 1c)[29–31].
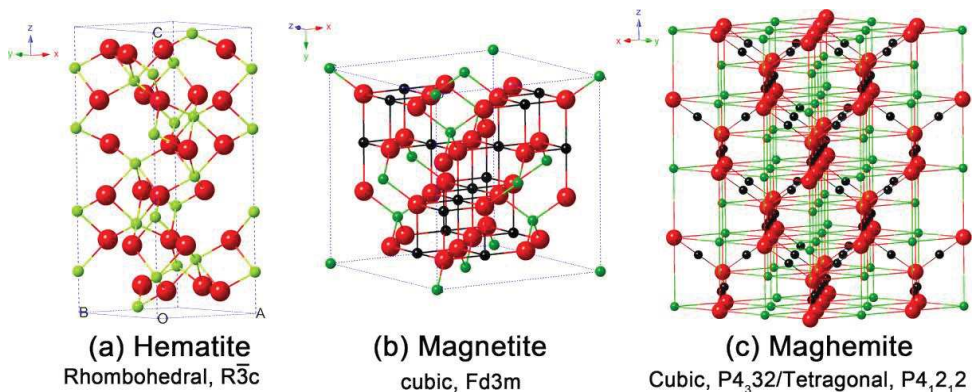
Figure 1. Crystal structure of the hematite, magnetite and maghemite (the black ball represents Fe^{2+}, the green ball represents Fe^{3+} and the red ball represents O^{2-})[29].

Each of these three iron oxides has unique biochemical, magnetic, catalytic properties which provide suitability for specific technical and biomedical applications. Hematite possesses weak ferromagnetic behaviour at room temperature, it is paramagnetic above its Curie temperature (956 °K) and it is the most stable iron oxide at room temperature. As hematite, maghemite it is an n-type semiconductor under ambient conditions. Magnetite, instead, can be both an n- and p-type semiconductor, as the Fe^{2+} ions present in its structure, can be partially replaced by other divalent ions (Co, Mn, Zn, etc)[30]. The most interesting aspect of IONPs is their high magnetization that can be triggered by applying an external magnetic field: this allows not only to generate heating in a localized point, but also to target the NPs to the area of interest[27]. Indeed, γ-Fe_2O_3 and Fe_3O_4 are readily magnetized thanks to their spinel structures.

IONP synthesis

During the last years, many publications have described different synthetic routes for the synthesis of IONPs with good shape-control, high stability and monodisperse distribution. Several popular methods including co-precipitation, thermal decomposition and hydrothermal synthesis can all be directed at the synthesis of high-quality MNPs:

- **Co-Precipitation**: is an easy and convenient way to synthesize IONPs from aqueous Fe^{2+}/Fe^{3+} salt solutions by the addition of a base at room temperature. The size, shape, and composition of the NPs depends on the

type of salts used (e.g. chlorides, sulfates, nitrates), the Fe^{2+}/Fe^{3+} ratio, the reaction temperature, the pH value and ionic strength of the media. This type of synthesis guarantees high reproducibility and high yield of production.

- **Thermal Decomposition:** This method is based on the thermal decomposition of compounds in high-boiling organic solvents containing stabilizing surfactants. It produces monodisperse NPs with a control over size and shape. In principle, the decisive parameters for the control of the size and morphology of the NPs are the ratios of the starting reagents.

- **Hydrothermal Synthesis:** This method is based on a phase transfer and separation mechanism that occurs at the interfaces of the liquid, solid, and solution phases present during the synthesis under hydrothermal conditions. It leads to the production of NPs with a good uniformity in size and shape.

Table 1 summarizes the advantages and disadvantages of the above mentioned synthesis.

Table 1. Summary comparison of IONPs synthetic methods.

Synthetic method	Synthesis	Reaction temp. [8C]	Solvent	Surface-agents	Size distribution	Shape control	Yield
co-precipitation	very simple, ambient conditions	20–90	water	needed	relatively narrow	not good	high/ scalable
thermal decomposition	complicated, inert atmosphere	100–320	organic compound	needed	very narrow	very good	high/ scalable
hydrothermal synthesis	simple, high pressure	220	water-ethanol	needed	very narrow	very good	medium

Co-precipitation is preferred in terms of simplicity of the synthetic route, while thermal decomposition is the most reliable for size and morphology control. Hydrothermal synthesis, on the other hand, is a relatively little explored method for IONPs synthesis, although it allows the synthesis of high-quality NPs.

However, all the synthesis methods generally lead to the production of metastable oxides that easily undergo to oxidation when exposed to air, leading to a partial loss of their magnetic behaviour. Thus, in an oxidative atmosphere, they tend to form

aggregates. It is, therefore, necessary to stabilized the NPs surface with a specific coating[32].

Surface Modifications

To increase colloidal stability and prevent agglomeration of IONPs, different surface modifications have been developed, using chemicals or biological materials during or after the synthesis process. The high interactions of IONPs and the surrounding media need to be contrasted by efficient coating, that protect and stabilize the surface, providing new physicochemical properties (optical, electrical and thermal)[33].

Different groups of materials can be applied as coating, including organic ligands, such as natural or synthetic polymers and/or surfactants, and inorganic materials, like silica, precious metals (Ag and Au) and metal oxides (NiO and CoO)[34]. Figure 2 depicts a graphical overview of different types of IONPs functionalization that have been designed for the required application.
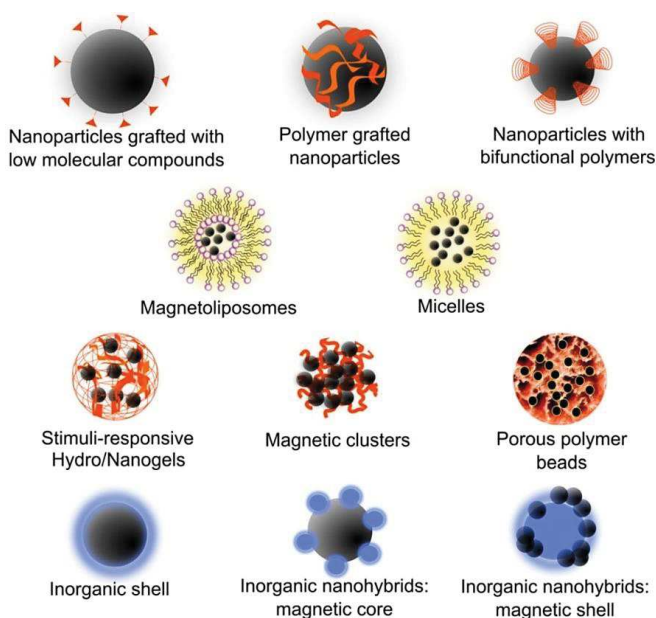

Figure 2. IONPs arrangements with molecules, polymers and inorganic chemicals (not at scale)[35].

The different architectures created by functionalization allow the addition of reactive functional groups on the particle surface that can be exploited for conjugation of biologically active substances or biomolecules. Table 2 reports the most used coating compounds, classified on the functional end group present on the NPs surface after functionalization.

Table 2. Chemical compounds, sorted by functional group, used for the primary coating and of IONPs.

Functional end-group	Compound
-NH$_2$	-Chitosan
	-Polyethylenimine
	-Poly(L-lysine)
	-Polyethylene glycol with terminal -NH$_2$
	-Ethylenamine
	-Aminosilane
-OH	-Polyethylene glycol
	-Dextran
	-Polyvinylalcohol
-COOH	-Polyacrylic acid
	-Carboxymethylcellulose
	-Polyethylene glycol with terminal -COOH
	-Alginate
	-Polymethacrylic acid
	-Citrate

One of the most common group includes silane and its derivatives. Indeed, this compound is characterized by an easy controlled reaction and a wide number of commercially available silane derivatives with a well-documented chemistry. Furthermore, the use of silane-compounds guarantees an high surface coverage and a strong binding, that create very stable core-shell structures. The coating obtained presents the functional end-group oriented towards the external media and, through this active group in its structure, is able to combine with biomolecules, drugs and metals. Among the silane-compounds, the 3-Aminopropyltriethoxysilane (APTES) is of great interest[36]. Thanks to the high biocompatibility and the high number of

functional end groups that can be grafted on the NPs surface, it is considered a good candidates for the functionalization of IONPs. The general silanization sequence is reported in Figure 3.
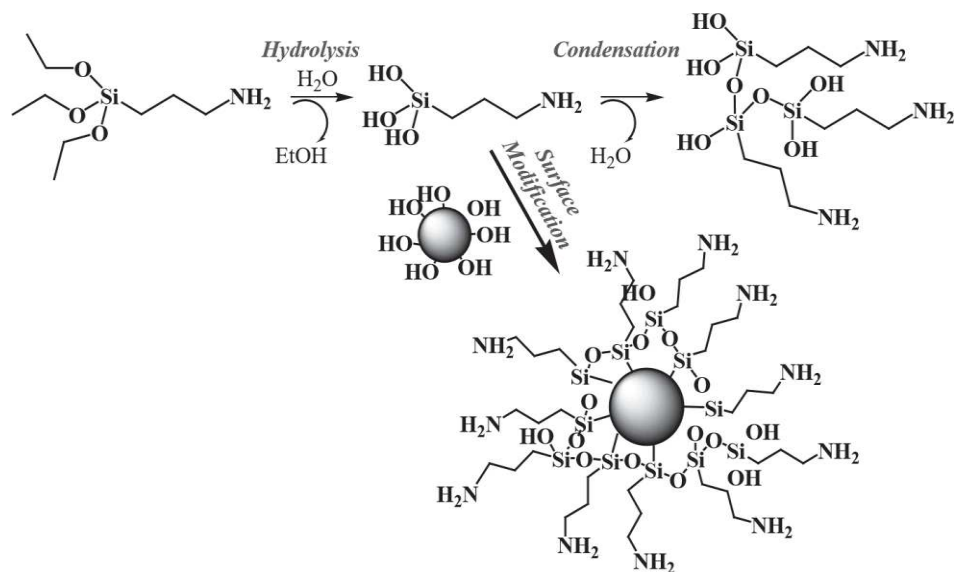
Figure 3. Reaction mechanism IONPs and APTES. First step is the hydrolysis of triethoxyl groups into trihydroxyl groups and then poly-condensation of the hydroxyl groups and the reaction with the surface IONPs surface[36].

Briefly, when APTES is suspended in a solution of ethanol and water, reactive silanol groups are formed by the replacements of the alkoxide groups into hydroxyl groups. The silanol groups condense with other silanol groups to produce siloxane bonds (Si–O–Si) and with the -OH present on the NPs surface to produce NP-O-Si bonds[37]. The result is the formation of a three dimensional mesh around the core of the NPs characterized by the presence of functional groups (-OH or -NH_2) exposed on their surface, that are available for functionalization with biopolymers[38].

APPLICATIONS

Due to their chemical-physical characteristics, NPs are applied in many different fields and in particular in nanobiotechnology. This field deals with the design and the application of NPs combined to the biological world to achieve nanoscale tasks. Some of these are non-biological tasks and have applications in industrial areas, whereas others are related to biology or medicine[39] (Table 3).

Table 3. Nanoparticles applications in industry, biomedicine, food and agriculture, environment.

Field	Applications
Industry	Reinforced plastics
	Industrial catalyst
	Functional nanocomposites
	Nanopigments
	Superplastic ceramics
Biomedicine	Cancer therapy
	Imaging
	Protein aggregation
	Drug delivery
	Antibacterial
Food and agriculture	Nutraceutical
	Food packaging
	Reduce pesticides
	Nutrient delivery
	Improving texture
Environment	UV protection
	Pollution monitoring sensors
	Pollutant s cavengers
	Biodegradable polymers
	Waste water treatment

Industrial applications

Currently there are many examples of nanomaterials used in industry. The cosmetic industry, for example, uses nanomaterials in the form of metal oxides as filters for UV radiation[40,41], while the electronics uses carbon nanotubes as transmitters of field[42,43]. MNPs are used for the realization of technological products that confer properties such as anti-wear and anti-scratch in the paint industry. The food industry also is influenced by the use of nanomaterials, in fact the use of a nanocomposite coating allows to improve packaging of food through an antimicrobial action[44,45].

In particular, IONPs are employed in almost all fields from electronics to chemicals, from engineering to energy[46]. For example, IONPs are used as a coloring and anti-corrosion agent in construction materials and coatings, as pigments in steel and

automobile primers to reduce corrosion of the metal itself [47]. For food related applications, they have been used for enzyme immobilization, protein purification, and food analysis. The commonly used techniques have limitations such as the time-consuming pre-treatments, expensive instrumentation or skilled operators. IONPs have been used also for a timesaving, scalable, gentle, easily automated magnetic separation of a target compounds from crude samples. The specific target can be purified after several rounds of magnetic separation and washing processes[48]. Thanks to their magnetic characteristics and their surface, IONPs have been also used in nanobiotechnology for the creation of nanobiocatalysts. Enzyme conjugated NPs can, indeed, overcome some of the limitations that enzymes[49].

Enzymes as biocatalysts

Enzymes are highly effective biocatalysts, that commonly enhance, in organisms, reaction rates by a factor of 10^5 to 10^{17}. They mediate a specific chemo-, regio-, and stereo-selectivity of reaction that demonstrate their superiority compared to chemical catalysts[50], although chemical catalysts can be used at very high temperatures. Thanks to their characteristics and their green chemistry, enzymes are useful in many areas of research, including organic synthesis, immunoassays, and substrate sensing, and in industry, such as paper, textile and food industry[51]. Of great interest for industries are enzymes produced by microorganisms since they can be produced in high quantity and in a short time. Moreover, recombinant DNA techniques can be used to enhance the enzyme production or to modify the enzyme structure to obtain an enzyme that is stable in the desired conditions[52,53]. On the other hand, the application of free enzymes in industry is hampered by high cost, thermal instability, activity inhibition, denaturing agents sensitivity and the impossibility of separating/reusing the enzyme at the end of the reaction [54–56]. To overcome such limitations, researchers attempted to immobilize enzyme on different solid supports, such as polymeric resins and inorganic materials[57–60]. Enzyme immobilization, indeed, aim to improve the enzyme stability, increase the volume loading of biocatalyst and simply both enzyme recycling and the downstream process[61].

Several works in literature report that immobilized enzymes have increased pH working range and improved thermal stability[62]. Furthermore the binding of the

enzyme on a solid support can enhance the enzyme activity and modify the substrate specificity[63–65].

The minimal diffusional limitation, the maximum surface area and the high effective enzyme loading make NPs one of the most interesting supports for enzyme immobilization [65,66]. If compared to other scaffold for enzyme immobilization, nano-biocatalysts can load a higher amount of enzyme, enhancing significantly the mass transfer efficiency[67]. Among NPs, the use of MNPs has been extensively studied due to their magnetic properties that make easier the recovery of the nano-biocatalyst by the application of a magnetic field[68,69]. And in particular, IONPs have been studied for the biodiesel production and food processing[70,71].

L-aspartate oxidase

L-aspartate oxidase (LASPO, EC 1.4.3.16) is a prokaryotic enzyme that catalyses the oxidative deamination of L-aspartate into oxaloacetate and ammonia, thanks to the reduction, in the first step of the reaction, and the subsequent re-oxidation of the FAD co-factor (Figure 4).
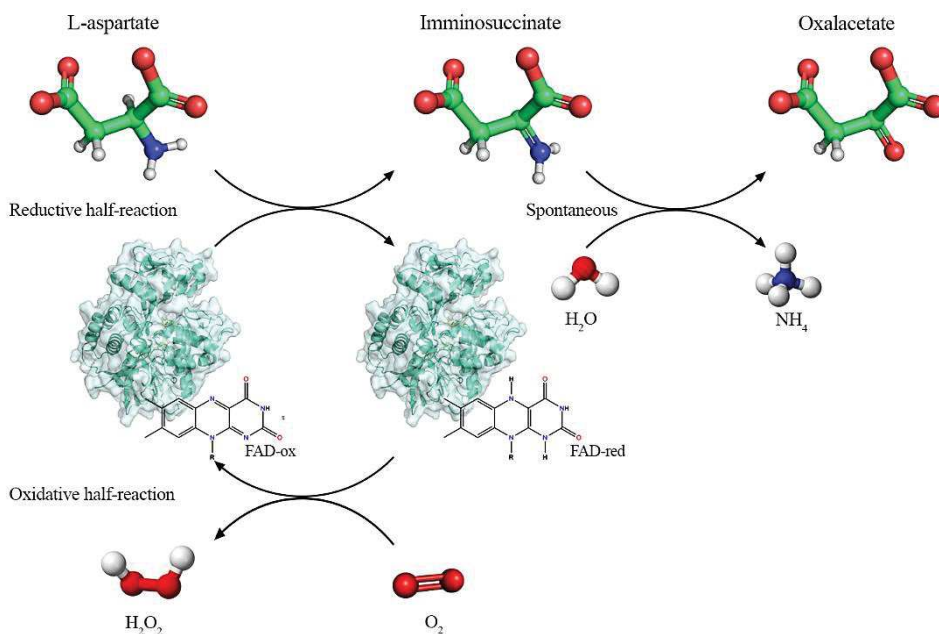

Figure 4. Catalytic reaction of LASPO. L-aspartate is oxidized to iminosuccinate followed by a non-enzymatically hydrolyzation to oxaloacetate.

In prokaryotes, LASPO is involved in the first reaction step of the *de novo* biosynthesis of the nicotinamide adenine dinucleotide (NAD^+). *In vivo*, the iminosuccinate produced by the reaction is condensed with dihydroxyacetone phosphate resulting in the production of quinolinate and, eventually, NAD^+. While, *in vitro,* it was demonstrated that LASPO can use both O_2 and fumarate in the FAD re-oxidation, allowing to catalyse its reaction both in aerobiosis and anaerobiosis. Under aerobic condition, the LASPO oxidizes L-aspartate to iminosuccinate, which is then hydrolyzed to oxaloacetate through a non-enzymatic pathway[72].

LASPO was isolated from different microorganism, such as *E.coli*, *B. subtilis* and *P. putida,* but the most interesting for industrial applications is those isolated from *Solfolobus tokodaii*, a thermophilic microorganism. This enzyme is a monomeric protein of 52 kDa composed by 472 residues that are organized in three distinct folding domains: a capping domain, a FAD-binding domain and a C-terminal domain[73,74] (Figure 5).
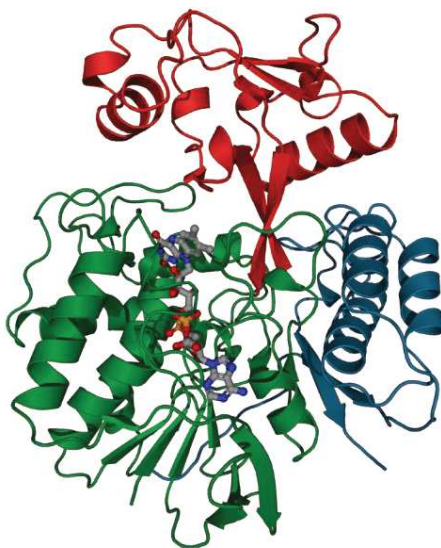
Figure 5. *Solfolobus tokodaii* LASPO overall structure: the FAD-binding, capping and C-terminal domains are shown respectively in green, red and blue. The FAD cofactor is represented as a stick model (adapted from PDB entry 2E5V).

LASPO has an high thermal stability that makes it very promising for industrial applications. Indeed, it is stable up to 80 °C without any remarkable changes in its activity. Besides the possibility to work at high temperature for more than 400 min,

LASPO is also attractive because it is stable in the 7-10 pH range, it presents a weak inhibition by the D-isomer of aspartate and by product of reaction (i.e., iminosuccinate or oxaloacetate), but also for its tight interaction with the cofactor[74]. For these characteristics, LASPO was expressed as a recombinant protein in *E.coli*, exploiting the molecular tools of this well studied microorganism to obtain an high yield of protein produced. The LASPO obtained was used for the resolution of a racemic solution of D,L-aspartate, leading to a pure solution of D-aspartate that is employed in the pharmaceutical industry for parenteral nutrition, as food additive and in sweetener manufacturing. Since the industrial application of LASPO is hampered by the high cost per enzymatic unit, various attempts to immobilized it on different supports are reported in literature. The amino groups of the enzyme were used for the conjugation to Relizyme™ H403/S R, a rigid methacrylic support previously activated with glutaraldehyde, and to SEPABEADS® EC-EP/S resin, a methacrylate hydrophobic support[75]. In these conditions, they obtained different conjugation yield, due to the different charge of the support, respectively 100 % and 50 %. Furthermore, the first conjugation approach lead to an high and rapid deamination of L-aspartate, while the second one reach the complete conversion of the racemic mixture in 4 hours. This thermostable enzyme was also immobilized as cross-linked enzyme aggregates (CLEA). This technology improved the performance of the enzyme because it is based on a single step process in which the purification and immobilization are a single operation. At the end of the process, LASPO retain 100% of the starting activity and the enzyme was successfully used for complete reactions for five consecutive times.

Amylase

Amylases are enzymes that hydrolyse starch molecules and, according to the sugars produced by the reaction, they can be classified into α-, β- and γ-amylases. Starch is one of the most important energy source for a large number organisms[76]. It is a polysaccharide composed by amylose and amylopectin, which constitute the 20-25 % and the 75-80 % of the macromolecule, respectively. The first one is formed by a linear chain of glucose units linked by α-1, 4-glycosidic linkage, while the second one presents, every 15-45 glucoses, a branching where the glucose units are linked by α-

1, 6 glycoside bonds (Figure 6). Starch hydrolysis leads to the production of destrins, maltose and maltotriose[77].
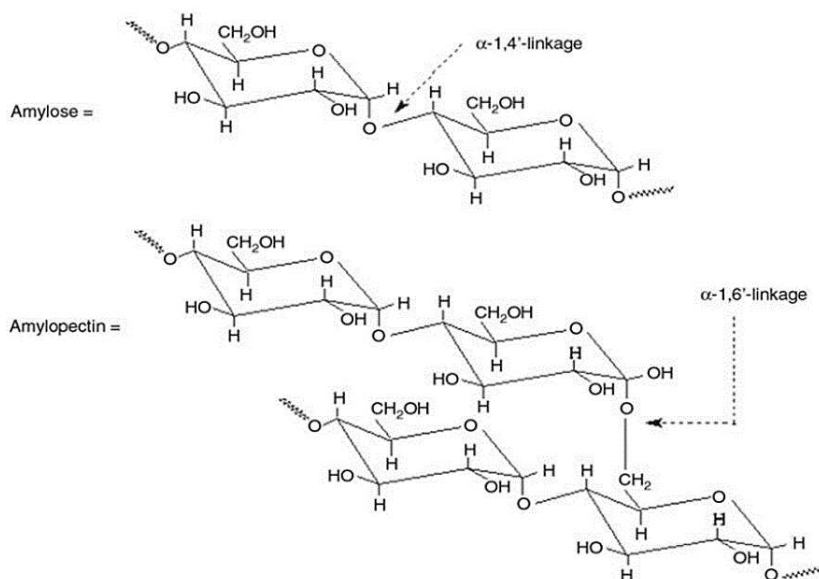
Figure 6. Structure of starch units amylose and amylopectin.

α-Amylase (1,4-a-D-glucan-glucanhydrolase, EC. 3.2.1.1) is an endo-enzyme that cleaves the glycoside bond within starch in non-crystalline regions, it cleaves the α-1-4 linkage. This class of enzyme has been isolated from different sources, from plant to animals[78], but the most interesting for industrial applications are α-amylases isolated from microorganisms. Their production, indeed, has a high cost effectiveness, thanks to the small time and space required for production[78]. Among bacterial species, the most widely used are the *Bacillus* spp. and *B. amyloliquefaciens* and *B. licheniformis*. In particular, they are used for commercial production of the enzyme for industrial application such as food, fermentation, textiles and paper industries[79]. These two bacteria produce thermostable α-amylase[80]. Thermostability is an important characteristic as enzymatic liquefaction and saccharification of starch are performed at high temperatures (100–110°C). In particular, α-amylase isolated from *B. licheniformis* is a monomeric protein of 62 kDa composed by 483 residues that are organized in three distinct folding domains (Figure 7)[81].

Figure 7. Overall structure of amylase from Bacillus licheniformis. Domain A, B and C are shown in green, blue and red respectively (adapted from PDB entry 1BLI).

This enzyme is stable in the pH range between 6 and 11 and its optimal temperature is 90°C[82] and, for these reasons, it is very interesting for industrial applications. Several attempts have been done to immobilized α-amylase from different sources on different support, in order to create a feasible biocatalysts. The immobilization of α-amylase from *Aspergillus oryzae* on two amino-functionalized silica-coated MNPs, bare or covered with chitosan, broaden the pH and temperature range of activity of the enzyme, increasing also its storage stability[83]. The immobilization of the thermostable amylase from *Bacillus licheniformis* on a calcium alginate matrix produces a biocatalyst that can be reused efficiently for seven cycles[79].

Nanoactuation

Actuators operate by converting external stimuli into mechanical motion that can then be used to do work or move objects. At the micron scale, actuation is a extensively explored field that has been realized through the design of microelectromechanical systems. At a nanoscale, actuation can be defined as actuation of a specific action using a nanoscale object with the input of an external force acting on it.

Among the unique properties of nanomaterials, the capability of absorbing energy, in form of radio-frequency, light and or magnetic field, have raised great interest in the

scientific community[84]. Gold NPs (AuNPs), for example, have been used for the remote control of biochemical reactions, selective control of gene interference, photothermal therapy and for drug delivery[85–87]. AuNPs can absorb light , in the near infrared (NIR) range, and can convert optical energy in thermal energy, transferring the heat generated to the surrounding matrix. Thanks to the strong absorbance over a wide range in the optical region, also carbon nanotubes (CNTs) have been remotely nanoactuated through the application of light. Near infrared light was efficiently used to activate thermophilic enzymes[88]. Even though it was demonstrated the production of heat through these methods, their use is limited due to the reduced depth penetration of NIR light. To overcome this limitation, the use of alternating magnetic field (AMF) has been explored for a localized production of heat[89–91].

The possibility to remotely actuate MNPs by a wide range of frequencies has opened new perspective not only in medicine but also in industrial application.

Medicine can exploit the capability of the IONPs to produce heat under alternating magnetic field, a phenomenon known as magnetic hyperthermia[29]. Magnetic hyperthermia is based on the production of heat as a consequence of Neel and Brown relaxation (Figure 8).
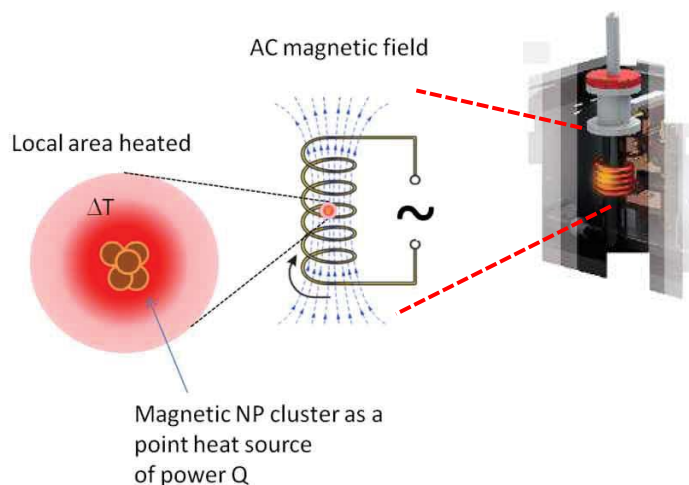

Figure 8. Nanoactuation of MNPs by applying an AMF.

In contrast, the actuation of NPs for industrial application and in particular in the biocatalysis is still scarcely unexplored. Some authors, actuate the enzyme linked to the NPs by applying a low frequency AMF. They use the conversion of magnetic

energy into rotational motion of the enzyme-particle system to increase the collision rate with the substrate[92,93], or to trigger conformational changes on the enzyme three-dimensional structure[94]. The use of heat generated by magnetic NPs to regulate enzyme activity has been also reported, but limited to deswelling-swelling of thermosensitive polymers attached to the NP surface that force to interact substrate-bound therapeutic drugs with enzymes that trigger their release[95–97].The effect of the heat generated by high frequencies of AMF on enzymes directly attached to NPs has been tough scarcely studied. Only Suzuki and colleagues have recently reported the specific activation of α-amylase and DNA ligase immobilized on ferromagnetic microparticles triggered by AMF [56,98]. However, this effect has not been reported yet using superparamagnetic NPs, nor it has been studied the effect of the enzyme orientation on the NP surface and of conformational changes caused by the conjugation strategy. In the case of ferromagnetic microparticles, the application of a magnetic field triggers their aggregation that cannot be easily reversed since it would be necessary to heat the particles above their Curie temperature (858 K for iron oxide)[99]. Instead, in the case of superparamagnetic NPs, their magnetic properties do not persist when the external magnetic field is removed. This is an important advantage of superparamagnetic NPs over ferromagnetic ones since it allows the reuse of the nanobiocatalyst.

Medical applications

In the last decades we assisted to a great expansion of NPs as tools for medical applications. A high number of experimental evidences support the benefits of nanomaterial-based agents in terms of selectivity, sensitivity, affinity and detection limits. FDA reports that an average of ~13 nanomedicines per 5 years have been approved for specific clinical indications since the mid-1990s. This comprises approval for both novel materials along with the use of existing materials for new clinical indications[100]. The list includes liposomes, polymeric micelles, inorganic and polymeric NPs, as well as nanorods and quantum dots. Among all the NPs used, the application of IONPs is becoming increasingly important in biomedicine thanks to their high biocompatibility and their low toxicity in the human body, combined with the ability to manipulate them using an external magnetic field. IONPs have been described and used in drug delivery, hyperthermia, magnetic resonance imaging, as spoilers for magnetic resonance spectroscopy, and more recently as sensors for metabolites and other biomolecules and as microbial agents (Figure 9)[35,101–107].
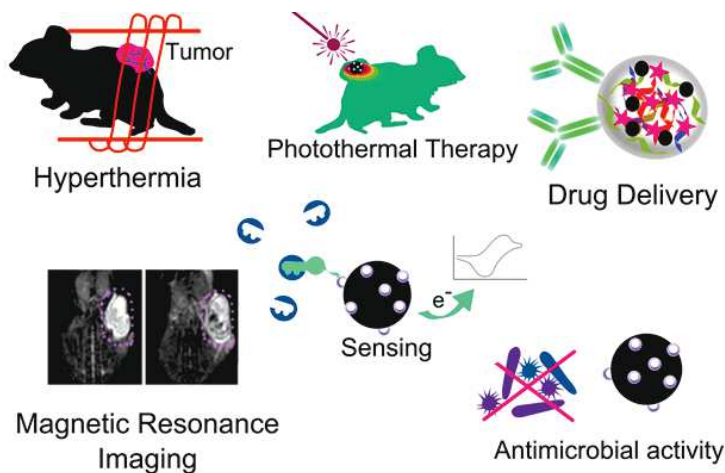

Figure 9. IONPs applications in nanomedicine.

Antibiotic resistance and nano-antibiotics

Antibiotics are low molecular weight molecules (200-2000 Daltons) that are able to inhibit bacterial growth through different mechanisms. They can be classified into natural, semi-synthetic and synthetic. The first group is produced by microorganisms as secondary metabolites, the second one is produced as chemical modification of the natural antibiotic, while the last group is the result of chemical synthesis. Antibiotics are grouped into classes according to their chemical structures, their chemical-physical properties and their spectrum of action.

According to the recent survey of the World Health Organization[108], antibiotic resistance is one of the biggest threats to global health, contributing to longer hospital permanence, higher medical costs and increased mortality. At least 700,000 people die annually due to resistant bacterial infections and this number is predicted to increase up to 10 million by the 2050 with the consequent social and economic burden. This public health treat is exacerbated by the scarcity of novel antibiotics expected to enter in clinical therapy in the near future[109]. One promising approach in the field of antimicrobial therapy is the use of nanotechnology-tailored agents for preventing and treating bacteria-resistant infections. Among different nanomaterial, silver and zinc oxide NPs are the most extensively studied. They exhibit remarkable antimicrobial activity: they affect adversely different process in bacteria such as cell-wall synthesis and cell division, they destabilize and disrupt the outer membrane, inhibit respiration and purine metabolism, and reduces the intracellular ATP levels[110–112].

The research on IONPs as microbial agent is increasing in the last years as IONPs can be used as an alternative to conventional antimicrobial agents. Furthermore, they can also act as carriers for drugs that could kill bacteria species without damaging the human host cells. It is well known that the antimicrobial activity of IONPs depends on their crystalline structure, indeed, magnetite has been reported to have activity against both Gram positive and Gram negative bacteria, while maghemite is less active, but more stable[113–117]. Thus, the conjugation of antibiotic drugs to maghemite is necessary for its tuneable activity against specific microorganisms. "Nanoantibiotics" present some advantages, such as a reduced susceptibility to bacterial resistance, a fine delivery to the site of infection and the possibility to

stimulate them with different sources such as heat, pH, magnetic field, light, etc. The use of IONPs in combination with amoxicillin penicillin, ampicillin, streptomycin and vancomycin [118–122] has already been reported. These results indicate that biocompatible MNPs enable antibiotic delivery and promote its antimicrobial activity. The conjugation of antibiotics has been reported not only for their antimicrobial activity, but also as biosensor. Indeed, more recently, antibiotic-carrying IONPs have been used for the detection and enrichment of bacteria from infected samples [123]. While, previous studies have reported that vancomycin-carrying IONPs could be used for the detection of a broad range of bacteria including Gram-positives such as *S. aureus* and Gram-negatives such as *E. coli* [124–126].

Glycopeptide antibiotic

Glycopeptide antibiotics (GPAs) are secondary metabolites produced by actinomycetes species. They have a heptapeptide core consisting of aromatic proteogenic and non proteogenic amino acids synthetized by the Non Ribosomal Peptide Synthetase (NRPS), an enzymatic complex that allows the cyclization the molecules through the formation of carbon-carbon or ether bonds. The amino acid residues, which together constitute the aglycone, present various substituents such as hydroxyls, methyls, sugars, chlorine atoms and lipid chains.

The first GPA introduced in clinics was vancomycin, produced by the actinomycete *Amycolatopsis* and the second one was teicoplanin, produced by *Actinoplanes theichomyceticus*. The new generation of glycopeptide antibiotics is composed of semi-synthetic derivatives of natural glycopeptides, among them telavancin, ornitavancin and dalbavancin have already been approved by FDA for clinical usage[127,128].

GPAs block the synthesis of peptidoglycan (or murein) of the bacterial cell wall. The peptide skeleton of the antibiotic binds, through five hydrogen bonds, to the D-Ala-D-Ala dimer of the peptidoglycan precursor. The binding prevents transpeptidation and transglycosylation reactions necessary for peptidoglycan synthesis, leading to the death of the cell[129,130]. This class of antibiotics is therefore active only on Gram positive bacteria; the Gram negative have, indeed, an external lipopolysaccharide

membrane that does not allow the interaction with its molecular target. GPAs are frequently used to treat serious infections caused by Gram positive bacteria, such as *Staphylococcus aureus*, *Enterococcus* spp. and *Clostridium difficile*. They are considered "last resort" drugs used against methicillin-resistant *S. aureus* strains (MRSA), which, today, are the main cause of complex nosocomial infections that, in the most serious cases, can lead to the death of patient for septicemia.

Teicoplanin

Teicoplanin is a natural glycopepetide antibiotic produced by *A. theichomyceticus* ATCC 31121[131]. Although its chemical synthesis is possible, the complexity of its chemical structure makes the fermentation the only way used for its production. Indeed, teicoplanin is produced as a complex of molecules structurally related: the five major components are designated as A2-1 to 5, one is an hydrolysis component, designated as A3-1 , and four minor components designated RS-1 to 4 (Figure 10).
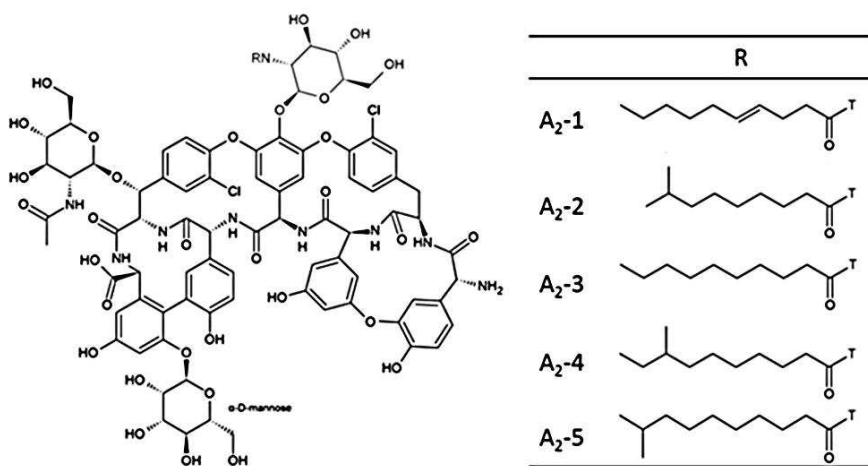
Teicoplanin

Figure 10. Teicoplanin structure. On right side are represented the five major components**.**

The core is formed of seven aromatic amino acids all oxidatively linked. The S)-4-hydroxyphenylglycine, in position 1, and 3,5-dihydroxyphenylglycine, in position 3, are linked together by an ether bond. The residues of tyrosine and β-hydroxytyrosine in positions 2 and 6 contain 2 chlorine atoms. In addition, to the aryl groups present

in position 4, 6 and 7 are attached three sugar moieties, N-acyl-β-D-glucosamine, one of N-acetyl-β-D-glucosamine and one of α-D-mannose, respectively. The acyl moiety is a fatty acid residue containing 9 to 12 carbon atoms is present as a substituent of the N-acyl-β-D-glucosamine[132]. The presence of the fatty acid increases the teicoplanin antimicrobial activity, allowing a better penetration of the antibiotic at the cellular and tissue level. Compared to vancomycin, teicoplanin has a longer half-life (about 40 hours), a feature that allows a single daily administration of the antibiotic intramuscularly.

The N and C terminal of the teicoplanin close around the D-ala D-ala, forming a binding pocket for the ligand: the mannose moiety in position 7, at the C termini of the antibiotic, interacts with the side chain of the amino acid 1 in the N-termini, through the hydroxyl group, forming the floor of the binding pocket. The back of the binding site is formed by both the backbone and the side chains of the aminoacid 2, 4 and 6, while the top of the pocket is created by the sugar moiety attached to the residue 4[133](Figure 11). The acyl chain lies on the back face of the antibiotic, avoiding the formation of back-to back dimers observed in other GPAs, such as vancomycin[134].
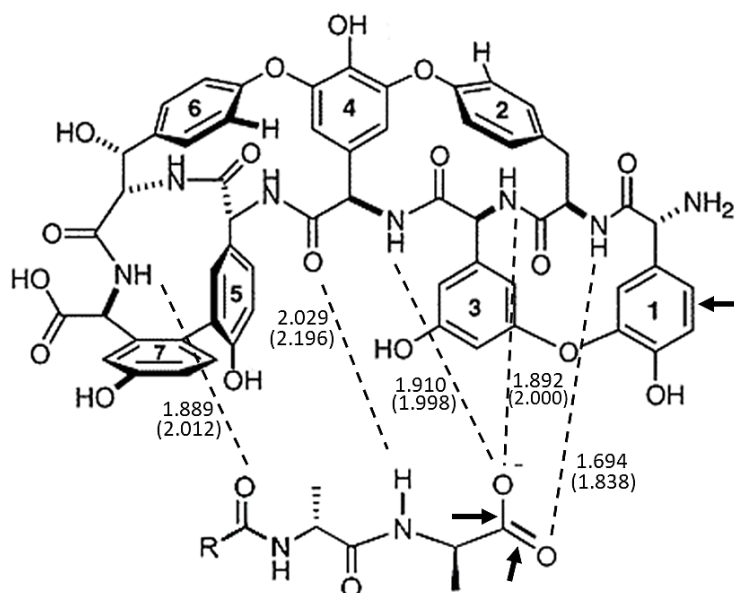

Figure 11. Teicoplanin aglycone interaction with D-Ala-D-Ala. Dotted lines indicate the hydrogen bonds stabilizing the complex, bond distances are given in angstroms. Arrows mark the weak interaction between the resonating glycopeptide aromatic bonds and the D-Ala terminations[135].

II. AIM OF THE PROJECT

The overall aim of this PhD thesis is to synthesize and functionalize superparamagnetic iron oxide nanoparticles (IONPs) to create NP-systems that can be efficiently used in industry and in medicine. This project originates from the observation that, thanks to their magnetic and biocompatible characteristics, IONPs can be used as a platform for the biomolecule conjugation.

The aim of first part of the project was to synthetize IONPs through a co-precipitation method to obtain an easy, reproducible and scalable method for their production. To better understand if the characteristics of the IONPs obtained were always similar, several chemical-physical characterizations were conducted.

After obtaining a better comprehension of the system, the second part of this work was focused on the use of IONPs as a platform for the conjugation of enzymes of potential interest for industrial application. Taking into consideration the capability of L-aspartate oxidase (LASPO) and α-amylase (AMY) to work at high temperature and their widespread use in industry, this two enzymes were chosen for the creation of efficient nano-biocatalysts. To this aim, different conjugation strategies were developed and their chemical-physical characteristics were investigated. Next, a biochemical characterization was carried on. The conjugation of enzymes to NPs can provide the subsequent advantages:

- Enhancement of enzymes activity in a wider range of temperature and pH.
- Enhancement of the enzyme stability over temperature
- Capability of recover and reuse the NP-enzyme systems, reducing the costs per enzyme units.

As a further improvement of the current industrial applications, this project aim was to evaluate the possibility to nano-actuate enzyme-NPs thanks to the capability of IONPs to respond to an AMF. The effect of the AMF on the NP-enzyme systems was studied varying the AMF parameters.

The last part of this project was focused on the development of a platform for biomedical applications by the design of a nano-antibiotic that exploits the IONP

characteristics, such as biocompatibility and superparamagnetic behaviour, and the antimicrobial activity of the teicoplanin. This system can provide several putative advantages such as:

- protection of the nanoconjugated drug from degradation and oxidation
- increase solubility, antimicrobial activity and biodistribution
- controlled and sustained delivery of the antibiotic to the site of the infection.

To this aim different techniques were used to investigate the antimicrobial activity: classical assay, such as MIC, MBC and agar diffusion assay, and morphological studies, fluorescence microscopy and electron microscopy.

Papers

Papers related to this PhD project are insert in the thesis chapter in which they can be useful to better explain the procedures or the results.

III. MATERIALS AND METHODS

CHEMICALS

APTES, 1-ethyl-3-(3-dimethylaminopropyl) carbodiimide (EDC), Hydroxysuccinimide (NHS), 4-amino antipyrine (4-AAP), L-aspartate acid, Phenol, Orange II, Tris-HCl; Sodium tetraborate, Starch from potatoes, Potassium sodium tartrate, tetrahydrate, 3,5-Dinitrosalicylic acid, D-(+)-Maltose, monohydrate teicoplanin, iron trichloride ($FeCl_3 \cdot$ 6 H_2O), iron dichloride ($FeCl_2$ ·4 H_2O), ammonium hydroxide (NH_4OH), nitric acid (HNO_3), ferric nitrate ($Fe(NO_3)_3 \cdot$ 9 H_2O), sodium 2-(N-morpholino)ethanesulfonic acid hemisodium salt (MES), 2′,7′-dichlorodihydrofluorescein (DCFH-DA), ethanol, phosphate-buffered saline (PBS), sodium chloride, formaldehyde, glutaraldehyde, sodium cacodylate, osmium tetroxide all purchased from Sigma Aldrich. Horse Radish Peroxidase, EIA grade (POD) was purchased from Roche (10814407001), sulfosuccinimidyl 4-(N-maleimidomethyl)cyclohexane-1-carboxylate (sulfo-SMCC), bis (sulfosuccinimidyl) suberate (BS3) and LIVE/DEAD BacLight fluorescence assay kit were purchased from ThermoFisher Scientific. Amino terminated polyethylene glycol (700 Da PEG-NH_2) was purchased from Rapp Polymere. Epon-Araldite 812 was purchased from Electron Microscopy Science.

SYNTHESIS

A common co-precipitation method was used to synthetize IONPs. Briefly, 8.89 g of $FeCl_3 \cdot 6$ H_2O and 3.28 g $FeCl_2 \cdot 4$ H_2O were mixed in 380 mL of water under a vigorous stirring for 30 min, while slowly dropping 1.5 mL of HCl (37%) to completely dissolve the salts. Following this step, 25 mL of NH_4OH (25%) were added. Particles were washed several times with MilliQ water and 40 mL of 2 M HNO_3 were added and heated at 90°C for 5 min. The particles were separated by a magnet from the reaction mixture, then 60 mL of 0.34 M solution of $Fe(NO_3)_3 \cdot 9$ H_2O was added. The suspension was heated at 90°C for 30 min. The supernatant was removed and IONPs were collected by a magnet, suspended in MilliQ water and left in dialysis overnight. IONPs were stored at 4°C.

APTES FUNCTIONALIZATION

For the amino functionalization of IONPs a1 mL of 1.5 M solution of APTES in ethanol was added to 150 mg of IONPs and stirred for 1h at room temperature Then, the temperature was increased to 90°C and stirred for an additional hour. The amino-modified IONPs (so far named NP-APTES) were collected by a magnet, washed several times and suspended in MilliQ water.

CHARACTERIZATION

Transmission Electron Microscopy (TEM)

TEM bright field measurements were performed with the samples diluted in H_2O MilliQ using a TECNAI G2 microscope operating at 200 kV for IONPs, NP-APTES, NP-LASPO and NP-AMY preparations; using JEOL 1010 electron microscope for NP-TEICO preparation.

Dynamic Light Scattering (DLS) and electrophoretic mobility (ζ-potential) Analysis

The hydrodynamic diameter and polydispersity index (PDI) of NPs were measured in 0.9 % NaCl after a proper dilution of the stock solution. ζ-potential measurements were performed at 25 °C with the samples diluted in 1mM KCl. For NP-APTES, stability measurements, DLS analysis and ζ-potential were carried out in 0.9 % NaCl in a range of pH from 3 to 12 and at different NaCl concentrations. Measurements were performed using 90 Plus Particle Size Analyzer (Brookhaven Instrument Corporation).

Magnetic characterization of NPs

SQUID magnetometry was used to determine the magnetic properties of IONPs and NP-APTES. 10 µL of the samples were dried on a piece of cotton and analysed with a field that vary from 50000 Oe to -50000 Oe at 300 K. using MPMS-XL (Quantum Design).

Amine group on the NPs-surface determination

The amino content of the NPs was measured by the Orange II spectrophotometric assay[136,137]. 1 mL of a solution of 1 mM Orange II pH 3 was added to 1 mg of NPs and maintained under stirring for 30 min at 40°C. The particles were precipitated and washed with an acidic water solution until all the unbound dye was removed. To desorb the bound dye, a solution at pH 12 was added to the NPs. The amount of desorbed dye was then measured at a wavelength of 480 nm with a Varian Cary 50 UV/vis spectrophotometer.

ENZYME CONJUGATIONS

Enzymes

Amylase from *Bacillus licheniphormis* (AMY) was purchased from SIGMA (25,1 mg/mL, 932 U/mg). L aspartate Oxidase (LASPO) used is this work is the wild type from *Sulfolobus tokodaii* that was overexpressed in *Escherichia coli* cells and purified to > 95% purity as described by Bifulco et al[74]. The purified batch of LASPO (2.255U/mL; 0.37U/mg) was stored in 20 mM Tris–HCl buffer at pH 7.5 and 10% glycerol. D-amino acid oxidase from *Rhodotorula gracilis* (DAAO) was produced as recombinant protein in *E.coli* and purified as stated. The purified DAAO (90 U/mg) was stored in 50 mM Potassium Phosphate buffer pH 7.5, 2 mM EDTA, 10% glycerol and 5mM 2-mercaptoethanol. LASPO and DAAO were provided by the laboratory of Prof. Loredano Pollegioni of the Biotechnology and Life Sciences Department of Università degli Studi dell'Insubria, Varese.

L-aspartate oxidase reduction

TCEP *reducing gel.* The enzyme reduction of LASPO was exploited through the TCEP reducing gel (PIERCE) according to the manufacturer protocol. Briefly, 1 mg of enzyme was added to an equal volume of TCEP reducing gel. The sample was incubated at RT under mechanical stirring for 45 min. The enzyme was centrifuged at 1000 rpm for 30 seconds. The supernatant was removed and discarded. After incubation, the sample was transferred into a spincup column, previously placed in a new tube, and centrifuge at 1000 rpm for 1 minute.

DTT reduction. 500 uL LASPO were reacted at room temperature and under stirring with 100 mM DTT or 200 mM DTT for 1 h. The sample was loaded with 1.5 mL of buffer on a PD10 column after its conditioning with 5 mM Sodium Pyrophosphate Buffer at pH 8.5. The reduced protein was eluted with 2 mL of buffer and the yellow fraction of the column was collected.

To determine the number of reduced thiol groups, was used the Ellman's Reagent. This reagent reacts with sulphydryl groups to produce 1 mol of 2-nitro-5-thiobenzoic acid (which absorbs at 412 nm) per mole of sulphydryl group.

Conjugations

LASPO conjugation was performed with five different strategies: for the standard protocol, 16 mg of NP-APTES were sonicated in 5 mM sodium pyrophosphate buffer at pH 8.5. Then a solution of EDC (65 mM final concentration) and NHS (13 mM final concentration) were added under sonication in a final volume of 2 mL, following by the addition of 200 μg of pure LASPO. The reaction was carried for 2 h at room temperature on a rotating plate tube stirrer. Subsequently, LASPO conjugated NPs (NP-LASPO1) were collected by a magnet and washed twice with 2 mL of 5 mM sodium pyrophosphate buffer, pH 8.5.

For the sulfo-SMCC- cysteine (NP-LASPO2), 1 mg of NP-APTES were suspended in 5 mM sodium pyrophosphate buffer pH 5, followed by the addition of a solution of sulfo-SMCC at a final concentration of 4 μM in a final volume of 1 mL. The reaction was incubated for 30 min at room temperature under mechanical stirring. After several washes, 1 mg of the previously reduced enzyme was added and the reaction was maintained under mechanical stirring for 30 min at room temperature. Then the particles were isolated by a magnet and suspended, after several washes, in 5 mM sodium pyrophosphate buffer pH 5.

For the conjugation of LASPO through the enzyme primary amine (NP-LASPO3), a BS3 solution (10 μM final concentration) was added to 1 mg of NP-APTES in 10 mM borate buffer pH 8.2. The reaction was maintained under mechanical stirring for 30 min at room temperature, then 1 mg of enzyme was added and the reaction was conducted at 40°C for 2 h in a final volume of 1 mL. After the addition of 100 mM Tris-HCl, the particles were isolated and, after several washes, were suspended in 1

mL of 10 mM borate buffer pH 8.2. For the NTA functionalization method (NP-LASPO4), the NTA-Cu^{2+} (40 µM final concentration) was introduced onto the NP-APTES following the same procedure of the BS3 functionalization method. The reaction was carried on in a final volume of 1 mL. The particles obtained were then incubated for 1 h at room temperature in presence of 1 mg of enzyme. The resulting NP-LASPO4 were isolated and, after several washes, were suspended in 1 mL of 10 mM borate buffer pH 8.2.

For the NP-LASPO3- pegylated, NP-APTES were modified with 18 µM of PEG-NH$_2$ in 1 mL final volume, using the BS3 protocol. After the addition of a BS3 solution, which reacted with the PEG-NP-APTES 30 min at room temperature, 1 mg of St-LASPO was added and the reaction was conducted for 2 h at 40°C. The resulting conjugated enzyme was stored at 4 °C until use.

8 mg of NP-APTES were sonicated in 20 mM sodium phosphate buffer and 6,7 mM HCl at pH 7 (NP-AMY1) or at pH 9 (NP-AMY2). Then a solution of EDC and NHS, in a final concentration of respectively 39 mM and 26 mM, was added under sonication in a final volume of 2 mL. Finally, 400 μg of α-amylase were added and the reaction was carried out for 24 h at 4°C on a rotating plate tube stirrer. Subsequently, α-amylase conjugated NPs were collected by a magnet and washed twice with 2 mL of buffer. For the conjugation of amylase through the enzyme primary amine (NP-AMY3), a BS3 solution (10 µM final concentration) was added to 0.2 mg of NP-APTES in 10 mM borate buffer pH 8.2. The reaction was maintained under mechanical stirring for 30 min at room temperature, then 1 mg of enzyme was added and the reaction was conducted at 40°C for 2 h in a final volume of 1 mL. After the addition of 100 mM Tris-HCl, the particles were isolated and, after several washes, were suspended in 1 mL of 10 mM borate buffer pH 8.2. The resulting conjugated enzyme was stored at 4 °C until use.

DAAO was conjugated as stated in the article entitled "Synthesis, characterization and programmable toxicity of iron oxide nanoparticles conjugated with D-amino acid oxidase" attached at the end of this chapter.

Enzymatic assay

The LASPO and NP-LASPO activity was assayed as reported in detailed in the article entitle "L-aspartate oxidase magnetic nanoparticles: synthesis, characterization and L-aspartate bioconversion." attached at the end of this chapter. Briefly, the activity was assayed by measuring the initial rate of production of hydrogen peroxide with a coupled peroxidase/dye assay. The standard assay mixture contained 10 mM L-aspartate in 50 mM sodium pyrophosphate buffer, pH 8.5, 1.5 mM 4-aminoantipyrine, 2 mM phenol, 20 mM FAD, 2.5 U of peroxidase, and StLASPO in a total volume of 1 mL. The activity was detected spectrophotometrically at 505 nm ($\varepsilon= 6.58$ mM^{-1} cm^{-1}). One unit (U) is defined as the amount of enzyme that catalyzes the degradation of 1 mmol of L-aspartate per min.

The 3,5-dinitrosalicyclic acid colorimetric assay was used to assess the enzymatic activity of the free and conjugated AMY[138]. For all experiments, starch was prepared gelatinized by heating until boiling for 10 min in the buffer of desired pH.

The NP-DAAO activity was determined as stated in the article entitled "Synthesis, characterization and programmable toxicity of iron oxide nanoparticles conjugated with D-amino acid oxidase" attached at the end of this chapter. Briefly, The activity was determined by measuring the absorbance increase accompanying the H_2O_2-induced oxidation of O-dianisidine at 440 nm (~13 mM^{-1}cm^{-1}). The standard assay mixture contained 89 mM D-Ala, 1.3 M O-dianisidine in H_2O MilliQ, 0.8 U of peroxidase and 4 μg NP-DAAO. One unit corresponds to the amount of enzyme that converts 1 μmol of substrate per min.

Nanoactuation

For LASPO the hyperthermia analysis were performed at 829 kHz and 252 Gauss. For AMY hyperthermia analysis were carried on in the range of 419-829 kHz frequency and an amplitude of 252 Gauss and with substrate at different pH values. For DAAO hyperthermia analysis were carried on in the range of 419-829 kHz frequency and an amplitude of 252 Gauss .The measurements were performed using D500 series (Nanoscale Biomaterial).

ANTIBIOTIC CONJUGATION

Microbial Strains and Culture Conditions

Escherichia coli ATCC 35218, *Bacillus subtilis* ATCC 6633 and *Staphylococcus aureus* ATCC 6538P were obtained from the American Type Culture Collection (ATCC). *E. coli* and *B. subtilis* were propagated overnight in Luria Bertani medium (LB, 2% tryptone, 2% yeast extract, 1% NaCl) while *S. aureus* in Muller Hilton broth (MHB) with continuous shaking at 200 rpm and 37°C. For exponential growth, overnight cultures were transferred to fresh medium: inocula were prepared to start the cultures with an optical density at 600 nm (OD600 nm) of 0.1 in the final medium. For long-term preservation, bacterial cultures were stored at -20°C in 20% glycerol.

Conjugation

For the preparation of teicoplanin-conjugated NPs (NP-TEICO), a solution of teicoplanin (500 µg), 13 mM EDC and 26 mM NHS was prepared and added to the NP-APTES (4 mg/mL) dispersed in 30 mM MES buffer pH 6.0 in a final volume of 1 mL. The reaction was mixed for 6 h at room temperature. NP-TEICO were washed twice and resuspended in fresh 30 mM MES buffer at pH6.

HPLC Analysis

Teicoplanin was measured by HPLC following the method previously reported[131]. HPLC analyses were performed on a 5-µm particle size Symmetry C18 (VWR International LCC, Radnor, PA, USA) column (4.6 × 250 mm). The column was eluted at 1 mL/min flow rate with a 30-minute linear gradient from 15% to 65% of Phase B, followed by 10 min with 100% Phase B. Phase A was 32 mM $HCOONH_4$ pH 4.5: CH_3CN 90:10 (v/v) and Phase B was 32 mM $HCOONH_4$ pH 4.5:CH_3CN 30:70 (v/v) mixture. The chromatography was performed with a model 1100 HPLC system (Elite Lachrom VWR Hitachi LL) and UV detection was at 236 nm.

Binding Stability and activity stability

To evaluate the stability of NP-TEICO in different media and different temperatures, NP-TEICO were suspended in MES buffer at 5.5, 6.0 and 7.12 and stored at -20, 4 and 25°C. At defined time point, the sample was centrifuged and the amount of

teicoplanin was quantified by spectrophotometric assay. Teicoplanin was appropriately diluted in MES buffer and the absorbance was measured at 280 nm, using quartz cuvette.

Antimicrobial susceptibility test

Antimicrobial activities of IONPs, NP-APTES and NP-TEICO were tested against the *E. coli*, *B. subtilis* and *S. aureus* strains by agar diffusion assay method[139]. Briefly, bacterial cultures after an overnight LB or MHB growth, were used to inoculate the test strains in agar plates containing Difco Nutrient Agar (DNA agar, Difco) for *B. subtilis* and *E. coli* or Muller-Hilton Agar (MHA) for *S. aureus* and left to dry. 10 μL of IONPs, NP-APTES, and NP-TEICO preparations in 30 mM MES buffer pH 6 and of teicoplanin solution in the same buffer were loaded directly on the inoculated plates. Plates were incubated at 37°C for 24 h. The diameters of zones of bacterial growth inhibition surrounding the droplets were measured.

Determination of the minimum inhibitory concentration

The minimum inhibitory concentrations (MICs) of teicoplanin and NP-TEICO were determined against *B. subtilis* and *S. aureus* by broth dilution method using MHB, as recommended by the Clinical & Laboratory Standards Institute guidelines[140]. About 5×10^4 exponentially growing bacterial cells were inoculated into MHB containing increasing concentrations (in terms of teicoplanin of 0; 0.5, 1; 2; 4; 8; 16; 32; 64; 64; 128 μg/mL) of teicoplanin and NP-TEICO in 30 mM MES buffer pH 6, and shaken for 16 h at 37°C. MICs were the minimal concentrations of teicoplanin or of NP-TEICO at which no turbidity was detectable.

Determination of the minimum bactericidal concentration

The minimum bactericidal concentrations (MBC) of teicoplanin and NP-TEICO were determined against *B. subtilis* and *S. aureus* according to Clinical & Laboratory Standards Institute guidelines. This is an extension of the MIC procedure: 200 μL of dilutions in which no visible bacterial growth was present were plated on MHA. After incubation at 37 ° C for 16 hours, the colonies on the plate were counted.

Determination of tolerance level

Tolerance level of each strain against teicoplanin and NP-TEICO was determined as reported in literature using the formula: Tolerance = MBC/MIC[141].

Kinetic Growth Curve

The growth kinetics of *B. subtilis*, *S.aureus* and *E. coli* in absence and presence of IONPs, NP-APTES and NP-TEICO. The mother cultures of test organisms were prepared in LB broth taking loop full of bacteria from the specified slant culture, and cultured overnight at 37 °C and 200 r.p.m agitation. The NPs stock solution was prepared by dispersing the IONPs, NP-APTES and NP-TEICO (4 mg/mL) in 30 mM MES buffer pH 6.0. The NPs stock solutions were added to bacterial cultures prepared in Falcon tube in a final volume of 10 mL. The growth kinetic studies were performed by measuring optical density (O.D.) at 600 nm using an UV-Vis V-560 Spectrophotometer (JASCO, MD, USA) at regular time interval. The reaction mixtures without NPs and with free teicoplanin were taken as controls. Upon addition of IONPs, NP-APTES and NP-TEICO, data collection for growth curve was immediately started with dead time of 5 min.

CFU measurement

The number of viable cells were quantified by measuring colony forming units (CFUs) for all types of bacteria upon treatment with teicoplanin, IONPs, NP-APTES, and NP-TEICO, as reported above. For CFU measurement, 10 µL of sample from the stationary phase of growth kinetics were spread on the nutrient agar plates after 10^4 and 10^5 times dilution in LB or MHB. The plates were incubated overnight at 37°C. The number of viable cells after treatment with teicoplanin, IONPs, NP-APTES, and NP-TEICO were quantified and compared with the control culture without any addition.

Interaction pattern

Fluorescence

To visualize the interaction pattern of IONPs, NP-APTES and NP-TEICO with bacteria was used LIVE/DEAD BacLight fluorescence assay (L7007, Molecular probes, ThermoFisher Scientific). Following the manufacturer's protocol, bacteria

were culture over night at 37 °C 200 rpm, appropriately diluted and treated. From these cultures, 10 mL of each bacterial solutions were centrifuged at 7000 r.p.m for 15 min. The supernatants were discarded and the pellets were suspended in saline solution (0.9 %). Samples were incubated at RT for one hour (mixing every 15 min). The suspensions were centrifuged at 7000 r.p.m for 15 min, pellets were collected and suspended in an equal volume and centrifuged at 7000 r.p.m for 15 min. Finally, the pellets were suspended in saline solution (0.9 %). 3 µL of dye mixture were added to each 1 mL of the prepared bacterial samples and incubated in dark for 15 min after proper mixing of bacterial suspensions. Fluorescence images were taken by trapping 5 µL of stained bacterial samples between a slide and cover slip. For imaging the samples, an optical microscope with appropriate filters was employed (Axiophot, Carl

Electron microscopy

The interaction pattern was also studied with TEM analysis. After 7 h of exposure to IONPs, NP-APTES, NP-TEICO and Teicoplanin, pellets were washed with PBS and fixed in Karnovsky solution (4% formaldehyde, 2% glutaraldehyde, 0.1 M sodium cacodylate, pH 7.2 overnight at 4 °C. Samples were washed three times in 0.1 M sodium cacodylate for 10 min and postfixed in dark for 1 hour with 1% osmium tetroxide in 0.1 M sodium cacodylate-buffer (pH 7.2) at RT. After dehydration with a series of ethyl alcohol, samples were embedded in an Epon-Araldite 812 1:1 mixture. Thin sections (90 nm), obtained with a Pabisch Top-Ultra ultramicrotome (Emme 3 S.r.l., Milan, Italy), were observed with a Morgagni electron microscope (Philips, Eindhowen, NL) operated at 80 KeV.

Cell cultures

Two different cell lines were used to evaluate the NP-TEICO in vitro cytotoxicity: as a tumor model SKOV-3 cell line from ovary adenocarcinoma and as non-tumor cell line, the hASCs (human Adipose-derived Stem Cells) cell line. hASC were isolated and cultured as reported in the article entitled "Effects of Metal Micro and Nano-Particles on hASCs: An In Vitro Model", while SKOV-3 were cultured as stated in the article entitled "Synthesis, characterization and programmable toxicity of iron

oxide nanoparticles conjugated with D-amino acid oxidase", attached at the end of this chapter.

Cell Exposure and Viability

Cell viability was determined measuring ATP content by the RealTime-Glo™ MT Cell Viability Assay (Promega, Milan, Italy) according to the manufacturer's instructions. Briefly, 500 cells were plated in a 96-well plates in 200 µL of cell medium (RPMI for SKOV-3 and DMEM/DMEM F12 1:1 for ASC). After 24 h, cells were exposed to increasing concentrations (0, 6, 46, 364 µg/mL) of IONPs, NP-TEICO and TEICO and a solution 2X of substrate and NanoLuc® Enzyme was added. Cells were incubated at 37°C and 5% CO_2-humidified atmosphere for all the experiment period. Luminescence was read every 24h using the Infinite F200 plate reader (Tecan Group, Männedorf, Switzerland).

Statistical analysis

Each plotted value is the mean of three independent experiments. All data for were analyzed with one-way Analysis of Variance ANOVA ($\alpha = 0.05$), completed with Dunnett's test ($p < 0.05$) in order to determine which groups were significantly different from control. Statistical significant differences was fixed at $p \leq 0.05$ (*).

CrossMark
click for updates

Synthesis, characterization and programmable toxicity of iron oxide nanoparticles conjugated with D-amino acid oxidase†

Riccardo Balzaretti,[*a] Fabian Meder,[b] Marco P. Monopoli,[bc] Luca Boselli,[b] Ilaria Armenia,[a] Loredano Pollegioni,[ad] Giovanni Bernardini[ad] and Rosalba Gornati[ad]

D-amino acid oxidase (DAAO) is an enzyme which generates reactive oxygen species (ROS) and it is believed to have potential uses as a novel therapeutic molecule if internalized by cancer cells or if they are localized close to their plasma membrane. When conjugated onto iron oxide nanoparticles (NPs), the enzyme can be magnetically directed to targeted locations with an increased efficacy. A subsequent injection of DAAO substrate D-alanine can initiate ROS production and induce apoptosis of cells surrounding the NP-DAAO complex. Here, we describe a platform for optimal bioconjugation using monodisperse γ-Fe$_2$O$_3$ NPs ($\sim$10 nm) resulting in high DAAO loading, stable NP-DAAO dispersions and more than 90% enzymatic activity recovery, which is retained using the particles in human serum. Lastly, since the NP-DAAO system is designed for cancer therapy, we proved its efficacy in killing SKOV-3, U87 and HCT-116 cancer cells.

Nanobiotechnology has found widespread applications[1] in biomedicine as diagnostic imaging tools,[2,3] drug delivery systems,[4,5] vaccines[6,7] and in immunotherapy.[8] NPs can be employed to produce a great variety of bioconjugates by grafting biomolecules onto a NP carrier. In oncology, for example, recent studies have shown that engineered NPs are capable of reaching specific targeted areas of the body and of releasing the therapeutic drug locally.[9–12] This novel approach has the potential to increase the drug efficacy and to eliminate the side effects.[13] To guide the bioconjugates through the body, one can use magnetic NPs that, after intravenous administration, can be directed to the cancerous tissue with an external magnetic field.[14] Magnetic NPs alone are used as an effective anticancer agent during hyperthermic therapy in which NPs exposed to an alternating magnetic field produce heat that kills all the surrounding cells.[15–19]

D-Amino acid oxidase from *Rhodotorula gracilis* (*Rg*DAAO, EC 1.4.3.3) is a flavoenzyme that utilizes D-amino acids to produce reactive oxygen species (ROS)[20] and can be used to induce apoptosis. In particular the co-administration with D-alanine as

substrate, gives the corresponding α-keto acid, ammonia and H$_2$O$_2$. Despite the benefit in using this enzyme in therapeutic applications, the main limitations are the low enzyme stability, the low efficacy in cellular internalization and the lack of specific molecular targeting. To overcome these limitations, in the past few years different attempts have been made in the development of NP-DAAO systems where the enzyme was covalently bound to the amino groups of APTES functionalized NPs. That resulted in an increased cellular internalization of the enzyme, a prolonged enzymatic activity and storage stability, and the possibility of targeting to the cancer mass with the help of an external magnetic field. However, while the APTES functionalization represents a good amino group donor, its activation *via* glutaraldehyde can affect the enzyme integrity[21] leading to a loss of DAAO activity.[22,23] Cappellini *et al.*[24] reported a higher yield for the NP-DAAO synthesis when conducted *via* EDC/NHS instead of with glutaraldehyde. Furthermore, also the NP diameter and aggregation influence the amount of loaded enzyme.[25]

Here, we present a NP-DAAO system starting from the synthesis of γ-Fe$_2$O$_3$ NPs to obtain small and monodispersed γ-Fe$_2$O$_3$–APTES NPs to increase as much as possible the surface area available for the surface functionalization.

γ-Fe$_2$O$_3$ NP cores were synthetized following Geppert *et al.*[26] (ESI†) and they were subsequently functionalized with APTES using a standard protocol and then conjugated with DAAO by coupling with 1-ethyl-3-(3-dimethylaminopropyl) carbodiimide hydrochloride (EDC) and *N*-hydroxysuccinimide (NHS), as summarized in Fig. 1. The *Rg*DAAO enzyme was provided by the laboratory of Prof. Loredano Pollegioni of the Biotechnology and Life Sciences Department of Università degli Studi

aDepartment of Biotechnology and Life Sciences, University of Insubria, Varese, Italy. E-mail: riccardo.balzaretti@uninsubria.it

bCentre for Bionano Interactions, University College Dublin, Dublin, Ireland

cDepartment of Pharmacy and Medical Chemistry, Royal College of Surgeons in Ireland, 123 St. Stephen Green, Dublin 2, Ireland

dThe Protein Factory Research Center, Politecnico di Milano, University of Insubria, Milan, Varese, Italy

† Electronic supplementary information (ESI) available: Synthesis of γ-Fe$_2$O$_3$ NPs, TEM analysis, DLS and DCS details, cell culture details, comparison with the previous NP-DAAO system. See DOI: 10.1039/c6ra25349k
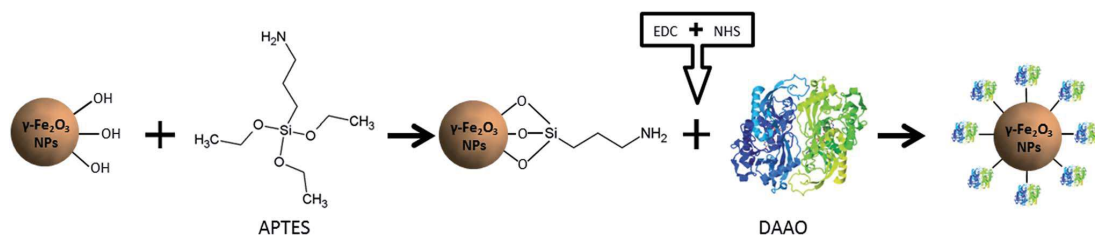
Fig. 1 Schematic representation of the NP–DAAO system formation process.

dell'Insubria, Varese. The γ-Fe_2O_3 NPs, NP-APTES and NP-APTES–DAAO were characterized by Dynamic Light Scattering (DLS), by Differential Centrifugal Sedimentation (DCS) and by Transmission Electron Microscopy (TEM) (ESI†).

The DLS characterization analysis (Fig. 2a) reports a diameter of about 38 nm for the synthetized γ-Fe_2O_3 NPs and about 47 nm for the APTES functionalized ones. After conjugation with the enzyme, the NP-DAAO complex acquires a larger diameter of approximately 185 nm.

The DCS characterization (Fig. 2b) is similar to the one obtained by DLS. The surface functionalization with APTES and DAAO results in a change in the particle sedimentation time. The NP-APTES and NP-DAAO have respectively an apparent size of 24 nm and 76 nm: this is due to a change in sample density as also reported elsewhere.[27,28]

At a glance, the TEM pictures (ESI†) do not suggest any notable changes in NP size as shown by DLS and DCS analysis. However, the TEM picture analyses (ESI†) reported that γ-Fe_2O_3 NPs, NP-APTES and NP-DAAO possess an average size of respectively 8.5, 10.3 and 11.0 nm. These results can be probably due to a slight NPs aggregation during DLS and DCS analysis.

The amount of DAAO bound on the NP surface was determined by considering the difference between the starting amount of RgDAAO and the protein recovered in the supernatant at the end of the conjugation reaction. The quantification of conjugated DAAO was performed using the extinction coefficient at 455 nm ($\sim$12.6 mM^{-1} cm^{-1})[20] and an UV-Vis V-560 Spectrophotometer (JASCO, MD, USA). The amount of stock DAAO used for the conjugation to NP-APTES has been chosen starting from the ratio of µg of DAAO per NP-APTES surface area (calculated from the average particle diameter, assuming spherical particles) used by Cappellini *et al.*[24] and then moving to DAAO saturation per NP-APTES. For one mg of NP-APTES particles up to 446 µg of RgDAAO was bound (Fig. 3a). Moreover, to determine the functionality of the NP-DAAO particles, we checked their enzymatic activity by measuring the absorbance increase accompanying the H_2O_2-induced oxidation of *o*-dianisidine. This reaction was initiated by the addition of the enzyme and the absorbance increase was monitored at 440 nm for 1 min.

The conjugation yield and the activity recovery of these NP-DAAO particles were of 100% and 91% respectively (Fig. 3a). Since the specific activity of the RgDAAO stock solution was 59 U mg^{-1}, we estimated up to 24 U per mg of NP-APTES. The NPs here synthesized showed a smaller diameter compared to the ones used by Cappellini *et al.*[24] and this allowed a 7 fold increase of the DAAO/NP (w/w) ratio.

Then, we detected the thermal stability of the NP-DAAO system, as enzymatic residual activity, after 1 hour incubation

Sample	γ-Fe_2O_3 NPs	NP-APTES	NP-DAAO
Z-Average (d.nm)	38.3 ± 0.4	47 ± 0.2	185.1 ± 6.1
Polydispersity Index (PDI)	0.191	0.123	0.279

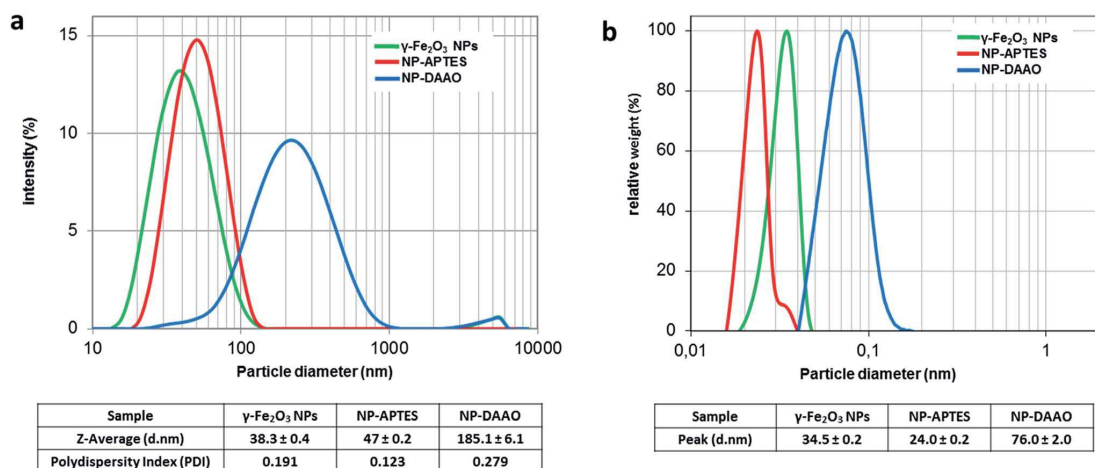| Sample	γ-Fe_2O_3 NPs	NP-APTES	NP-DAAO
Peak (d.nm)	34.5 ± 0.2	24.0 ± 0.2	76.0 ± 2.0

Fig. 2 DLS (a) and DCS (b) analysis of γ-Fe_2O_3 NPs, NP-APTES and NP-DAAO. The polydispersity index is from cumulant fitting.
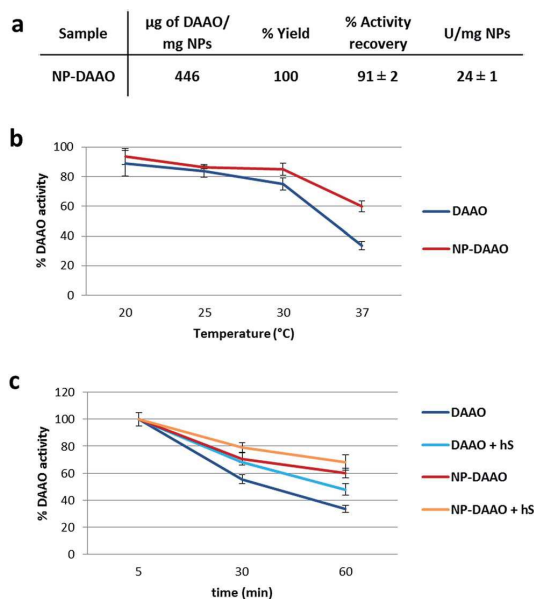
Paper

Fig. 3 (a) NP-DAAO system features; U are enzymatic units of DAAO. (b) Thermal stability, measured as enzymatic activity, of the NP-DAAO system after 1 h incubation; (c) effect of 10% human serum (hS) on NP-DAAO during 1 h incubation. Error bars represent mean ± SD, $N = 3$.
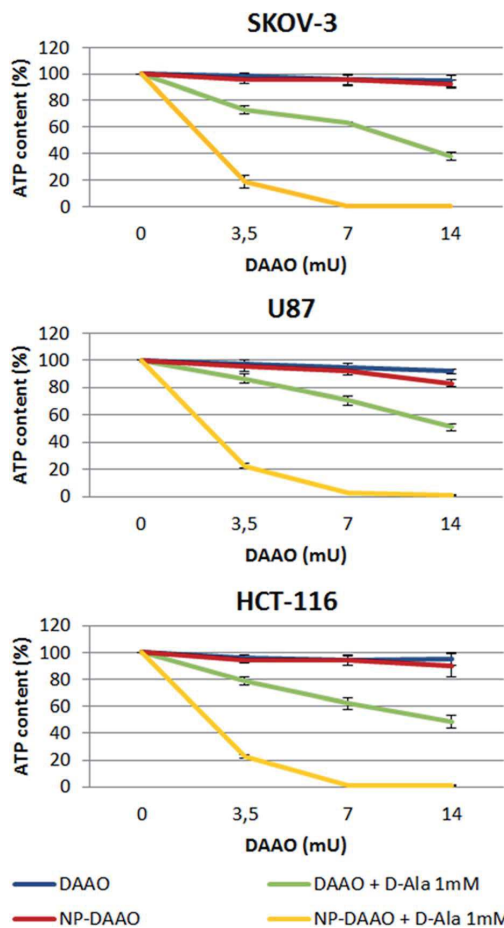

Fig. 4 Cell viability is expressed as a percentage of ATP content after 24 h exposure to 3.5, 7 or 14 mU of NP-DAAO or free DAAO, with and without the substrate D-Ala. Error bars represent mean ± SD, $N = 3$.

at different temperature (Fig. 3b) (ESI†). At 37 °C the NP-DAAO system is about 1.8 fold more stable compared to free DAAO.

Since this NP-DAAO system, thought for cancer therapy, has to be injected intravenously to perform its activity, we checked its stability also at 37 °C when exposed to 10% human serum (Sigma-Aldrich) (Fig. 3c). These results indicate that human serum has an active role in preserving the activity of both DAAO and NP-DAAO system.

Lastly, we tested the efficacy of the NP-DAAO system on the three tumor cell lines SKOV-3, HCT116 and U87 (Sigma-Aldrich) (Fig. 4). In this experiment, 10 000 cells were exposed for 24 h to an increasing amount, expressed as DAAO units, of free DAAO or NP-DAAO with or without D-alanine (D-Ala). Hence, the cell viability was determined as ATP content by recording the luminescent signal after using the CellTiter-Glo Luminescent Cell Viability Assay (Promega). The results reported in Fig. 4 show a very low cytotoxicity when cells are exposed to 7 mU of NP-DAAO particles without D-alanine. However, when D-Ala is added a full cell death was apparent. If compared to the NP-DAAO particles present in literature,[23] the new particles result less cytotoxic whilst the effectiveness remains unchanged in the presence of the substrate: this can be explained by the lower amount of NP-DAAO particles required to reach the same DAAO activity (ESI†). We have performed preliminary experiments exposing human adipose stem cells (hASC), isolated from adipose tissue, to NP-DAAO. The results have shown that hASC are less responsive than tumor cell lines to the H_2O_2 produced by the NP-DAAO in presence of D-Ala.

Conclusions

In conclusion, the new NP-DAAO particles represent a remarkable improvement of this NP-enzyme system.

With a reduced amount of NPs required for the same enzymatic activity, we have obtained a safer and more efficient NP-DAAO system that might be used for cancer therapy, but also for biocatalysis. The new NPs, thanks to their smaller size, can bind about 7 times more enzyme than the previous ones[28] thus increasing the efficacy and reducing the NP-DAAO system toxicity before external stimulation of ROS production (ESI†). Since smaller NPs might result more cytotoxic,[29] *in vivo* experiments will be performed to assay their toxicity and half-life once injected into the blood stream.

It has been previously reported that enzymes conjugated to NPs may present a higher activity, a better specificity, a prolonged half-life, an enhanced thermal stability and, in some

cases, even an enzymatic acceleration.[30–32] In agreement with these reports, we have observed a prolonged storage half-life (ESI†) and an enhanced thermal stability (Fig. 3b). Conversely, we did not notice an increase of the enzymatic activity. In addition, the susceptibility of the NP-enzyme system to a magnetic field allows, in nanomedicine, its targeting to the desired area of the body, and, in biocatalysis, its efficient recovery enabling its reuse for several times and preventing the contamination of the final product.[30]

Acknowledgements

Notes and references

1 A. G. Cattaneo, R. Gornati, E. Sabbioni, M. Chiriva-Internati, E. Cobos, M. R. Jenkins and G. Bernardini, *J. Appl. Toxicol.*, 2010, **30**, 730–744.

2 S. K. Nune, P. Gunda, P. K. Thallapally, Y.-Y. Lin, M. L. Forrest and C. J. Berkland, *Expert Opin. Drug Delivery*, 2009, **6**(11), 1175–1194.

3 Y.-X. J. Wang, S. Xuan, M. Port and J.-M. Idee, *Curr. Pharm. Des.*, 2013, **19**, 6575–6593.

4 S. Onoue, S. Yamada and H.-K. Chan, *Int. J. Nanomed.*, 2014, **9**, 1025–1037.

5 L. Liu, Q. Ye, M. Lu, Y.-C. Lo, Y.-H. Hsu, M.-C. Wei, Y.-H. Chen, S.-C. Lo, S.-J. Wang, D. J. Bain and C. Ho, *Sci. Rep.*, 2015, **5**, 10881.

6 D. Boraschi and P. Italiani, *Vaccines*, 2015, **3**, 930–939.

7 Y. Fan and J. J. Moon, *Vaccines*, 2015, **3**, 662–685.

8 C. Petrarca, E. Clemente, V. Amato, P. Pedata, E. Sabbioni, G. Bernardini, I. Iavicoli, S. Cortese, Q. Niu, T. Otsuki, R. Paganelli and M. Di Gioacchino, *Clin. Mol. Allergy*, 2015, **13**, 13.

9 S. Barua and S. Mitragotri, *Nano Today*, 2014, **9**, 223–243.

10 C. Castellini, S. Ruggeri, S. Mattioli, G. Bernardini, L. Macchioni, E. Moretti and G. Collodel, *Syst. Biol. Reprod. Med.*, 2014, **60**, 143–150.

11 T. Coccini, R. Gornati, F. Rossi, E. Signoretto, I. Vanetti, G. Bernardini and L. Manzo, *J. Nanomed. Nanotechnol.*, 2014, **5**, 227.

12 M. Masserini, *ISRN Biochem.*, 2013, 238428.

13 J. R. Kanwar, G. Mahidhara and R. K. Kanwar, *Nanomedicine and Cancer Therapies*, 2013, vol. 2, pp. 1–18.

14 M. Liberatore, M. Barteri, V. Megna, P. D'Elia, S. Rebonato, A. Latini, F. De Angelis, F. Scaramuzzo, A. Francesca, M. E. De Stefano, N. A. Guadagno, S. Chondrogiannis, A. M. Maffione, D. Rubello, A. Pala and P. M. Colletti, *Clinical Nuclear Medicine*, 2015, **40**(2), e104–e110.

15 E. K. Lim, E. Jang, K. Lee, S. Haam and Y. M. Huh, *Pharmaceutics*, 2013, **5**(2), 294–317.

16 J. H. Lee, K. J. Chen, S. H. Noh, M. A. Garcia, H. Wang, W. Y. Lin, H. Jeong, B. J. Kong, D. B. Stout, J. Cheon and H. R. Tseng, *Angew. Chem., Int. Ed.*, 2013, **52**, 1–6.

17 M. H. Cho, E. J. Lee, M. Son, J. H. Lee, D. Yoo, J. W. Kim, S. W. Park, J. S. Shin and J. Cheon, *Nat. Mat.*, 2012, **11**, 1038–1043.

18 C. R. Thomas, D. P. Ferris, J.-H. Lee, E. Choi, M. H. Cho, E. S. Kim, J. F. Stoddart, J.-S. Shin, J. Cheon and J. I. Zink, *J. Am. Chem. Soc.*, 2010, **132**, 10623–10625.

19 K. Katagiri, Y. Imai, K. Koumoto, T. Kaiden, K. Kono and S. Aoshima, *Small*, 2011, **7**(12), 1683–1689.

20 L. Pollegioni, G. Molla, S. Sacchi, E. Rosini, R. Verga and M. S. Pilone, *Appl. Microbiol. Biotechnol.*, 2008, **78**(1), 1–16.

21 I. Migneault, C. Dartiguenave, M. J. Bertrand and K. C. Waldron, *BioTechniques*, 2004, **37**(5), 790–802.

22 H. C. Hsieh, I. C. Kuan, S. L. Lee, G. Y. Tien, Y. J. Wang and C. Y. Yu, *Biotechnol. Lett.*, 2009, **31**, 557–563.

23 A. Bava, R. Gornati, F. Cappellini, L. Caldinelli, L. Pollegioni and G. Bernardini, *Nanomedicine*, 2013, **8**(11), 1797–1806.

24 F. Cappellini, C. Recordati, M. De Maglie, L. Pollegioni, F. Rossi, M. Daturi, R. Gornati and G. Bernardini, *Future Sci. OA*, 2015, **1**, 4.

25 J. Conde, J. T. Dias, V. Grazú, M. Moros, P. V. Baptista and J. M. de la Fuente, *Front. Chem.*, 2014, **2**, 48.

26 M. Geppert, M. Hohnholt, L. Gaetjen, I. Grunwald, M. Bäumer and R. Dringen, *J. Biomed. Nanotechnol.*, 2009, **5**, 285–293.

27 M. P. Monopoli, D. Walczyk, A. Campbell, G. Elia, I. Lynch, F. B. Bombelli and K. A. Dawson, *J. Am. Chem. Soc.*, 2011, **133**(8), 2525–2534.

28 Z. Krpetić, A. M. Davidson, M. Volk, R. Lévy, M. Brust and D. L. Cooper, *ACS Nano*, 2013, **7**(10), 8881–8890.

29 M. Saji, M. Ilyas, C. Basheer, M. Tariq, M. Daud, N. Baig and F. Shehzad, *Environ. Sci. Pollut. Res. Int.*, 2015, **22**(6), 4122–4143.

30 S. A. Ansari and Q. Husain, *Biotechnol. Adv.*, 2012, **30**(3), 512–523.

31 B. J. Johnson, W. Russ Algar, A. P. Malanoski, M. G. Ancona and I. L. Medintz, *Nano Today*, 2014, **9**, 102–131.

32 S. Ding, A. A. Cargill, I. L. Medintz and J. C. Claussen, *Curr. Opin. Biotechnol.*, 2015, **34**, 242–250.

PAPER

Check for updates

L-aspartate oxidase magnetic nanoparticles: synthesis, characterization and L-aspartate bioconversion

Ilaria Armenia, [ID][a] Riccardo Balzaretti, [ID][a] Cristina Pirrone,[a] Chiara Allegretti,[b] Paola D'Arrigo,[bcd] Mattia Valentino,[cd] Rosalba Gornati,[ac] Giovanni Bernardini [ID] *[ac] and Loredano Pollegioni[ac]

The FAD-containing enzyme L-aspartate oxidase (LASPO) catalyzes the stereospecific oxidative deamination of L-aspartate and L-asparagine functioning under both aerobic and anaerobic conditions. LASPO possesses distinctive features that make it attractive for biotechnological applications. In particular, it can be used for the production of D-aspartate from a racemic mixture of D,L-aspartate, a molecule employed in the pharmaceutical industry, for parenteral nutrition, as a food additive and in sweetener manufacture. Since the industrial application of LASPO is hampered by the high cost per enzymatic unit, several attempts have been performed to improve its reusability, such as LASPO immobilization on various matrices. In this context, magnetic nanoparticles (NPs) have recently become available for the immobilization of enzymes. In this work, we have covalently immobilized LASPO from the thermophilic archaea *Sulfolobus tokodaii* on iron oxide NPs using 1-ethyl-3-(3-dimethylaminopropyl) carbodiimide and hydroxysuccinimide as cross-linking agents. The NP-LASPO system showed a better stability than the free enzyme, was reused five times reaching full L-aspartate conversion and yielded a productivity (>3 μmol per h per unit) similar to that obtained with the free enzyme or with the enzyme immobilized on classical chromatographic supports. The NP-LASPO system can be easily recovered after each cycle. These results indicate that the prepared NP-LASPO system has promising industrial applications.

Introduction

The FAD-containing enzyme L-aspartate oxidase (LASPO, EC 1.4.3.16) catalyzes the stereospecific oxidative deamination of L-aspartate and L-asparagine to the corresponding imino acid and, following spontaneous hydrolysis, an α-keto acid (*i.e.* oxaloacetate from L-aspartate) along with the production of ammonia and hydrogen peroxide. The ability of LASPO to use both O_2 and fumarate in reoxidation of the reduced flavin cofactor enables it to function under both aerobic and anaerobic conditions.[1] This agrees with the physiological role of the enzyme in prokaryotes, which is to catalyze the first step of NAD+ biosynthesis. Notably, LASPO distinguishes from the family members of the amino acid oxidases, most closely resembling the succinate dehydrogenase/fumarate reductase

family of flavoproteins; indeed, LASPO is not evolutionarily related to the L-amino acid oxidase members.[2]

In past years, we focused on LASPO from the thermophilic archaea *Sulfolobus tokodaii* (StLASPO), a monomeric protein (comprising 472 residues, 52 kDa) which folds into three distinct domains: a FAD-binding domain, a capping domain, and a helical domain.[3] StLASPO is produced as a recombinant protein in *E. coli*, while classical L-amino acid oxidases with a broad substrate specificity are not. It is produced as active holoenzyme (the flavin cofactor is tightly, but non-covalently, bound to the protein moiety) reaching up to 9% of the total proteins in the crude extract and 13.5 mg L^{-1} in the fermentation broth.[3,4]

We focused on this enzyme since it possesses distinctive features that make it attractive for biotechnological applications.[5] Indeed, LASPO possesses high thermal stability (it is fully stable up to 80 °C), high temperature optimum, stable activity in a broad range of pH (7.0–10.0), weak inhibition by the product and by the D-isomer of aspartate, and a quite low Km for dioxygen (0.3 mM). These properties make StLASPO a potential useful novel tool in biocatalysis where it can be used in applications resembling those developed for D-amino acid oxidase of opposite enantioselectivity.[6] In particular, it can be used for the production of D-aspartate, a molecule

[a]Dipartimento di Biotecnologie e Scienze della Vita, Università degli Studi dell'Insubria, Via J.H. Dunant 3, 21100 Varese, Italy. E-mail: giovanni.bernardini@uninsubria.it

[b]Dipartimento di Chimica, Materiali e Ingegneria Chimica "Giulio Natta", Politecnico di Milano, Piazza Leonardo da Vinci 32, 20133 Milano, Italy

[c]The Protein Factory, Politecnico di Milano, ICRM CNR Milano, Università degli Studi dell'Insubria, Via Mancinelli 7, 20131 Milano, Italy

[d]CNR – Istituto di Chimica del Riconoscimento Molecolare (ICRM), Via Mancinelli 7, 20131 Milano, Italy

employed in the pharmaceutical industry, for parenteral nutrition, as food additive and in sweetener manufacturing.[5] On this side, when applied in the free form, the resolution of a 50 mM racemic mixture of D,L-aspartate was obtained in one day using 9 U of StLASPO (final e.e. > 99.5%).[4]

To facilitate industrial applications by improving reusability and, hence, by reducing the costs, StLASPO was immobilized on various matrices. The best results in terms of immobilization yield and volumetric activity have been obtained through the free amino groups of the enzyme by using the supports Relizyme™ HA403/S R and SEPABEADS® EC-EP/S or when prepared as cross-linked enzyme aggregates. The Relizyme-StLASPO immobilized preparation was reused for three cycles keeping full oxidation of L-aspartate, in ≤2 hours starting from a 50 mM racemic mixture: in a semi-preparative scale reaction, 66 mg of D-aspartate per day were produced using 20 U of StLASPO.[7]

With the development of nanotechnology, magnetic nanoparticles (NPs) have become available for the immobilization of enzymes. Magnetic NPs, when small enough, show superparamagnetic behaviors with a fast response to applied magnetic fields and with negligible residual magnetism and coercitivity. This means that these NPs can be magnetized with an external magnetic field and immediately redispersed once the magnet is removed.[8] We have recently functionalized iron oxide NPs with D-amino acid oxidase for therapeutic purposes and obtained a magnetic nano-enzymatic system capable of producing, in presence of its substrate, reactive oxygen species.[9,10] This system, which possesses relatively low toxicity,[11] might be driven to the target area by an external magnetic field. Magnetic nano-enzymes can be used in several other fields such as biosensors for environmental pollutants and clinical sensors for biomolecules. A caveat, when using NPs, is always a concern about their safety.[12] Iron NPs, however, have been shown to exert a relatively low toxicity.[11,13]

The application of StLASPO has few limitations due to the high cost per enzymatic unit and inability of separation. Among the approaches useful to improve the enzyme stability, the immobilization has proven particularly valuable. On this side, significant improvement has been made by enzyme immobilization onto magnetic nanocarriers. They can be advantageously employed as industrial catalysts since they have high surface area, large surface-to-volume ratio, lower hindrance, allow to regulate the orientation of the enzyme on the support and to easily remove the enzyme by applying a magnetic field.[14,15]

To generate an immobilized StLASPO system differing in mechanical, physical and diffusional properties, we focused on the setup of magnetic NP-LASPO that can be easily recovered from the reaction mixture and, potentially, applied under different practical conditions as compared to classical resin-immobilized enzyme preparations. Following the optimization of the immobilization procedure, the NP-LASPO system was characterized for the main physical–chemical properties and then used to convert L-aspartate into oxaloacetate and ammonia. The flavoenzyme system can be reused for 4 cycles with no loss of activity. This result paves the way to the set-up of innovative biocatalytic processes.

Experimental

Chemicals

Iron oxide nanoparticles (Fe_3O_4NPs, <50 nm), (3-aminopropyl)triethoxylsilane (APTES), 1-ethyl-3-(3-dimethylaminopropyl)carbodiimide (EDC), hydroxysuccinimide (NHS), 4-amino antipyrine (4-AAP), L-aspartic acid, glycine, phenol: all purchased from Sigma Aldrich (Milan, Italy). Horseradish peroxidase (POD) was purchased from Roche (Milan, Italy).

Enzyme preparation

StLASPO was overexpressed in *E. coli* cells and was purified to >95% purity by the procedure described by (ref. 4). The purified StLASPO was stored in 20 mM Tris–HCl buffer at pH 7.5 and 10% (v/v) glycerol; its specific activity was ~0.43 U mg^{-1} of protein on L-aspartate as substrate.

Functionalization of NPs with APTES

Fe_3O_4NPs were functionalized according to the protocol of (ref. 16). Briefly, 5 mL of 2% (v/v) APTES in milliQ water were added to a suspension of Fe_3O_4NPs (150 mg) and the reaction was maintained under mechanical stirring for 5 h at 50 °C. Amino-functionalized nanoparticles (NP-APTES) were then separated from unbound APTES by a commercial parallelepiped neodymium magnet (Webcraft GmbH, Uster, Switzerland; Ni–Cu–Ni plated; magnetization: N45; size: 30 × 30 × 15 mm), washed several times with water and anhydrified with ethanol overnight. NPs were suspended in water, isolated and dried at 50 °C overnight.

Synthesis of NP-LASPO

16 mg of NP-APTES were sonicated in 5 mM sodium pyrophosphate buffer at pH 8.5. Then a solution of EDC (65 mM final concentration) and NHS (13 mM final concentration) were added under sonication in a final volume of 2 mL. Finally, 200 μg of pure StLASPO were added and the reaction was carried out for 2 h at room temperature on a rotating plate tube stirrer. Subsequently, StLASPO conjugated NPs (NP-LASPO) were collected by a magnet and washed twice with 2 mL of 5 mM sodium pyrophosphate buffer, pH 8.5. The resulting conjugated enzyme was stored at 4 °C until use.

Characterization

Shape, size, and size distribution of Fe_3O_4NPs, NP-APTES and NP-LASPO were investigated by transmission electron microscopy (TEM) with JEOL 1010 electron microscope (JEOL, Tokyo, Japan). Samples were dispersed in milliQ water on carbon coated copper grids and dried at room temperature.

Activity assay

Activity of StLASPO and NP-LASPO was assayed by measuring the initial rate of production of hydrogen peroxide with a coupled peroxidase/dye assay at different temperatures. The standard assay mixture contained 10 mM L-aspartate in 50 mM sodium pyrophosphate buffer, pH 8.5, 1.5 mM 4-

aminoantipyrine, 2 mM phenol, 20 µM FAD, 2.5 U of peroxidase, and 30 µg of StLASPO in a total volume of 1 mL. The colored product generated by peroxidase from H_2O_2 and 4-aminoantipyrine was detected spectrophotometrically at 505 nm ($\varepsilon = 6.58$ mM^{-1} cm^{-1}).[4] One unit (U) is defined as the amount of enzyme that catalyzes the degradation of 1 µmol of L-aspartate per min.

Oxidation of L-aspartate by conjugated StLASPO

The oxidation of L-aspartate was carried out by adding 50 µL of 50 mM amino acid solution (in water, prepared and adjusted to the desired pH with 0.5 M NaOH) and 150 µL of water to the immobilized enzyme (4 mg of support corresponding to ≈ 0.104 U of StLASPO). All reactions were performed at 70 °C, in a thermomixer set to 600 rpm and at different pH values (in the 8–11 range). The dependence of the residual activity after 60 min of incubation on pH was fitted using an equation for a single ionization according to Harris and Colleagues.[17]

To investigate the stability of NP-LASPO on temperature, the same reaction was performed at pH 10.0 in the 25–80 °C range: samples were collected at different time intervals for measurements. For the recycling of the NP-LASPO, at the end of each cycle NPs were collected with a magnet, washed several times and stored in the storage buffer. In all cases, the oxidation of L-aspartate was assayed by HPLC separation (see below).

HPLC analysis

The OPA-NAc reagent was prepared by dissolving 4 mg of *ortho*-phthalaldehyde (OPA) in 300 µL of methanol, followed by the addition of 250 µL of 0.4 M borate buffer at pH 9.4.[18] To this mixture, 15 µL of 1 M N-acetylcysteine (NAc) in 1 M NaOH were added, and then the solution was diluted with 435 µL of distilled water. At fixed intervals, 10 µL aliquots were withdrawn from the reaction mixture and diluted with 40 µL of distilled water: 10 µL of this solution were derivatized with 25 µL of OPA-NAc reagent, diluted with 25 µL of HPLC eluent and analyzed by HPLC chromatography on a symmetry C8 column (100 Å, 5 µm, 3.9 mm × 150 mm; Waters, Milano, Italy). Eluent: 50 mM sodium acetate buffer, pH 5.2/acetonitrile 9/1; isocratic flux ofz 1 mL min^{-1}; absorbance detection at 340 nm.[7] The separation allows to easily distinguish and quantify L-aspartate from glycine (used as internal standard) and thus to calculate the bioconversion yield; R_t (glycine): 10.5 min, R_t (L-aspartate) 4.5 min.

Results and discussion

Optimization of StLASPO conjugation

StLASPO was conjugated to NP-APTES using EDC/NHS reaction by a two-step process. The scheme of NP activation and enzyme conjugation is illustrated in Fig. 1. With this two steps reaction, different conjugations can occur (Fig. 1): an enzyme molecule could interact with just one NP-APTES (product A), an enzyme molecule could react with amino groups of different NPs (product B) and an enzyme molecule could react with more than one amino groups of the same NP (product C).[19,20]

In order to identify the best conditions for the enzyme conjugation, several factors have been taken into consideration: EDC : NHS ratio, NPs: enzyme ratio, the presence of FAD (the enzyme cofactor), substrate or product (Table 1). At each condition, the immobilization yield and the enzyme activity bound to NP-APTES were determined.

The concentrations of EDC and NHS have to be carefully chosen to yield complete activation of the binding sites and, at the

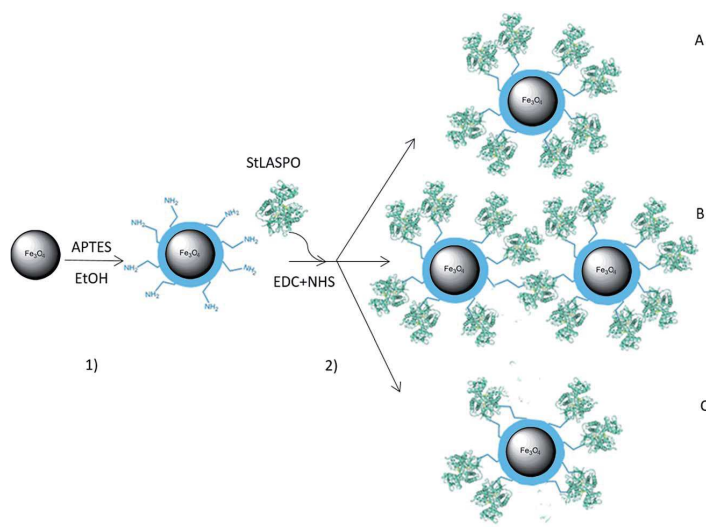**Fig. 1** Synthetic route for StLASPO conjugation on Fe$_3$O$_4$NPs (not in scale). The protein structure corresponds to PDB code 2E5V. (1) Functionalization of Fe$_3$O$_4$NPs with APTES; (2) conjugation of StLASPO through covalent linkage *via* EDC/NHS. The enzyme can interact with just one NP-APTES (product A) or with amino groups of different NPs (product B) or with more than one amino groups of the same NP (product C).

Table 1 Conditions for StLASPO conjugation to Fe$_3$O$_4$NPs. StLASPO was used at concentration of 100 µg mL^{-1}; EDC : NHS molar ratios are reported in the second column[a,b,c]

NP-APTES (mg)	EDC : NHS ratio	Other components	V_f (mL)	Yield (%)	Relative activity (%)	Specific activity (U mg^{-1} enzyme)
4	1 : 2	—	1	75	4	0.32
4	1 : 2	FAD	1	100	14	0.43
4	1 : 2	L-Aspartate	1	100	15	0.43
4	1 : 2	Succinate	1	77	5	0.33
4	1 : 2	L-Aspartate + FAD	1	86	5	0.37
4	1 : 2	Succinate + FAD	1	77	7	0.33
8	1 : 2	—	2	84	4	0.36
8	1 : 2	FAD	2	100	15	0.43
8	1 : 2	L-Aspartate	2	100	12	0.43
8	1 : 2	Succinate	2	92	5	0.40
8	1 : 2	L-Aspartate + FAD	2	85	6	0.37
8	1 : 2	Succinate + FAD	2	88	7	0.38
8	1 : 1	—	2	91	8	0.39
8	1 : 2	—	2	84	4	0.36
8	2 : 1	—	2	85	8	0.37
8	2 : 2	—	2	88	9	0.38
8	2 : 3	—	2	75	10	0.32
8	3 : 2	—	2	74	10	0.32
8	5 : 1	—	2	67	13	0.29
8	5 : 5	—	2	79	8	0.34
8	10 : 1	—	2	86	11	0.37
8	10 : 5	—	2	80	8	0.34
4	5 : 1	—	2	39	6	0.17
8	5 : 1	—	2	95	11	0.41
16	5 : 1	—	2	100	15	0.43
24	5 : 1	—	2	100	12	0.43
4	5 : 1	FAD	2	37	8	0.16
8	5 : 1	FAD	2	52	10	0.22
16	5 : 1	FAD	2	94	10	0.41
24	5 : 1	FAD	2	95	12	0.41

[a] Reaction conditions: during StLASPO conjugation, 100 µM FAD 1 mM L-aspartate and/or 200 µM succinate were added. [b] Yield has been calculated from units present in the supernatant of the immobilization reaction relatively to the total units. [c] Relative activity is reported as the ratio between the activity assayed for the NP-LASPO and the activity of the free enzyme.

same time, to prevent formation of unwanted surface by-products,[21] such as the N acetyl-substituted, derivative of the unstable intermediate of the EDC. Indeed, during the reaction in aqueous solution, O-acetyl urea is formed and, if it fails to react with an amine, undergoes to hydrolysis.[22] Furthermore, an excess of EDC may promote unwanted polymerization due to the abundance of both amines and carboxylates on protein molecules leading to a protein-to-protein cross-linking.[20] There is also the risk that the NHS esters formed on the protein molecule may then couple to other protein molecules to give poorly defined polymers.[23] As a general rule, the amount of StLASPO activity bound to the NPs increases at higher EDC : NHS ratios (reaching the maximum at a 5 : 1 value) and using increasing NP-APTES amounts.

The presence of FAD significantly increases both the units and the amount of the enzyme bound to NPs at low (1 : 2) EDC : NHS ratio. The positive effect of the flavin cofactor is less evident at higher EDC : NHS ratios (e.g., its presence resulted in a 1.3 fold increase in immobilized StLASPO activity at 5 : 1 EDC : NHS ratio and using 4 mg of NP-APTES).

Similarly, the substrate L-aspartate also positively affects StLASPO immobilization in an active form, while the product

analogue succinate does not. Notably, the use of the FAD and L-aspartate together results in an enzyme conformational change that does not favor its immobilization.

Under the best experimental conditions – i.e. 16 mg of NP-APTES in 5 mM sodium pyrophosphate buffer, pH 8.5, 65 mM EDC, 13 mM NHS, 200 µg of enzyme, final volume 2 mL – the amount of enzyme bound to NPs was approximately 100%, with an enzymatic activity of 0.026 U mg^{-1} of NPs and a relative activity of 15% (Table 1). Relative activity values strongly depend on the enzyme and the conditions used. Indeed, relative activities ranging from less than 10% to more than 80% in relation to the diameter of the NP, its functionalization and the immobilized enzyme are reported in the literature.[24–26] Furthermore, the reduction of relative activity might be due also to the chemistry of EDC/NHS conjugation that determines non-specific bindings between NP-APTES and the enzyme molecules. Actually, when the covalent bonds are formed close to the active site, an activity loss due to conformational changes can occur.[27,28] Under the best conjugation conditions, the specific activity of the immobilized enzyme for the L-aspartate is 0.43 U mg of enzyme (Table 1), comparable to the specific activity of the free enzyme. As for the
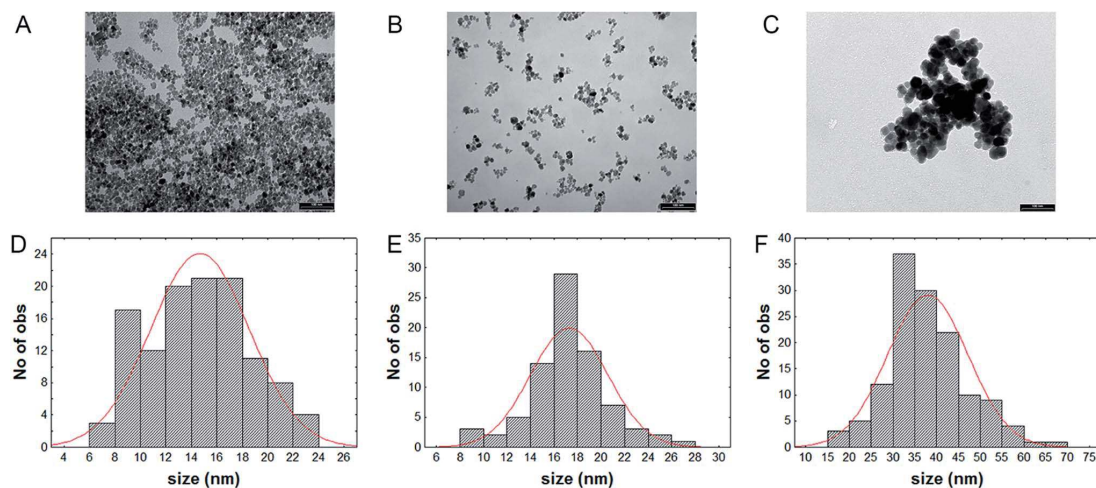
Fig. 2 Transmission electron microscopy (TEM) and size distribution of Fe$_3$O$_4$NPs (A and D), NP-APTES (B and E), NP-LASPO (C and F). Bars in panel A–C indicate 100 nm.

relative activity, specific activity depends on the enzyme and the conditions of the immobilization process. Therefore, the conjugation can affect also the specific activity.[29–31]

NP-LASPO properties

TEM images indicate that Fe$_3$O$_4$NPs and NP-APTES show a spherical shape, with an average diameter of 14.6 ± 3.8 nm and 17.2 ± 3.2 nm respectively, and with a good dispersion (Fig. 2A and B). On the other end, NP-LASPO show the tendency to aggregate and a more irregular shape, with an average diameter of 38.0 ± 9.8 nm (Fig. 2C). This slight tendency to aggregation can be explained by the possibility that several carboxylic groups located on the enzyme surface may react with the amine groups of different NP-APTES causing a cross-linking leading to aggregation.[32] However, this phenomenon is not massive since no NPs precipitation was apparent.

The immobilized NP-LASPO maintains the absolute stereo-selectivity of the free enzyme, i.e., the D-isomer of L-aspartate

is not oxidized. The addition of exogenous, free FAD positively affect the activity of NP-LASPO: a 2-fold increase in the activity of the enzyme immobilized on the NPs was obtained in the presence of a large excess of exogenous cofactor in the HRP-coupled assay mixture, this indicating that half of StLASPO is immobilized in the apoprotein, inactive form.

To investigate the storage stability, the NP-LASPO system was stored in 5 mM sodium pyrophosphate buffer (pH 8.5) at 25 °C: 70% of the initial activity was maintained after 35 days.

The effect of pH on the catalytic activity of NP-LASPO was investigated in the 8.0 to 11.0 range, by following the disappearance of the L-aspartate peak by HPLC separation (Fig. 3).

Fig. 4, panel A left, displays the activity curves of the enzyme at different pH values. At pH 9, 10 and 11 the complete oxidation of L-aspartate is observed in 3 hours, while at pH 8 the reaction stops to approximately 90% of conversion. When compared to the free enzyme form, the immobilized enzyme shows a full stability at pH values 9–11 after 60 min of incubation, while for the free StLASPO the stability strongly decreases at pH > 8 (Fig. 4A, right). Similarly, earlier studies demonstrated that immobilized enzymes are frequently more stable than free enzymes in an alkaline environment.[24,29]

The effect of temperature on the catalytic activity of conjugated StLASPO was investigated in the 25–80 °C range (Fig. 4B). The NP-enzyme system shows a good activity in the range of 60–80 °C: the fastest L-aspartate oxidative deamination is apparent at 70 °C. Only at ≤37 °C a partial conversion of the 50 mM L-aspartate solution was obtained after 420 min. Fig. 4B right shows that the thermostability of NP-LASPO after 30 min of incubation parallel the behavior observed for the free enzyme.

The catalytic parameters of StLASPO immobilized on the Fe$_3$O$_4$NPs were determined by a HRP-coupled spectrophotometric assay at pH 10.0 at 25 °C. The apparent V_{max} at air oxygen-saturation for the NP-LASPO system is 0.11 μmol per min
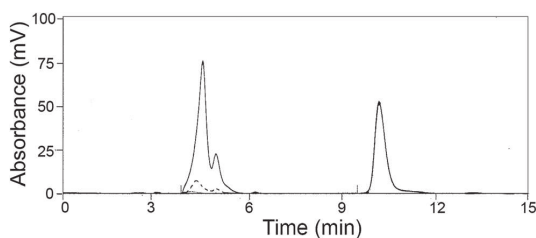

Fig. 3 HPLC separation of L-Asp solution during oxidation by NP-LASPO. Conditions: 50 μL of 50 mM L-aspartate in milliQ water, pH 9.0, added of 8 mg of NP-LASPO (0.10 U) and incubated at 70 °C. (—) before NP-LASPO addition; (-··-) 30 and (···) 60 min after NP-LASPO addition. Glycine, Rt 10.5 min, was used as internal standard.
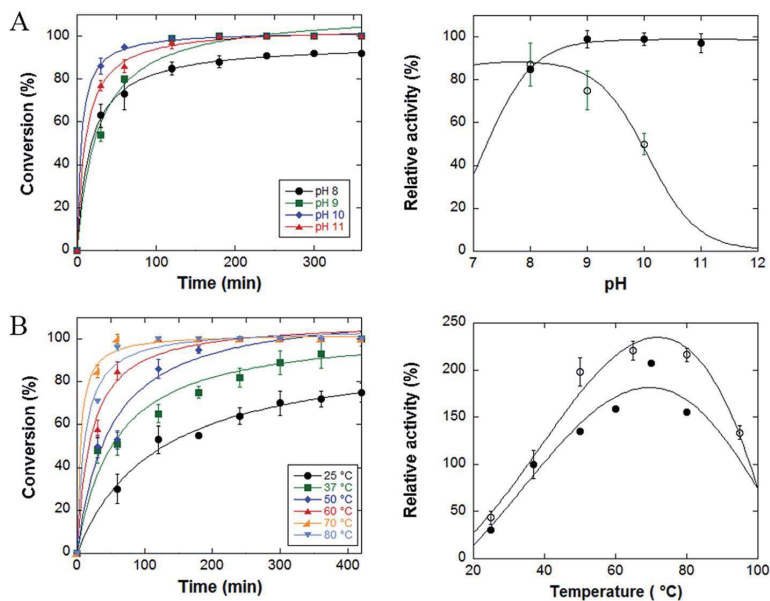
Fig. 4 (A) Left: effect of pH on the time course of oxidation of L-aspartate. Conditions: 50 μL of 50 mM L-aspartate, 0.10 U of NP-LASPO, 70 °C. Right: comparison of residual activity after 60 min of incubation as function of pH for free StLASPO (open symbols) and NP-LASPO (filled symbols). Data are expressed as percentage of the activity values measured at the beginning of the reaction. (B) Left: effect of temperature on the time course of oxidative deamination of L-aspartate. Conditions: 50 μL of 50 mM L-aspartate at pH 10.0, 0.208 U of NP-LASPO. Right: comparison of residual activity after 30 min of incubation as function of pH for free StLASPO (open symbols) and NP-LASPO (filled symbols). The value at 37 °C was set as 100%. The values are the average of at least three measurements; bars represent standard error.

per mg of protein and K_m for L-aspartate is 4.3 mM. The corresponding values for the free enzyme form are 0.98 μmol per min per mg enzyme and 1.3 mM at pH 8.0 and 37 °C.[4] The higher K_m of NP-LASPO suggests a lower affinity for L-aspartate by the immobilized enzyme so a higher substrate concentration is needed to achieve a given enzyme activity. Diffusional limitations and steric effects may contribute to the increased apparent K_m value due to a decrease in the accessibility of substrate to the enzyme active site. Similar effects are frequently reported for enzyme immobilized with EDC/NHS protocol, *e.g.*, Tee and colleagues[33] suggest that the high loading of the enzyme molecules using a zero-length cross-linker might restrict the access of the substrate to the active sites.

Bioconversion by NP-LASPO

The enzyme immobilization on magnetic NPs allows a simple recovery of the biocatalyst and its reuse, making this system interesting for industrial applications. To determine the number of reaction cycles that immobilized StLASPO can carry out, the same batch of enzyme was reused for subsequent cycles. Full oxidative deamination of 50 μL of 50 mM L-aspartate was obtained in 240 min using optimal operational conditions, *i.e.*, at pH 10, 50 °C and using 0.2 U of the NP-enzyme system. Under these conditions, a full conversion was observed for three sequential cycles, while a longer reaction time was required for the following cycles (Fig. 5): after 420 min of reaction, ≤70% of

the substrate was converted in the fifth and sixth cycle. Notably, under optimized conditions, the Relizyme-StLASPO fully converted 25 mM L-aspartate for three sequential cycles of 4 hours
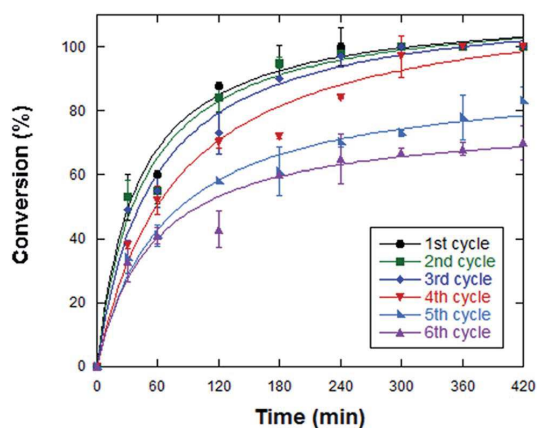

Fig. 5 Dependence of NP-LASPO activity at 50 °C and pH 10 on recycling. Conditions: 50 μL of 50 mM L-aspartate, 0.20 U of NP-LASPO, 50 °C and pH 10. The values are the average of at least three measurements; bars represent standard errors.

onlyd,[7] pointing to partial inactivation of the immobilized flavoenzyme. Taking into consideration the four cycles that resulted in full L-aspartate oxidation, 50 μmoles of substrate were converted per unit of NP-LASPO. As compared to the free enzyme form, which fully converted 30 mL of 25 mM L-aspartate in 24 h by using 9 U of StLASPO[4] corresponding to 3.5 μmoles per h per unit, the NP-LASPO converted 3.1 μmole per h per unit at pH 10.0 and 50 °C. Indeed, the Relizyme-StLASPO – using 10 mL of 100 mM D,L-Asp, at pH 10.0 and 70 °C – converted 1 μmoles per h per unit (or ~4.4 μmoles per h per unit using 0.5 mL of 142 mM D,L-Asp).[7]

Conclusions

In this work, the stereo-selective flavoenzyme L-aspartate oxidase from the thermophilic archaea *Sulfolobus tokodaii* has been covalently immobilized on Fe_3O_4NPs using EDC and NHS as cross-linking agents. The optimal conditions for the enzyme immobilization were identified by investigating the interaction effect of different variables.

The NP-LASPO showed a better stability than the free enzyme at pH ≥ 9.0 and was reused five times reaching full L-aspartate conversion, similarly to that previously obtained for the Relizyme-StLASPO preparation which employed a 2.5-fold higher amount of enzyme and longer times.[7] L-Aspartate conversion by NP-LASPO yielded a productivity similar to that obtained using the free enzyme (that cannot be recycled) or the enzyme bound to the amino support Relizyme™ HA403/S R (3.1 *vs.* 1–4 μmol per h per unit of enzyme at 50 mM L-aspartate concentration). These results indicate that the prepared NPs are favorable for immobilization of LASPO and the immobilized enzyme has promising industrial applications.

Acknowledgements

Notes and references

1 G. Tedeschi, A. Negri, M. Mortarino, F. Ceciliani, T. Simonic, L. Faotto and S. Ronchi, *Eur. J. Biochem.*, 1996, **239**, 427–433.

2 P. Macheroux, O. Seth, C. Bollschweiler, M. Schwarz, M. Kurfürst, L. C. Au and S. Ghisla, *Eur. J. Biochem.*, 2001, **268**, 1679–1686.

3 H. Sakuraba, K. Yoneda, I. Asai, H. Tsuge, N. Katunuma and T. Ohshima, *Biochim. Biophys. Acta, Proteins Proteomics*, 2008, **1784**, 563–571.

4 D. Bifulco, L. Pollegioni, D. Tessaro, S. Servi and G. Molla, *Appl. Microbiol. Biotechnol.*, 2013, **97**, 7285–7295.

5 L. Pollegioni, P. Motta and G. Molla, *Appl. Microbiol. Biotechnol.*, 2013, **97**, 9323–9341.

6 L. Pollegioni and G. Molla, *Trends Biotechnol.*, 2011, **29**, 276–283.

7 P. D'Arrigo, C. Allegretti, A. Fiorati, L. Piubelli, E. Rosini, D. Tessaro, M. Valentino and L. Pollegioni, *Catal. Sci. Technol.*, 2015, **5**, 1106–1114.

8 A. H. Lu, E. L. Salabas and F. Schüth, *Angew. Chem., Int. Ed.*, 2007, **46**, 1222–1244.

9 A. Bava, R. Gornati, F. Cappellini, L. Caldinelli, L. Pollegioni and G. Bernardini, *Nanomedicine*, 2013, **8**, 1797–1806.

10 R. Balzaretti, F. Meder, M. P. Monopoli, L. Boselli, I. Armenia, L. Pollegioni, G. Bernardini and R. Gornati, *RSC Adv.*, 2017, **7**, 1439–1442.

11 F. Cappellini, C. Recordati, M. De Maglie, L. Pollegioni, F. Rossi, M. Daturi, R. Gornati and G. Bernardini, *Future Sci. OA*, 2015, **1**, 4.

12 A. G. Cattaneo, R. Gornati, E. Sabbioni, M. Chiriva-Internati, E. Cobos, M. R. Jenkins and G. Bernardini, *J. Appl. Toxicol.*, 2010, **30**, 730–744.

13 R. Gornati, E. Pedretti, F. Rossi, F. Cappellini, M. Zanella, I. Olivato, E. Sabbioni and G. Bernardini, *J. Appl. Toxicol.*, 2016, **36**, 385–393.

14 C. G. C. M. Netto, H. E. Toma and L. H. Andrade, *J. Mol. Catal. B: Enzym.*, 2013, **85–86**, 71–92.

15 H. Vaghari, H. Jafarizadeh-Malmiri, M. Mohammadlou, A. Berenjian, N. Anarjan, N. Jafari and S. Nasiri, *Biotechnol. Lett.*, 2016, **38**, 223–233.

16 A. Bava, F. Cappellini, E. Pedretti, F. Rossi, E. Caruso, E. Vismara, M. Chiriva-Internati, G. Bernardini and R. Gornati, *BioMed Res. Int.*, 2013, **2013**, 314091.

17 C. M. Harris, L. Pollegioni and S. Ghisla, *Eur. J. Biochem.*, 2001, **268**, 5504–5520.

18 Y. Mutaguchi and T. Ohshima, *Biochemistry*, 2014, **4**, 2–5.

19 H. Jędrzejewska and R. Ostaszewski, *J. Mol. Catal. B: Enzym.*, 2013, **90**, 12–16.

20 G. T. Hermanson, *Bioconjugate techniques*, Academic Press, 3rd edn, 2013.

21 S. Sam, L. Touahir, J. Salvador Andresa, P. Allongue, J. N. Chazalviel, A. C. Gouget-Laemmel, C. H. De Villeneuve, A. Moraillon, F. Ozanam, N. Gabouze and S. Djebbar, *Langmuir*, 2010, **26**, 809–814.

22 S. K. Vashist, *Diagnostics*, 2012, **2**, 23–33.

23 L. S. Wong, F. Khan and J. Micklefield, *Chem. Rev.*, 2009, **109**, 4025–4053.

24 M. Jain, A. Mariya Sebatini, P. Radha, S. Kiruthika, C. Muthukumaran and K. Tamilarasan, *J. Mol. Catal. B: Enzym.*, 2016, **128**, 1–9.

25 F. Kazenwadel, H. Wagner, B. E. Rapp and M. Franzreb, *Anal. Methods*, 2015, **7**, 10291–10298.

26 K. Turcheniuk, A. V. Tarasevych, V. P. Kukhar, R. Boukherroub and S. Szunerits, *Nanoscale*, 2013, **5**, 10729–10752.

27 J. Xu, J. Sun, Y. Wang, J. Sheng, F. Wang and M. Sun, *Molecules*, 2014, **19**, 11465–11486.

28 H. J. Park, J. T. McConnell, S. Boddohi, M. J. Kipper and P. A. Johnson, *Colloids Surf., B*, 2011, **83**, 198–203.

29 C. Yen, Y. Chuang, C. Ko, L. O. Chen, S. Chen, C. Lin, Y. Chou and J. Shaw, *Molecules*, 2016, **21**, 972.

30 B. Sahoo, S. K. Sahu and P. Pramanik, *J. Mol. Catal. B: Enzym.*, 2011, **69**, 95–102.

31 S. L. Hosseinipour, M. S. Khiabani, H. Hamishehkar and R. Salehi, *J. Nanopart. Res.*, 2015, **17**(9), 382.

32 R. A. Sperling and W. J. Parak, *Philos. Trans. R. Soc., A*, 2010, **368**, 1333–1383.

33 B. L. Tee and G. Kaletunç, *Biotechnol. Prog.*, 2009, **25**, 436–445.

Effects of Metal Micro and Nano-Particles on hASCs: An In Vitro Model

Silvia Palombella [1], Cristina Pirrone [1], Federica Rossi [1] (ID), Ilaria Armenia [1] (ID),
Mario Cherubino [1], Luigi Valdatta [1], Mario Raspanti [2], Giovanni Bernardini [1,3] and
Rosalba Gornati [1,3,*] (ID)

[1] Department of Biotechnology and Life Sciences, University of Insubria, via J.H. Dunant 3, 21100 Varese,
    Italy; s.palombella@studenti.uninsubria.it (S.P.); cristina.pirrone@hotmail.it (C.P.);
    federica.rossi@uninsubria.it (F.R.); i.armenia@uninsubria.it (I.A.); mario.cherubino@uninsubria.it (M.C.);
    luigi.valdatta@uninsubria.it (L.V.); giovanni.bernardini@uninsubria.it (G.B.)
[2] Department of Medicine and Surgery, University of Insubria, Via Guicciardini 9, 21100 Varese, Italy;
    mario.raspanti@uninsubria.it
[3] The Protein Factory Research Center, Politecnico of Milano, ICRM-CNR Milano and University of Insubria,
    Via Mancinelli 7, 20131 Milano, Italy
* Correspondence: rosalba.gornati@uninsubria.it; Tel.: +39-0332-421314

Abstract: As the knowledge about the interferences of nanomaterials on human staminal cells are scarce and contradictory, we undertook a comparative multidisciplinary study based on the size effect of zero-valent iron, cobalt, and nickel microparticles (MPs) and nanoparticles (NPs) using human adipose stem cells (hASCs) as a model, and evaluating cytotoxicity, morphology, cellular uptake, and gene expression. Our results suggested that the medium did not influence the cell sensitivity but, surprisingly, the iron microparticles (FeMPs) resulted in being toxic. These data were supported by modifications in mRNA expression of some genes implicated in the inflammatory response. Microscopic analysis confirmed that NPs, mainly internalized by endocytosis, persist in the vesicles without any apparent cell damage. Conversely, MPs are not internalized, and the effects on hASCs have to be ascribed to the release of ions in the culture medium, or to the reduced oxygen and nutrient exchange efficiency due to the presence of MP agglomerating around the cells. Notwithstanding the results depicting a heterogeneous scene that does not allow drawing a general conclusion, this work reiterates the importance of comparative investigations on MPs, NPs, and corresponding ions, and the need to continue the thorough verification of NP and MP innocuousness to ensure unaffected stem cell physiology and differentiation.

Keywords: cytotoxicity; cellular uptake; cell morphology; gene expression; adipose stem cells

1. Introduction

It is well known that many human tissues, including skin, liver, muscle, pancreas, lung, adipose tissue, placenta, bone marrow, peripheral blood, as well as neural tissue, contain an undifferentiated cell population facilitating tissue repair and remodelling over the course of a lifetime [1,2]. The research on adult stem cells (SCs) began in the 1950s when researchers discovered that the bone marrow contained at least two kinds of SCs: hematopoietic and mesenchymal stem cells. In recent years, there has been a considerable increase in the comprehension of SC biology for their involvement in maintaining the homeostasis of healthy tissues or in tumour formation and proliferation. Furthermore, SCs have shown great potential in many medical applications, such as regenerative medicine, bone marrow transplantation, orthopaedic injuries, autoimmune diseases, and cardiovascular and liver diseases [3–5]. It is, therefore, evident how dangerous it could be to perturb SC homeostasis acting

on their turnover, which may lead to SC depletion that, in turn, is responsible for pathological consequences [6]. In this scenario, a circumstance that has also to be taken into account is the exponential growth that nanotechnology has had in this last decade in several areas, including medical biotechnology within which the theranostics plays an important role. Theranostics is a discipline that combines diagnostic and therapeutic properties in the same compound [7]; this concept refers to the optimization of medical nanotechnologies, which are in search of the ideal system, able to recognize and target, in a peculiar way, the area of interest to promote an efficient site-directed action and provide accurate imaging for diagnostic follow-up. In this context, magnetic nanoparticles (NPs) with intrinsic theranostic characteristics can give an optimal solution [8–11]. Considering this overview, it is easy to imagine that the human body is easily exposed to the possibility of coming into contact, intentionally or not, with NPs that may enter the body, encounter SCs of different tissues, then act on them perturbing their physiology. Consequently, SCs might represent a possible weak point, and their susceptibility to NPs should be carefully evaluated. Moreover, appropriate assessment of the biological effects of NPs is particularly arduous as their in vitro and in vivo behaviours depend on several factors, including composition, shape, size, dosage, and route of exposure [12–14]. Although Ni represents a well-known problem for allergy and dermatitis [15], Fe, Co, and Ni are very promising for nanotechnological applications. In nanomedicine, for instance, iron and cobalt in particular, find applications as highly-sensitive contrast agents in magnetic resonance imaging (as an alternative to radionuclides), vectors for drug delivery, and theranostics, combining imaging analysis and hyperthermia therapy [8,10,16–18]. Moreover, we think that SCs, due to their higher sensitivity to the xenobiotic compounds, will play an increasingly important role in in vitro cell based tests for developmental toxicology studies, as well as target organ toxicity [6].

For all these reasons, and with the purpose to face some of these aspects, we have planned to study the behaviour of microparticles (MPs) and NPs of iron (Fe), cobalt (Co), and nickel (Ni), three transition metals of the group 8 of the periodic table, on SCs. In this paper, we reported our findings on cytotoxicity, morphology, cellular uptake, and gene expression of human adipose-derived mesenchymal stem cells (hASCs) exposed to zero-valent metal MPs, NPs, or salts.

2. Results

2.1. Micro- and Nanoparticle Characterization

The MPs and NPs used in this research were analysed by microscopy (Figure 1). Scanning electron microscopy images (SEM) observations displayed MPs with different sizes, irregular round shapes, and a strong tendency to cluster in aggregates. The MPs showed an average diameter of 6 μm ± 1.5; 0.8 μm ± 0.15 and 4 μm ± 0.5 for Fe, Co, and Ni, respectively, confirming the label information (Figure 1a–c). Transmission electron microscopy (TEM) analysis of NPs showed particles of different shape whose size is between 10 and 50 nm (Figure 1d–f).

2.2. Cell Viability

Figure 2 indicates cytotoxicity induced by Fe, Co, and Ni MPs, NPs, and ions evaluated measuring cellular adenosine triphosphate (ATP) content after 96 h exposure of hASCs maintained in CHANG MEDIUM® C or Dulbecco's Modified Eagle Medium/Dulbecco's Modified Eagle Medium Nutrient Mixture F12 (DMEM/DMEM-F12) to be sure that the cell toxicity was due only to the MPs, NPs, and ions exposure and not influenced by the cell culture medium. The response was, in most cases, concentration-dependent, and no differences were evidenced between the two culture media. As expected, the effects were significantly different among the three metals. The most striking data are those referred to Fe and Ni MPs (Figure 2a,c) which evidenced a high toxicity for Fe MPs and no effect for Ni MPs compared to the other two formulations. Conversely, Co MPs, NPs, and $CoCl_2$ elicited a dose-dependent response similar in all the three formulations (Figure 2b). In addition, NiNPs exposure showed a cell toxicity comparable to that of CoNPs.

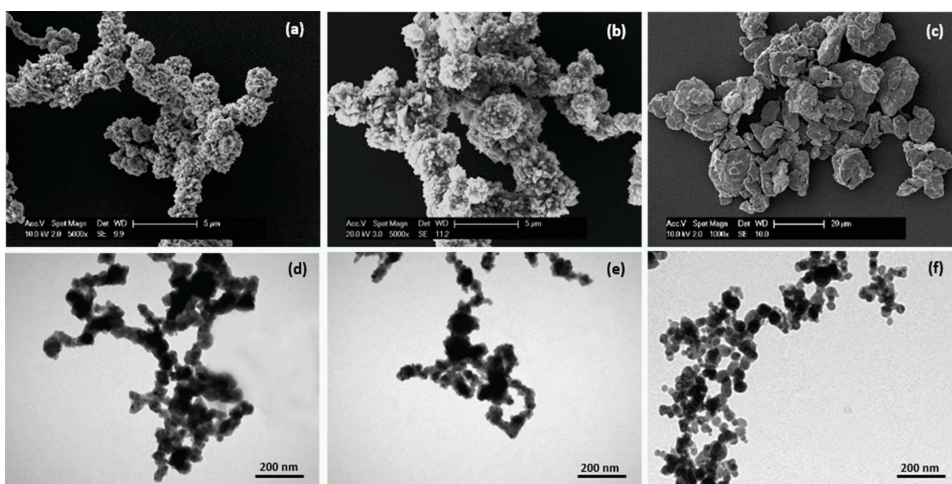**Figure 1.** Scanning electron microscopy images of metal microparticles deposited on a glass coverslip: Fe (**a**), Co (**b**), and Ni (**c**) and transmission electron microscopy images of metal nanoparticles deposited on formvar carbon-coated grids: Fe (**d**), Co (**e**), and Ni (**f**). Certain heterogeneity in the size and shape is observed for all the particles.
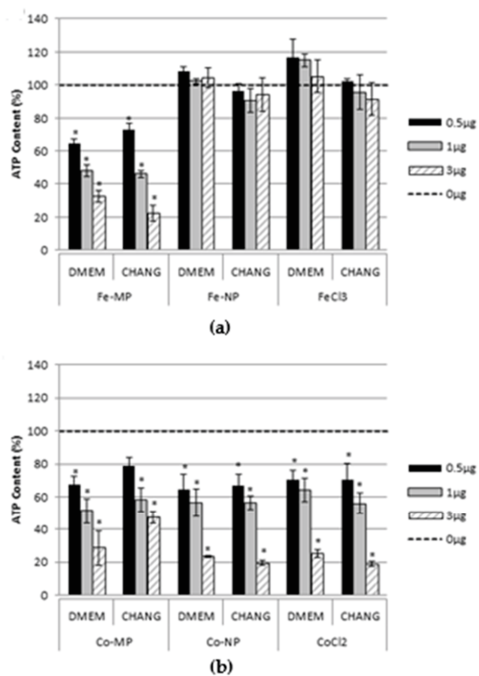

Figure 2. *Cont*.
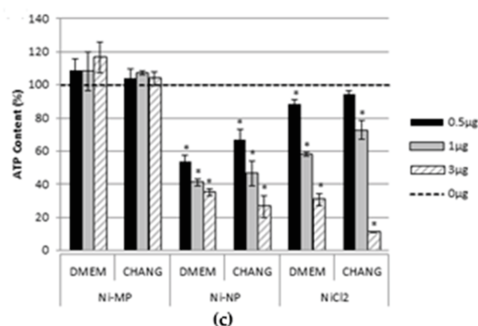
Figure 2. Percentage of ATP content, normalized to control, in hASCs exposed to Fe, (**a**), Co (**b**), and Ni (**c**), microparticles (MPs), nanoparticles (NPs), or salt for 96 h. Bars represent standard errors. * Dunnett's test, $p < 0.05$. Each plotted value is the mean of three independent experiments.

2.3. Cellular Uptake and Morphology

Figure 3 shows the cellular uptake of MPs and NPs evaluated by optical microscopy after 24 h of exposure. Although Fe, Co, and Ni MPs appear different in shape and size, none of them appeared to enter the cells (Figure 3a,c,e). Conversely, several Fe, Co, and Ni NPs seemed to be inside the cells (Figure 3b,d,f). Cell appears to maintain the classical fibroblast-like morphology characteristic of unexposed hASCs [4].
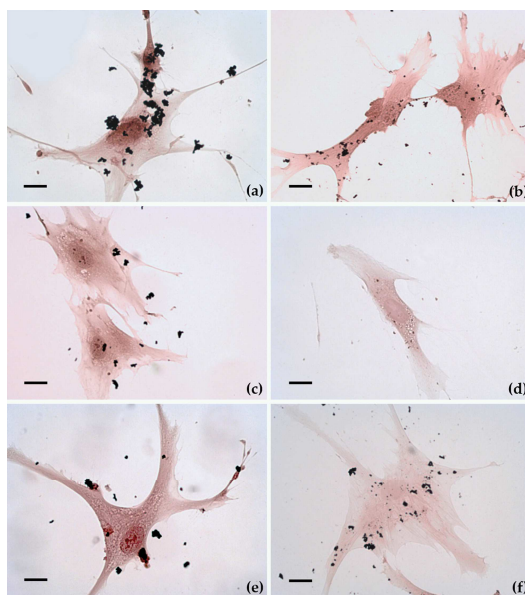
Figure 3. Optical microscopy photographs of hASCs exposed for 24 h to micro and nanoparticles and stained with haematoxylin-eosin solution. Micro- and nanoparticles are visible as black corpuscles. FeMPs (**a**), FeNPs (**b**), CoMPs (**c**), CoNPs (**d**), NiMPs (**e**), and NiNPs (**f**). All cells maintain the classical fibroblast-like morphology. Original magnification: 20×. Bar indicates 40 µm.

TEM analysis, reported in Figure 4, confirmed the optical microscopy observations. Both MPs and NPs, at the concentration and exposure time used in these experiments, provoked some ultrastructural

modifications, but no severe cellular damage. The cell body was rounded and the nucleus was large, indented, and eccentric, with abundant euchromatin and a prominent nucleolus (not shown in these pictures). Even though we have not observed NPs inside the nucleus, nor in the mitochondria, we cannot exclude their internalization in these compartments. Ultrastructural analysis seemed to also exclude rough endoplasmic reticulum (RER) and Golgi apparatus involvement compared to unexposed cells. Vesicles and lysosomes of different size, containing low electron-dense material, were present in the cytoplasm (Figure 3b,d). These characteristics suggested that exposed hASCs maintained the typical characteristics [19]. However, it is clear that NPs were massively internalized as agglomerations, mainly by endocytic mechanisms (Figure 4b,d,f). Once internalized, most of the NPs remained inside the cytoplasmic vesicles which may also contain amorphous cellular material (Figure 4b,d). No differences were observed among the three considered NPs and the internalization appeared to be nonspecific. In these pictures, NPs are identified as high electron density material as NPs preserve the morphology observed in the cell-free environment (Figure 1). The cell membrane is characterized by pronounced pseudopodia-like protrusions, especially in MPs exposed cells that also show several empty vacuoles (Figure 4a–c). These findings represent the typical alterations of an early apoptotic state.
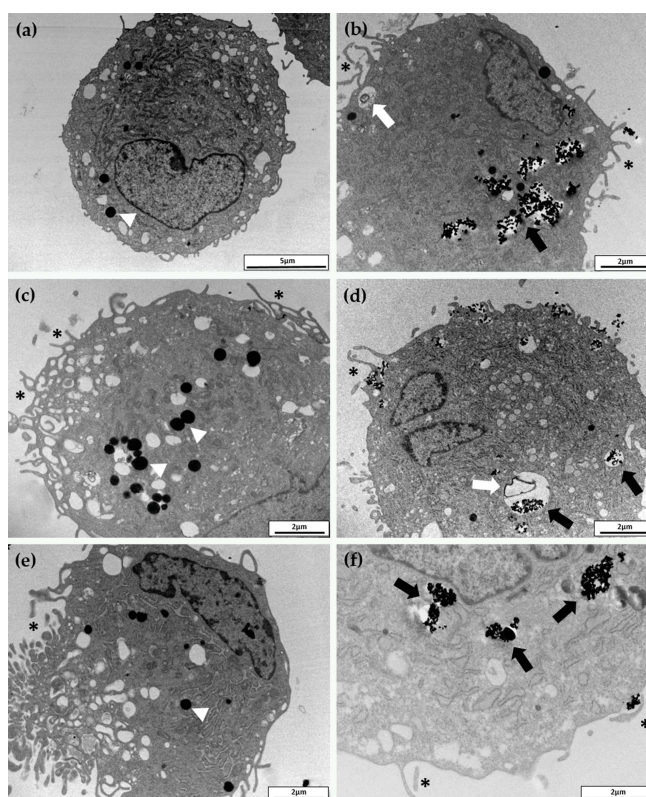
Figure 4. Transmission electron microscopy images of typical hASCs exposed for 24 h to FeMPs (**a**), FeNPs (**b**), CoMPs (**c**), CoNPs (**d**), NiMPs (**e**), and NiNPs (**f**). NPs were identified as high-electron-density objects when inside the cell and localized inside the vesicles (black arrows). No differences were observed among the three considered NPs and the internalization appeared to be nonspecific. White arrows indicate lysosomes of different sizes containing amorphous material. Several pronounced pseudopodia-like protrusions (*) are present both in NP- and in MP-exposed cells. Nuclei and mitochondria do not contain NPs. Arrowheads indicate lipid droplets.

Conversely, these cells seemed unable to internalize the MPs (Figure 4a,c,e). TEM observations were supported by SEM analysis. In particular, important information was obtained by using secondary electrons (SE) (Figure 5a,c,e) and backscattered electrons (BSE) (Figure 5b,d,f). Figure 5b,d,f show micrographs of cells covered with large electron-dense materials (bright spots) confirming that all the MPs resided around and not inside the cells.
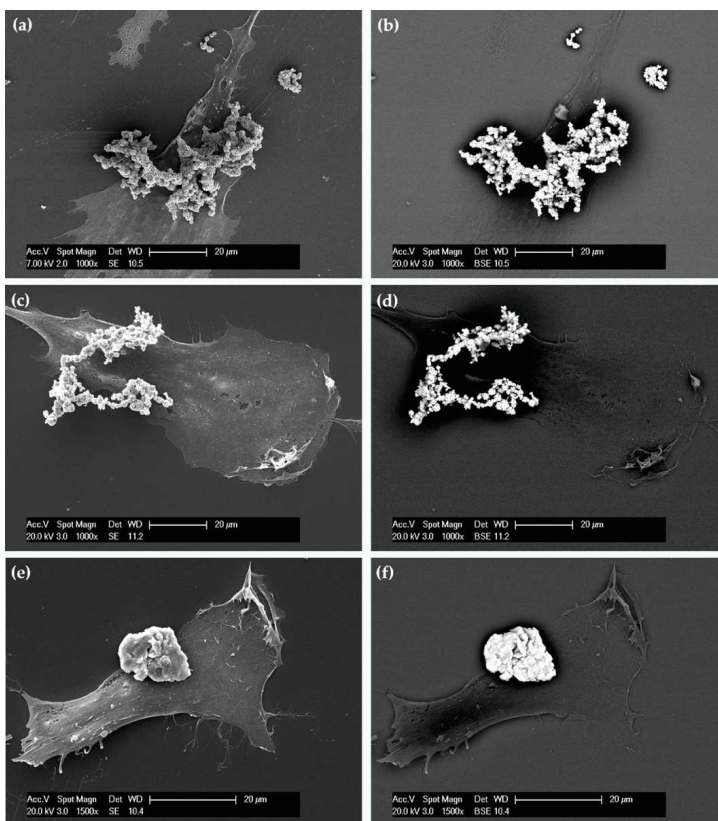
Figure 5. Scanning electron micrographs of typical hASCs exposed for 24 h to FeMPs (**a**,**b**), CoMPs (**c**,**d**), and NiMPs (**e**,**f**). The same field of view is shown with secondary electron (SE, left) and backscattered electron (BSE, right) imaging. In BSE imaging, the clusters of metal microparticles appear as bright spots.

2.4. Gene Expression

The genes considered in this research are those implicated in some cell processes, such as oxidative stress, apoptosis, inflammatory response, neovascularization, tissue regeneration, and internalization. In Figure 6 we have reported only the results of those genes whose expression was significantly changed. As reported in Figure 6a, Fe MPs induced upregulation of vascular endothelial growth factor A (*VEGFA*), interleukin 8 (*IL8*), interleukin 1b (*IL1b*), and a downregulation of superoxide dismutase 1 (*SOD*) after 96 h of exposure. Although not statistically significant, iron, in all its formulation, induced the expression of adaptor-related protein complex 2 alpha 1 subunit (*AP2A1*). Figure 6b shows an upregulation of *IL1b* and B-cell lymphoma 2 (*BCL2*) genes after 24 h of Fe NP exposure. Surprisingly, cobalt caused only the downregulation of interleukin 6 (*IL6*) expression after 96 h of exposure (Figure 6c).
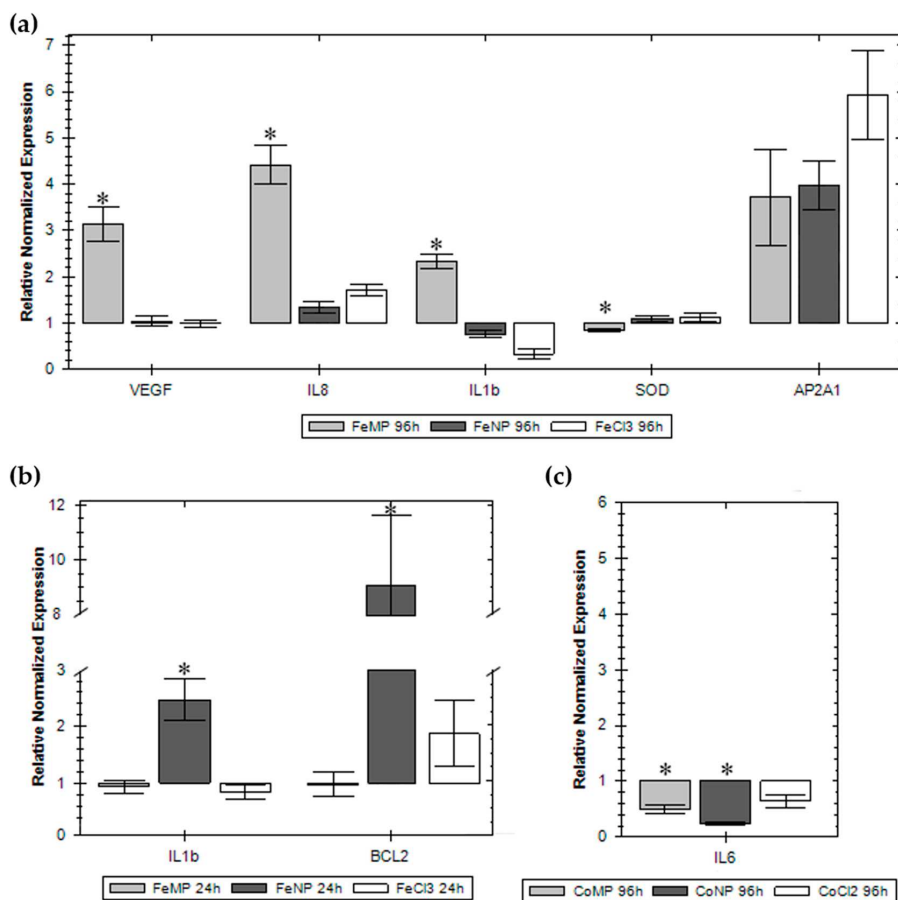
Figure 6. Real-time PCR of the most significant gene expression modifications. *VEGF*, *IL8*, *IL1b*, *SOD* and *AP2A1* in cells exposed for 96h to Fe MPs, NPs and ion (**a**). *IL1b* and *BCL2* in cells exposed for 24 h to Fe MPs, NPs and ion (**b**). *IL6* in cells exposed for 96h to Co MPs, NPs and ion (**c**). Normalization has been done with at least three housekeeping genes. The mRNA expression is reported as the fold change compared to the unexposed cells whose expression has been fixed at one. * Dunnett's test, $p < 0.05$. Each plotted value is the mean of three independent samples.

3. Discussion

Differences in the toxicological characteristic of nanosized and non-nanosized particles have been extensively studied for titanium dioxide particles [20,21]. Conversely, formulations, based on iron, cobalt, and nickel, which also have several applications that have not received the same attention. Furthermore, notwithstanding the increasing literature on nanotoxicity, still scarce and contradictory are the papers that deal with possible interferences of nanomaterials on SCs. Some authors did not find any influence of NPs on SC viability/proliferation and differentiation [22–25]; other researchers have instead observed marked effects [26–28]. In this paper, we have faced a comparative study based on size–effect of commercially zerovalent iron, cobalt, and nickel MPs and NPs using the hASCs as a model. There are several factors that intervene to maintain the SC microenvironment which are critical: oxygen tension, hormones, growth factors, cytokines, nutrients and extracellular matrix; this is why we first evaluated cell viability of hASCs maintained in two different culture media. Our results suggested

that, in our experimental conditions, the medium did not influence the behaviour of the exposed hASCs. Even though our experiments confirmed the previous results on cell viability for the NP formulation whose cytotoxicity ranking was CoNPs > NiNPs > FeNPs, conversely, hASCs appeared more sensitive to NP exposure. As cytotoxicity could be ascribed to metal dissolution in growth media during exposure, cobalt, which easily releases ions when placed in aqueous systems, displayed the same effect for the three formulations [14]. Unforeseen was the high cytotoxicity shown by FeMPs, and this behaviour was supported by our results on gene expression but, to our knowledge, not from the literature [29,30]. The NiMPs, often used as electrodes catalysts or components of catalytic converters, resulted in a lack of toxicity [31,32]. The Ni ion is introduced with the diet and it is a component of some enzymes of our body; as in the culture medium, NiNPs release less than 10% as Ni^{2+} [14], a low toxicity would be expected . On the contrary, as also reported by Ahamed [33], our results showed that both NiNPs and Ni ions exert significant effects on hASCs. To note, the medium does not influence cytotoxicity.

Our investigations, conducted by TEM, confirm that zero-valent metal NPs are mainly internalized by endocytosis and persist in the cytoplasm inside vesicles [34,35]. These results are also supported by our previous paper in which we have proved that cobalt oxide NPs, but not zero-valent cobalt NPs, can cross the plasma membrane [36]. Conversely, SEM analysis proved that MPs are not internalized; consequently, any effects on hASCs have to be ascribed to the release of ions in the culture medium, or to the reduced oxygen and nutrients exchange efficiency, due to the presence of MP agglomerate around the cells. As assessed with various in vitro assays, exposed cells can die by apoptosis and/or necrosis, phenomena that depend on the concentration, chemical nature, and size of metal NPs [37]. At low toxic doses, however, metal NPs can induce pro-inflammatory effects. The literature reports that macrophages exposed to AgNP were rapidly induced to secrete *IL8* and oxidative stress genes, such as hemeoxygenase-1 and heat shock protein 70 (*Hsp70*), in a size-dependent way [38]. Moreover, the ability to induce the innate immunity, measured as production of *IL1b*, and the induction of inflammasomes was higher for small AgNPs and ZiONPs [39].

The gene expression of the exposed hASCs conducted in this research does not appear heavily influenced nor strictly related to the cytotoxicity dose-response curves or to the size, as well as to the nature, of the compounds used in this study. The overall picture shows modifications in mRNA expression of some genes involved in the inflammatory response; the main noteworthy changes are due to FeMPs after 96 h of exposure that clearly induce *IL8*, *IL1b*, and *VEGFA*. Even though not statistically significant and independently to the size, iron raises the mRNA expression of *AP2A1*, a protein involved in clathrin-dependent endocytosis; consequently, its induction may be related to an increase in NP endocytosis [40]. CoMPs and CoNPs, after 96 h of exposure, influenced *IL6*, a multifunctional cytokine [41] that, together with *VEGFA*, it is known to be a putative paracrine factor secreted by hASCs and involved in cytoprotection, proliferation, and angiogenesis [42]. None of the formulations used affected stress-related genes (catalase, *CAT*; *SOD*, metallothionein 1A, *MT1A*; *Hsp70*) even though their main function is to protect cells from various injuries, such as elevated temperature, mechanical damage, hypoxia, and reactive oxygen species [14]. Lastly, the genes related to apoptosis (tumour protein 53, *P53*; caspase 3, *CASP3*; early growth response protein 1, *EGR1*; *BCL2*) are not influenced by the treatment; the only exception was the increase of BCL2, a protein that blocks the programmed cell death and apoptosis pathway, after 24 h exposure to FeNPs.

It is known that each cell line has its own sensitivity to NP and MP exposure and, notwithstanding the multidisciplinary approach adopted in this research, the results depict a heterogeneous scene with regard to the interactions of nanoparticles, microparticles, and salts with hASCs. In this context, is difficult to depict a general conclusion. Nevertheless, it is rather clear that parameters such as chemistry, shape, and size sometimes greatly affect the behaviour of hASCs, but do not alter their natural differentiation time. Probably, MPs lead cells to an apoptotic state due more to the presence of agglomerates around the cells, than to their composition. This work reiterates the importance of comparative investigations on MPs, NPs, and the respective ions to avoid experimental artefacts in

the evaluation of nanotoxicity. Furthermore, we think that it is necessary to stress the adoption of in silico toxicology methods to conceive informative models on the in vitro and in vivo effects. Therefore, it will be indispensable to continue the thorough control of NPs' and MPs' innocuousness to ensure that they do not perturb SC homeostasis acting on their physiology, differentiation, and turnover that may lead to SC depletion that, in turn, is responsible for pathological consequences.

4. Materials and Methods

All subjects gave their informed consent for inclusion before they participated in the study. The study was conducted in accordance with the Declaration of Helsinki, and the protocol was approved by the Ethics Committee of University of Insubria, Varese.

4.1. Micro- and Nanoparticle Characterizations

MPs were purchased from American Elements (Los Angeles, CA, USA) with the following characteristics: FeMPs (purity 99.9%, aerodynamic particle size < 10 μm), CoMPs (purity 99.8%, aerodynamic particle size < 2 μm), and NiMPs (purity 99.9%, aerodynamic particle size < 5 μm). NPs were purchased from IOLITEC (Heilbronn, Germany) with the following characteristics: FeNPs (purity 99.9%, aerodynamic particle size < 25 nm), CoNPs (purity 99.8%, aerodynamic particle size < 28 nm) and NiNPs (purity 99.8%, aerodynamic particle size < 20 nm).

For MP characterization, 5 μL of a diluted ethanol suspension were deposited on a glass coverslip and analysed by SEM (FEI XL-30 FEG, Eindhoven, The Netherlands) operated at an acceleration voltage of 7 kV. Conversely, 5 μL of a diluted ethanol suspension of NPs were deposited on a formvar carbon-coated copper grid and observed by TEM microscope (Morgagni, Philips, Eindhoven, The Netherlands) operating at 80 kV [14].

4.2. Patient Samples

hASCs were isolated from mammary adipose tissue, obtained from five healthy women (average age 43 ± 4) who underwent surgery for gigantomasty at the "Ospedale di Circolo", Varese, Italy. All patients were in good health who have not undergone to heavy weight loss diet, their body mass index (BMI) was from 18.8 to 29 kg/m^2 (mean 24.58 ± 5.24 kg/m^2), non-smokers, without a history of metabolic disorders, and not receiving medications at the time of surgery. Gigantomastia allowed us to obtain large amounts of adipose tissue from the same depot. Furthermore, the severe selection of the patients guaranteed adipose tissue of good quality and rich in hASCs.

4.3. hASC Isolation and Culture

The stromal cellular fraction of human mammary adipose tissue, obtained according to Gronthos and Zannettino protocol [43], was divided in two fractions. Half of these cells were seeded in a flask with complete 1:1 DMEM/DMEM-F12 medium (Sigma Aldrich, Milan, Italy) containing 10% FBS, 2 mM L-glutamine, 1% penicillin/streptomycin, and 0.1% gentamicin. The remaining fraction of cells was seeded in CHANG C medium (Irvine Scientific, Santa Ana, CA, USA) supplemented with 2 mM L-glutamine, 1% penicillin/streptomycin. After 6 h non-attached cells were removed and adherent stem cells were fed with fresh medium. hASCs were characterized by flow cytometry, as reported in our previous paper [4]. For all subsequent experiments hASCs were used at passage 5.

4.4. Cell Exposure and Viability

Cell viability was determined measuring ATP content by the CellTiter-Glo® Luminescent Cell Viability Assay (Promega, Milan, Italy) according to the manufacturer's instructions and as reported by Bava et al. [44]. This experiment was conducted in hASCs cultured in DMEM/DMEM-F12 and CHANG medium. Briefly, 300 cells were seeded into 96-well plates and treated after 24 h. Cells were exposed for 96 h in increasing concentrations (0, 0.5, 1, 3 μg/200 μL) of Fe, Co, or Ni MPs and NPs

and their corresponding salts (FeCl$_3$, CoCl$_2$·6H$_2$O, NiCl$_2$). MPs and NPs were resuspended in fresh culture media and then dispersed by an ultrasonic bath for 15 min before each treatment. The range of concentrations of each metal has been determined in preliminary experiments. After the exposure, plates were equilibrated for 30 min at room temperature then the culture medium was replaced by 1:1 phosphate buffered saline (PBS):CellTiter-Glo reagent. Plates were shaken for 2 min and left at room temperature for 10 min before recording luminescent signals using the Infinite F200 plate reader (Tecan Group, Männedorf, Switzerland).

4.5. Uptake and Morphology

These experiments were performed in steady state. For optical microscopy 5000 cells were cultured in DMEM on 24 mm^2 coverslip into a six-well culture plates, cultivated at 37 °C in 5% CO$_2$ and then exposed to 1.2 µg/200 µL of Fe, Co, or Ni MPs and NPs for 24 h. After the exposure, MPs and NPs were removed; cells were washed with PBS, fixed for 10 min with methanol at room temperature, and then stained with haematoxylin-eosin solution according to the standard procedures.

For TEM analysis, 100,000 cells were cultured in a T25 flask, and exposed as above reported. After the exposure, MPs and NPs were removed; cells were washed with PBS, harvested, fixed, embedded as previously described [45], and finally observed by a Morgagni electron microscope (Philips, Eindhoven, The Netherlands) operating at 80 kV. For SEM observation, 1000 cells were cultured on a 24 mm^2 coverslip, placed into a six-well culture plates, and treated as above. After the exposure, MPs and NPs were removed; cells were washed with PBS and fixed in Karnovsky solution (4% formaldehyde, 2% glutaraldehyde, 0.1 M sodium cacodylate, pH 7.2) for 1 h. Samples were then dehydrated with a series of ethanol (20%, 50%, 70%, 90%, 100%), treated with hexamethyldisilazane (HMDS), mounted on standard SEM stubs with conductive carbon-based adhesive, and gold-coated in an Emitech K-550 sputter-coater (Emitech Ltd., Ashford, UK) in a controlled argon atmosphere at a pressure of 0.1 mbar. All observations were carried out on a FEI XL-30 FEG field emission scanning electron microscope (FEI, Eindhoven, The Netherlands) operated at an acceleration voltage of 7 kV.

4.6. RNA Isolation, Reverse Transcription, and Real-Time PCR

A suitable number of cells (20,000–80,000) were seeded into six-well plates and exposed for 24 or 96 h to Fe, Co, or Ni MPs and NPs (exposure concentration was 1.2 µg/200 µL at 24 h and 0.6/200 µL at 96 h, referred to a cell ATP reduction of about 60–80%). Exposed and not exposed cells were then washed twice with PBS and harvested. We have also arranged a set of samples in which cells were exposed to FeCl$_3$, CoCl$_2$·6H$_2$O, or NiCl$_2$ at a nominal concentration of 6 and 3 µg mL^{-1} in terms of Fe, Co, and Ni. Total RNA was isolated using the Direct-zol RNA Miniprep (Zymo Research, Milan, Italy) according to the protocol, quantified by the QuantiFluor® RNA System (Promega, Milan, Italy) and reverse transcribed by iScriptTM cDNA Synthesis Kit (Bio-Rad, Segrate, Italy) according to the manufacturer's instructions. The Quantitative Real-Time PCR (qPCR) was performed with iTaq™ Universal SYBR® Green Supermix (Bio-Rad, Segrate, Italy) technology using CFX Connect® Real-Time PCR Detection System apparatus (Bio-Rad, Segrate, Italy). Specific primers were designed by Beacon Designer 7® (Bio-Rad, Segrate, Italy) within their own sequence, and on an exon-exon junction (possibly separated by an intron of at least 1000 bp) in order to prevent genomic DNA amplification. The analysis was performed on genes involved in oxidative stress (*CAT*; *SOD*; *MT1A*; *Hsp70*), apoptosis (*P53*; *CASP3*; *BCL2*; *EGR1*), inflammatory response (*IL6*; *IL8*; *IL1b*), neovascularization, tissue regeneration (*HIF1α*; *VEGFA*), and internalization (*AP2A1*), see Table 1 [46–52]. Housekeeping genes (*ACTβ: β-actin*; *B2M: beta-2-microglobulin*; *GAPDH: glyceraldehyde-3-phosphate dehydrogenase*; *RPL13A: ribosomal protein L13A*; *RPS18: ribosomal protein S18*; *PPIA: peptidylprolyl isomerase A*) were selected as described in Palombella et al. [53]. qPCR reaction was set up with 300 nM of each primer and 5 ng of cDNA in a total volume of 10 µL. The thermocycler program included an initial hot start cycle at 95 °C for 3 min followed by 40 amplification cycles consisting of a denaturation step at 95 °C for 10 s and an

annealing-extension phase at 60 °C for 30 s. A melt-curve was performed at the end of each run. Technical triplicates were run for all samples.

Table 1. Primers used in this work. Fw: forward, Rv: reverse.

Gene Name		Sequence 5′–3′	Amplicon Leght (bp)	NCBI Accession Number
ACTβ	Fw	ATGGGTCAGAAGGATTCC	78	NM_001101.3
	Rv	CTCGATGGGGTACTTCAG		
B2M	Fw	CTATCCAGCGTACTCCAA	93	NM_004048.2
	Rv	GAAACCCAGACACATAGC		
GAPDH	Fw	TTTGGCTACAGCAACAGG	107	NM_001289746.1
	Rv	GGTCTCTCTCTTCCTCTTG		
RPL13A	Fw	TATGAGTGAAAGGGAGCC	82	NM_001270491.1
	Rv	ATGACCAGGTGGAAAGTC		
RPS18	Fw	GAGGTGGAACGTGTGATC	109	NM_022551.2
	Rv	GGACCTGGCTGTATTTTC		
PPIA	Fw	AACCACCAGATCATTCCTT	86	NM_001300981.1
	Rv	GCGAGAGCACAAAGATTC		
MT1A	Fw	CTCCTGCAAGAAGAGCTG	87	NM_005946.2
	Rv	TTCTCTGATGCCCCTTTG		
Hsp70	Fw	AGGCGGAGAAGTACAAAG	85	NM_005345.5
	Rv	ATGTTGAAGGCGTAGGAC		
CAT	Fw	TACCCTCTCATCCCAGTT	85	NM_001752.3
	Rv	GGTCGAAGGCTATCTGTT		
SOD	Fw	CAGATGACTTGGGCAAAG	82	NM_000454.4
	Rv	CCAATTACACCACAAGCC		
P53	Fw	CCACCATCCACTACAACT	92	NM_000546.5
	Rv	GGAGTCTTCCAGTGTGAT		
CASP3	Fw	GAGGCCGACTTCTTGTAT	92	NM_004346.3
	Rv	CAAAGCGACTGGATGAAC		
BCL2	Fw	CCTTCTTTGAGTTCGGTG	98	NM_000633.2
	Rv	CAGGTACTCAGTCATCCA		
EGR1	Fw	GCAGAAGGACAAGAAAGC	94	NM_001964.2
	Rv	CGGGTAAGAGGTAGCAAC		
HIF1α	Fw	CAAGTCCTCAAAGCACAG	75	NM_001530.3
	Rv	TGGTAGTGGTGGCATTAG		
VEGF	Fw	GGAGTCCAACATCACCAT	80	NM_001171623.1
	Rv	GCTGTAGGAAGCTCATCT		
IL6	Fw	ACTCACCTCTTCAGAACG	113	NM_000600.3
	Rv	CCTCTTTGCTGCTTTCAC		
IL8	Fw	GCCAAGGAGTGCTAAAGA	103	NM_000584.3
	Rv	TGGTCCACTCTCAATCAC		
IL1b	Fw	CTACGAATCTCCGACCAC	90	NM_000576.2
	Rv	AACCAGCATCTTCCTCAG		
AP2A1	Fw	CTGGTGGAATGTCTGGAG	117	NM_014203.2
	Rv	GATGATGAGGCTGATGGT		

4.7. Statistical Analysis

Cytotoxicity results were expressed as mean F ± SE. With respect to qPCR, the comparative ΔΔCt method was used to present normalized gene expression. All data were analysed with one-way Analysis of Variance ANOVA (α = 0.05), completed with Dunnett's test ($p < 0.05$) in order to determine which groups (NPs, MPs, ions) were significantly different from control. Statistical significant differences was fixed at $p \leq 0.05$ (*). Each plotted value is the mean of three independent experiments.

References

1. Klimczak, A.; Kozlowska, U. Mesenchymal Stromal Cells and Tissue-Specific Progenitor. *Stem Cells Int.* **2016**, *2016*, 4285215. [CrossRef] [PubMed]

2. Gage, F.H. Mammalian Neural Stem Cells. *Science* **2000**, *287*, 1433–1438. [CrossRef] [PubMed]

3. Caplan, A.I.; Bruder, S.P. Mesenchymal stem cells: Building blocks for molecular medicine in the 21st century. *Trends Mol. Med.* **2001**, *7*, 259–264. [CrossRef]

4. Cherubino, M.; Valdatta, L.; Balzaretti, R.; Pellegatta, I.; Rossi, F.; Protasoni, M.; Tedeschi, A.; Accolla, R.S.; Bernardini, G.; Gornati, R. Human Adipose-Derived Stem Cells Promote Vascularization of Collagen-Based Scaffolds Transplanted into Nude Mice. *Regen. Med.* **2016**, *11*, 261–271. [CrossRef] [PubMed]

5. Conrad, C.; Huss, R. Adult Stem Cell Lines in Regenerative Medicine and Reconstructive Surgery. *J. Surg. Res.* **2005**, *124*, 201–208. [CrossRef] [PubMed]

6. Suma, R.N.; Mohanan, P.V. Stem Cells, a New Generation Model for Predictive Nano Toxicological Assessment. *Curr. Drug. MeTab.* **2015**, *16*, 932–939. [CrossRef] [PubMed]

7. Edmundson, M.; Nguyen, T.K.T.; Song, B. Nanoparticles Based Stem Cell Tracking in Regenerative Medicine. *Theranostics* **2013**, *3*, 573–582. [CrossRef] [PubMed]

8. Cattaneo, A.G.; Gornati, R.; Sabbioni, E.; Chiriva-Internati, M.; Cobos, E.; Jenkinsf, M.R.; Bernardini, G. Nanothecnology and human health: Risks and beneficts. *J. Appl. Toxicol.* **2010**, *30*, 730–744. [CrossRef] [PubMed]

9. Rancoule, C.; Magné, N.; Vallard, A.; Guy, J.B.; Rodriguez-Lafrasse, C.; Deutsch, E.; Chargari, C. Nanoparticles in radiation oncology: From bench-side to bedside. *Cancer Lett.* **2016**, *375*, 256–262. [CrossRef] [PubMed]

10. Sabbioni, E.; Fortaner, S.; Farina, M.; Del Torchio, R.; Olivato, I.; Petrarca, C.; Bernardini, G.; Mariani-Costantini, R.; Perconti, S.; Di Giampaolo, L.; et al. Cytotoxicity and morphological transforming potential of cobalt nanoparticles, microparticles and ions in Balb/3T3 mouse fibroblasts: An in vitro model. *Nanotoxicology* **2014**, *8*, 455–464. [CrossRef] [PubMed]

11. Shi, J.; Wang, B.; Chen, Z.; Liu, W.; Pan, J.; Hou, L.; Zhang, Z. A Multi-Functional Tumor Theranostic Nanoplatform for MRI Guided Photothermal-Chemotherapy. *Pharm. Res.* **2016**, *33*, 1472–1485. [CrossRef] [PubMed]

12. Di Gioacchino, M.; Verna, N.; Gornati, R.; Sabbioni, E.; Bernardini, G. Metal nanoparticle health risk assessment. In *Nanotoxicology: From In Vivo and In Vitro Models to Health Risks*; Sahu, S.C., Casciano, D., Eds.; John Wiley & Sons, Ltd.: Chichester, UK, 2009; pp. 519–542.

13. Gornati, R.; Papis, E.; Di Gioacchino, M.; Sabbioni, E.; Dalle Donne, I.; Milzani, A.; Bernardini, G. In vivo and in vitro models for nanotoxicology testing. In *Nanotoxicology: From In Vivo and In Vitro Models to Health Risks*; Sahu, S.C., Casciano, D., Eds.; Wiley & Sons Ltd.: Chichester, UK, 2009; pp. 279–302.

14. Gornati, R.; Pedretti, E.; Rossi, F.; Cappellini, F.; Zanella, M.; Olivato, I.; Sabbioni, E.; Bernardini, G. Zerovalent Fe, Co and Ni nanoparticle toxicity evaluated on SKOV-3 and U87 cell lines. *J. Appl. Toxicol.* **2016**, *36*, 385–393. [CrossRef] [PubMed]

15. Braga, M.; Quecchia, C.; Perotta, C.; Timpini, A.; Maccarinelli, K.; Di Tommaso, L.; Di Gioacchino, M. Systemic nickel allergy syndrome: Nosologic framework and usefulness of diet regimen for diagnosis. *Int. J. Immunopathol. Pharmacol.* **2013**, *26*, 707–716. [CrossRef] [PubMed]

16. Klostergaard, J.; Seeney, C.E. Magnetic nanovectors for drug delivery. *Nanomedicine* **2012**, *8*, 37–50. [CrossRef] [PubMed]

17. Lacroix, L.M.; Delpech, F.; Nayral, C.; Lachaize, S.; Chaudret, B. New generation of magnetic and luminescent nanoparticles for in vivo real-time imaging. *Interface Focus* **2013**, *3*, 1–19. [CrossRef] [PubMed]

18. Parkes, L.M.; Hodgson, R.; Lu, L.T.; Tung, L.D.; Robinson, I.; Fernig, D.G.; Thanh, N.T.K. Cobalt nanoparticles as a novel magnetic resonance contrast agent–relaxivities at 1.5 and 3 Tesla. *Contrast Media Mol. Imaging* **2008**, *3*, 150–156. [CrossRef] [PubMed]

19. Manea, C.M.; Rusu, M.C.; Constantin, D.; Mănoiu, V.M.; Moldovan, L.; Jianu, A.M. Ultrastructural features of human adipose-derived multipotent mesenchymal stromal cells. *Rom. J. Morphol. Embryol.* **2014**, *55*, 1363–1369. [PubMed]

20. Lai, J.C.K.; Lai, M.B.; Jandhyam, S.; Dukhande, V.V.; Bhushan, A.; Daniels, C.K.; Leung, S.W. Exposure to titanium dioxide and other metallic oxide nanoparticles induces cytotoxicity on human neural cells and fibroblasts. *Int. J. Nanomed.* **2008**, *3*, 533–545.

21. Wang, J.; Zhou, G.; Chen, C.; Yu, H.; Wang, T.; Ma, Y.; Jia, G.; Gao, Y.; Li, B.; Sun, J.; et al. Acute toxicity and biodistribution of different sized titanium dioxide particles in mice after oral administration. *Toxicol. Lett.* **2007**, *168*, 176–185. [CrossRef] [PubMed]

22. Ciofani, G.; Genchi, G.G.; Liakos, I.; Cappello, V.; Gemmi, M.; Athanassiou, A.; Mazzola, B.; Mattoli, V. Effects of cerium oxide nanoparticles on PC12 neuronal-like cells: Proliferation, differentiation, and dopamine secretion. *Pharm. Res.* **2013**, *30*, 2133–2145. [CrossRef] [PubMed]

23. Hedlund, A.; Ahrén, M.; Gustafsson, H.; Abrikossova, N.; Warntjes, M.; Jönsson, J.I.; Uvdal, K.; Engström, M. Gd_2O_3 nanoparticles in hematopoietic cells for MRI contrast enhancement. *Int. J. Nanomed.* **2011**, *6*, 3233–3240. [CrossRef]

24. Samberg, M.E.; Loboa, E.G.; Oldenburg, S.J.; Monteiro-Riviere, N. Silver nanoparticles do not influence stem cell differentiation but cause minimal toxicity. *Nanomedicine* **2012**, *7*, 1197–1209. [CrossRef] [PubMed]

25. Tautzenberger, A.; Lorenz, S.; Kreja, L.; Zeller, A.; Musyanovych, A.; Schrezenmeier, H.; Landfester, K.; Mailänder, V.; Ignatius, A. Effects of fluorescence-labelled nanoparticles on mesenchymal stem cell differentiation. *Biomaterials* **2010**, *31*, 2064–2071. [CrossRef] [PubMed]

26. Choi, S.Y.; Song, M.S.; Ryu, P.D.; Lam, A.T.; Joo, S.W.; Lee, S.Y. Gold nanoparticles promote osteogenic differentiation in human adipose-derived mesenchymal stem cells through the Wnt/beta-catenin signaling pathway. *Int. J. Nanomed.* **2015**, *10*, 4383–4392. [CrossRef]

27. Hackenberg, S.; Scherzed, A.; Kessler, M.; Hummel, S.; Technau, A.; Froelich, K.; Ginzkey, C.; Hagen, R.; Kleinsasser, N. Silver nanoparticles: Evaluation of DNA damage, toxicity and functional impairment in human mesenchymal stem cells. *Toxicol. Lett.* **2011**, *201*, 27–33. [CrossRef] [PubMed]

28. Mancuso, L.; Cao, G. Acute toxicity test of CuO nanoparticles using human mesenchymal stem cells. *Toxicol. Mech. Methods* **2014**, *24*, 449–454. [CrossRef] [PubMed]

29. Rudge, S.R.; Kurtz, T.L.; Vessely, C.R.; Catterall, L.G.; Williamson, D.L. Preparation, characterization, and performance of magnetic iron-carbon composite microparticles for chemotherapy. *Biomaterials* **2000**, *21*, 1411–1420. [CrossRef]

30. Tan, Y.K.; Best, S.L.; Donnelly, C.; Olweny, E.; Kapur, P.; Mir, S.A.; Gnade, B.; McLeroy, S.; Pearle, M.S.; Cadeddu, J.A. Novel iron oxide microparticles used to render stone fragments paramagnetic: Assessment of toxicity in a murine model. *J. Urol.* **2012**, *188*, 1972–1977. [CrossRef] [PubMed]

31. Indech, R. Nanotechnological Processing of Catalytic Surfaces. U.S. Patent 20060115389 A1, 1 June 2006.

32. Toghill, K.E.; Xiao, L.; Phillips, M.A.; Compton, R.G. The non-enzymatic determination of glucose using an electrolytically fabricated nickel microparticle modified boron-doped diamond electrode or nickel foil electrode. *Sens. Actuators B* **2010**, *147*, 642–652. [CrossRef]

33. Ahamed, M. Toxic response of nickel nanoparticles in human lung epithelial A549 cells. *Toxicol* **2011**, *25*, 930–936. [CrossRef] [PubMed]

34. Greulich, C.; Diendorf, J.; Simon, T.; Eggeler, G.; Epple, M.; Köller, M. Uptake and intracellular distribution of silver nanoparticles in human mesenchymal stem cells. *Acta Biomater.* **2011**, *7*, 347–354. [CrossRef] [PubMed]

35. Papis, E.; Rossi, F.; Raspanti, M.; Dalle-Donne, I.; Colombo, G.; Milzani, A.; Bernardini, G.; Gornati, R. Engineered cobalt oxide nanoparticles readily enter cells. *Toxicol. Lett.* **2009**, *189*, 253–259. [CrossRef] [PubMed]

36. Bossi, E.; Zanella, D.; Gornati, R.; Bernardini, G. Cobalt oxide nanoparticles can enter inside the cells by crossing plasma membranes. *Sci. Rep.* **2016**, *6*, 22254. [CrossRef] [PubMed]

37. Petrarca, C.; Clemente, E.; Amato, V.; Pedata, P.; Sabbioni, E.; Bernardini, G.; Iavicoli, I.; Cortese, S.; Niu, Q.; Otsuki, T.; et al. Engineered metal based nanoparticles and innate immunity. *Clin. Mol. Allergy* **2015**, *13*, 13. [CrossRef] [PubMed]

38. Lim, D.H.; Jang, J.; Kim, S.; Kang, T.; Lee, K.; Choi, I.H. The effects of sub-lethal concentrations of silver nanoparticles on inflammatory and stress genes in human macrophages using cDNA microarray analysis. *Biomaterials* **2012**, *33*, 4690–4699. [CrossRef] [PubMed]

39. Yang, E.J.; Kim, S.; Kim, J.S.; Choi, I.H. Inflammasome formation and IL-1β release by human blood monocytes in response to silver nanoparticles. *Biomaterials* **2012**, *33*, 6858–6867. [CrossRef] [PubMed]

40. Macro, L.; Jaiswal, J.K.; Simon, S.M. Dynamics of clathrin-mediated endocytosis and its requirement for organelle biogenesis in Dictyostelium. *J. Cell Sci.* **2012**, *125*, 5721–5732. [CrossRef] [PubMed]

41. Simpson, R.J.; Hammacher, A.; Smith, D.K.; Matthews, J.M.; Ward, L.D. Interleukin-6: Structure-function relationships. *Protein Sci.* **1997**, *6*, 929–955. [CrossRef] [PubMed]

42. Gnecchi, M.; Zhang, Z.; Ni, A.; Dzau, V.J. Paracrine mechanisms in adult stem cell signalling and therapy. *Circ. Res.* **2015**, *103*, 1204–1219. [CrossRef] [PubMed]

43. Gronthos, S.; Zannettino, A.C. Methods for the purification and characterization of human adipose-derived stem cells. *Methods Mol. Biol.* **2011**, *702*, 109–120. [CrossRef] [PubMed]

44. Bava, A.; Cappellini, F.; Pedretti, E.; Rossi, F.; Caruso, E.; Vismara, E.; Chiriva-Internati, M.; Bernardini, G.; Gornati, R. Heparin and carboxymethylchitosan metal nanoparticles: An evaluation of their cytotoxicity. *BioMed Res. Int.* **2013**, *2013*, 314091. [CrossRef] [PubMed]

45. Bava, A.; Gornati, R.; Cappellini, F.; Caldinelli, L.; Pollegioni, L.; Bernardini, G. D-amino acid oxidase-nanoparticle system: A potential novel approach for cancer enzymatic therapy. *Nanomedicine* **2013**, *8*, 1797–1806. [CrossRef] [PubMed]

46. Ahamed, M.; Ali, D.; Alhadlaq, H.A.; Akhtar, M.J. Nickel oxide nanoparticles exert cytotoxicity via oxidative stress and induce apoptotic response in human liver cells (HepG2). *Chemosphere* **2013**, *93*, 2514–2522. [CrossRef] [PubMed]

47. Bardack, S.; Dalgard, C.L.; Kalinich, J.F.; Kasper, C.E. Genotoxic changes to rodent cells exposed in Vitro to Tungsten. Nickel, Cobalt and Iron. *Int. J. Environ. Res. Public Health* **2014**, *11*, 2922–2940. [CrossRef] [PubMed]

48. Defo, M.A.; Bernatchez, L.; Campbell, P.G.C.; Couture, P. Waterborne cadmium and nickel impact oxidative stress responses and retinoid metabolism in yellow perch. *Aquat. Toxicol.* **2014**, *154*, 207–220. [CrossRef] [PubMed]

49. Efremenko, A.Y.; Campbell, J.L.; Dodd, D.E.; Oller, A.R.; Clewell, H.J. Time- and concentration-dependent genomic responses of the rat airway to inhaled nickel subsulfide. *Toxicol. Appl. Pharmacol.* **2014**, *279*, 441–454. [CrossRef] [PubMed]

50. Hussainzada, N.; Lewis, J.A.; Baer, C.E.; Ippolito, D.L.; Jackson, D.A.; Stallings, J.D. Whole adult organism transcriptional profiling of acute metal exposures in male zebrafish. *BMC Pharmacol. Toxicol.* **2014**, *15*, 1–15. [CrossRef] [PubMed]

51. Palomäki, S.; Pietilä, M.; Laitinen, S.; Pesälä, J.; Sormunen, R.; Lehenkari, P.; Koivunen, P. HIF-1α is upregulated in human mesenchymal stem cells. *Stem Cells* **2013**, *31*, 1902–1909. [CrossRef] [PubMed]

52. Silva, E.A.; Mooney, D.J. Effects of VEGF temporal and spatial presentation on angiogenesis. *Biomaterials* **2010**, *31*, 1235–1241. [CrossRef] [PubMed]

53. Palombella, S.; Pirrone, C.; Cherubino, M.; Valdatta, L.; Bernardini, G.; Gornati, R. Identification of reference genes for qPCR analysis during hASC long culture maintenance. *PLoS ONE* **2017**, *12*, e0170918. [CrossRef] [PubMed]

IV. RESULTS AND DISCUSSION

SYNTHESIS AND FUNCTIONALIZATION

In the literature, various methods to synthesize IONPs are described, among these procedures the chemical co-precipitation of Fe^{2+} and Fe^{3+} ions by an alkali such as NH_4OH, in an aqueous solution is the most commonly used. For these thesis project, IONPs were synthetized by a co-precipitation method described in the in the article entitled "Synthesis, characterization and programmable toxicity of iron oxide nanoparticles conjugated with D-amino acid oxidase" attached at the end of the *Materials and Methods* Chapter. The synthesis lead to the production of NPs with a diameter of 9.37 ± 0.5 nm as measured by transmission electron microscopy (Figure 12, a-d). The co-precipitation method employed is a relatively easy and convenient way to synthesize iron oxides as it works at low temperatures (<90°C), with low reaction times and with a high production yield and reproducibility[29,142].

To create a platform for biomolecule conjugation, amino-groups were introduced on the particles surface by 3-aminopropyltriethoxysilane (APTES) coating. The functionalization mechanism is based on the formation of the Fe-O-Si bond between the NP and the silane. The general sequence of silanization involves the hydrolysis of the trietoxylated groups in trihydroxy groups and, therefore, the polycondensation of the hydroxyl groups of the silane with the hydroxyl groups from the NP surface[38]. DLS and ζ potential analysis were used to verify the correct coating of the particles. DLS shows that APTES coated NPs (NP-APTES) present a hydrodynamic radius of 35.5 ± 0.5 nm, double respect to that of uncoated IONPs (Figure 12 e). An higher hydrodynamic size of NPs measured by DLS, in comparison with the TEM analysis, can be attributed to the formation of extra hydrate layers in aqueous solutions and the fact that DLS cannot discriminate between inorganic and organic material[143,144]. ζ potential measurements confirmed the APTES functionalization, indeed, the superficial charge of NP-APTES increased up to three-fold respect to that of IONPs, i.e., 33.49 ± 0.2 mV versus 11 ± 0.8 mV. This increase can be explained by the presence of free positive amine groups of APTES on the NP surface. The amount of primary amine groups that were present on NP surface and available for subsequent

functionalization were quantified by the Orange II assay[136,137]. This assay is based on the electrostatic interactions between the anionic dye and the protonated amino groups in acidic solution. By this assay, it was estimated that each NP-APTES carries an average of 22 amino groups on its surface.

IONPs and NP-APTES were further characterized performing vibrating sample magnetometry analysis. The saturated magnetization value of the IONPs and that of NP-APTES were 58.7 and 36.4 Am^2/kg Fe_2O_3, respectively. These values are in the range of those of the bulk material, for IONPs, while for the NP-APTES are slightly low. The coating with APTES reduced the response to the magnetic field. Surface coating, on the other hand, does not affect the superparamagnetic behaviour of the particles, both IONPs and NP-APTES show indeed a superparamagnetic behaviour (Figure 12 f).
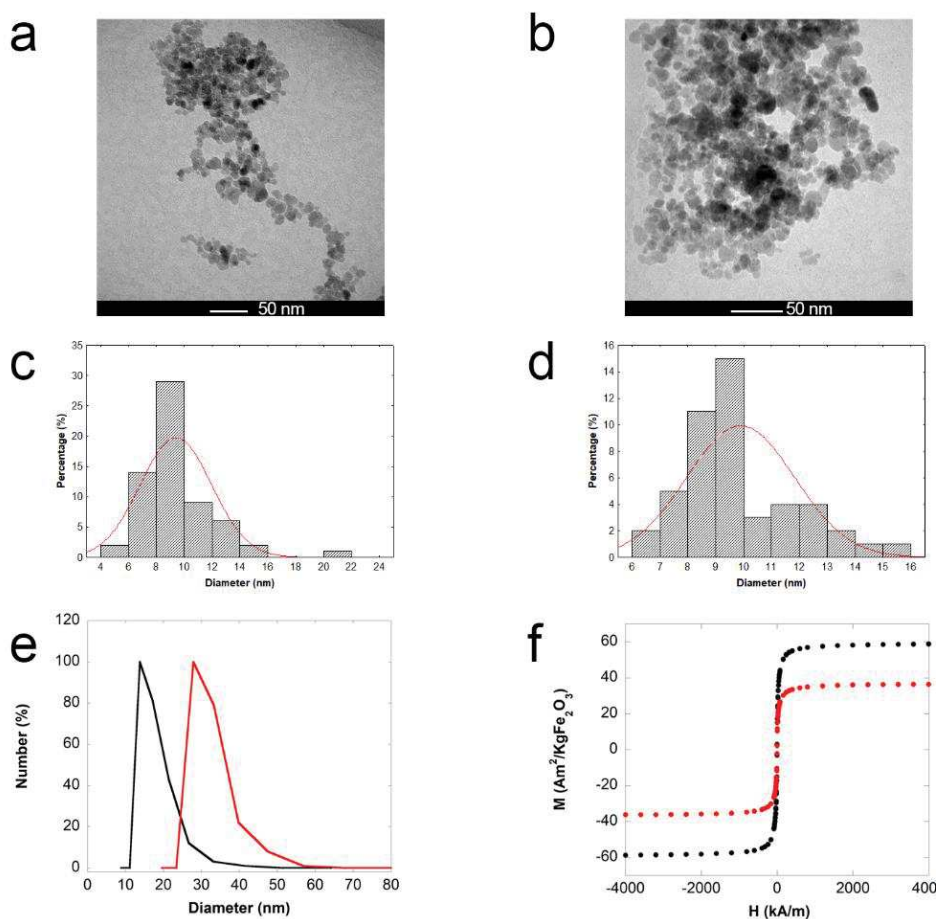
Figure 12 Characterization of IONPs and NP-APTES. a, b) TEM micrograph of IONPs and NP-APTES, scale bar 50 nm. Size distribution of IONPs (c) and NP-APTES (d). e) DLS analysis of IONPs (black) and NP-APTES (red). f) Vibrating magnetometry analysis of IONPs (black) and NP-APTES (red).

Another important parameter for IONPs is the specific absorption rate (SAR) that is defined as the amount of energy/power absorbed by the sample per mass unit (W/kg). For IONPs and NP-APTES, this parameter was analysed under an AMF of 710 kHz and 300 Gauss. SAR values confirm the magnetic heating ability of the NPs synthetized after the APTES functionalized even if we assist to a decrease in SAR value. Indeed, the SAR is 393 ± 9 W/g for IONPs and 242 ± 13 W/g for NP-APTES.

As the coupling reaction of the biomolecules is carried on different pH and ionic strength conditions, the colloidal stability of the NP-APTES was studied in a range of 3 to 12 pH and in the range to 0.01-100 mM NaCl (Figure 13).
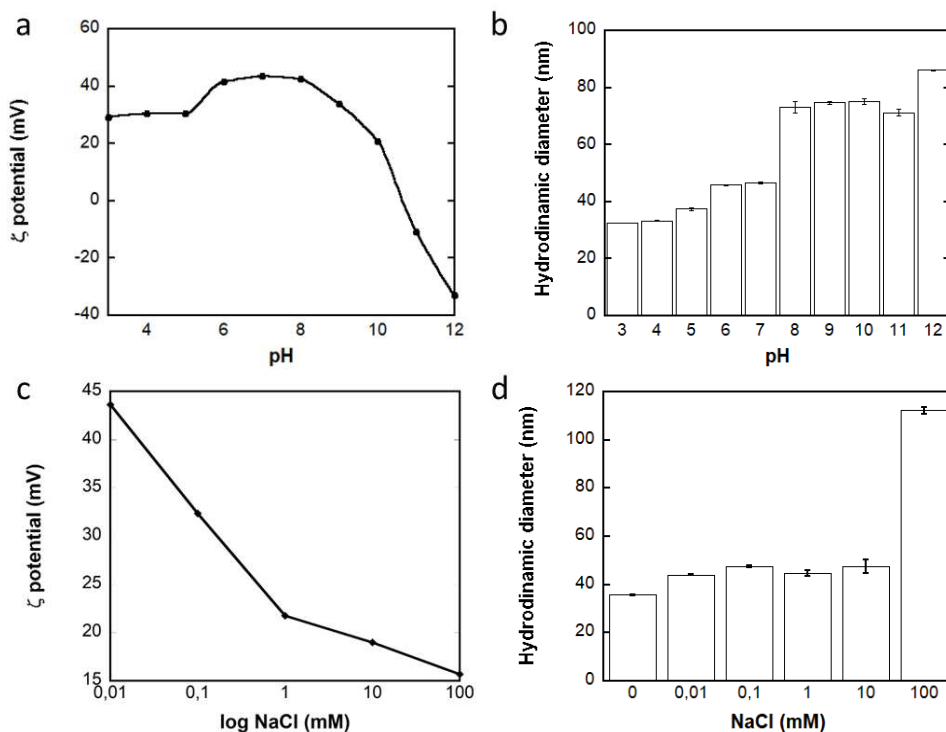
Figure 13. Stability of NP-APTES in different pH medium (a,b) and NaCl concentration (c, d). Results a media of three independent measurements.

No significant stability loss was observed in the 3 to 7 pH range and no significant increase in the hydrodynamic diameters is observed in that range. Contrariwise, a significant loss of stability occurs at alkaline conditions and at high NaCl concentration ($\geq$ 100 mM), indeed it is possible to observe a weak ζ potential.

NPS-ENZYME SYSTEMS

Nanobiocatalysis, as the combination of nanotechnology and biocatalysis, is rapidly emerging as a new frontier of biotechnology. Immobilized enzymes have a lot of advantages over their soluble counterparts, mainly related to stability, reusability and operational processing. Because of their singular properties, such as biocompatibility, large and modifiable surface and easy recovery, IONPs facilitate separation of the linked enzymes that can be easily obtained, lowering dramatically the costs of enzymes, by applying an external magnetic field.

L-aspartate oxidase

The FAD-containing enzyme LASPO catalyzes the stereospecific oxidative deamination of L-aspartate to oxalacetate, ammonia and hydrogen peroxide. This flavoenzyme from the thermophilic archea *Sulfolobus tokodaii* (LASPO) presents an high thermostability and a stable activity in a broad range of pH values that make it very attractive for biotechnological applications. LASPO can be used for the production of D-aspartate, a molecule employed in the pharmaceutical industry, for parenteral nutrition, as food additive and in sweetener manufacturing. Since the industrial application of this enzyme is hampered by the high cost per enzymatic unit, here are reported different conjugation strategies.

Optimization of enzyme conjugation

It is demonstrated that the conjugation of enzymes to NPs has a critical role on their activity because of deleterious conformational changes, reduction of flexibility, alteration of the hydration shell and blockage or hindering of the active site [145–147]. Therefore, taking into consideration the L-aspartate oxidase structure, we design different conjugation strategies with the aim to obtain different orientations of the enzyme on the NPs and to secure enzyme-NP systems with both good conjugation yield and high relative activity (Figure 14):

- **Strategy 1 (NP-LASPO1):** the enzyme molecules are directly conjugated to the amino groups of the NP-APTES through their carboxylate moieties after their activation with EDC and NHS using the carbodiimide chemistry. The

analysis of LASPO crystalline structure (PDB entry 2E5V), showed the presence of a high number of exposed carboxylic groups that were reacted with the EDC forming an active O-acylisourea intermediate that could be displaced by the nucleophilic attack of the amino groups present on the NP-APTES surface.

- **Strategy 2 (NP-LASPO2):** enzyme molecules are covalent bound via thiol groups from cysteine residues present on their surface. The presence of a unique cysteine residue exposed on the LASPO surface ensure the site-directed attachment of the enzyme through an orientation far from its active site. For this strategy, the amino groups of the NPs need to be transformed to thiol-reactive groups by modification with sulfosuccinimidyl 4-(N-maleimidomethyl)cyclohexane-1-carboxylate) (Sulfo-SMCC) and the protein need to be reduced.

- **Strategy 3 (NP-LASPO3):** enzyme molecules are covalently bound via their amine reactive moieties after the activation of the amine moieties of NP-APTES with bis(sulfosuccinimidyl)suberate (BS3). Thus, playing with the pH reaction, it should ensure a conjugation through the amino terminal of the enzyme, with a specific orientation of the enzyme in which its active site is facing the NP surface.

- **Strategy 4 (NP-LASPO4):** enzyme molecules are bound in an oriented way through their histidine tag by coordination with Cu^{+2}. The established bond, although non-covalent, is strong as hexa histidine tags show the apparent equilibrium dissociation constant in the nM range[148]. The His-tagged is present in the C-terminus of the protein that is placed opposite to the active site. Thus, this binding strategy should also render a site-directed orientation with the binding site far from the active site of the enzyme.
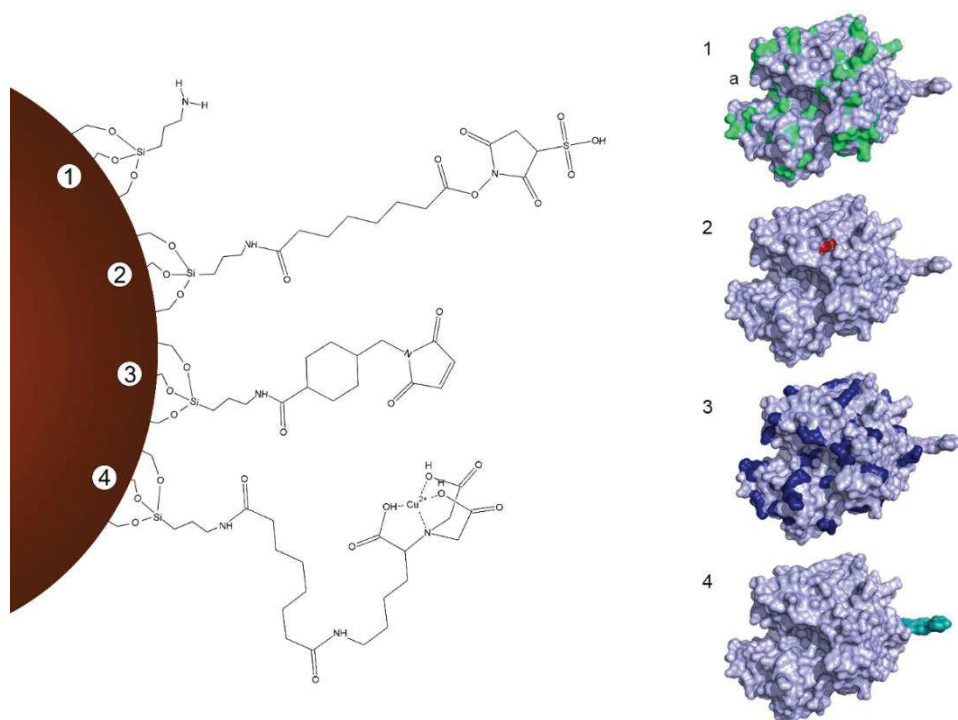
Figure 14. Conjugation chemistry used to functionalize IONPs. On the left, from top to bottom, we have schematized the above-described strategies 1) APTES, 2) APTES-sulfo-SMCC, 3) APTES-BS3, and 4) APTES-NTA-Cu^{2+}. On the right, is reported the three-dimensional structure of the LASPO and are highlighted the residues involved in each conjugation strategy. From top to bottom: carboxylic groups (strategy 1), cysteine (strategy 2), amino-groups (strategy 3) and histidine tag (strategy 4). The enzyme structure was taken from the Protein Data Bank (PDB) entry 2E5V and visualized using PyMol v2.1.

To identify the best conditions for the enzyme conjugation for each strategy several factors have been taken into consideration: pH of reaction, amount of cross-linker, time of reaction.

It is well known that ionic interaction can occur between NPs and biomolecules depending on the pH of reaction media. Thus to better understand the orientation of the enzyme after ionic interaction with NP-APTES, a study of the 3D structure was carried on in more detail. It is well known that the side of the protein with the higher charge residues is the one that will faster react with the NP-APTES via a rapid ionic adsorption and that a slower site-directed covalent binding reaction occurs via activated amino-groups. Given that, the enzyme charge distribution was studied (Figure 15).
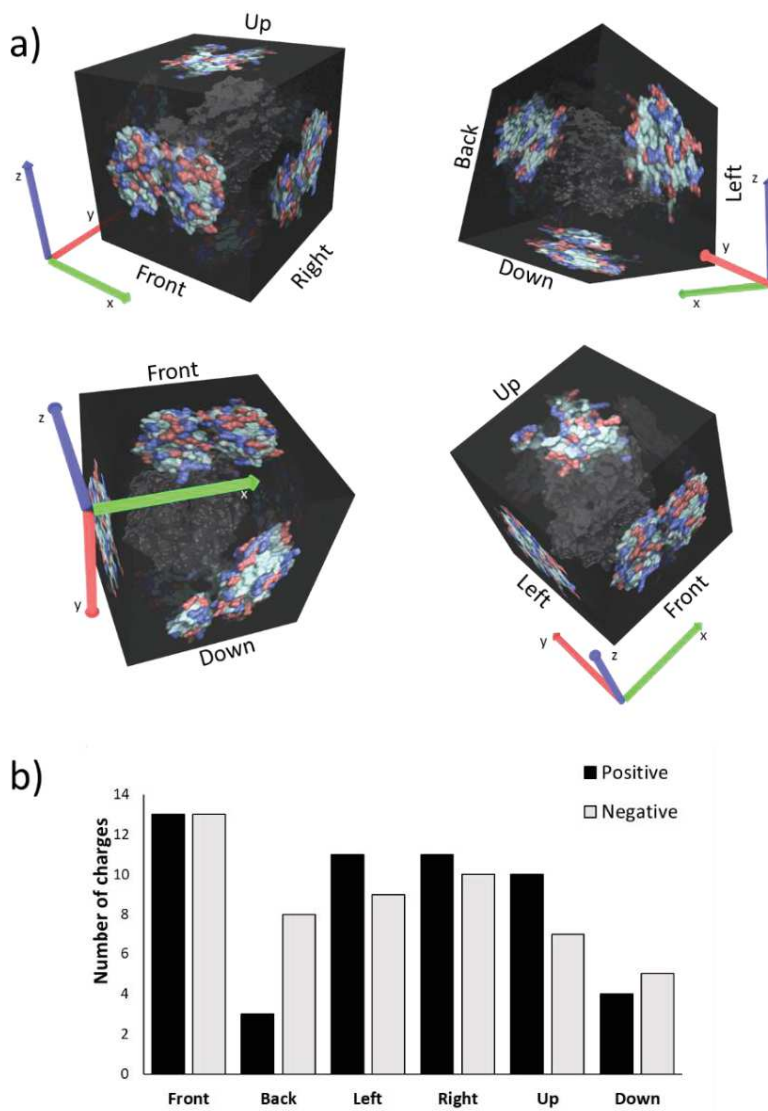
Figure 15. 3D structure of LASPO showing the positive and negative charge surface distribution. The enzyme structure was taken from the Protein Data Bank (PDB) entry 2E5V and visualized using PyMol v2.1. Negative and positive charges are displayed in red and blue, respectively. (a) graphic representation of interaction plane of the enzyme. (b) Number of charged residues per plane of interaction.

Results underline that the region in which the active site is located (front side) is the one with the highest negative charged residues, while the region with the lowest negative charge is on the bottom part of the LASPO molecule. Interestingly, the region with the active site is also the one with the highest positive charges. Accordingly, the region of the enzyme that will react faster is the one in which the active site is present.

To confirm the possibility of ionic interactions, further analysis were carried on. An analysis of the surface potential of the enzyme was performed using the Adaptive Poisson-Boltzmann Solver (APBS). This software is designed to analyze the solvation properties of small molecules as well as macro-molecules, such as proteins[149].

The surface potential was calculated at the different pH that were used in the conjugation conditions. Figure 16 shows the surface potential (a) and the electrostatic potential iso-contours (b), positive and negative charged surface are indicated in blue and red, respectively.
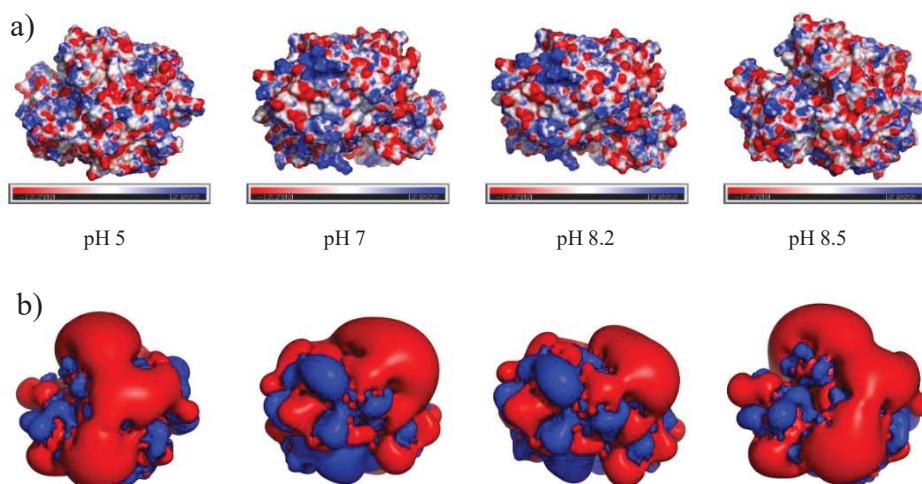
Figure 16. Analysis of the surface potential of the enzyme. The PDB entry 2E5V was selected for this 3D representation. APBS was used to calculate the surface potential and the analysis results were visualized using Pymol v2.1. (a) ±10 kT/e electrostatic potential of LASPO in PyMOL plotted on the solvent-accessible surface. (b) ±0.6 kT/e electrostatic potential isocontours of LASPO in PyMOL. The enzyme molecules are oriented to visualized the surface potential in the nearby of the residue used for the conjugation.

Figure 16 depicts an high concentration of negative charge (red) near the active site, were the N-terminus is located in all the condition considered, even though at pH 7 it is possible to observe the highest density of negative charges. At pH 8.2, instead, the concentration of negative charges are lower, suggesting the possibility of less ionic interactions.

Table 4 reports the results of the best condition for each strategy: it is possible to notice that the different coupling strategies led to different relative activities and number of conjugated enzyme molecules per NP.

Table 4. Enzyme-NPs conjugated reaction parameters.

	Cross linker	$\mu g_{enzyme}/mg_{NPs}$	Relative Activity (%)*	Active enzyme molecules/NP
NP-LASPO1	EDC/NHS	7	17	5
NP-LASPO2	Sulfo-SMCC	25	87	22
NP-LASPO3	BS^3	37	86	17
NP-LASPO4	NTACu^{2+}	6	25	2

*Relative activity is the ratio between the activity assayed for the enzyme-conjugated NPs and the activity of the free enzyme.

Strategy 1 was the worst one not only in terms of recovered activity after enzyme immobilization, but also in number of molecules per NP. Although the concentrations of EDC and NHS was carefully chosen to yield complete activation of the binding sites and, at the same time, to prevent formation of unwanted surface by-products, the low relative activity obtained with this strategy suggest the presence of protein-to-protein crosslinking due to the abundance of both amines and carboxylates on protein molecules[150].

For **strategy 2**, the NP-APTES were further modified to have thiol-reactive groups on the particles surface using Sulfo-SMCC. To evaluate the correct functionalization of the NP-APTES, the residual amino groups present on the NP surface were quantified using Orange II assay: the number of amino-group per mg of NPs decreased from 15 to 11 nmol. Results indicate a reduction of the amino groups of the 27 % suggesting the presence of thiol-reactive groups. A reduction step was needed to activate the cysteine of the enzyme: Tris[2-carboxyethyl] phosphine hydrochloride (TCPE) was used to reduce the cysteine present on the enzyme surface. TCEP is known to be an efficient reductant of alkyl disulfides in a wide pH range. Furthermore, it is stable in aqueous solutions and does not undergo to rapid oxidation that often occurs with other reducing agents such as dithiotreitol (DTT) and β-mercaptoethanol (BME, 2-ME)[151] Additionally, TCEP does not interfere with commonly used sulfhydryl-reactive reagents (e.g., maleimide crosslinkers). Using this strategy, the best relative activity and the highest number of molecules per NP was obtained (NP-LASPO2). The binding through the cysteine moiety was confirmed, as only when the protein was previously reduced with TCPE reducing gel the conjugation was possible.

Besides, to demonstrate that the binding of the enzyme was achieved through the cysteine present on the enzyme molecule and not through unspecific binding, the NP-LASPO2 was incubated with DTT to reduce the disulfide bond: the reversibility of the disulphide bond formed was checked, the 100% of the enzyme molecules was released and no activity is detected in the NP-LASPO after the DTT addition.

Also **Strategy 3** resulted in a high relative activity and a high number of molecules per NP. In this case, the immobilization conditions were set in order to promote the direct covalent binding of the enzyme via the primary amine group of its N-terminus. Thus, the pH of reaction selected was 8.2, slighter higher than its pKa but lower than that for ε-amine of lysine residues (~ 10.5)[152]. Moreover, in literature, is reported that the pKa value of the amine of lysine residues can be lower than the tabled values, depending on the surrounding environment[153,154]. However, at this pH value the enzyme has net negative charge (pI 6.75) while BS3-activated NPs have a net positive one, as demonstrated also by ζ potential measurements (+27,95 mV). Thus, we cannot ensure the covalent binding via the enzyme amino terminus, as ionic adsorption reactions are much faster than covalent ones. Indeed, a slight ionic adsorption was observed when NP-APTES without BS3 activation were used as control, i.e. 10 μg of the enzyme is bound to 1 mg of NPs.

Taking into consideration the APBS data, it is possible to speculate that first, an initial rapid ionic adsorption of LASPO through this front plane of interaction occurred followed by a much slower site-directed covalent attachment via reaction of amino-groups facing the NP surface with its BS3 activated aminated groups. Although we cannot ensure a direct binding via its amino-terminal group, the final enzyme orientation obtained should be similar in both cases.

A further step was carried on to avoid this ionic adsorption and higher ionic strengths were used during enzyme immobilization. As this strategy did not work, we also tried to diminish the net positive charge of the NPs by carrying out the partial modification of its amino groups with an aminated-750 Da polyethylene glycol (PEG)[27,28] after their activation with BS3. However, the decrement in the net surface charge of the PEGylated-NPs was not enough to avoid LASPO ionic adsorption.

Finally, the enzyme we also bound by chelation of its histidine tag present on the C-terminus of the protein (**Strategy 4**), to orientate the enzyme so that its active site is completely exposed to the reaction media. Although, the orientation obtained should be similar to Strategy 3, this strategy has the advantage that it is not necessary to modify the enzyme previously. To confirm the specific orientation of the enzyme through its His-tag and exclude the possibility of ionic interactions the reaction of was carried on in presence of imidazole: no immobilization was observed. However, with this binding strategy we have obtained the worst results in terms of relative activity and enzyme molecules per NP.

These results confirm that the activity of the NP-enzyme systems strongly depends on the chemistry of conjugation that can cause conformational changes of the enzyme or lead to non-specific bindings with the NPs[155,156].

The enzyme-NPs systems obtained, were then analyzed by DLS and ζ potential (Table 5). After the enzyme conjugation, negative ζ potential values of the enzyme functionalized NPs is expected as LASPO has a net negative charge at the pH value of the measurements. With all the conjugation strategies a partial aggregation of the NPs was observed, although NP-LASPO4 was the one showing more aggregation. In this case, the surface functionalization of the particles, reduced their net charge, causing a decrease in their colloidal stability.

Table 5. Physical parameters of the different enzyme-NP systems.

	NP-LASPO1	NP-LASPO2	NP-LASPO3	NP-LASPO4
radius [nm] (TEM)	5.2 ± 0.5	4.9 ± 1.2	4.9 ± 1.4	5.6 ± 1.3
diameter [nm] (DLS)	84.4 ± 0.2	341 ± 0.8	220 ± 0.4	930 ± 0.4
Polydispersity Index (DLS)	0.319	0.2	0.212	0.301
ζ-potential [mV]	-22.9 ± 0.5	-32.6 ± 1.2	-16,45 ± 0.5	-15.88 ± 0.2

Biochemical characterization

The nano-systems produced were biochemically characterized and the catalytic parameters of the conjugated LASPO were determined by HPR-coupled spectrophotometric assay at pH 8.5 at 25°C, as previously reported[74]. The apparent Vmax at air oxygen saturation for all the NP-LASPO systems and Km for L-aspartate are reported in Table 6.

Table 6. Catalytic parameters of all the NP-LASPO conjugations.

	Specific activity (U/mg enzyme)	$V_{max, app}$ (μmol x min x mg enzyme)	Km (mM)
NP-LASPO1	0.36	0.33	4.55
NP-LASPO2	0.40	0.094	4.17
NP-LASPO3	0.34	0.289	1.17
NP-LASPO4	0.15	0.37	1.56

The different enzyme systems results in different Km: for NP-LASPO 3 and NP-LASPO 4 is similar to the one of the free enzyme (i.e. 1.3 mM), while the Km values for the others preparations are higher, suggesting a lower affinity for L-aspartate, so a higher substrate concentration is needed to achieve a given enzyme activity. This behaviour can be attributed to diffusional limitations and steric effects that cause a reduction in the accessibility of substrate to the enzyme active site. Furthermore, data in literature suggest that a high loading of enzyme molecules can cause a substrate accessibility reduction to the active site of the enzyme[79].

The effect of temperature on the catalytic properties of all the NP-LASPO systems was studied in the range of 25-70°C.
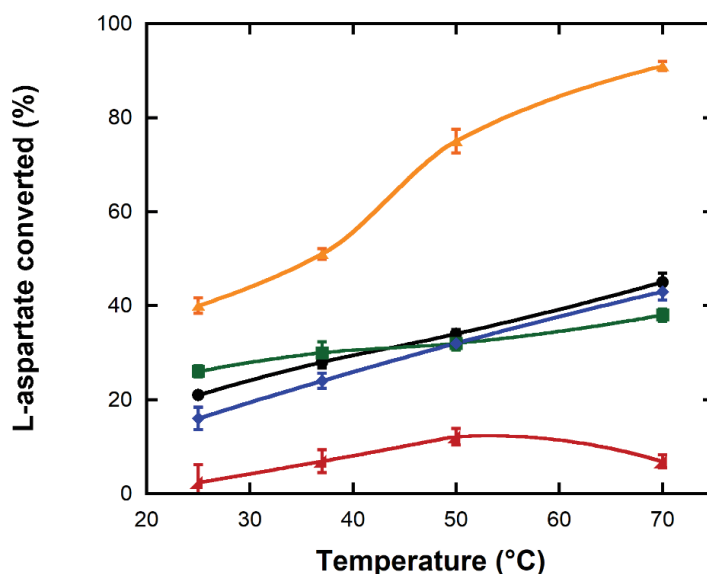
Figure 17. Effect of temperature on the activity conjugated or non-conjugated LASPO after 30 min of incubation: LASPO (orange), NP-LASPO 1 (black) NP-LASPO 2 (green), NP-LASPO 3 (blue) and NP-LASPO 4 (red)

Figure 17 reports the activity of the nanosystems after 30 min of reaction. NP-LASPO1, NP-LASPO2 and NP-LASPO3 have their optimum at 70°C black, green and blue curves) that is similar to that of the free LASPO, while the optimal temperature of NP-LASPO4 resulted shifted to 50°C (red curve). These results indicate that the conjugation of the enzyme through different residues influences the enzyme activity, acting on the enzyme 3D structures. The conjugation may avoid the stretching and the natural conformational changes that are necessary for the enzyme activity.

To further characterize the NP-LASPO systems, it was also studied the thermostability of all the batches incubating the enzyme at different temperatures and assessing the residual activity of the systems after 0 to 60 min of incubation (Figure 18).

As Figure18 suggests, all the NP-LASPO preparations are stable for at least 60 min for all the temperature considered. From 25°C to 90°C no significant differences were observed in term of activity loss between the different preparations. Except for NP-LASPO1, all the preparation retained the 90% of the starting activity.
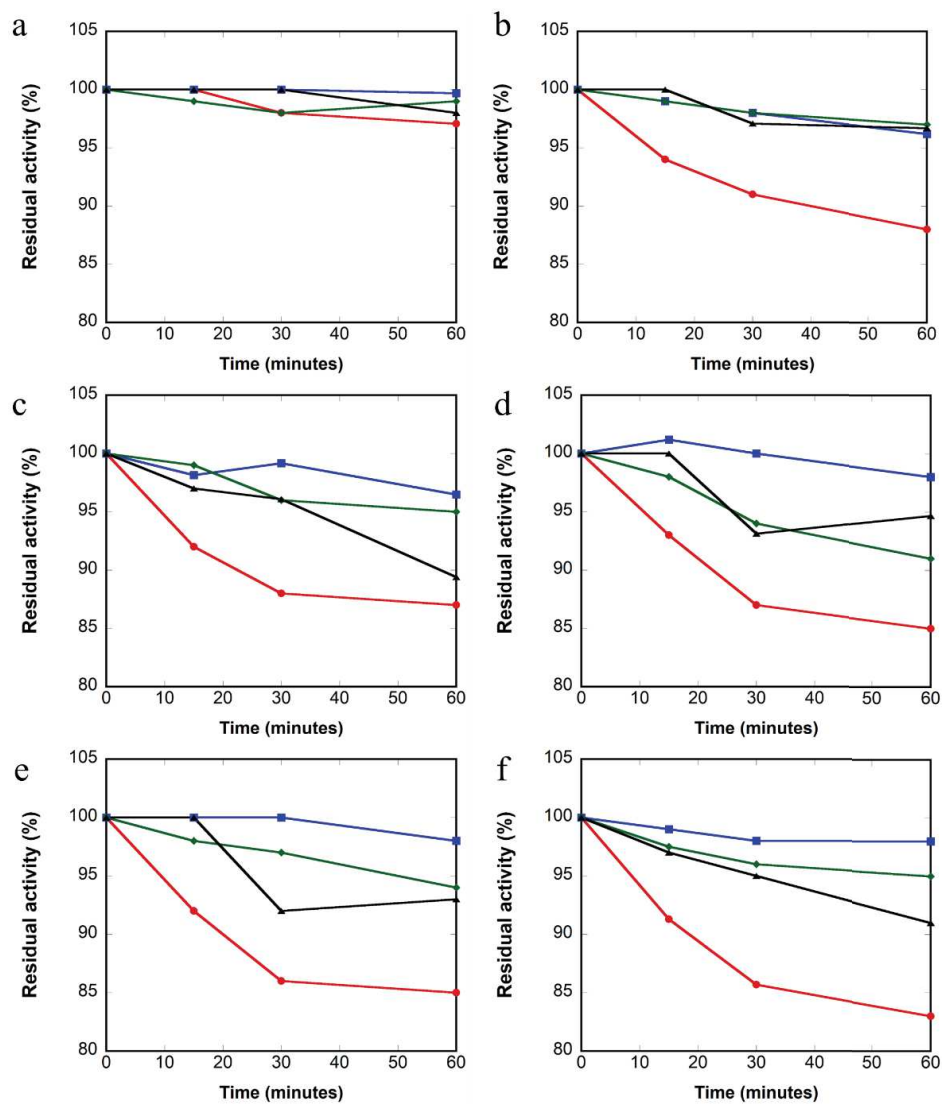
Figure 18. Thermal stability of NP-LASPO1 (red), NP-LASPO2(blue), NP-LASPO3 (green) and NP-LASPO4 (black) at different temperature: 25°C (a), 37°C (b), 50°C (c), 70°C (d), 80°C (e) and 90°C(f). Triplicate experiments were done for each condition, standard errors were lower than 5%.

Remote enzyme activation by AMF nanoactuation.

To evaluate the possibility to activate the immobilized enzymes solely by an AMF without heating the medium in which they are suspended, an AMF of 252 Gauss and 829 kHz was applied on the different NP-enzyme systems obtained.

As shown in Figure 19, by applying an AMF at a frequency of 829 kHz, it was possible to nanoactuate the LASPO enzyme immobilized on the NPs. To assess this, the values of the enzymatic activity detected after exposure to the AMF were compared to those obtained heating the sample during the same time, but using conventional thermal energy transfer (i.e., incubating test tubes in a thermoblock). NP-LASPO1, NP-LASPO2 and NP-LASPO3, when exposed to an AMF, show an activity that corresponds to that obtained incubating the NP-enzyme systems in a thermoblock at 30°C, 60°C and 45°C, respectively. Since the curve of the activity of NP-LASPO4 is not monotonic (Figure 16), for this NP-enzyme system, we cannot discriminate if the activity is comparable to the one obtained at 40°C or at 60°C. The global temperature in all cases was 21ºC, as expected as the volume fraction of the NPs was very low and, thus, it is possible to consider them thermally isolated from each other.
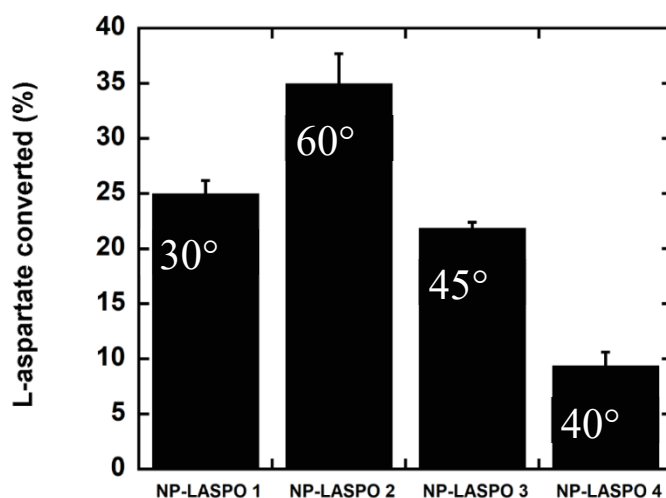
Figure 19. Activity of conjugated thermophilic enzymes under a 252 Gauss AMF with a frequency of 829 kHz and after 30 min.

The obtained results clearly showed that it was possible to nanoactuate the enzymes by AMF application whatever conjugation strategy was used without increasing the whole media temperature.

Comparing the activation efficiency in the case of NP-LASPO2 and NP-LASPO3, there are not significant differences between both enzyme-NPs preparations in terms of mean diameter after NPs functionalization, number of enzyme molecules per NP

or their relative activity after immobilization. Besides, the optimal temperatures of both immobilized enzyme preparations were similar to that of the free enzyme when heated using conventional thermal energy transfer systems. Though, when NPs were placed under an AMF, the enzyme activation efficiency was clearly better in the case of NP-LASPO2. The differences between the enzyme preparations could be attributed to the orientation of the enzyme once conjugated to the NPs. In the case of NP-LASPO 2 the active site is located far away from the NP surface while the opposite occurs in the case of NP-LASPO 3. Thus, it seems that orientation of the enzyme once attached to the NP surface could also play a critical role in the efficiency of the enzyme activation triggered by AMF. This should be a consequence of a different mechanism of thermal energy transference and inherent different rigidities of the zones through which the enzyme is attached to the support. Checking the 3D structure of LASPO, its back-region where binding took place when using Strategy 2 is much more rigid than the region near the active site used for the attachment in Strategy 3. This last zone has to be intrinsically more flexible to allow the conformational changes that are triggered by the presence of the enzyme substrate. The higher the rigidity of an enzyme area, the less is the susceptibility to its denaturation when exposed to a denaturant agent (co-solvents, temperature, etc).

Operational stability under an AMF

As one of the advantages of immobilized enzymes is the possibility to recover and reuse the enzyme, the operational stability of NP-LASPO preparations with the highest relative activity (NP-LASPO2 and NP-LASPO3) was evaluated after consecutive cycles of AMF activation. The operational stability is indicated as the number of reactions that could be carried on using the same batch of immobilized enzyme. Each cycle consisted of 30 min of reaction under a 252 Gauss and 829 kHz AMF. After each cycle of reaction, the immobilized enzyme was recovered through magnetic separation and reused to catalyze L-aspartate oxidation. Figure 20 shows that NP-LASPO 2 maintained all its activity for 3 cycles, while, after the same number of repeated uses, NP-LASPO3 retained only half of its original activity. Although the mechanism of energy transfer should be different from when the reaction media is heated globally, these results not only showed that it is possible to reuse the nano-

enzymes but also reinforce the importance of enzyme orientation to develop more efficient enzymatic processes under AMF activation.
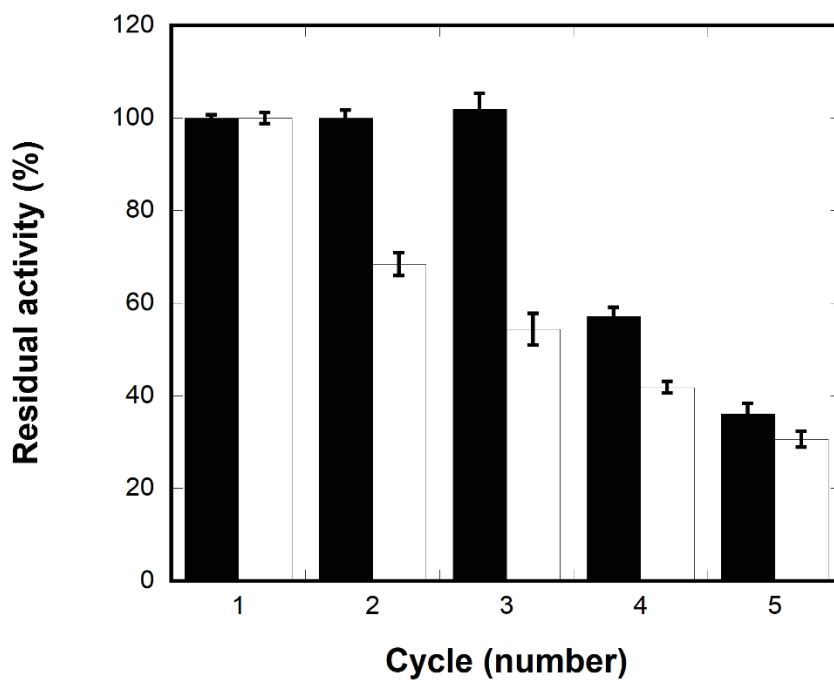
Figure 20. Operational stability of NP-LASPO2 and NP-LASPO3 systems exposed to an AMF of 829 kHz and 252 Gauss.

α-amylase

α-amylase is an endo-enzyme that cleaves the glycosidic bond within starch in the non-crystalline regions (cleaves a- 1-4 linkage) leading to the production of destrins, maltose and maltotriose. This enzyme has been isolated from different sources, from plant to animals. For industrial applications, the a-amylase from isolated from microrganisms are the most used due to the cost effectiveness, the less time and space required for production and the easy modification of the genome for the optimization. The protein isolated from *Bacillus licheniformis* seems to be very interest for the paper and textile industries thanks to the high temperature optimum of 100°C and the wide stability over pH values.

Optimization of enzyme conjugation

As for the conjugation of LASPO, the conjugation of α-amylase was carefully design taking into consideration its 3D structure. Two different conjugation strategies were used to obtain an enzyme-NP systems with both good conjugation yield and high relative activity. (Figure 21):

- **Strategy 1:** the carboxylic group of the enzyme were used to react with the amino groups of the NP-APTES after their activation with a carbodiimide chemistry. The analysis of its crystal structure (PDB entry 1BLI), showed the presence on the surface of a high number of exposed carboxylic groups. In this case, the reaction was carried on at two different pH of reaction, i.e. pH 7 (NP-AMY1) and pH 9 (NP-AMY2).

- **Strategy 2:** enzyme molecules are covalently bound to the NP-APTES through via their amine reactive moieties after the NP-APTES activation with BS3 (NP-AMY3). In particular, the reaction carried on at pH 8.2 should ensure a conjugation through the amino terminal of the enzyme.
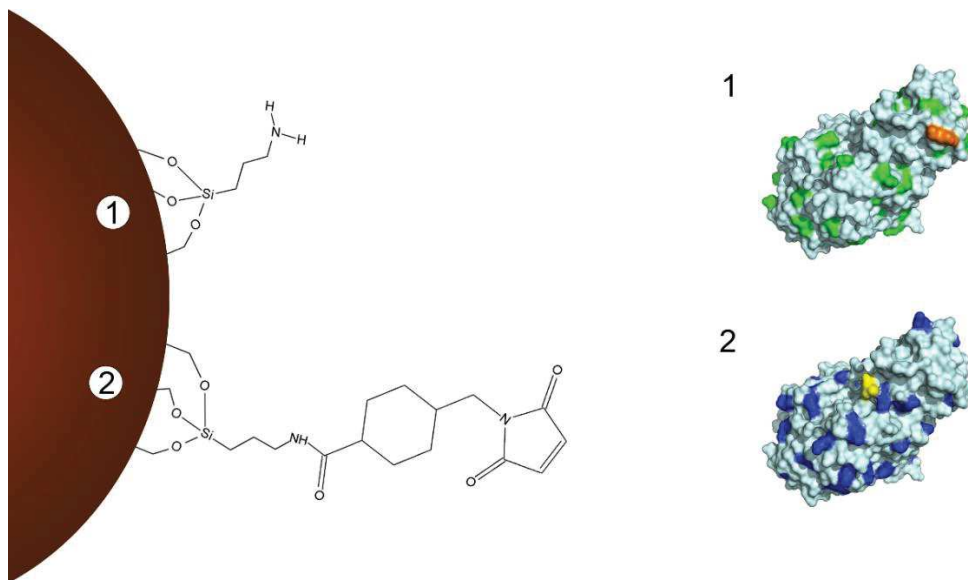
Figure 21 Conjugation chemistry used to functionalize IONPs. On the left, from top to bottom, we have schematized the above-described strategies 1) APTES, 2) APTES-BS3. On the right, is reported the three-dimensional structure of the amylase and are highlighted the residues involved in each conjugation strategy. From top to bottom: carboxylic groups in green and in orange the C-terminus (Strategy 1), amino-groups in blue and N-terminus in yellow (Strategy 2). The enzyme structure was taken from the Protein Data Bank (PDB) entry 1BLI and visualized using PyMol v2.1.

First of all, to better understand the possible ionic interactions of the enzyme with the NP-APTES the charge surface distribution of amylase was studied through a computational approach (Figure 22). The structure of the enzyme was visualized with Pymol v.2.1 and the positive and negative were counted taking into account different plane of interactions.
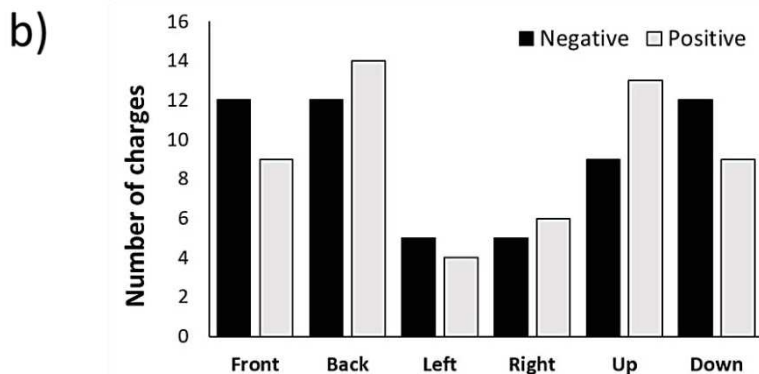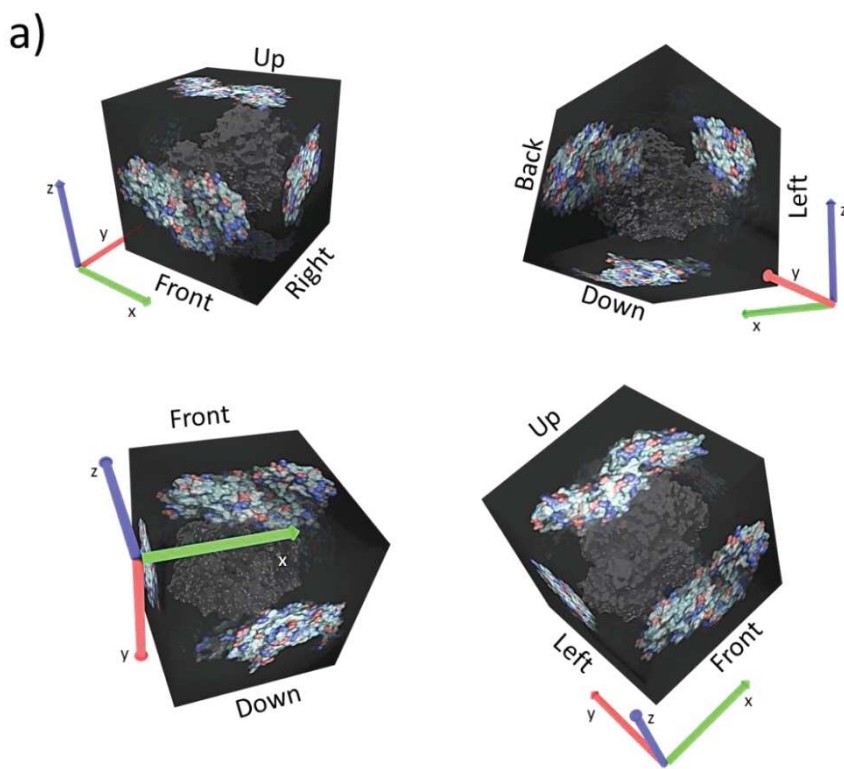
Figure 22. 3D structure of amylase showing the positive and negative charge surface distribution. The enzyme structure was taken from the Protein Data Bank (PDB) entry 1BLI and visualized using PyMol v2.1. Negative and positive charges are displayed in red and blue, respectively. (a) graphic representation of interaction plane of the enzyme. (b) Number of charged residues per plane of interaction.

The study of the 3D structure of amylase revealed that the back region of the enzyme is those that presents the highest number of positive charges, while the left one is the less charged region of the enzyme. Interestingly, the region with the active site is the one with the highest negative charges. Thus, the regions of the enzyme that will react faster are located on the opposite side and the upper side of the enzyme, respect to the active site.

The possibility that ionic interactions occur between the enzyme and the NP was analyzed by an *in silico* study of surface potential of the through the APBS software. The surface potential was calculated at the different pHs that were used in the conjugation conditions. Figure 23 shows the surface potential (a) and the electrostatic potential iso-contours (b), positive and negative charged surface are indicated in blue and red, respectively.
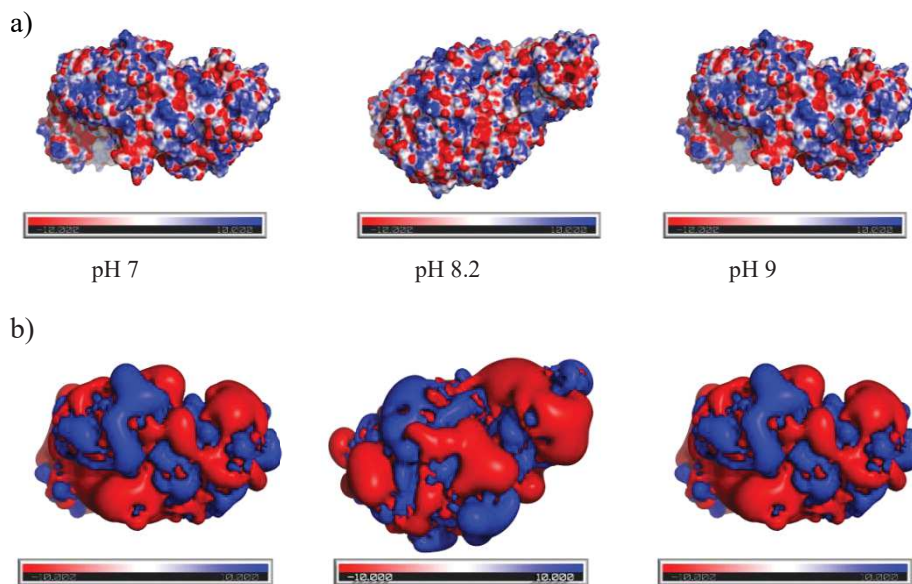
Figure 23. Analysis of the surface potential of the enzyme. The PDB entry 1BLI was selected for this 3D representation. APBS was used to calculate the surface potential and the analysis results were visualized using Pymol v2.1. (a) ±10 kT/e electrostatic potential of LASPO in PyMOL plotted on the solvent-accessible surface. (b) ±0.6 kT/e electrostatic potential iso-contours of LASPO in PyMOL. The enzyme molecules are oriented to visualized the surface potential in the nearby of the residue used for the conjugation.

No significant differences in the surface potential of the enzyme were observed at the considered conditions. So it is possible to hypothesize that the medium pH is not affecting the immobilization in term of surface charge modifications.

For amylase, only two different conjugation strategies were used as this protein does not present cysteine residue and it is not a His-tagged recombinant variant. The amylase crystal structure showed, instead, a homogenous distribution of carboxylic groups within its surface. Thus, **Strategy 1** should lead to a random binding of the enzyme with respect to the orientation of its active site towards the NP surface, as depicted also by Figure 21.

However, this conjugation strategy could also promote the formation of a covalent cross-linked enzyme@NP network depending on the pH of reaction. Thus, as consequence of the presence on amylase´s surface of primary amine groups with different pKa values from the N-terminus (pka∼7.8) and lysine residues (pka∼10.4). At pH 7.0 (NP-AMY1), only the N-terminus residue would be deprotonated and thus reactive towards the carboxylic groups of neighboring enzyme molecules activated as NHS-esters. Thus, their covalent conjugation to the most abundant amine groups of the NP surface is favoured. However, at alkaline pH values (NP-AMY2), ε-amine of lysine's side chain become reactive towards the activated carboxylic moieties. Thus, due to the high abundance of Lys moieties at AMY surface, the crosslinking among enzyme molecules could compete with the direct covalent binding to the NPs. Indeed, although the two conditions used to link the enzyme (pH 7 and pH 9) led to similar conjugation yields, different relative activities were obtained (61 and 36 %, respectively) (Table 7).

Strategy 2, resulted in similar reaction parameters than NP-AMY, but whit a lower relative activity. The reaction conditions promote the direct covalent binding of the enzyme via the primary amine group of its N-terminus. The reaction media pH 8.2 is slighter higher than its pKa but lower than that for ε-amine of lysine residues (∼ 10.5)[152].

Table 7. Enzyme-NPs conjugated reaction parameters.

	Cross linker	pH	$\mu g_{enzyme}/mg_{NPs}$	Relative Activity (%)	Active enzyme molecules/NP
NP-AMY1	EDC/NHS	7	22.5	61	3
NP-AMY2	EDC/NHS	9	22	36	3
NP-AMY3	BS3	8.2	23	54	3

The obtained conjugation yield was confirmed by the measurement of remaining unreacted amino-groups on the NPs surface after the enzyme binding. For all pH conditions used, the number of amino groups per mg of NPs decreased from 15 to 6 nmol. Although the final amount of enzyme attached was the same in all cases (~22 µg/mg NP), the lower enzyme activity of the enzyme@NPs obtained for NP-AMY 2 should be a consequence of the crosslinking effect mentioned above. Indeed, AMY@NPs obtained at this pH has a larger mean hydrodynamic diameter (Table 8). Negative ζ potential values of the enzyme functionalized NPs is expected as amylase has a net negative charge at the pH value of the measurements. With all the conjugation strategies a partial aggregation of the NPs was observed, although NP-AMY2 was the one showing more aggregation.

Table 8. Physical parameters of the different enzyme-NP systems.

	NP-AMY1	NP-AMY2	NP-AMY3
radius [nm] (TEM)	6.1 ± 0.6	6.2 ± 0.8	6.2 ± 0.5
diameter [nm] (DLS)	392 ± 0.6	873.3 ± 0.3	197.7 ± 0.4
Polydispersity Index (DLS)	0.185	0.321	0.191
ζ-potential [mV]	-9.04 ± 0.7	-38.05 ± 0.676	-19.04 ± 0.8

Biochemical characterization

The nano-systems produced were biochemically characterized and the catalytic parameters of the conjugated NP-AMY were determined by 3,5-dinitrosalicyclic acid colorimetric assay. The apparent Vmax all the NP-AMY systems and their Km for starch are reported in Table 9.

Table 9. Catalytic parameters of all the NP-AMY conjugations.

	Specific activity (U/mg enzyme)	$V_{max, app}$ (μmol x min x mg enzyme)	Km (mM)
NP-AMY1	763	1592	0.073
NP-AMY2	566	1023	0.051
NP-AMY3	603	1065	0.052

The NP-AMY systems were further investigated studying the effect of the temperature on their enzymatic activity (Figure 24).
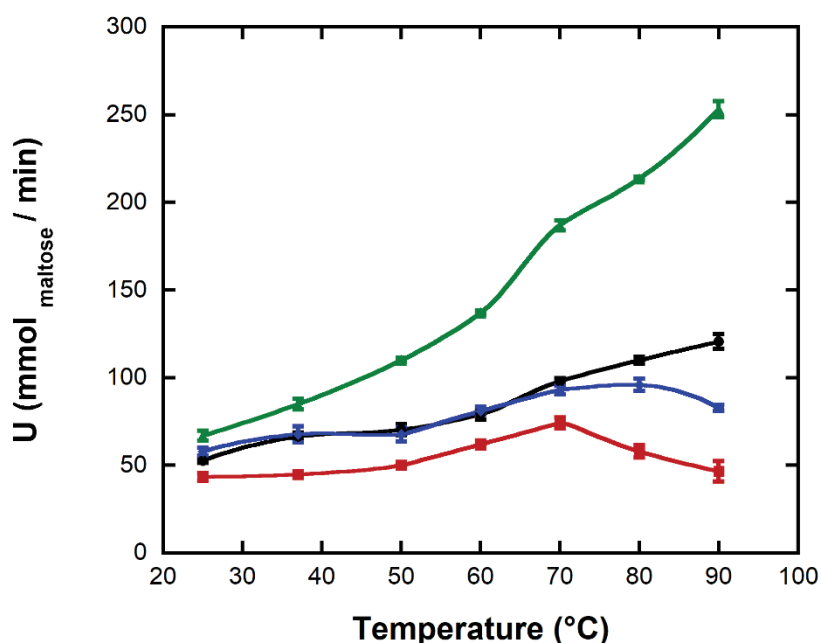
Figure 24. Effect of temperature on the activity of conjugated and non-conjugated amylase after 30 min of incubation: Amylase (green), NP-AMY 1 (black) NP-AMY 2 (red) and NP-AMY3 (blue).

The optimal temperature of NP-AMY1 was the same of that of the free enzyme, i.e., 90°C, while that of NP-AMY2 resulted shifted to 70°C, the optimum temperature of NP-AMY 3, instead, is 80°C.

As the enzyme works at high temperature, i.e. 70-90°C, the NP-AMY systems were further characterized studying their thermostability at different temperatures and assessing the residual activity of the systems after 60 min of incubation (Figure 25).
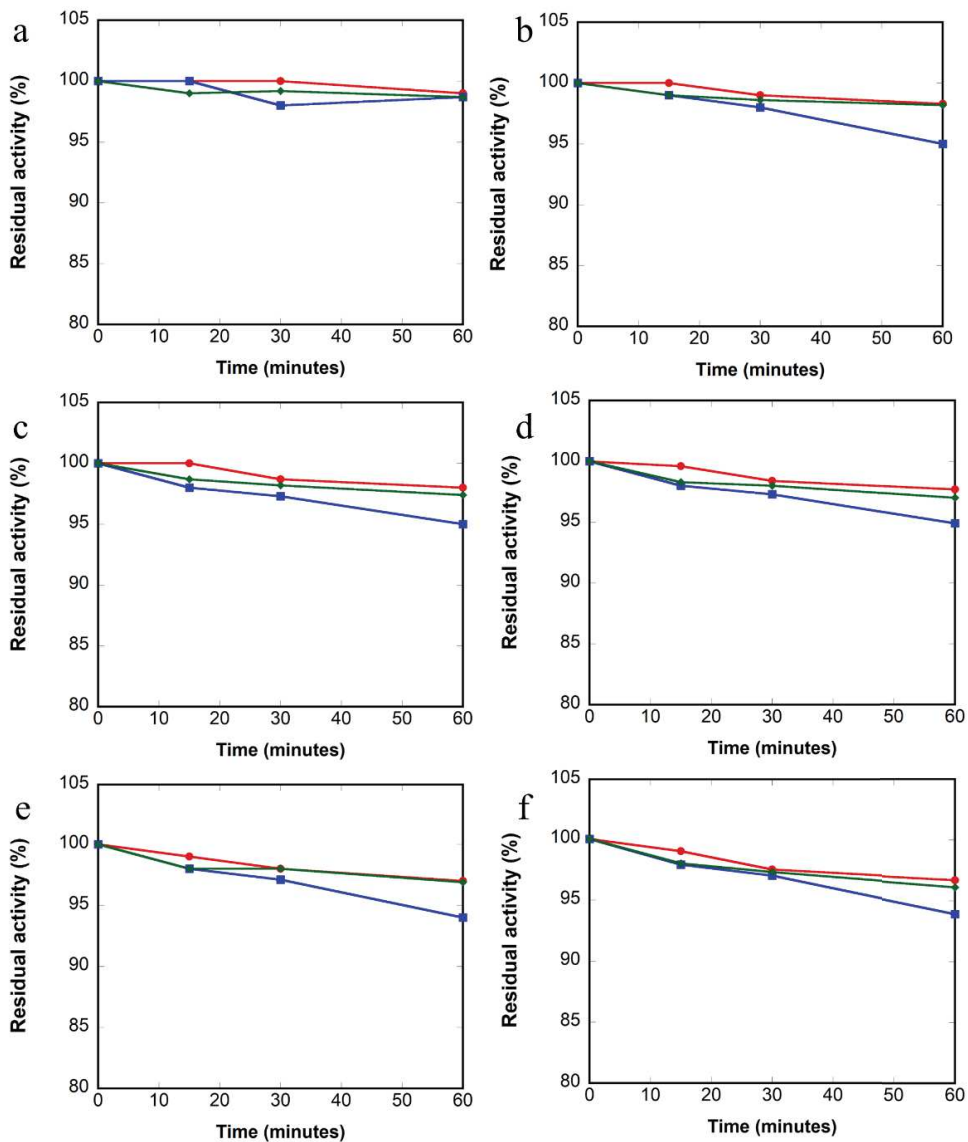
Figure 25. Thermal stability of NP-AMY1 (red), NP-AMY2(blue) and NP-AMY3 (green) at different temperature: 25°C (a), 37°C (b), 50°C (c), 70°C (d), 80°C (e) and 90°C(f). Triplicate experiments were done for each condition, standard errors were lower than 5%.

As shown in Figure 25, the three different conjugation strategies of amylase lead to the production of thermostable nano-enzymatic systems. At all the temperatures considered, indeed, the activity loss in 60 min was only of 6 % in case of NP-AMY2, while for both NP-AMY1 and NP-AMY3 was observed only the 4% of activity loss.

Remote enzyme activation by AMF nanoactuation.

As shown in Figure 26, by applying an AMF at a frequency of 829 kHz, we have been able to remotely activate all the AMY. To assess this, we compared the values of the enzymatic activity detected after exposure to the AMF to those obtained heating the sample during the same incubation time, but incubating test tubes in a thermoblock.

After 30 min of exposure to AMF, NP-AMY1, NP-AMY2 and NP-AMY3 produced 140, 74 and 99 µmol x min of maltose, respectively (Figure 26). These activities obtained with AMF are comparable to those that can be obtained heating the sample for 30 min in a thermoblock at 90°C for NP-AMY1, at 70°C for NP-AMY2 and 80°C for NP-AMY3.
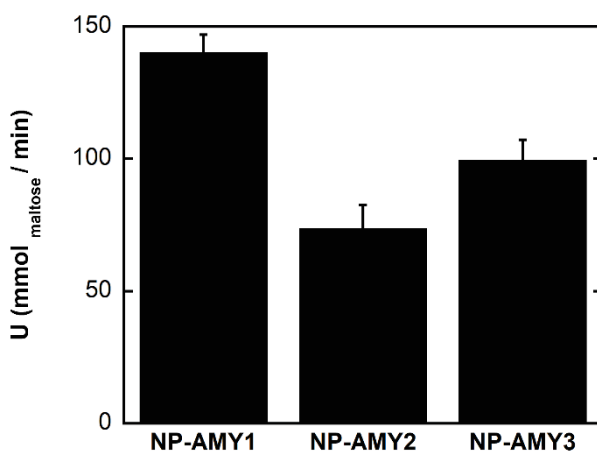
Figure 26. Activity of conjugated amylase under a 252 Gauss AMF with a frequency of 829 KHz and after 30 min.

To further study the effects of AMF on the nano-conjugated amylase, the frequency of the AMF was varied from 410 to 829 kHz, while the field was maintained at 252 Gauss (Figure 27).
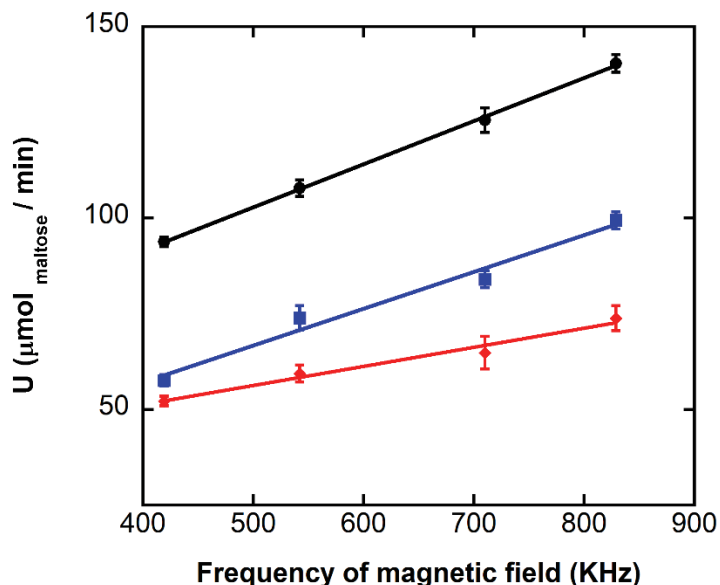
Figure 27. Dependence of the enzymatic activity on AMF frequency. NP-AMY 1 (black), NP-AMY 2 (red) and NP-AMY3 (blue) were exposed to a 252 Gauss AMF with frequencies ranging from 410 to 829 kHz.

It was observed an increase of enzyme activity when increasing the frequency of the applied AMF. The higher the frequency of the applied field, the higher the increase in the amount of heat generated by the particles, which resulted in turn in a higher activation of the immobilized enzyme.

All these results clearly show that, by means if an AMF, we have transferred energy to the IONPs and to their linked enzymes. However, the efficiency of this activation was different depending on the coupling strategy, being the best options NP-AMY1 for the amylase. In the case of NP-AMY2 and NP-AMY3, the low activation efficiency observed could be a consequence of the thermal enzyme destabilization caused by both immobilization strategies. However, we cannot exclude a contribution due to the observed NPs aggregation triggered by enzyme binding, as it is well known that the heating efficiency of NPs drastically decreases after aggregation[157]. In all the conditions considered, the application of the magnetic field and de subsequent activation of the thermophilic enzyme immobilized on them, did not caused an increase in the reaction media. This can be explained by the fact that the amount of NPs used were thermally isolated due to the low concentration used.

To confirm that the reaction media temperature do not increase during the application of the AMF of 829 kHz and 252 Gauss, a reaction containing the NP-AMY preparations and the thermolable enzyme D-aminoacid oxidase (DAAO) were carried on. Table 10 reported the activity register for the two enzyme used.

Table 10. Activity of conjugated amylase and of the free DAAO under an AMF of 829kHz and 252 Gauss.

	U ($\mu g_{maltose}$ x mg_{NP})	U ($\mu g_{substate}$ x mg_{enzyme})
NP-AMY1/DAAO	115 ± 0.5	33 ± 0.2
NP-AMY2/DAAO	75 ± 0.7	33 ± 0.3
NP-AMY3/DAAO	98 ± 0.4	33 ± 0.8

It is possible to observe that the enzymes are both active: NP-AMY was activated as it is at 90°, 70°C and 80°C for NP-AMY 1, NP-AMY 2 and NP-AMY 3 respectively. While DAAO show an enzymatic activity comparable of the one obtained when the reaction is carried on at room temperature. These data prove that the application of a magnetic field in presence of NPs does not cause an excess of heating in the reaction media. Thus, it will be possible to carry on multi-enzymatic processes of biotechnological interest in which one of enzyme/substrate/product is thermolable, while the other needs an high temperature to work.

As further proof of the heating transfer from the NPs to the enzyme, DAAO was immobilized on NP-APTES as reported in the article entitled "Synthesis, characterization and programmable toxicity of iron oxide nanoparticles conjugated with D-amino acid oxidase" attached at the end of the *Material and Method* chapter. Then an AMF field of 252 Gauss and frequencies in the 410 to 829 kHz range was applied in presence of NP-DAAO and free amylase (Figure 28).
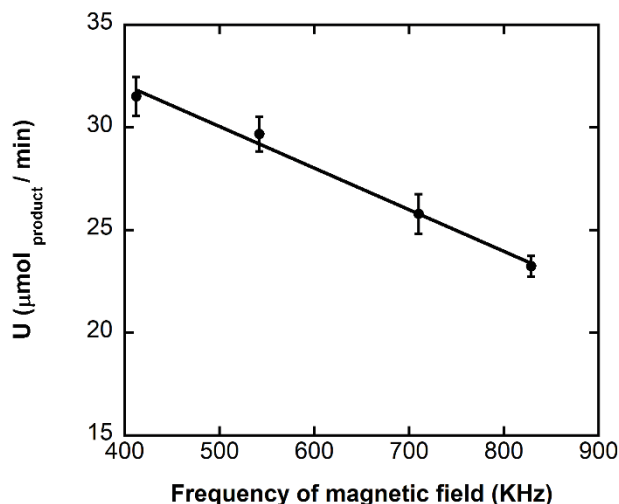
Figure 28. Dependence of the enzymatic activity of NP-DAAO on AMF frequency (410 to 829 kHz).

Figure 28 depicts that as the frequency of the AMF gets higher, the enzyme activity became lower, as the enzyme was incubated in increasing reaction temperature. DAAO is indeed a themolable enzyme with an optimum temperature of 37°C, that gets partially denaturated when the temperature increase. On the other hand, the free amylase, present in the reaction media, registered an activity comparable to those obtained incubating the enzyme at room temperature.

Operational stability under an AMF

The possibility to recover and reuse the NP-AMY preparations was evaluated under an AMF of 252 Gauss and 829 kHz. Each cycle consisted of 30 min of reaction. After each cycle, the conjugated enzyme was recovered using a magnet and reused it to digest starch (Figure 29).
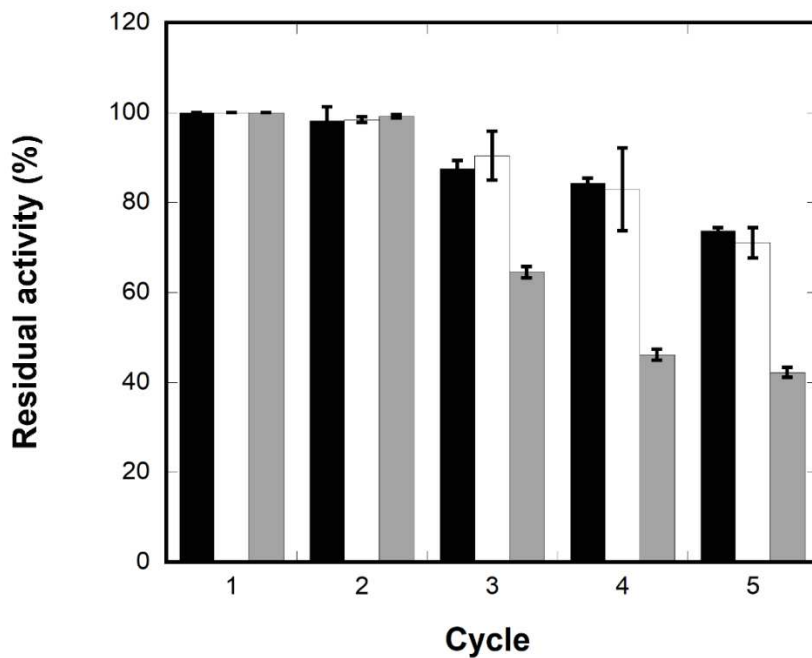
Figure 29. Operational stability of NP-AMY 1, NP-AMY2 and NP-AMY3 systems exposed to an AMF of 829 KHz and 252 Gauss.

Figure 29 shows that the three different NP-AMY systems maintained the full activity for 2 cycles. After three cycles, the activity of NP-AMY3 significantly decrease of 40% of the starting activity. As for NP-LASPO systems, these results not only showed that it is possible to establish reuse cycles but also reinforce the importance of enzyme orientation in order to develop more efficient enzymatic processes under AMF activation.

NP-ANTIBIOTIC SYSTEM

In recent years, the widespread use of antibiotics has led to the onset of resistance in microorganisms. Even the use of last resort antibiotics such as teicoplanin and vancomycin undergo to restrictions because of the emerging resistance in enterococci and staphylococci with the subsequent need to develop new antibiotics products[134]. In this context, the advent of nanotechnology has given a large contribution to the problem. Indeed, there are many studies concerning nanomaterials, and in particular NPs, as antimicrobial agents. Although iron oxide is not considered antibacterial, this material in the form of NPs acquires characteristics such good biocompatibility and low toxicity and superparamagnetism, that make it interesting as antibiotic support for applications in the biomedical field.

Here, IONPs are used as a platform for the conjugation of the glycopeptide antibiotic teicoplanin, which has been in clinical practice since 1988 in Europe and 1998 in Japan[158].

Results regarding this section are reported in detailed in the paper entitled "Magnetic nanoconjugated teicoplanin: a novel tool for bacterial infection site targeting", attached at the end of this chapter.

NP-TEICO binding and activity stability

Supplementary information to the paper "Magnetic nanoconjugated teicoplanin: a novel tool for bacterial infection site targeting".

The stability of NP-TEICO was studied at different pHs (5.5, 6 and 7.1) and temperatures of storage (-20°C, 4°C and 25°C). The release of teicoplanin was measured in the supernatant by the HPLC analyses: the 100% of antibiotic remained bind for one month at all the conditions tested (Figure 30).
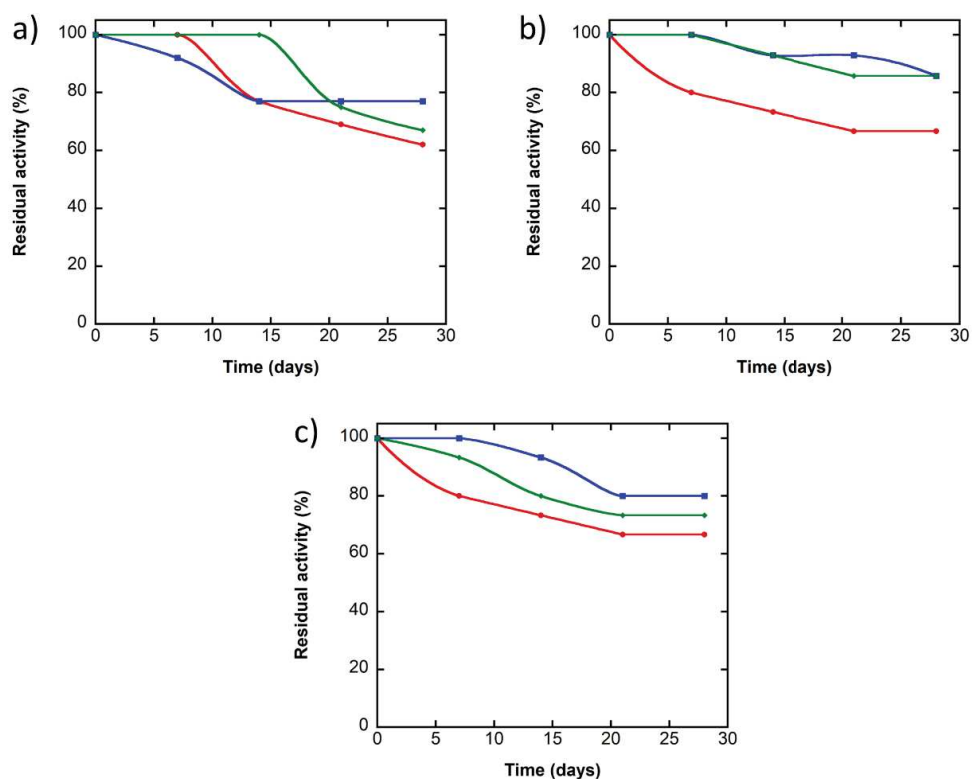
Figure 30. Antimicrobial time stability of NP-TEICO stored at pH 5.5 (a), pH 6.0 (b) and pH 7.2 (c) and temperature: -20°C (red), 4°C (blue) and 25°C (green).

On the other hand, the antimicrobial activity of NP-TEICO - measured by the antimicrobial susceptibility test versus *B. subtilis* - was maintained from 60 to 90% of its initial antimicrobial activity after three weeks depending on the storage conditions. When store at pH 5.5, the nano-antibiotic system shows the worst maintenance of its microbial activity at all the storage temperature (Figure 30a). Conversely, if the NP-TEICO are store at pH 6.0 at 4°C and 25°C they maintain the 90% of the staring activity after 28 days (Figure 30b). Storage at physiological pH, indeed, lead to the loss of 20-40 % of the starting activity (Figure 30c). In the same conditions, a water solution of teicoplanin (500 μg/mL) maintained the 90% (± 0.5) of its initial antimicrobial activity.

Magnetic Nanoconjugated Teicoplanin: A Novel Tool for Bacterial Infection Site Targeting

Ilaria Armenia, Giorgia Letizia Marcone, Francesca Berini, Viviana Teresa Orlandi, Cristina Pirrone, Eleonora Martegani, Rosalba Gornati, Giovanni Bernardini and Flavia Marinelli*

Department of Biotechnology and Life Sciences, University of Insubria, Varese, Italy

Nanoconjugated antibiotics can be regarded as next-generation drugs as they possess remarkable potential to overcome multidrug resistance in pathogenic bacteria. Iron oxide nanoparticles (IONPs) have been extensively used in the biomedical field because of their biocompatibility and magnetic properties. More recently, IONPs have been investigated as potential nanocarriers for antibiotics to be magnetically directed to/recovered from infection sites. Here, we conjugated the "last-resort" glycopeptide antibiotic teicoplanin to IONPs after surface functionalization with (3-aminopropyl) triethoxysilane (APTES). Classical microbiological methods and fluorescence and electron microscopy analysis were used to compare antimicrobial activity and surface interactions of naked IONPs, amino-functionalized NPs (NP-APTES), and nanoconjugated teicoplanin (NP-TEICO) with non-conjugated teicoplanin. As bacterial models, differently resistant strains of three Gram-positive bacteria (*Staphylococcus aureus*, *Enterococcus faecalis,* and *Bacillus subtilis*) and a Gram-negative representative (*Escherichia coli*) were used. The results indicated that teicoplanin conjugation conferred a valuable and prolonged antimicrobial activity to IONPs toward Gram-positive bacteria. No antimicrobial activity was detected using NP-TEICO toward the Gram-negative *E. coli.* Although IONPs and NP-APTES showed only insignificant antimicrobial activity in comparison to NP-TEICO, our data indicate that they might establish diverse interaction patterns at bacterial surfaces. Sensitivity of bacteria to NPs varied according to the surface provided by the bacteria and it was species specific. In addition, conjugation of teicoplanin improved the cytocompatibility of IONPs toward two human cell lines. Finally, NP-TEICO inhibited the formation of *S. aureus* biofilm, conserving the activity of non-conjugated teicoplanin versus planktonic cells and improving it toward adherent cells.

Keywords: antibiotic resistance, iron oxide nanoparticles, glycopeptide antibiotics, antimicrobial activity, teicoplanin, *Staphylococcus aureus* biofilm

INTRODUCTION

According to a recent survey of the World Health Organization (WHO, 2017), antibiotic resistance represents one of the greatest threats to global health today and contributes significantly to longer hospital permanence, higher medical costs, and increased mortality. At least 700,000 people die annually because of infections caused by resistant bacteria. This number is predicted to increase up

to 10 million by 2050 and is consequentially associated with a social and economic burden. This public health threat is exacerbated by the paucity of novel antibiotics expected to enter clinical use in the near future (Fedorenko et al., 2015). A corollary to acute illness is the increased number of chronic bacterial infections due to the prevalence of biofilm colonization (Arciola et al., 2018). Currently, medical device-related infections account for more than 60% of all the hospital-acquired infections in the United States (Weiner et al., 2016). Biofilms are complex, three-dimensional bacterial communities living in a self-produced extracellular matrix. The biofilm-forming bacteria survive better than their free-living (planktonic) counterparts in hostile environments; they are 10 to 100 times less susceptible to antimicrobial agents and are protected against the host immune system, making the treatment of these infections quite challenging (Davis, 2003; Venkatesan et al., 2015).

One promising approach in the field of antimicrobial therapy is the use of nanotechnology-tailored agents for preventing and treating infections caused by resistant bacteria. Unique and well-defined features distinguish nanoparticles (NPs) from their bulk counterparts, such as large surface area-to-volume ratio and dimensions that are comparable to those of biomolecules, effectively providing a platform with a high number of functional sites and possible interactions with bacterial cells and biofilms. Of all the NPs tested for antimicrobial activity thus far, silver NPs (AgNPs) have been studied most intensively (Natan and Banin, 2017). Although researchers have widely agreed that the broad-spectrum antibacterial activity of AgNPs can be predominantly ascribed to the release of Ag ions, AgNPs demonstrate unique properties because they adhere to the bacterial surface, altering membrane properties and thus delivering Ag ions more effectively to the bacterial cytoplasm and membrane (Durán et al., 2016). Consequently, the antibacterial effect of AgNPs is observed at concentrations with a 10-fold lower magnitude than those used for bulk Ag ions. The antibacterial activity of AgNPs is reported to be mediated by a multiplicity of still-not-completely understood mechanisms following their interaction with the bacterial surface, which act in parallel (i.e., oxidative stress, membrane depolarization, and protein and DNA interaction), thus explaining why bacterial resistance does not easily arise (Hajipour et al., 2012; Natan and Banin, 2017; Baranwal et al., 2018). Very recent studies (Xiang et al., 2017; Xie et al., 2017, 2018) show that the antibacterial activity of AgNPs may be successfully exploited in preparing nanocomposite materials to be used as antibacterial coatings of titanium-based metallic implants and poly(ether ether ketone) medical devices, which are both widely employed in dentistry and orthopedic applications. Entrapping AgNPs in graphene oxide nanosheets wrapped with a thin layer of collagen (Xie et al., 2017), in hybrid polydopamine/graphene oxide coatings (Xie et al., 2018), or in biocompatible polymers such as poly(lactic-co-glycolic) acid (Xiang et al., 2017) endows medical implants with a long-lasting self-antibacterial activity. *In vivo* studies using these innovative coatings in animal models confirm that combining the unique properties of different nanomaterials prevents bacterial infection and provides a good cytocompatibility of the medical devices (Xie et al., 2017, 2018).

A synergic, but as yet less exploited strategy when developing nano-based antimicrobial agents involves using NPs as nanocarriers for antibiotics, taking advantage of the high surface-to-volume ratio platform that they offer for attaching a large number of molecules. The advantages of using NPs in this way depend on the nature of both the NPs and the drugs under consideration, as recently reviewed (Natan and Banin, 2017). These advantages might include (i) protecting the nanoconjugated drug from degradation and oxidation; (ii) increasing drug solubility, antimicrobial activity, and biodistribution; (iii) delivering the antibiotic to the site of the infection; and (iv) enhancing drug penetration into biofilms, facilitating the killing of encased bacteria. As antibiotic nanocarriers, iron oxide nanoparticles (IONPs) have recently attracted increased interest thanks to their unique magnetic properties (Dinali et al., 2017). In fact, IONPs can be guided by an external magnetic field to a targeted organ/biofilm and specifically localized at the site of infection (Wu et al., 2015; Stepien et al., 2018). In addition, IONPs are easily produced and functionalized, and they possess a high drug-loading capacity, low cell toxicity, and high biocompatibility (Ali et al., 2016; Dinali et al., 2017). In the last decade, relatively few studies have investigated the potential of surface-modified IONPs as antibacterial agents in depth. Core-shell Fe_3O_4-AgNPs were tested as antimicrobial agents against Gram-positive and Gram-negative bacteria where the silver shell was responsible for antimicrobial action (Chudasama et al., 2009). Biocompatible polyvinyl alcohol-coated IONPs were used in biomedical applications and reported to be active against *Staphylococcus aureus* in a dose-dependent manner (Tran et al., 2010). Similarly, chitosan-coated IONPs were shown to have a higher antimicrobial activity than naked IONPs due to the positive surface potential, which interacted better with negatively charged bacterial cell surfaces (Arakha et al., 2015a). According to other authors (Huang et al., 2010; Ebrahiminezhad et al., 2014), IONP surface functionalization with (3-aminopropyl) triethoxysilane (APTES) elicited an antimicrobial effect by creating a high density of amino groups, which could interact with negatively charged sites on the bacterial cells through electrostatic interactions. The well-developed surface chemistry of IONPs made it possible to incorporate a variety of commonly used antibiotics such as the β-lactam amoxicillin, penicillin, and ampicillin, the aminoglycoside streptomycin, and the glycopeptide vancomycin (Chifiriuc et al., 2013; Grumezescu et al., 2014; Hussein-Al-Ali et al., 2014; El Zowalaty et al., 2015; Wang et al., 2017), providing evidence that biocompatible magnetic NPs might enable site-specific antibiotic delivery. Vancomycin-carrying, folic acid-tagged chitosan NPs were successfully used to deliver vancomycin to bacterial cells (Chakraborty et al., 2010, 2012), and vancomycin-modified mesoporous silica NPs were used for selective recognition and killing of Gram-positive bacteria over macrophage-like cells (Qi et al., 2013). An alternative use of IONPs functionalized with vancomycin – an antibiotic that binds to bacterial cell walls – was to apply them as ligands for the affinity capture of a wide range of bacteria from biological samples, including Gram-positive bacteria such as *S. aureus* and Gram-negative

bacteria such as *Escherichia coli* (Gu et al., 2003; Lin et al., 2005; Kell et al., 2008). Because of the magnetic properties of vancomycin-functionalized IONPs, vancomycin-captured bacteria can be magnetically separated and concentrated from large volumes into much smaller volumes, allowing bacterial analysis and detection based on, for example, genomic DNA (Kell et al., 2008; Zhu et al., 2015).

In this work, we employed IONPs as carriers of the lipoglycopeptide antibiotic teicoplanin, which has been used in clinical practice since 1988 in Europe and 1998 in Japan. Teicoplanin is considered a drug of "last resort" for treating severe infections by multiresistant Gram-positive pathogens, including the methicillin-resistant *S. aureus* (MRSA) and the anaerobe *Clostridioides difficile* (Marcone et al., 2018). Teicoplanin is a complex molecule with a peptide core of seven aromatic amino acids tailored with sugar residues, chlorine atoms, methyl groups, and a lipid chain. It forms five specific hydrogen bonds with the D-alanyl-D-alanine terminus of the peptidoglycan precursors of the bacterial cell wall, blocking its synthesis and consequently causing cell lysis (Binda et al., 2014). The antibacterial spectrum of teicoplanin activity against Gram-positive bacteria is similar to that of vancomycin, but teicoplanin shows an increased potency, particularly against some resistant clinical isolates belonging to *Staphylococcus*, *Streptococcus*, and *Enterococcus* genera (Van Bambeke, 2006). In addition, teicoplanin is active on vancomycin-resistant enterococci with VanB-phenotype (Van Bambeke, 2006; Binda et al., 2014). The superior antimicrobial potency of the lipoglycopeptide teicoplanin in comparison to the glycopeptide vancomycin is due to the *in vivo* membrane anchoring of the hydrophobic tail of teicoplanin, which strengthens the bond to membrane-localized peptidoglycan precursors and promotes synergic back-to-back dimerization of antibiotic molecules (Allen and Nicas, 2003; Treviño et al., 2014). In addition, lipidation seems to represent the key functional difference between vancomycin and teicoplanin, which is related to their differing abilities of inducing glycopeptide antibiotic resistance response in enterococci and actinomycetes (Dong et al., 2002; Binda et al., 2018). To the best of our knowledge, this is the first study exploring the feasibility of conjugating teicoplanin to IONPs and testing the potential of nanoconjugated teicoplanin as a promising tool for treating bacterial infections caused by resistant bacteria.

MATERIALS AND METHODS

Materials

All chemical reagents, including acetonitrile (CH_3CN), ammonium formate ($HCOONH_4$), ammonium hydroxide (NH_4OH), APTES, boric acid (H_3BO_3), crystal violet ($C_{25}N_3H_{30}Cl$), 2′,7′-dichlorodihydrofluorescein (DCFH-DA), N-(3-dimethylaminopropyl)-N′-ethylcarbodiimide hydrochloride (EDC), ethanol (C_2H_6O), ferric nitrate [$Fe(NO_3)_3 \times 9H_2O$], formaldehyde (CH_2O), glutaraldehyde ($C_5H_8O_2$), iron dichloride ($FeCl_2 \times 4H_2O$), iron trichloride ($FeCl_3 \times 6H_2O$), N-hydroxysuccinimide (NHS), nitric acid (HNO_3), osmium tetroxide (OsO_4), phosphate-buffered

saline (PBS), sodium cacodylate ($C_2H_7AsO_2$), sodium chloride (NaCl), sodium hydroxide (NaOH), sodium 2-(N-morpholino)ethanesulfonic acid hemisodium salt (MES), and teicoplanin, were purchased from Sigma-Aldrich, Milan, Italy. The LIVE/DEAD BacLight fluorescence assay kit was purchased by Thermo Fisher Scientific, Monza, Italy. Epon-Araldite 812 was purchased from Electron Microscopy Sciences, Hatfield, PA, United States. All the chemical reagents were used without additional purification.

Microbial Strains and Culture Conditions

Escherichia coli ATCC 35218, *Bacillus subtilis* ATCC 6633, *S. aureus* ATCC 6538P (methicillin susceptible *S. aureus*, MSSA), *S. aureus* ATCC 43300 (MRSA), *Enterococcus faecalis* ATCC 29212, and *E. faecalis* ATCC 51299 (VanB phenotype) were obtained from the American Type Culture Collection (ATCC). *E. faecalis* 9160188401-EF-34 (VanA phenotype) is a clinical isolate, which was kindly provided by Laboratorio Microbiologia Clinica – Ospedale di Circolo, Varese, Italy. *E. coli* and *B. subtilis* were propagated overnight in Luria Bertani medium (LB, 2% tryptone, 2% yeast extract, and 1% NaCl), and the *S. aureus* and *E. faecalis* strains in Müller Hinton broth 2 (MHB2, 0.3% beef infusion solids, 1.75% casein hydrolysate, and 0.15% starch) with continuous shaking at 200 rpm and 37°C. For exponential growth, overnight cultures were transferred to fresh medium: inocula were prepared to start the cultures with an optical density at 600 nm ($OD_{600\ nm}$) of 0.1 in the final medium. For long-term preservation, bacterial cultures were stored at −20°C in 20% glycerol. Media were acquired from Sigma-Aldrich, Milan, Italy, unless otherwise stated.

Synthesis of the IONPs

Iron oxide (Fe_2O_3) NPs were synthesized using the coprecipitation method reported by Balzaretti et al. (2017). Briefly, under vigorous stirring for 30 min, 8.89 g of $FeCl_3 \times 6H_2O$ and 3.28 g $FeCl_2 \times 4H_2O$ were mixed in 380 mL of water, while slowly adding 1.5 mL of HCl (37%) dropwise into the solution to completely dissolve the salts. Following this step, 25 mL of NH_4OH (25%) was added. Particles were washed several times with Milli-Q water and 40 mL of 2 M HNO_3 was added and heated at 90°C for 5 min. Then, particles were separated by a magnet from the reaction mixture; subsequently, 60 mL of 0.34 M solution of $Fe(NO_3)_3 \times 9H_2O$ was added. The suspension was heated at 90°C for 30 min. The supernatant was removed and IONPs were collected by a magnet, suspended in Milli-Q water, and left in dialysis overnight. IONPs were stored at 4°C.

Functionalization With APTES

To prepare functionalized IONPs, a standard protocol (Balzaretti et al., 2017) was followed: a 1.5 M solution of APTES in ethanol was added to 150 mg of IONPs and stirred for 1 h at room temperature. Then, the temperature was increased to 90°C and the solution was stirred for an additional hour. The amino-modified IONPs (NP-APTES) were collected by a magnet, washed several times, and suspended in Milli-Q water.

Teicoplanin Conjugation to NP-APTES

To prepare teicoplanin-conjugated NPs (NP-TEICO), a solution containing teicoplanin (500 µg), 13 mM EDC, and 26 mM NHS was prepared and added to the NP-APTES (4 mg/mL) dispersed in 30 mM MES buffer at pH 6.0 in a final volume of 1 mL. The reaction was mixed for 6 h at room temperature. NP-TEICO were washed twice and resuspended in fresh 30 mM MES buffer at pH 6.0.

Characterization of NPs

The shape, size, and size distribution of IONPs, NP-APTES, and NP-TEICO were investigated by transmission electron microscopy (TEM) using a JEOL 1010 electron microscope (Tokyo, Japan). Samples for TEM were dispersed in Milli-Q water on carbon-coated copper grids and dried at room temperature. The hydrodynamic diameter size and polydispersity index (PDI) of IONPs, NP-APTES, and NP-TEICO were measured in 0.9% NaCl. Zeta potential was measured on samples diluted in 1 mM KCl at 25°C. Measurements were performed at 25°C using a 90 Plus Particle Size Analyzer (Brookhaven Instruments Corporation, NY, United States).

HPLC Analysis

Teicoplanin was measured by HPLC according to the method previously reported in Taurino et al. (2011). HPLC analyses were performed on a 5-µm particle size Symmetry C18 (VWR International LCC, Radnor, PA, United States) column (4.6 mm × 250 mm). The column was eluted at a 1 mL/min flow rate with a 30-min linear gradient from 15 to 65% of Phase B, followed by 10 min with 100% Phase B. For Phase A we used a 32 mM $HCOONH_4$, pH 7.0:CH_3CN 90:10 (v/v) mixture, and for Phase B a 32 mM $HCOONH_4$, pH 7.0:CH_3CN 30:70 (v/v) mixture. Chromatography was performed with a model 1100 HPLC system (Elite Lachrom Hitachi LLC, VWR, Milan, Italy) and UV detection was at 236 nm.

Agar Diffusion Test

Antimicrobial activities of IONPs, NP-APTES, and NP-TEICO were tested against *E. coli* ATCC 35218, *B. subtilis* ATCC 6633, and *S. aureus* ATCC 6538P by employing an agar diffusion assay (Finn, 1959). Briefly, bacterial cultures were grown in MHB2 until an $OD_{600\ nm}$ of 0.4 was reached and then used to prepare agar plates containing Müller-Hinton Agar (MHA). 10 µL of IONPs, NP-APTES, NP-TEICO (4 mg/mL loaded with 500 µg/mL of teicoplanin in the case of NP-TEICO), and of teicoplanin (500 µg/mL) in 30 mM MES buffer, pH 6.0, were loaded manually onto the inoculated plates. The plates were incubated at 37°C for 24 h. The diameters of the zones of bacterial growth inhibition surrounding the droplets were measured.

Determination of Minimum Inhibitory Concentration and Minimum Bactericidal Concentration

Minimum inhibitory concentrations (MICs) of non-conjugated and nanoconjugated teicoplanin were determined toward *B. subtilis*, *S. aureus,* and *E. faecalis* strains by applying the broth dilution method using MHB2, as recommended by the Clinical and Laboratory Standards Institute guidelines (CLSI, 2018). About 5×10^5 exponentially growing bacterial cells were inoculated into MHB2 containing increasing concentrations of teicoplanin and NP-TEICO in 30 mM MES buffer, pH 6.0, and shaken for 16–20 h at 37°C. NP-TEICO concentrations to be added were calculated considering the amount of teicoplanin loaded onto IONPs (nanoconjugated teicoplanin) under the reaction conditions described above. MICs were the minimal concentrations of nanoconjugated and non-conjugated teicoplanin at which no turbidity could be detected.

To evaluate the minimum bactericidal concentrations (MBCs), 100 µL of bacterial cultures used for the MIC test were plated onto MHA and incubated at 37°C for 24 h. MBCs were the minimal concentrations of nanoconjugated and non-conjugated teicoplanin at which no growth could be detected. The tolerance level of each tested bacterial strain toward nanoconjugated and non-conjugated teicoplanin was determined according to May et al. (1998) using the following formula: Tolerance = MBC/MIC.

Growth Kinetic Analysis

Growth kinetics of *B. subtilis* ATCC 6633, *S. aureus* ATCC 6538P, and *E. coli* ATCC 35218 populations were followed by measuring $OD_{600\ nm}$ using an UV-Vis V-560 Spectrophotometer (JASCO, MD, United States) at regular time intervals. Preinocula were prepared from overnight cultures in LB or MHB2 at 37°C and at 200 rpm. Experiments were conducted in 50-mL tubes containing a final volume of 10 mL of LB or MHB2 added after 1 h of growth from inocula with equivalent volumes of IONPs, NP-APTES, and NP-TEICO preparations (4 mg/mL) previously resuspended in 30 mM MES buffer, pH 6.0, or with the teicoplanin control solution (500 µg/mL).

Viability Assay

Viable counts (expressed as colony-forming units per mL, CFU/mL) were estimated by employing the plate count technique. For CFU measurement, a standard volume (10 µL) of undiluted or serially diluted samples collected from stationary phase cultures on treatment with teicoplanin, IONPs, NP-APTES, and NP-TEICO, as reported above, were plated on nutrient agar. Plates were incubated for 24 h at 37°C to evaluate the viable cells.

Fluorescence Microscopy Analysis

To investigate the effect of IONPs, NP-APTES, and NP-TEICO on bacterial cells, the LIVE/DEAD BacLight fluorescence assay was used (L7007, Molecular probes, Thermo Fisher Scientific). Following the manufacturer's protocol, bacteria were cultivated overnight at 37°C and agitated at 200 rpm, appropriately diluted, and treated for 5 h with 4 mg/mL of IONPs, NP-APTES, and NP-TEICO and teicoplanin (500 µg/mL). From these cultures, 10 mL of each bacterial solution was centrifuged at 7000 rpm for 15 min. The supernatants were discarded and the pellets were suspended in saline solution (0.9%). The samples were incubated at room temperature for 1 h (mixing every 15 min) and then washed twice with saline solution. Finally, the pellets were resuspended in an equal volume of saline solution (0.9%). Then, 3 µL of dye mixture was added to each 1 mL of the prepared bacterial

samples and incubated in the dark for 15 min after properly mixing the bacterial suspensions. Fluorescence images were taken by trapping 5 μL of stained bacterial samples between a slide and a cover slip. For imaging the samples, an optical microscope with appropriate filters was employed (Axiophot; Carl Zeiss, Milan, Italy). ImageJ (Schneider et al., 2012) was used to quantify total fluorescence intensity of the bacteria. Intensities were expressed as percentage (%) relative to the saturation fluorescence within the field; red and green fluorescence stains corresponded to live or dead bacteria, respectively (Borcherding et al., 2014; Arakha et al., 2015a,b).

Transmission Electron Microscopy Analysis

The interaction pattern of NPs with bacteria was also studied by TEM. After 5 h of exposure to 4 mg/mL IONPs, NP-APTES, NP-TEICO, or teicoplanin (500 μg/mL), pellets were washed with PBS and fixed in Karnovsky solution (4% formaldehyde, 2% glutaraldehyde, 0.1 M sodium cacodylate, pH 7.2) overnight at 4°C. The samples were washed three times with 0.1 M sodium cacodylate for 10 min and postfixed in the dark for 1 h with 1% osmium tetroxide in 0.1 M sodium cacodylate buffer, pH 7.2, at room temperature. After dehydration with a series of ethyl alcohol, the samples were embedded in an Epon-Araldite 812 1:1 mixture. Thin sections (90 nm), obtained with a Pabisch Top-Ultra ultramicrotome (Emme 3 S.r.l., Milan, Italy), were observed with a Morgagni electron microscope (Philips, Eindhoven, Netherlands) operated at 80 keV.

Biofilm Assay

S. aureus ATCC 6538P cultures, grown overnight in LB, were diluted in fresh medium to reach a cell density of 10^7 CFU/mL and dispensed in 24-well plates, adding increasing concentrations of nanoconjugated or non-conjugated teicoplanin (2.5, 5, and 10 μg/mL) and of naked IONPs or NP-APTES (20, 40, and 80 μg/mL). The amounts of NPs to be added took into account the teicoplanin loaded on NPs under the reaction conditions described above. Following incubation at 37°C for 24 h, the adherent biomass was quantified by crystal violet (CV) staining. Biofilms were stained with CV 0.1% for 20 min, washed twice with PBS, and air dried overnight at room temperature; the CV was then dissolved in 33% acetic acid for 10 min. The amount of solubilized dye was spectrophotometrically measured at 595 nm (Infinite 200 PRO; TECAN, Männedorf, Switzerland). To assess the effect of teicoplanin and of NP preparations on the cell viability of planktonic and adherent cell subpopulations, cells from the planktonic phase were collected and adherent cells were recovered by scraping the wells and then suspended in 1 mL of phosphate buffer. Cultures were diluted and CFU were estimated by plate counting in MHA plates. Viable counts of planktonic cells were expressed as CFU/mL and adherent cells as CFU per well (CFU/well).

To test the effect of teicoplanin and NP preparations on biofilm dispersal, biofilms were prepared as indicated previously and incubated at 37°C for 48 h before adding nanoconjugated or non-conjugated teicoplanin (5, 25, and 50 μg/mL) and naked

IONPs or NP-APTES (40, 200, and 400 μg/mL). Following 24-h incubation at 37°C, biofilm biomass was evaluated by CV staining and the cell viability of adherent and planktonic cells was estimated by applying the viable count technique, as previously described.

Cell Cultures

Two different cell lines were used to evaluate NP-TEICO *in vitro* cytotoxicity: a tumor model SKOV-3 cell line from ovarian adenocarcinoma and a non-tumor cell line, hASCs (human adipose-derived stem cells). SKOV-3 cells were cultured as reported in the literature (Cappellini et al., 2015). hASCs were isolated and cultured as previously reported (Palombella et al., 2017).

Cytotoxicity Test

Cell cytotoxicity was determined by measuring ATP content using the RealTime-Glo™ MT Cell Viability Assay (Promega, Milan, Italy) according to the manufacturer's instructions. Briefly, 500 cells were plated in 96-well plates in 200 μL of cell medium (RPMI for SKOV-3 and DMEM/DMEM F12 1:1 for hASC). After 24 h, the cells were exposed to increasing concentrations of nanoconjugated or non-conjugated teicoplanin or to the corresponding concentrations of NPs (considering the teicoplanin loaded per mg of NPs) and then a solution 2× the substrate and NanoLuc® Enzyme were added. The cells were incubated at 37°C and in 5% CO_2-humidified atmosphere, and luminescence was read every 24 h using the Infinite F200 plate reader (Tecan Group, Männedorf, Switzerland).

Statistics

All experiments were repeated at least three times on separate dates. Mean and standard deviation (SD) calculations were performed using Microsoft Excel 2003 (Microsoft Corporation, Redmond, WA, United States). Data were analyzed by means of one-way analysis of variance (Origin_7.0 SR0; Origin lab Corporation, Northampton, MA, United States). Significant effects of treatments were estimated ($p < 0.05$, $p < 0.01$, and $p < 0.0001$).

RESULTS

Characterization of Synthetized NPs

Numerous methods for synthesizing IONPs have been reported in the literature (Wu et al., 2015). In this study, we used the coprecipitation method previously optimized by Balzaretti et al. (2017), by which IONPs with good stability and size distribution and no tendency to aggregation could be produced. We confirmed that the NPs obtained had a spherical shape and an average diameter of 10.5 ± 4 nm, as shown by TEM micrograph (**Figures 1A,D**). The functionalization protocol, used to introduce amino groups on the IONPs (**Figure 2**), led to an insignificant increase in the diameter of NP-APTES, which was 10.6 ± 3.6 nm (**Figures 1B,E**). Teicoplanin was conjugated by following a slightly modified protocol, which was previously used for enzyme conjugation (Armenia et al., 2017): carboxylic groups

FIGURE 1 | TEM images and size distribution of IONPs **(A,D)**, NP-APTES **(B,E)**, and NP-TEICO **(C,F)**.

FIGURE 2 | Synthetic route for teicoplanin conjugation to IONPs (not in scale). The first step is functionalization of the IONPs with APTES, followed by the conjugation of teicoplanin by covalent bonding of the terminal carboxylic groups of the antibiotic molecules with the amino groups of NP-APTES via EDC/NHS cross-linking.

of teicoplanin molecules reacted with the amino groups on the surface of NP-APTES after EDC/NHS antibiotic activation (see below, **Figure 2**). Teicoplanin conjugation led to a more irregular shape of the particles and a slight tendency to aggregation. It is known that correctly conformed teicoplanin molecules tend to dimerize back-to-back in aqueous solutions and that dimerization plays an important role in their biological activity (Treviño et al., 2014). However, this phenomenon was not strong as no NP precipitation occurred. NP-TEICO had an average diameter of 13.6 nm (**Figures 1C,F**).

Transmission electron microscopy observations were complemented by measuring dynamic light scattering (DLS) of the hydrodynamic size of IONPs (**Table 1**); their diameter was estimated to be 14.2 ± 0.5 nm with an average size distribution (PDI) of 0.127, indicating a slight polydispersity typical for the

coprecipitation synthesis (Wu et al., 2015). For NP-APTES, an increase in the hydrodynamic diameter (26.8 ± 0.2 nm) due to the presence of the APTES shell around the NP core was registered. The hydrodynamic diameter of NP-TEICO was much larger (568.2 ± 0.6 nm) (**Table 1**), probably due to aggregate formation in the medium used for DLS analysis and to the effect of the glycopeptide side chains and their tendency to dimerize, which might slow down particle diffusion and increase their apparent size (Szpak et al., 2013; **Table 1**). The difference in NP sizes measured by DLS versus TEM is generally attributed to the formation of extra hydrate layers in aqueous solutions (De Palma et al., 2007; Gonçalves et al., 2017). In addition, antibiotic shells conjugated to NPs are usually not sufficiently electron dense to be visible under the electron microscope. The measurement of zeta potential (**Table 1**) showed that the superficial charge of

TABLE 1 | Physical parameters of synthesized IONPs, NP-APTES, and NP-TEICO.

	Baseline	Polydispersity	Diameter (nm)	Conductance (μS)	Mobility	Z potential (mV)
IONPs	9.9	0.127	14.2 ± 0.5	421	1.5	11.0 ± 0.8
NP-APTES	9	0.18	26.8 ± 0.2	373	1.9	22.5 ± 0.5
NP-TEICO	9	0.189	568.2 ± 0.6	400	1	12.8 ± 0.6

NP-APTES was twofold higher than for IONPs, that is, 22.5 ± 0.2 versus 11 ± 0.8 mV, due to the presence of the amino groups of APTES. A reduction in the surface charge was indeed observed after teicoplanin conjugation: NP-TEICO zeta potential was 12.8 ± 0.6 mV, indicating that NP-APTES were successfully loaded with teicoplanin.

Preparation of NP-TEICO

Teicoplanin was conjugated to NP-APTES using standard EDC/NHS chemistry: EDC reacted with the carboxylic group of the antibiotic, forming an active O-acylisourea intermediate that could be displaced by the nucleophilic attack of the amino groups present on the NP-APTES surface (**Figure 2**; Hermanson, 2013). Different reaction conditions (reaction medium, EDC/NHS ratio, teicoplanin concentration, time, and temperature of reaction) were explored to improve teicoplanin conjugation on NP-APTES. The quantity of teicoplanin bound to the surface of NP-APTES was estimated by subtracting the unreacted teicoplanin present in the supernatant from the added total antibiotic amount. Teicoplanin was quantified by reverse-phase HPLC as previously reported (Taurino et al., 2011). First trails in water, PBS, and MES buffer indicated that the latter, at pH 6.0, was the most preferable medium for the conjugation reaction (data not shown). As reported in **Table 2**, HPLC analyses confirmed that under the best experimental conditions tested so far, that is, 4 mg/mL of NP-APTES in 30 mM MES buffer, pH 6.0, 13 mM EDC, 26 mM NHS, 500 μg/mL of teicoplanin, the teicoplanin conjugation yield was

approximately 90%. Under these conditions, more than 100 μg of teicoplanin was loaded per mg of NP-APTES.

NP-TEICO prepared in this way remained chemically stable when stored at pHs ranging from 5.5 to 7.1 and temperatures from −20 to 25°C. Under these conditions, release of teicoplanin from NP-TEICO was measured by HPLC analysis of incubation buffer; 100% of the antibiotic remained fully attached to NPs for 1 week and decreased by approximately 10% in 1 month (data not shown). Consistently, the antimicrobial activity of NP-TEICO – measured by the antimicrobial susceptibility test versus *S. aureus* ATCC 6538P and *B. subtilis* ATCC 6633 (see below) – was also maintained. After 3 weeks, NP-TEICO maintained from 70 to 90% of its initial antimicrobial activity. Under the same conditions, a water solution of teicoplanin (500 μg/mL) maintained 90% of its initial antimicrobial activity.

Antimicrobial Activity of NP-TEICO

Antibacterial activity of NP-TEICO was initially investigated by comparing the growth inhibitory effects of two commonly used representative species of Gram-positive bacteria, that is, *S. aureus* ATCC 6538P and *B. subtilis* ATCC 6633, and the Gram-negative *E. coli* ATCC 35218, using an agar diffusion assay. **Figure 3** reveals that NP-TEICO inhibited the growth of *S. aureus* and

TABLE 2 | Reaction conditions tested for teicoplanin conjugation to NP-APTES via EDC/NHS chemistry in 30 mM MES, pH 6.0.

Teicoplanin (μg/mL)	EDC (mM)	NHS (mM)	Temperature (°C)	Time (h)	Yield (%)
100	26	13	4	2	10 ± 0.7
100	26	13	4	4	10 ± 1.5
100	26	13	4	6	12 ± 1.0
100	26	13	25	2	25 ± 0.5
100	26	13	25	4	30 ± 0.4
100	26	13	25	6	65 ± 0.8
100	13	26	25	2	70 ± 1.7
100	13	26	25	4	85 ± 1.4
50	13	26	25	6	100 ± 1.2
100	13	26	25	6	100 ± 0.7
500	13	26	25	6	90 ± 0.9
1000	13	26	25	6	50 ± 0.5

NP-APTES were used at a concentration of 4 mg/mL. Conjugation yield was calculated by estimating the amount of residual teicoplanin in the reaction medium by HPLC.
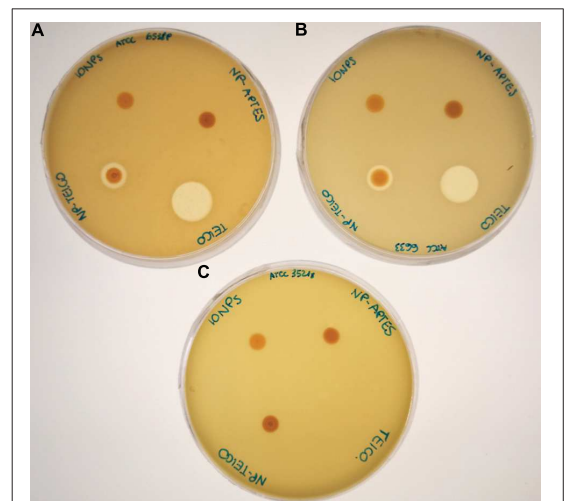
FIGURE 3 | Agar diffusion assay for measuring the antimicrobial activity of IONPs, NP-APTES, NP-TEICO, and non-conjugated teicoplanin versus the two Gram-positive bacteria *S. aureus* ATCC 6538P **(A)** and *B. subtilis* ATCC 6633 **(B)**, and versus the Gram-negative *E. coli* ATCC 35218 **(C)**.

B. subtilis, whereas no inhibition halos were observed for *E. coli,* thus demonstrating that NP-TEICO maintained the typical activity and spectrum of action of teicoplanin. Sizes of inhibition halos for the nanoconjugated teicoplanin were not comparable with the ones determined by the non-conjugated teicoplanin, as expected, considering the probably slower diffusion rate of NP-loaded antibiotic in agar medium. Conversely, IONPs and NP-APTES did not show any inhibition halos toward either the Gram-positive or the Gram-negative bacteria. These data indicate that the antimicrobial activity measured by the agar diffusion assay was conferred to NP-TEICO by the conjugation of the antibiotic and that it was not an intrinsic feature of IONPs.

Table 3 reports the MICs of nanoconjugated and non-conjugated teicoplanin toward clinically relevant strains of *S. aureus* and *E. faecalis.* Although the potency of nanoconjugated teicoplanin was slightly reduced in comparison with the non-conjugated antibiotic, NP-TEICO maintained a valuable antibiotic activity against MRSA and on vancomycin-resistant *E. faecalis* with a VanB phenotype. MICs and MBCs, and consequently the tolerance levels of NP-TEICO toward *B. subtilis, S. aureus,* and *E. faecalis,* showed the same trend as those measured for non-conjugated teicoplanin. NP-TEICO and non-conjugated teicoplanin were inactive toward the Gram-negative *E. coli* and toward the vancomycin- and teicoplanin-resistant *E. faecalis* clinical isolate with a VanA phenotype (Van Bambeke, 2006; Binda et al., 2014).

Effects of NPs on Bacterial Growth Kinetics and Cell Viability

As the antimicrobial activity of IONPs and their derivatives is a matter of intensive debate (Auffan et al., 2008; Chatterjee et al., 2011; Borcherding et al., 2014; Arakha et al., 2015a; Ansari et al., 2017), we further investigated the effects of IONPs, NP-APTES, and NP-TEICO on bacterial cell viability, by adding our NP preparations at the log phase of the growth kinetics of *S. aureus* ATCC 6538P, *B. subtilis* ATCC 6633, and *E. coli* ATCC 35218 populations. Cultures with no added NP or to

which only teicoplanin was added were used as negative and positive controls. Figure 4 indicates that the three bacterial species responded differently to NP interaction. *S. aureus* growth kinetics (Figure 4A) were dramatically affected by the addition of NP preparations and, as expected, by the treatment with teicoplanin. Albeit with a slightly different kinetics, cell density appeared equally reduced by two-thirds on 5 h of incubation. Indeed, NP-TEICO and non-conjugated teicoplanin drastically reduced the population growth of *B. subtilis,* whereas the effects of IONPs and NP-APTES were clearly less relevant (Figure 4B). Finally, teicoplanin was completely inactive toward the Gram-negative *E. coli,* whereas the addition of IONPs, NP-APTES, and NP-TEICO halved the population growth in a comparable mode (Figure 4C).

Significantly, CFU measurements at the end of the growth kinetics reported in Figure 5 clearly indicate that exposure of Gram-positive bacteria to teicoplanin and NP-TEICO cleared the bacteria population, confirming the comparable antibiotic activity of the nanoconjugated versus the non-conjugated antibiotic (Figure 5). As expected, teicoplanin and NP-TEICO were ineffective against *E. coli* cells, which conforms to the antimicrobial spectrum of the antibiotic. In addition, exposure to IONPs and NP-APTES was not bactericidal for any of the tested strains as the cells survived quite well, and in some cases (*E. coli*) even better than the untreated cultures. Thus, we can conclude that NP-TEICO retained an antibiotic activity that was comparable to that of the non-conjugated teicoplanin, whereas IONPs and NP-APTES showed a species-specific transient interaction with bacterial cells, which slowed down population growth but did not kill bacterial cells. This phenomenon merits further investigation.

Interaction Patterns of NPs With Bacterial Cells

To shed light on the interaction pattern at the IONPs-, NP-APTES- and NP-TEICO-bacteria interfaces, we investigated the effect of adding NP on bacterial cell integrity by using the

TABLE 3 | Comparison of MICs, MBCs, and tolerance levels between non-conjugated and nanoconjugated teicoplanin.

	MIC (µg/mL)		MBC (µg/mL)		Tolerance level	
	Non-conjugated teicoplanin	Nanoconjugated teicoplanin	Non-conjugated teicoplanin	Nanoconjugated teicoplanin	Non-conjugated teicoplanin	Nanoconjugated teicoplanin
B. subtilis ATCC 6633	2	2	>128	>128	>64	>64
S. aureus ATCC 6538P (MSSA)	1	2	128	128	128	64
S. aureus ATCC 43300 (MRSA)	0.5	2	64	>128	128	>64
E. faecalis ATCC 29212	0.5	1	32	32	64	32
E. faecalis ATCC 51299 (VanB)	0.5	2	64	>128	128	>64
E. faecalis 9160188401-EF-34 (VanA)	>128	>128	>128	>128	—	—
E. coli ATCC 35218	>128	>128	>128	>128	—	—

The values represent the average of the data from three independent experiments.

FIGURE 4 | Population growth kinetics of *S. aureus* ATCC 6538P **(A)**, *B. subtilis* ATCC 6633 **(B)**, and *E. coli* ATCC 35218 **(C)** exposed to teicoplanin (orange), IONPs (red), NP-APTES (green), and NP-TEICO (violet). Cultures without any addition (blue) were used as controls. Growth was recorded for 5 h. Black arrows indicate the addition (after 1 h of growth) of NP preparations and of teicoplanin to the bacterial populations. Triplicate experiments were conducted for each condition: standard errors were lower than 5%.

FIGURE 5 | Bacterial cell viability of *S. aureus* ATCC 6538P, *B. subtilis* ATCC 6633, and *E. coli* ATCC 35218 measured as CFUs after 5-h growth (see **Figure 4**) in the presence of IONPs (black bar), NP-APTES (gray bar), NP-TEICO (light gray bar), and teicoplanin (white bar) compared to the untreated control populations (lined bar). Triplicate experiments were conducted for each condition, and the error bars represent the standard errors. One-way ANOVA analyses, $*p < 0.05$ and $***p < 0.0001$.

were stained red by propidium iodide fluorescence dye (Arakha et al., 2015a). As shown in **Figures 6A–C**, untreated cells of *S. aureus* ATCC 6538P, *B. subtilis* ATCC 6633, and *E. coli* ATCC 35218 exhibited green fluorescence, indicating the presence of 99% viable cells. **Figures 6D–L** show that both Gram-positive and Gram-negative bacteria tended to aggregate on NPs when present. In the presence of IONPs and NP-APTES, the *S. aureus* population exhibited almost 90% of green viable cells (**Figures 6D,G**), whereas more than 50% cells turned to red fluorescence on exposure to NP-TEICO (**Figure 6J**). On the other hand, the *B. subtilis* population exposed to IONPs (**Figures 6E,H**) exhibited the presence of 75% green viable cells, whereas the 95% of *B. subtilis* cells treated with NP-TEICO were red (**Figure 6K**), indicating that nanoconjugated teicoplanin caused a severe loss of membrane integrity and cell viability. Control populations of *S. aureus* and *B. subtilis* treated with non-conjugated teicoplanin exhibited 98% of red non-viable cells (**Figures 6M,N**). In the presence of IONPs, NP-APTES, NP-TEICO, and teicoplanin, the fraction of red fluorescent *E. coli* cells was insignificant compared to untreated cells (**Figures 6F,I,L,O**). Once again, these observations confirm that the three bacterial species responded as expected to nanoconjugated and non-conjugated teicoplanin antibiotic action. They also suggest that naked IONPs and NP-APTES interacted with the different bacteria in a species-specific mode, likely depending on the diverse bacterial surface composition, as already suggested by other authors (Huang et al., 2010; Ebrahiminezhad et al., 2014; Arakha et al., 2015a; Dinali et al., 2017).

Transmission electron microscopy images (**Figures 7A,D,G,J,M**) indicated that the exposure of *S. aureus* ATCC 6538P cells to IONPs, NP-APTES, NP-TEICO, and teicoplanin significantly altered cell morphology in comparison to the untreated cells. IONPs, NP-APTES, and, to a significantly greater extent, NP-TEICO interacted with the cell wall of this Gram-positive species. In the presence of NP-APTES,
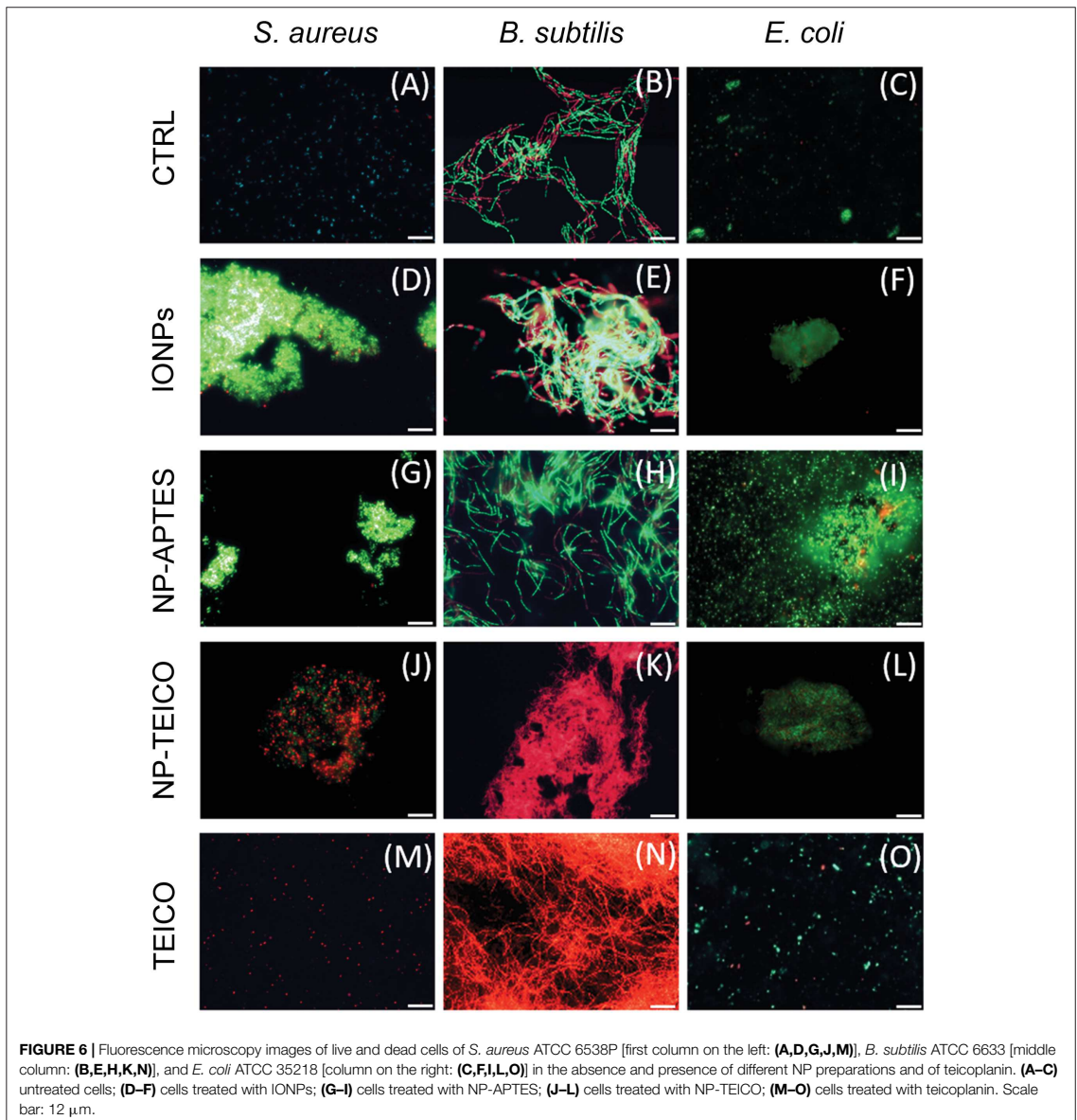
LIVE/DEAD BacLight fluorescence assay. According to the assay principle and as shown in **Figure 6**, viable cells having an intact cell membrane were stained green by the Syto9 fluorescence dye, whereas non-viable cells with deformed cell membranes

FIGURE 6 | Fluorescence microscopy images of live and dead cells of *S. aureus* ATCC 6538P [first column on the left: **(A,D,G,J,M)**], *B. subtilis* ATCC 6633 [middle column: **(B,E,H,K,N)**], and *E. coli* ATCC 35218 [column on the right: **(C,F,I,L,O)**] in the absence and presence of different NP preparations and of teicoplanin. **(A–C)** untreated cells; **(D–F)** cells treated with IONPs; **(G–I)** cells treated with NP-APTES; **(J–L)** cells treated with NP-TEICO; **(M–O)** cells treated with teicoplanin. Scale bar: 12 μm.

NP-TEICO, and teicoplanin, an increasing percentage of cells without cell walls, so-called ghost cells, became detectable (**Figures 8A,B**). Lysed cells, too, which presented damage in cell walls with cytoplasmic content leaking out, were visible within NP-APTES- and NP-TEICO-treated cells (**Figures 8A,C**). Furthermore, in the presence of NP-APTES and NP-TEICO, intracellular spherical membrane-layered, mesosome-like structures could be detected inside the cells (**Figures 8A,B**). Mesosomes were previously described by

other authors (Shimoda et al., 1995; Hartmann et al., 2010), as a consequence of cell membrane damage in *S. aureus* cells treated with antimicrobial peptides such as defensins and gramicidin S.

Conversely, most of the *B. subtilis* ATCC 6633 cells (**Figures 7B,E,H**) exposed to IONPs and NP-APTES showed the same morphology as untreated cells, with undamaged structures, although a few dead or dying cells were detected, characterized by a rough surface and by an interrupted cell membrane. Indeed,
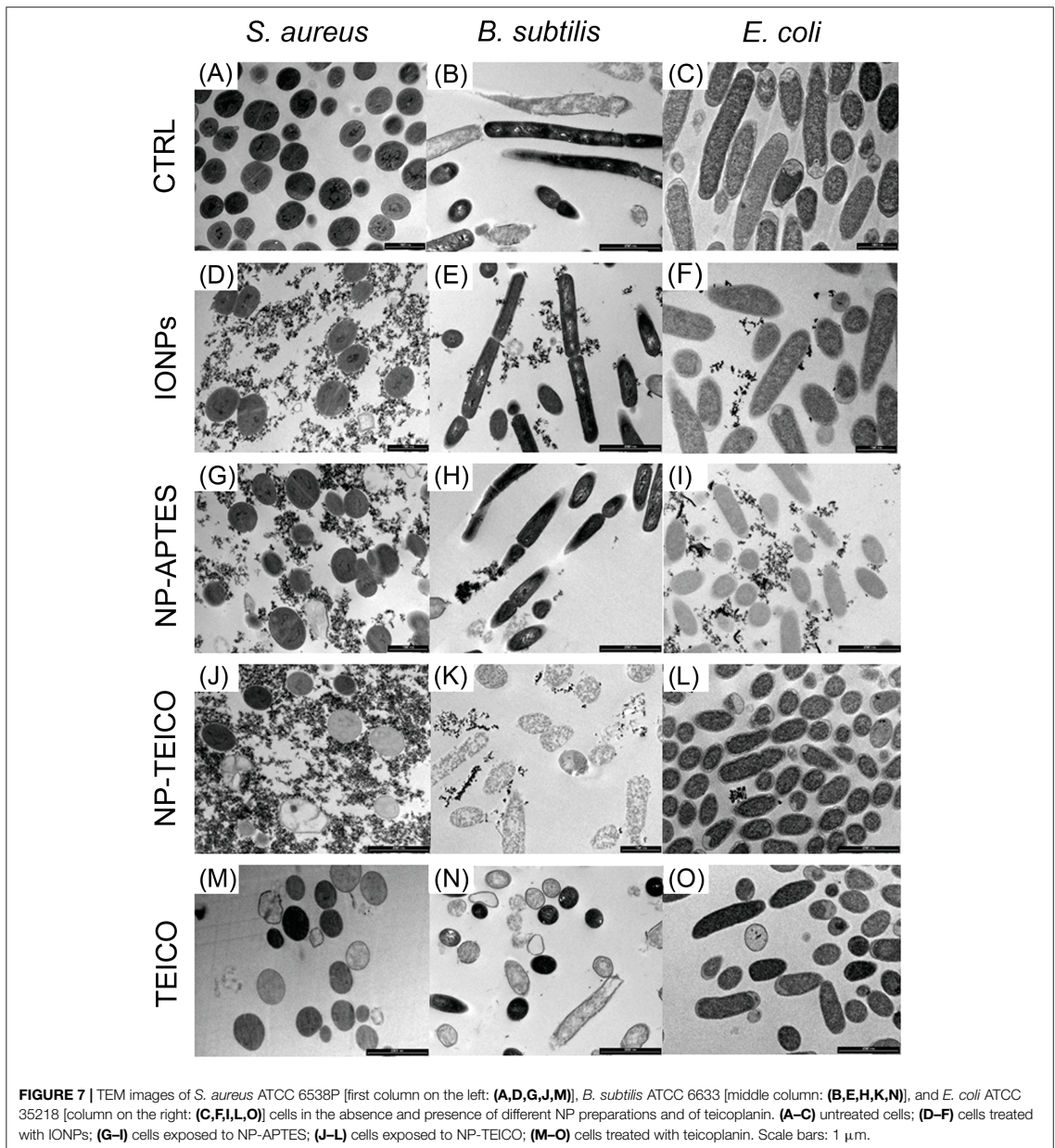
FIGURE 7 | TEM images of *S. aureus* ATCC 6538P [first column on the left: **(A,D,G,J,M)**], *B. subtilis* ATCC 6633 [middle column: **(B,E,H,K,N)**], and *E. coli* ATCC 35218 [column on the right: **(C,F,I,L,O)**] cells in the absence and presence of different NP preparations and of teicoplanin. **(A–C)** untreated cells; **(D–F)** cells treated with IONPs; **(G–I)** cells exposed to NP-APTES; **(J–L)** cells exposed to NP-TEICO; **(M–O)** cells treated with teicoplanin. Scale bars: 1 μm.

the effect of NP-TEICO and teicoplanin on cell integrity was dramatic (**Figures 7K,N**). Cells treated with NP-TEICO and teicoplanin lost their envelope integrity as a consequence of the antibiotic action (**Figures 8D,E**).

No specific alteration in cell morphology was observed in NP- or antibiotic-treated cells of *E. coli* in comparison to the untreated ones (**Figures 7C,F,I,L,O**). Interestingly, in this case,

IONPs and, to a much greater extent, NP-APTES tended to stick to the microorganism envelope, whereas the presence of NP-TEICO impeded this interaction. This observation seems to confirm the occurrence of an unspecific electrostatic interaction between positively charged NP-APTES and the negatively charged external cell membrane of this Gram-negative strain, which was previously suggested by other authors (Kell et al., 2008;

FIGURE 8 | TEM images of *S. aureus* ATCC 6538P **(A–C)** exposed to NP-APTES **(A)**, NP-TEICO **(B)**, teicoplanin **(C)**, and *B. subtilis* ATCC 6633 **(D,E)** exposed to NP-TEICO **(D)** and teicoplanin **(E)**. Scale bar: 500 nm. ▶indicates ghost cells; *indicates lysed cells; white arrows indicate mesosome-like structures.

Huang et al., 2010; Ebrahiminezhad et al., 2014; Arakha et al., 2015a; Dinali et al., 2017).

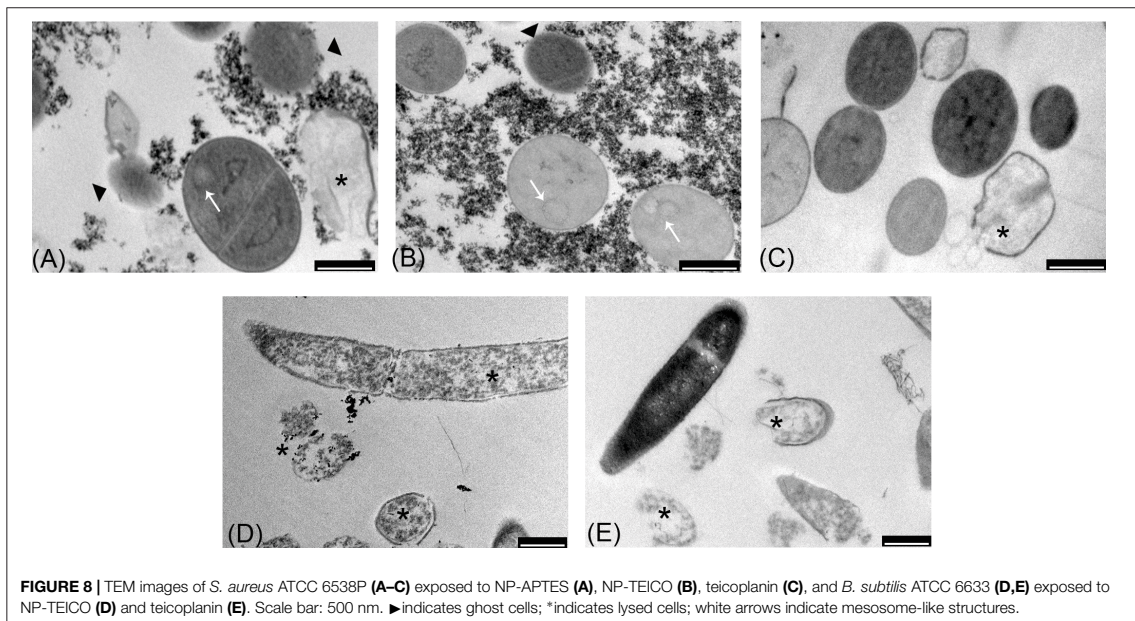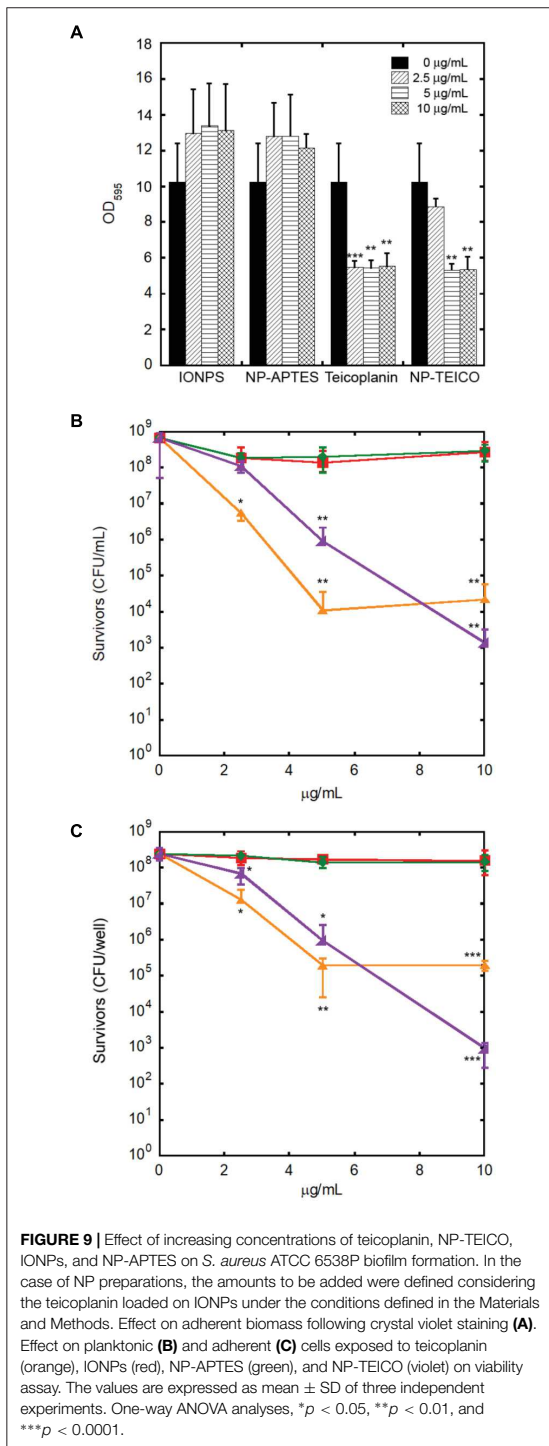## Effect of NPs on *S. aureus* Biofilm

Because of the clinical relevance of biofilm infections, the effect of our NP preparations was tested on *S. aureus* ATCC 6538P biofilm formation and eradication. As shown in **Figure 9A**, non-conjugated teicoplanin and nanoconjugated teicoplanin inhibited significantly the biofilm formation at a concentration of 2.5 μg/mL ($p = 8.03 \times 10^{-5}$) and 5 μg/mL ($p = 0.002$), respectively. No inhibitory effect on biofilm formation was observed after adding IONPs or NP-APTES in comparison to the untreated condition. In the same experimental setting, investigating the effect of IONPs, NP-APTES, NP-TEICO, and teicoplanin on the bacterial viability of adherent and planktonic cell subpopulations gave further information. It was confirmed that IONPs and NP-APTES did not influence the viability of the two subpopulations. Conversely, nanoconjugated and non-conjugated teicoplanin inhibited in a dose-dependent manner the cell viability of both planktonic (**Figure 9B**) and adherent (**Figure 9C**) cells. Teicoplanin at 5 μg/mL caused the decrease of approximately 5 log units in the survival of planktonic cells in comparison to the untreated control cells, whereas the NP-TEICO addition showed a comparable antimicrobial effect at the highest tested concentration of nanoconjugated teicoplanin corresponding to 10 μg/mL (**Figure 9B**). Increasing concentrations of non-conjugated teicoplanin caused a reduction of 2–3 log units in the survival of adherent cells, whereas, notably, the effect of nanoconjugated teicoplanin toward adherent cells was more pronounced (a reduction of 5 log units) than that of non-conjugated teicoplanin at 10 μg/mL and it was statistically

significant ($p = 0.010$) (**Figure 9C**). Conversely, neither non-conjugated teicoplanin nor nanoconjugated teicoplanin showed any dispersal effect on 48-h-old biofilms (data not shown), as expected, taking into account that this glycopeptide antibiotic inhibits cell wall synthesis in exponentially growing bacterial cells and is not active on bacterial cells entering into the stationary phase (Binda et al., 2014; Marcone et al., 2018).

Cytotoxicity of NP-TEICO

Cytotoxicity of NP-TEICO was evaluated using two different human cell lines, the well-established immortalized tumor cell line (SKOV-3) (Cappellini et al., 2015) and primary mesenchymal stem cells extracted from human adipose tissue, which are particularly sensitive to nanomaterials (Palombella et al., 2017). Results shown in **Figure 10** indicate that teicoplanin did not exert any effect on the cell viability of either of the human cell lines at any of the tested concentrations. Conversely, both SKOV-3 cells and hASC responded to the exposure of IONPs and NP-TEICO in a concentration-dependent manner. No significant decrease in cell viability was observed after adding nanoconjugated teicoplanin in the range of teicoplanin antibacterial MICs (0.78 μg/mL) (**Figures 10A,B**). The corresponding amounts of carrying NPs did not influence cell viability significantly (**Figures 10A,B**). At a concentration threefold higher than the antibacterial MICs of NP-TEICO (6 μg/mL), the effects of nanoconjugated teicoplanin and of the carrier NPs significantly differed from that of the free antibiotic. Naked IONPs reduced cell viability by more than 60% (after 24 h of exposure) to 50% (after 96 h) in SKOV-3 cells (**Figure 10C**), and by 50% (after 24 h) to 70% (after 96 h) in hASC (**Figure 10D**). NP-TEICO were less cytotoxic, reducing cell viability by 40% (after 24 h) to 20% (after
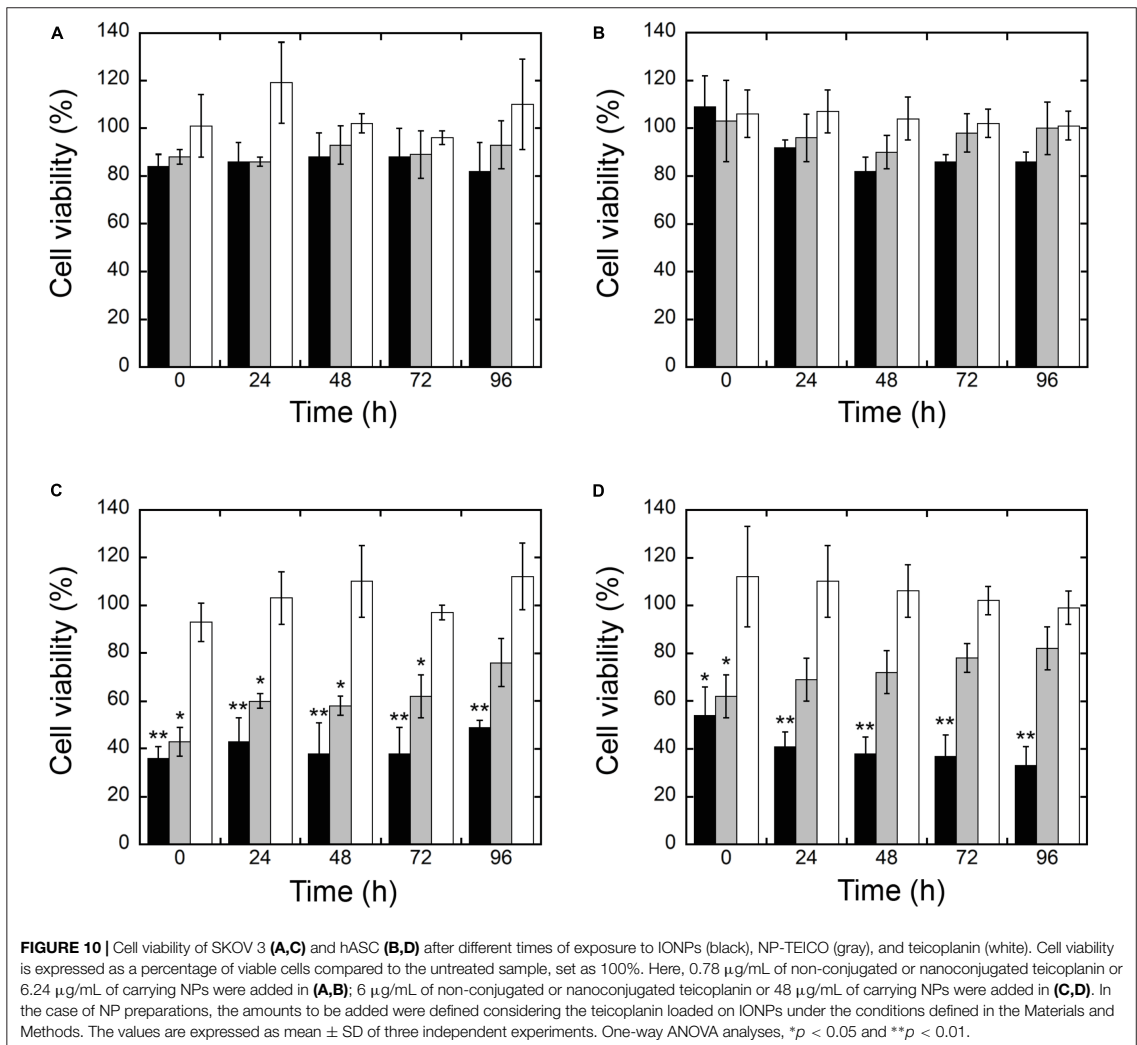
FIGURE 9 | Effect of increasing concentrations of teicoplanin, NP-TEICO, IONPs, and NP-APTES on *S. aureus* ATCC 6538P biofilm formation. In the case of NP preparations, the amounts to be added were defined considering the teicoplanin loaded on IONPs under the conditions defined in the Materials and Methods. Effect on adherent biomass following crystal violet staining **(A)**. Effect on planktonic **(B)** and adherent **(C)** cells exposed to teicoplanin (orange), IONPs (red), NP-APTES (green), and NP-TEICO (violet) on viability assay. The values are expressed as mean ± SD of three independent experiments. One-way ANOVA analyses, *$p < 0.05$, **$p < 0.01$, and ***$p < 0.0001$.

96 h) in SKOV-3 cells (**Figure 10C**) and by less than 30% (after 24 h) to 20% (after 96 h) in hASC (**Figure 10D**). Interestingly, conjugation of antibiotic molecules to IONPs surface tended to reduce their intrinsic cytotoxicity, as already reported by other authors who demonstrated that covering the NP surface shields toxicity and improves biocompatibility (Javed et al., 2017; Xiang et al., 2017; Xie et al., 2017, 2018).

DISCUSSION

In the era of antibiotic resistance, the lipoglycopeptide teicoplanin is an extremely important antibiotic used for the prophylaxis and treatment of serious infections caused by Gram-positive bacteria, including MRSA and *E. faecalis* (Van Bambeke, 2006; Marcone et al., 2018). It is used to treat endocarditis, bacteremia, and bone and joint infections. Because of its efficacy and safety, it is used in pediatrics, too. Its spectrum of antibacterial action is similar to that of the previously discovered glycopeptide vancomycin, but teicoplanin has several advantages over vancomycin in the treatment of serious infections: longer half-life, lower nephrotoxicity and ototoxicity, and lack of requirement for serum assays in treated patients. Because of its better stability *in vivo*, it can be administered once a day or with an alternate daily dosage and by intravenous bolus or by intramuscular injection. Oral administration of teicoplanin has also been demonstrated to be effective in the treatment of pseudomembranous colitis and *C. difficile*-associated diarrhea. In addition, teicoplanin is active on some of the vancomycin-resistant enterococci, which are increasingly spreading in hospitals (Binda et al., 2014).

Notwithstanding these important features, to the best of our knowledge, this is the first report of using teicoplanin to functionalize NPs. The teicoplanin molecule has an addressable functional group (the N-terminal carboxylic group of the heptapeptide chain) that we used to covalently bind the amino-activated IONPs. Although there are few published data on optimizing the fabrication of nanoconjugated antibiotics onto IONPs (Lin et al., 2005; Hussein-Al-Ali et al., 2014; Zhu et al., 2015; Dinali et al., 2017), we succeeded in anchoring more than 100 µg of teicoplanin per mg of NP-APTES in this work. The antimicrobial potency of nanoconjugated teicoplanin was slightly lower than that of the non-conjugated counterpart, particularly toward resistant clinical isolates, but NP-TEICO conserved the teicoplanin antimicrobial spectrum of activity toward Gram-positive bacteria and it was particularly active in controlling *S. aureus* biofilm formation. The external membrane of Gram-negative bacteria covering the peptidoglycan layer remained highly impenetrable to both NP-TEICO and teicoplanin, impeding their interaction with the molecular target (Binda et al., 2014). One of the positive features of NP-TEICO prepared in this way was that the formulation maintained chemical stability and antimicrobial activity for at least 1 month. This aspect is relevant, considering that one main advantage of using magnetic antibiotic nanocarriers *in vivo* could be that they can be recovered and recycled after single uses, reducing local dose administration and potential side effects and decreasing the risk of selective

FIGURE 10 | Cell viability of SKOV 3 **(A,C)** and hASC **(B,D)** after different times of exposure to IONPs (black), NP-TEICO (gray), and teicoplanin (white). Cell viability is expressed as a percentage of viable cells compared to the untreated sample, set as 100%. Here, 0.78 μg/mL of non-conjugated or nanoconjugated teicoplanin or 6.24 μg/mL of carrying NPs were added in **(A,B)**; 6 μg/mL of non-conjugated or nanoconjugated teicoplanin or 48 μg/mL of carrying NPs were added in **(C,D)**. In the case of NP preparations, the amounts to be added were defined considering the teicoplanin loaded on IONPs under the conditions defined in the Materials and Methods. The values are expressed as mean $\pm$ SD of three independent experiments. One-way ANOVA analyses, $*p < 0.05$ and $**p < 0.01$.

pressure on resistant strains. In addition, their targeted delivery to the site of infection/biofilm by using an external magnetic field might increase their *in situ* concentration, potentiating their local efficacy. For this reason, we consider the fact that NP-TEICO inhibited *S. aureus* biofilm formation, conserving the activity of non-conjugated teicoplanin versus the planktonic cells and improving it toward the adherent cells, to be promising. Different non-specific interactions such as electrostatic, hydrophobic, and van der Waal interactions are responsible for adhesion of bacteria on any material surfaces creating biofilms. Thus, it is possible that NP-TEICO anti-biofilm activity is potentiated (in comparison to the non-conjugated antibiotic) by intercepting these non-specific interactions, although in our experiments IONPs and NP-APTES had no effect on biofilm formation.

Unfortunately, *S. aureus* has dramatically re-emerged as a clinically relevant pathogen due to its resistance to antibiotics and the increased use of indwelling clinical devices. Millions of indwelling medical devices are implanted every year, and *S. aureus* is the major culprit for infections and failure of these devices (Arciola et al., 2018). *S. aureus* biofilms are also implicated in chronic wound infections such as diabetic foot ulcers, venous stasis ulcers, and pressure sores, which are quite resistant to antibiotic treatments. Teicoplanin carried by magnetically driven NPs can more easily reach deep tissue infections, which are difficult to treat using topical antibiotics due to the poor tissue penetration, and better penetrate the diffusion barriers that biofilms produce.

In the last decade, a certain level of intrinsic antimicrobial and cytotoxicity activity has been controversially attributed to the IONPs themselves. Although IONPs and NP-APTES have shown some antibacterial effect against diverse Gram-positive and Gram-negative bacteria, the real extent of this phenomenon and the underlying mechanism has hitherto not been well understood (Baranwal et al., 2018). Ansari et al. (2017) reported a dose-dependent antibacterial activity of IONPs against *Bacillus cereus* and *Klebsiella pneumoniae*. In contrast, Auffan et al. (2008) indicated that chemically stable IONPs were not toxic to *E. coli* at 700 mg/L, whereas Chatterjee et al. (2011) reported a dose-dependent effect on *E. coli* cells. Borcherding et al. (2014) showed that IONPs had a positive effect in promoting the growth of *Pseudomonas aeruginosa*. Arakha et al. (2015a) published an illuminating study and demonstrated, by combining a complete set of microbiological and biophysical methods, that IONPs did not show any significant antimicrobial activity toward *B. subtilis* and *E. coli*. Coating IONPs with positively charged chitosan, instead, conferred them with an increased so-called antimicrobial propensity against *B. subtilis* and *E. coli*, which depends on the interfacial interaction between NPs and bacterial surfaces (Arakha et al., 2015a,b).

In the present work, we compared the antimicrobial activity of NP-TEICO with that shown by IONPs and NP-APTES by using a set of methods (agar diffusion assay, BacLight fluorescence assay, bacterial growth kinetics, CFU measurement, and TEM observations) comparable to those previously used by Arakha et al. (2015a,b). Thus, we could conclude that the antibiotic activity of nanoconjugated and non-conjugated teicoplanin differed dramatically from the phenomenon described as antimicrobial propensity, which is based on an electrostatic attraction between cationic NPs and anionic bacterial cell surfaces (Arakha et al., 2015a,b). Electrostatic attraction promotes unspecific adhesion of NPs onto the cell wall of Gram-positive bacteria and the external cell membrane of the Gram-negative bacteria (Qi et al., 2013; Baranwal et al., 2018). This adhesion likely represents the mechanism by which IONPs and, to a greater extent, the positively charged NP-APTES impaired the growth of *S. aureus*, *B. subtilis*, and *E. coli* in our experiments of bacterial growth kinetics. This interfacial effect was transient and reversible, differing from the specific killing activity of teicoplanin and NP-TEICO toward the Gram-positive bacteria. Nevertheless, TEM observations suggested that we cannot completely rule out that cell adhesion of IONPs and of NP-APTES might provoke cytosolic shrinkage and cell membrane detachment (and eventually cell rupture), as observed in *S. aureus* and, with a lower frequency, in *B. subtilis*. In any case, this phenomenon was again sporadic, probably depending on surface composition and on the physiological state of single bacterial cells, as indicated by Dinali et al. (2017).

Although IONPs have been increasingly proposed for a wide range of biomedical applications, such as drug delivery, magnetic resonance imaging, thermal ablation therapy, and treatment of iron-deficient anemia, our understanding of their interaction with animal cells and animal models is still relatively limited (Natan and Banin, 2017; Feng et al., 2018). Recent studies showed that physicochemical properties, including particle size, PDI, surface charge, oxidation state of iron, and different surface coatings, greatly influence their biological effect *in vitro* and *in vivo* (Feng et al., 2018; Wang et al., 2018). Among the super magnetic NPs, IONPs were generally preferred because they are less toxic than those based on nickel and cobalt (Gornati et al., 2016). However, it was recently demonstrated that IONPs can enter eukaryotic cells not only by endocytosis, but also by diffusion through the plasma membrane, gaining direct access to the cytoplasm (Zanella et al., 2017). In addition, the intrinsic catalase-like activity of IONPs might antagonize the accumulation of toxic reactive oxygen species they have induced and thereby modulate the extent of cellular oxidative stress, autophagic activity, and programmed cell death (Wang et al., 2018). In this complex framework, a complete evaluation of the cytocompatibility of our NP-TEICO preparation *in vitro* and *in vivo* systems lies outside the scope of this work, although it would represent a future interesting extension of the study. Here, we demonstrated that at the concentrations that encompass the teicoplanin antibacterial MIC values, teicoplanin coating of IONPs reduced their intrinsic cytotoxicity toward two human cell lines, thus improving their potential biocompatibility. Further intensive *in vitro* and *in vivo* investigations are needed to develop an NP-TEICO-based drug formulation that could be administered systemically or topically to treat deep tissue infections and/or cover medical devices to prevent biofilm formation. Our results indicate that combining synergistically the unique properties of different nanomaterials would represent a good strategy, in this way providing a novel route to prevent and treat bacterial infections and, at the same time, reduce the intrinsic cytotoxicity of NPs, as already indicated by other authors (Xiang et al., 2017; Xie et al., 2017, 2018).

AUTHOR CONTRIBUTIONS

IA, GM, GB, and FM conceived the experiments, interpreted the results, and wrote the manuscript. IA developed and produced the NPs and performed the characterization. IA, FB, and GM conducted and interpreted the experiments on the microbiological activity of NPs. VO and EM conducted and analyzed the experiments on biofilms. CP and RG performed the microscopical observations and cell cytotoxicity tests and analyzed the results. All authors reviewed and approved the final manuscript.

FUNDING

ACKNOWLEDGMENTS

REFERENCES

Ali, A., Zafar, H., Zia, M., ul Haq, I., Phull, A. R., Ali, J. S., et al. (2016). Synthesis, characterization, applications, and challenges of iron oxide nanoparticles. *Nanotechnol. Sci. Appl.* 9, 49–67. doi: 10.2147/NSA.S99986

Allen, N. E., and Nicas, T. I. (2003). Mechanism of action of oritavancin and related glycopeptide antibiotics. *FEMS Microbiol. Rev.* 26, 511–532. doi: 10.1111/j.1574-6976.2003.tb00628.x

Ansari, S. A., Oves, M., Satar, R., Khan, A., Ahmad, S. I., Jafri, M. A., et al. (2017). Antibacterial activity of iron oxide nanoparticles synthesized by co-precipitation technology against *Bacillus cereus* and *Klebsiella pneumoniae*. *Polish J. Chem. Technol.* 4, 110–115. doi: 10.1515/pjct-2017-0076

Arakha, M., Pal, S., Samantarrai, D., Panigrahi, T. K., Mallick, B. C., Pramanik, K., et al. (2015a). Antimicrobial activity of iron oxide nanoparticle upon modulation of nanoparticle-bacteria interface. *Sci. Rep.* 5:14813. doi: 10.1038/srep14813

Arakha, M., Saleem, M., Mallick, B. C., and Jha, S. (2015b). The effects of interfacial potential on antimicrobial propensity of ZnO nanoparticle. *Sci. Rep.* 5:9578. doi: 10.1038/srep09578

Arciola, C. R., Campoccia, D., and Montanaro, L. (2018). Implant infections: adhesion, biofilm formation and immune evasion. *Nat. Rev. Microbiol.* 16, 397–409. doi: 10.1038/s41579-018-0019-y

Armenia, I., Balzaretti, R., Pirrone, C., Allegretti, C., D'Arrigo, P., Valentino, M., et al. (2017). L-aspartate oxidase magnetic nanoparticles: synthesis, characterization and L-aspartate bioconversion. *RSC Adv.* 7, 21136–21143. doi: 10.1039/C7RA00384F

Auffan, M., Achouak, W., Rose, J., Roncato, M. A., Chanéac, C., Waite, D. T., et al. (2008). Relation between the redox state of iron-based nanoparticles and their cytotoxicity toward *Escherichia coli*. *Environ. Sci. Technol.* 42, 6730–6735. doi: 10.1021/es800086f

Balzaretti, R., Meder, F., Monopoli, M. P., Boselli, L., Armenia, I., Pollegioni, L., et al. (2017). Synthesis, characterization and programmable toxicity of iron oxide nanoparticles conjugated with D-amino acid oxidase. *RSC Adv.* 7, 1439–1442. doi: 10.1039/c6ra25349k

Baranwal, A., Srivastava, A., Kumar, P., Bajpai, V. K., Maurya, P. K., and Chandra, P. (2018). Prospects of nanostructure materials and their composites as antimicrobial agents. *Front. Microbiol.* 9:422. doi: 10.3389/fmicb.2018.00422

Binda, E., Cappelletti, P., Marinelli, F., and Marcone, G. L. (2018). Specificity of induction of glycopeptide antibiotic resistance in the producing actinomycetes. *Antibiotics* 7:E36. doi: 10.3390/antibiotics7020036

Binda, E., Marinelli, F., and Marcone, G. L. (2014). Old and new glycopeptide antibiotics: action and resistance. *Antibiotics* 3, 572–594. doi: 10.3390/antibiotics3040572

Borcherding, J., Baltrusaitis, J., Chen, H., Stebounova, L., Wu, C. M., Rubasinghege, G., et al. (2014). Iron oxide nanoparticles induce *Pseudomonas aeruginosa* growth, induce biofilm formation, and inhibit antimicrobial peptide function. *Environ. Sci. Nano* 1, 123–132. doi: 10.1039/C3EN00029J

Cappellini, F., Recordati, C., Maglie, M., De Pollegioni, L., Rossi, F., Daturi, M., et al. (2015). New synthesis and biodistribution of the D-amino acid oxidase-magnetic nanoparticle system. *Future Sci. OA* 1, FS067. doi: 10.4155/Fso.15.67

Chakraborty, S. P., Sahu, S. K., Mahapatra, S. K., Santra, S., Bal, M., Roy, S., et al. (2010). Nanoconjugated vancomycin: new opportunities for the development of anti-VRSA agents. *Nanotechnol.* 21, 105103–105111. doi: 10.1088/0957-4484/21/10/105103

Chakraborty, S. P., Sahu, S. K., Pramanik, P., and Roy, S. (2012). In vitro antimicrobial activity of nanoconjugated vancomycin against drug resistant *Staphylococcus aureus*. *Int. J. Pharm.* 436, 659–676. doi: 10.1016/j.ijpharm.2012.07.033

Chatterjee, S., Bandyopadhyay, A., and Sarkar, K. (2011). Effect of iron oxide and gold nanoparticles on bacterial growth leading towards biological application. *J. Nanobiotechnol.* 9, 34–40. doi: 10.1186/1477-3155-9-34

Chifiriuc, M. C., Grumezescu, A. M., Andronescu, E., Ficai, A., Cotar, A. I., Grumezescu, V., et al. (2013). Water dispersible magnetite nanoparticles influence the efficacy of antibiotics against planktonic and biofilm embedded *Enterococcus faecalis* cells. *Anaerobe* 22, 14–19. doi: 10.1016/j.anaerobe.2013.04.013

Chudasama, B., Vala, A. K., Andhariya, N., Upadhyay, R. V., and Mehta, R. V. (2009). Enhanced antibacterial activity of bifunctional Fe3O4-Ag core-shell nanostructures. *Nano Res.* 2, 955–965. doi: 10.1007/s12274-009-9098-4

CLSI (2018). *Performance Standards for Antimicrobial Susceptibility Testing*, 28th Edn. Wayne, PA: Clinical and Laboratory Standards Institute.

Davis, D. (2003). Understandng biofilm resistance to antibacterial agents. *Nat. Rev. Drug Discov.* 2, 114–122. doi: 10.1038/nrd1008

De Palma, R., Peeters, S., Van Bael, M. J., Van Den Rul, H., Bonroy, K., Laureyn, W., et al. (2007). Silane ligand exchange to make hydrophobic superparamagnetic nanoparticles water-dispersible. *Chem. Mater.* 19, 1821–1831. doi: 10.1021/cm0628000

Dinali, R., Ebrahiminezhad, A., Manley-Harris, M., Ghasemi, Y., and Berenjian, A. (2017). Iron oxide nanoparticles in modern microbiology and biotechnology. *Crit. Rev. Microbiol.* 43, 493–507. doi: 10.1080/1040841X.2016.1267708

Dong, S. D., Oberthür, M., Losey, H. C., Anderson, J. W., Eggert, U. S., Peczuh, M. W., et al. (2002). The structural basis for induction of VanB resistance. *J. Am. Chem. Soc.* 124, 9064–9065. doi: 10.1021/ja026342h

Durán, N., Durán, M., de Jesus, M. B., Seabra, A. B., Fávaro, W. J., and Nakazato, G. (2016). Silver nanoparticles: a new view on mechanistic aspects on antimicrobial activity. *Nanomedicine* 12, 789–799. doi: 10.1016/j.nano.2015.11.01

Ebrahiminezhad, A., Rasoul-Amini, S., Davaran, S., Barar, J., and Ghasemi, Y. (2014). Impacts of iron oxide nanoparticles on the invasion power of *Listeria monocytogenes*. *Curr. Nanosci.* 10, 382–388. doi: 10.2174/15734137113096660109

El Zowalaty, M. E., Hussein-Al-Ali, S. H., Husseiny, M. I., Geilich, B. M., Webster, T. J., and Hussein, M. Z. (2015). The ability of streptomycin-loaded chitosan-coated magnetic nanocomposites to possess antimicrobial and antituberculosis activities. *Int. J. Nanomedicine* 10, 3269–3274. doi: 10.2147/IJN.S74469

Fedorenko, V., Genilloud, O., Horbal, L., Marcone, G. L., Marinelli, F., Paitan, Y., et al. (2015). Antibacterial discovery and development: from gene to product and back. *Biomed. Res. Int.* 2015:591349. doi: 10.1155/2015/591349

Feng, Q., Liu, Y., Huang, J., Chen, K., Huang, J., and Xiao, K. (2018). Uptake, distribution, clearance, and toxicity of iron oxide nanoparticles with different sizes and coatings. *Sci. Rep.* 8:2082. doi: 10.1038/s41598-018-19628-z

Finn, R. K. (1959). Theory of agar diffusion methods for bioassay. *Anal. Chem.* 31, 975–977. doi: 10.1021/ac60150a040

Gonçalves, L. C., Seabra, A. B., Pelegrino, M. T., de Araujo, D. R., Bernardes, J. S., and Haddad, P. S. (2017). Superparamagnetic iron oxide nanoparticles dispersed in pluronic F127 hydrogel: potential uses in topical applications. *RSC Adv.* 7, 14496–14503. doi: 10.1039/C6RA28633J

Gornati, R., Pedretti, E., Rossi, F., Cappellini, F., Zanella, M., Olivato, I., et al. (2016). Fe, Co and Ni nanoparticle toxicity evaluated on SKOV-3 and U87 cell lines. *J. Appl. Toxicol.* 36, 385–393. doi: 10.1002/jat.3220

Grumezescu, A. M., Gesta, M. C., Holban, A. M., Grumezescu, V., Vasile, B. S., Mogoanta, L., et al. (2014). Biocompatible Fe3O4 increases the efficacy of amoxicillin delivery against Gram-positive and Gram-negative bacteria. *Molecules* 19, 5013–5027. doi: 10.3390/molecules19045013

Gu, H., Ho, P. L., Tsang, K. W. T., Yu, C. W., and Xu, B. (2003). Using biofunctional magnetic nanoparticles to capture Gram-negative bacteria at an ultra-low concentration. *Chem. Commun.* 7, 1966–1967. doi: 10.1039/b305421g

Hajipour, M. J., Fromm, K. M., Akbar Ashkarran, A., Jimenez de Aberasturi, D., Larramendi, I. R., de Rojo, T., et al. (2012). Antibacterial properties of nanoparticles. *Trends Biotechnol.* 30, 499–511. doi: 10.1016/j.tibtech.2012.06.004

Hartmann, M., Berditsch, M., Hawecker, J., Ardakani, M. F., Gerthsen, D., and Ulrich, A. S. (2010). Damage of the bacterial cell envelope by antimicrobial peptides gramicidin S and PGLa as revealed by transmission and scanning electron microscopy. *Antimicrob. Agents Chemother.* 54, 3132–3142. doi: 10.1128/AAC.00124-10

Hermanson, G. T. (2013). "Zero-Length Crosslinkers," in *Bioconjugate Techniques*, 3rd Edn, eds J. Audet and M. Preap (London, UK: Academic Press), 259–268. doi: 10.1016/B978-0-12-382239-0.00004-2

Huang, Y. F., Wang, Y. F., and Yan, X. P. (2010). Amine-functionalized magnetic nanoparticles for rapid capture and removal of bacterial pathogens. *Environ. Sci. Technol.* 44, 7908–7913. doi: 10.1021/es102285n

Hussein-Al-Ali, S. H., El Zowalaty, M. E., Hussein, M. Z., Geilich, B. M., and Webster, T. J. (2014). Synthesis, characterization, and antimicrobial activity of an ampicillin-conjugated magnetic nanoantibiotic for medical applications. *Int. J. Nanomedicine* 9, 3801–3814. doi: 10.2147/IJN.S61143

Javed, Y., Akhtar, K., Anwar, H., and Jamil, Y. (2017). MRI based on iron oxide nanoparticles contrast agents: effect of oxidation state and architecture. *J. Nanopart. Res.* 19:366. doi: 10.1007/s11051-017-4045-x

Kell, A. J., Stewart, G., Ryan, S., Peytavi, R., Boissinot, M., Huletsky, A., et al. (2008). Vancomycin-modified nanoparticles for efficient targeting and preconcentration of Gram-positive and Gram-negative bacteria. *ACS* 2, 1777–1788. doi: 10.1021/nn700183g

Lin, Y. S., Tsai, P. J., Weng, M. F., and Chen, Y. C. (2005). Affinity capture using vancomycin-bound magnetic nanoparticles for the MALDI-MS analysis of bacteria. *Anal. Chem.* 77, 1753–1760. doi: 10.1021/ac048990k

Marcone, G. L., Binda, E., Berini, F., and Marinelli, F. (2018). Old and new glycopeptide antibiotics: from product to gene and back in the post-genomic era. *Biotechnol. Adv.* 36, 534–554. doi: 10.1016/j.biotechadv.2018.02.009

May, J., Shannon, K., King, A., and French, G. (1998). Glycopeptide tolerance in *Staphylococcus aureus*. *J. Antimicrob. Chemother.* 42, 189–197. doi: 10.1093/jac/42.2.189

Natan, M., and Banin, E. (2017). From Nano to Micro: using nanotechnology to combat microorganisms and their multidrug resistance. *FEMS Microbiol. Rev.* 41, 302–322. doi: 10.1093/femsre/fux003

Palombella, S., Pirrone, C., Rossi, F., Armenia, I., Cherubino, M., Valdatta, L., et al. (2017). Effects of metal micro and nano-particles on hASCs: an in vitro model. *Nanomaterials* 7:E212. doi: 10.3390/nano7080212

Qi, G., Li, L., Yu, F., and Wang, H. (2013). Vancomycin-modified mesoporous silica nanoparticles for selective recognition and killing of pathogenic Gram-positive bacteria over macrophage-like cells. *ACS Appl. Mater. Interfaces* 5, 10874–10881. doi: 10.1021/am403940d

Schneider, C. A., Rasband, W. S., and Eliceiri, K. W. (2012). NIH Image to ImageJ: 25 years of image analysis. *Nat. Methods* 9, 671–675.

Shimoda, M., Ohki, K., Shimamoto, Y., and Kohashi, O. (1995). Morphology of defensin-treated *Staphylococcus aureus*. *Infect. Immun.* 63, 2886–2891.

Stepien, G., Moros, M., Pérez-Hernández, M., Monge, M., Gutiérrez, L., Fratila, R. M., et al. (2018). Effect of surface chemistry and associated protein corona on the long-term biodegradation of iron oxide nanoparticles in vivo. *ACS Appl. Mater. Interfaces* 10, 4548–4560. doi: 10.1021/acsami.7b18648

Szpak, A., Kania, G., Skórka, T., Tokarz, W., Zapotoczny, S., and Nowakowska, M. (2013). Stable aqueous dispersion of superparamagnetic iron oxide nanoparticles protected by charged chitosan derivatives. *J. Nanoparticle Res.* 15, 1372–1382. doi: 10.1007/s11051-012-1372-9

Taurino, C., Frattini, L., Marcone, G. L., Gastaldo, L., and Marinelli, F. (2011). Actinoplanes teichomyceticus ATCC 31121 as a cell factory for producing teicoplanin. *Microb. Cell Fact.* 10, 82–94. doi: 10.1186/1475-2859-10-82

Tran, N., Mir, A., Mallik, D., Sinha, A., Nayar, S., and Webster, T. J. (2010). Bactericidal effect of iron oxide nanoparticles on *Staphylococcus aureus*. *Int. J. Nanomedicine* 5, 277–283. doi: 10.2147/IJN.S9220

Treviño, J., Bayón, C., Ardá, A., Marinelli, F., Gandolfi, R., Molinari, F., et al. (2014). New insights into glycopeptide antibiotic binding to cell wall precursors using SPR and NMR spectroscopy. *Chemistry* 20, 7363–7372. doi: 10.1002/chem.201303310

Van Bambeke, F. (2006). Glycopeptides and glycodepsipeptides in clinical development: a comparative review of their antibacterial spectrum, pharmacokinetics and clinical efficacy. *Curr. Opin. Investig. Drug* 7, 740–749.

Venkatesan, N., Perumal, G., and Doble, M. (2015). Bacterial resistance in biofilm-associated bacteria. *Future Microbiol.* 10, 1743–1750. doi: 10.2217/fmb.15.69

Wang, C., Zhang, K., Zhou, Z., Li, Q., Shao, L., Hao, R. Z., et al. (2017). Vancomycin-modified Fe3O4@SiO2@Ag microflowers as effective antimicrobial agents. *Int. J. Nanomedicine* 12, 3077–3094.

Wang, L., Wang, Z., Li, X., Zhang, Y., Yin, M., Li, J., et al. (2018). Deciphering active biocompatibility of iron oxide nanoparticles from their intrinsic antagonism. *Nano Res.* 11, 2746–2755. doi: 10.1007/s12274-017-1905-8

Weiner, L. M., Webb, A. K., Limbago, B., Dudeck, M. A., Patel, J., Kallen, A. J., et al. (2016). Antimicrobial-resistant pathogens associated with healthcare-associated infections: summary of data reported to the National Healthcare Safety Network at the Centers for Disease Control and Prevention, 2011-2014. *Infect. Control Hosp. Epidemiol.* 37, 1288–1301. doi: 10.1017/ice.2016.174

WHO (2017). *Antibacterial Agents in Clinical Development: an Analysis of the Antibacterial Clinical Development Pipeline, Including Tuberculosis.* Geneva: World Health Organization.

Wu, W., Wu, Z., Yu, T., Jiang, C., and Kim, W. S. (2015). Recent progress on magnetic iron oxide nanoparticles: synthesis, surface functional strategies and biomedical applications. *Sci. Technol. Adv. Mater.* 16:023501. doi: 10.1088/1468-6996/16/2/023501

Xiang, Y., Li, J., Liu, X., Cui, Z., Yang, X., Yeung, K. W. K., et al. (2017). Construction of poly(lactic-co-glycolic acid)/ZnO nanorods/Ag nanoparticles hybrid coating on Ti implants for enhanced antibacterial activity and biocompatibility. *Mater. Sci. Eng. C* 79, 629–637. doi: 10.1016/j.msec.2017.05.115

Xie, X., Mao, C., Liu, X., Tan, L., Cui, Z., Yang, X., et al. (2018). Tuning the bandgap of photo-sensitive polydopamine/Ag3PO4/graphene oxide coating for rapid, noninvasive disinfection of implants. *ACS Cent. Sci.* 4, 724–738. doi: 10.1021/acscentsci.8b00177

Xie, X., Mao, C., Liu, X., Zhang, Y., Cui, Z., Yang, X., et al. (2017). Synergistic bacteria killing through photodynamic and physical actions of graphene oxide/Ag/collagen coating. *ACS Appl. Mater. Interfaces* 9, 26417–26428. doi: 10.1021/acsami.7b06702

Zanella, D., Bossi, E., Gornati, R., Bastos, C., Faria, N., and Bernardini, G. (2017). Iron oxide nanoparticles can cross plasma membranes. *Sci. Rep.* 7:11413. doi: 10.1038/s41598-017-11535-z

Zhu, M., Liu, W., Liu, H., Liao, Y., Wei, J., Zhou, X., et al. (2015). Construction of Fe3O4/vancomycin/PEG magnetic nanocarrier for highly efficient pathogen enrichment and gene sensing. *ACS Appl. Mater. Interfaces* 7, 12873–12881. doi: 10.1021/acsami.5b02374

CONCLUSIONS

In this work, IONPs were successfully synthetized through a co-precipitation method that was developed as a modification of methods previously reported in literature. The particles obtained were fully characterized with different techniques, i.e. TEM, DLS, electrophoretic mobility and SQUID magnetometry. Such IONPs shown a good r eproducibility between batches not only for shape and size distribution, but also for hydrodynamic diameter and electrophoretic mobility.

The IONPs were then used as a platform for the conjugation of biomolecules, i.e. enzymes and glycopeptide antibiotic.

The use of immobilized enzymes in industrial applications often presents advantages over their soluble counterparts, mainly in view of stability, reusability and simpler operational processing. In this context, nanobiocatalysis, as the combination of nanotechnology and biocatalysis, is rapidly emerging as a new frontier of biotechnology.. Because of their singular properties, such as biocompatibility, large and modifiable surface and easy recovery, IONPs facilitate separation of the linked enzymes that can be easily obtained, lowering dramatically the costs of enzymes, by applying an external magnetic field. To this aim, two thermophilic enzymes (AMY and LASPO) were conjugated to IONPs through different conjugation strategies obtaining efficient biocatalysts. Here, it is demonstrated the importance of the orientation of the enzyme active site with respect to the NP surface: the nature and the position of the chemical bound that links the enzyme to the NP can modify the 3D structure of the enzyme and this can in turn influence the enzyme activity. Taking into consideration the superparamagnetism of the IONPs synthetized, the NP-enzyme systems were successfully activated by an AMF. Nevertheless, the temperature of the medium increases only slightly under AMF activation. This was also confirmed by the activity of a thermolable free enzyme present into the reaction pot during the AMF application to NP-enzyme systems.

These results also allow envisioning a future implementation of AMF-enzyme activation for biotechnological and biomedical applications, through a selective local thermo-activation of enzymes. In particular, the two enzymes used are attractive for biotechnological applications. Amylase is widely used in the starch industry for the

conversion of starch to medium-sized oligosaccharides. LASPO can be used for the production of D-aspartate from a racemic mixture of D,L-aspartate, a molecule employed in the pharmaceutical industry, for parenteral nutrition, as a food additive and in sweetener manufacture[72]. However, the industrial application of both enzymes is hampered by the high cost per enzymatic unit, which encourage exploring the use of thermophilic enzyme to improve their reusability due to their increased stability. Though, their use introduces the need to heat the reaction media to higher temperatures in order to maximize the efficiency of the reaction. As here shown that IONPs can generate enough local amount of thermal energy for the activation of both enzymes, a future implementation of AMF-enzyme activation should allow saving energy costs. Besides, as each enzyme was activated without raising the temperature of the reaction solution as a whole, it should be also feasible in a future the implementation of AMF-enzyme activation for the compatibility of different enzymes involved in multi-enzymatic processes of biotechnological interest.

In the second part of the project, IONPs was used as a platform for the conjugation of teicoplanin. Classical microbiological methods, together with morphological analysis by fluorescence and electron microscopy, were used to assess the antimicrobial activity of the nano-conjugated antibiotic. As bacterial models, different Gram-positive bacteria (*Staphylococcus aureus*, *Bacillus subtilis* and *Enterococcus faecalis*) and a Gram-negative representative (*Escherichia coli*) were used.

The results indicated that NP-TEICO have a high and prolonged antimicrobial activity toward Gram-positive bacteria. Furthermore, in comparison with IONPs and NP-APTES, NP-TEICO showed an significant antimicrobial activity. Sensitivity of bacteria to NPs varied according to the surface provided by the bacteria and it was strain-specific. Indeed, positively charged NP-APTES tended to establish electrostatic interactions with negatively charged bacteria. NP-TEICO inhibited *S. aureus* biofilm formation conserving the activity of teicoplanin versus planktonic cells and improving it towards adherent cells.

Although it would be worth to test NP-TEICO on a larger panel of susceptible and resistant Gram-positive bacteria, these initial data are encouraging and confirm that

the binding of teicoplanin confers to IONPs a marked and specific antimicrobial activity. Finally, new binding chemistries will be considered to improve the antimicrobial activity of the nano-system against Gram-positive bacteria and, possibly, to extend the activity spectrum also to Gram-negative bacteria, modulating the NP surface with different linkers and charges. For example, a more hydrophobic surface of the particles can be developed to permeate through the outer membrane bilayer by the self-promoting pathway, moreover it is possible to develop a nano-system as a combination of glycopeptide antibiotic and a polymyxins that can act in a synergic way to attach the Gram-negative cell wall.

BIBLIOGRAPHY

(1)   Wijnhoven, S. W. P.; Peijnenburg, W. J. G. M.; Herberts, C. A.; Hagens, W. I.; Oomen, A. G.; Heugens, E. H. W.; Roszek, B.; Bisschops, J.; Gosens, I.; Van De Meent, D.; *et al.* Nano-Silver - A Review of Available Data and Knowledge Gaps in Human and Environmental Risk Assessment. *Nanotoxicology* **2009**, *3*, 109–138.

(2)   European Commission. *L 275/38*; 2011; pp. 2010–2012.

(3)   Cyrys, J.; Stölzel, M.; Heinrich, J.; Kreyling, W. G.; Menzel, N.; Wittmaack, K.; Tuch, T.; Wichmann, H. E. Elemental Composition and Sources of Fine and Ultrafine Ambient Particles in Erfurt, Germany. *Sci. Total Environ.* **2003**, *305*, 143–156.

(4)   Hughes, L. S.; Cass, G. R.; Gone, J.; Ames, M.; Olmez, I. Physical and Chemical Characterization of Atmospheric Ultrafine Particles in the Los Angeles Area. *Environ. Sci. Technol.* **1998**, *32*, 1153–1161.

(5)   Guzmán, K. A. D.; Taylor, M. R.; Banfield, J. F. Environmental Risks of Nanotechnology: National Nanotechnology Initiative Funding, 2000-2004. *Environ. Sci. Technol.* **2006**, *40*, 1401–1407.

(6)   Pyrgiotakis, G.; Vedantam, P.; Cirenza, C.; McDevitt, J.; Eleftheriadou, M.; Leonard, S. S.; Demokritou, P. Optimization of a Nanotechnology Based Antimicrobial Platform for Food Safety Applications Using Engineered Water Nanostructures (EWNS). *Sci. Rep.* **2016**, *6*, 21073.

(7)   Bülbül, G.; Hayat, A.; Andreescu, S. Portable Nanoparticle-Based Sensors for Food Safety Assessment. *Sensors (Basel).* **2015**, *15*, 30736–30758.

(8)   Zhang, X.; Wang, X.; Sun, M.; Zhang, X.; Song, H.; Yan, Y.; Sun, J.; Li, X.; Fang, W. A Magnetic Nanoparticle Based Enzyme-Linked Immunosorbent Assay for Sensitive Quantification of Zearalenone in Cereal and Feed Samples. *Toxins (Basel).* **2015**, *7*, 4216–4231.

(9)   Burke, D. J.; Pietrasiak, N.; Situ, S. F.; Abenojar, E. C.; Porche, M.; Kraj, P.; Lakliang, Y.; Samia, A. C. S. Iron Oxide and Titanium Dioxide Nanoparticle Effects on Plant Performance and Root Associated Microbes. *Int. J. Mol. Sci.* **2015**, *16*, 23630–23650.

(10)   Saha, K.; Agasti, S. S.; Kim, C.; Li, X.; Rotello, V. M. Gold Nanoparticles in Chemical and Biological Sensing. *Chem. Rev.* **2012**, *112*, 2739–2779.

(11)   Stratakis, E.; Kymakis, E. Nanoparticle-Based Plasmonic Organic Photovoltaic Devices. *Mater. Today* **2013**, *16*, 133–146.

(12)   Nasrollahzadeh, M.; Bagherzadeh, M.; Karimi, H. Preparation, Characterization and Catalytic Activity of CoFe2O4 Nanoparticles as a Magnetically Recoverable Catalyst for Selective Oxidation of Benzyl Alcohol to Benzaldehyde and Reduction of Organic Dyes. *J. Colloid Interface Sci.* **2016**, *465*, 271–278.

(13)   Stark, W. J.; Stoessel, P. R.; Wohlleben, W.; Hafner, A. Industrial Applications of Nanoparticles. *Chem. Soc. Rev.* **2015**, *44*, 5793–5805.

(14)   Villaverde, A. Nanotechnology, Bionanotechnology and Microbial Cell Factories. *Microb. Cell Fact.* **2010**, *9*, 2–5.

(15)   Oberdörster, G.; Oberdörster, E.; Oberdörster, J. Nanotoxicology: An Emerging Discipline Evolving from Studies of Ultrafine Particles. *Environ. Health Perspect.* **2005**, *113*, 823–839.

(16)   Tartaj, P.; Morales, M. P.; González-Carreño, T.; Veintemillas-Verdaguer, S.; Serna, C. J. Advances in Magnetic Nanoparticles for Biotechnology Applications. *J. Magn. Magn. Mater.* **2005**, *290–291 PA*, 28–34.

(17)   Sun, S.; Murray, C. B.; Weller, D.; Folks, L.; Moser, A.; Murray, C. B.; Kagan, C. R.; Bawendi, M. G.; Alivisatos, A. P.; Collier, C. P.; *et al.* Monodisperse FePt Nanoparticles and Ferromagnetic FePt Nanocrystal Superlattices. *Science* **2000**, *287*, 1989–1992.

(18)   Wang, Y.; Yang, M.; Xu, B.; Yang, Z.; Hu, N.; Wei, L.; Cai, B.; Zhang, Y. Controlled Assembly of FePt Nanoparticles Monolayer on Solid Substrates. *J. Colloid Interface Sci.* **2014**, *417*, 100–108.

(19)   Ivanov, Y. P.; Chuvilin, A.; Lopatin, S.; Kosel, J. Modulated Magnetic Nanowires for Controlling Domain Wall Motion: Toward 3D Magnetic Memories.

(20)   Li, Y.; Hong, X.; Collard, D.; El-Sayed, M. Suzuki Cross-Coupling Reactions Catalyzed by Palladium Nanoparticles in Aqueous Solution. *Org. Lett.* **2000**, *2*, 2385–2388.

(21)   Lu, A.; Schmidt, W.; Matoussevitch, N.; Bönnemann, H.; Spliethoff, B.; Tesche, B.; Bill, E.; Kiefer, W.; Schüth, F. Nanoengineering of a Magnetically Separable Hydrogenation Catalyst. *Angew. Chemie* **2004**, *116*, 4403–4406.

(22)   Gobbo, O. L.; Sjaastad, K.; Radomski, M. W.; Volkov, Y.; Prina-Mello, A. Magnetic Nanoparticles in Cancer Theranostics. *Theranostics* **2015**, *5*, 1249–1263.

(23)   Nandwana, V.; De, M.; Chu, S.; Jaiswal, M.; Rotz, M.; Meade, T. J.; Dravid, V. P. Theranostic Magnetic Nanostructures (MNS) for Cancer. *Cancer Treat. Res.* **2015**, *166*, 51–83.

(24)   Hajba, L.; Guttman, A. The Use of Magnetic Nanoparticles in Cancer Theranostics: Toward Handheld Diagnostic Devices. *Biotechnol. Adv.* **2016**, *34*, 354–361.

(25)   Lux, F.; Sancey, L.; Bianchi, A.; Yannick; Crémillieux, S. R.; Tillement, & O. Gadolinium-Based Nanoparticles for Theranostic MRI-Radiosensitization. *Nanomedicine (Lond.)* **2015**, *10*, 1801–1815.

(26)   Mishra, S. K.; Kumar, B. S. H.; Khushu, S.; Tripathi, R. P.; Gangenahalli, G. Increased Transverse Relaxivity in Ultrasmall Superparamagnetic Iron Oxide Nanoparticles Used as MRI Contrast Agent for Biomedical Imaging. *Contrast Media Mol. Imaging* **2016**.

(27)   Hofmann-Amtenbrink, M.; von Rechenberg, B.; Hofmann, H. *Superparamagnetic Nanoparticles for Biomedical Applications*; 2009; Vol. 65.

(28)   Xu, C.; Sun, S. New Forms of Superparamagnetic Nanoparticles for Biomedical Applications. *Adv. Drug Deliv. Rev.* **2013**, *65*, 732–743.

(29)   Wu, W.; Wu, Z.; Yu, T.; Jiang, C.; Kim, W.-S. Recent Progress on Magnetic Iron Oxide Nanoparticles: Synthesis, Surface Functional Strategies and Biomedical Applications. *Sci. Technol. Adv. Mater.* **2015**, *16*, 023501.

(30)   Machala, L.; Tuček, J.; Zbořil, R. Polymorphous Transformations of Nanometric Iron(III) Oxide: A Review. *Chem. Mater.* **2011**, *23*, 3255–3272.

(31)   Zboril, R.; Mashlan, M.; Petridis, D. Iron(III) Oxides from Thermal Processess-Synthesis, Structural and Magnetic Properties, Mossbauer Spectroscopy Characterization, and Applications. *Chem. Mater.* **2002**, *14*, 969–982.

(32)   Nosrati, H.; Salehiabar, M.; Davaran, S.; Ramazani, A.; Manjili, H. K.; Danafar, H. New Advances Strategies for Surface Functionalization of Iron Oxide Magnetic Nano Particles (IONPs). *Res. Chem. Intermed.* **2017**, *43*, 7423–7442.

(33)   Wu, W.; He, Q.; Jiang, C. Magnetic Iron Oxide Nanoparticles: Synthesis and Surface Functionalization Strategies. *Nanoscale Res. Lett.* **2008**, *3*, 397–415.

(34)   Schüth, F. Controlled Nanostructures for Applications in Catalysis. *Phys. Chem. Chem. Phys.* **2011**, *13*, 2447–2448.

(35)   Hola, K.; Markova, Z.; Zoppellaro, G.; Tucek, J.; Zboril, R. Tailored Functionalization of Iron Oxide Nanoparticles for MRI, Drug Delivery, Magnetic Separation and Immobilization of Biosubstances. *Biotechnol. Adv.* **2015**, *33*, 1162–1176.

(36)   del Campo, A.; Sen, T.; Lellouche, J.-P.; Bruce, I. J. Multifunctional Magnetite and Silica–magnetite Nanoparticles: Synthesis, Surface Activation and Applications in Life Sciences. *J. Magn. Magn. Mater.* **2005**, *293*, 33–40.

(37)   Feng, B.; Hong, R. Y.; Wang, L. S.; Guo, L.; Li, H. Z.; Ding, J.; Zheng, Y.; Wei, D. G. Synthesis of Fe_3O_4/APTES/PEG Diacid Functionalized Magnetic Nanoparticles for MR Imaging. *Colloids Surfaces A Physicochem. Eng. Asp.* **2008**, *328*, 52–59.

(38)   Liu, Y.; Li, Y.; Li, X. M.; He, T. Kinetics of (3-Aminopropyl)Triethoxylsilane (Aptes) Silanization of Superparamagnetic Iron Oxide Nanoparticles. *Langmuir* **2013**, *29*, 15275–15282.

(39)   Clark, D. P.; Pazdernik, N. J. Nanobiotechnology. In *Biotechnology*; 2016; pp. 219–248.

(40)   Smijs, T. G.; Pavel, S. Titanium Dioxide and Zinc Oxide Nanoparticles in Sunscreens: Focus on Their Safety and Effectiveness. *Nanotechnol. Sci. Appl.* **2011**, *4*, 95–112.

(41)   Jiang, J.; Pi, J.; Cai, J. The Advancing of Zinc Oxide Nanoparticles for Biomedical Applications. *Bioinorg. Chem. Appl.* **2018**, *2018*.

(42)   Li, Y.; Sun, Y.; Yeow, J. T. W. Nanotube Field Electron Emission: Principles, Development, and Applications. *Nanotechnology* **2015**, *26*, 242001.

(43)   Bocharov, G.; Eletskii, A. Theory of Carbon Nanotube (CNT)-Based Electron Field Emitters. *Nanomaterials* **2013**, *3*, 393–442.

(44)   Arora, A.; Padua, G. W. Review: Nanocomposites in Food Packaging. *J. Food Sci.* **2010**, *75*, 43–49.

(45)   Azeredo, H. M. C. de. Nanocomposites for Food Packaging Applications. *Food Res. Int.* **2009**, *42*, 1240–1253.

(46)   Luther, W. Technological Analysis: Industrial Application of Nanomaterials - Chances and Risks. *Futur. Technol.* **2004**, *54*, 119.

(47)   Fouda, M. F. R.; El-Kholy, M. B.; Moustafa, S. A.; Hussien, A. I.; Wahba, M. A.; El-Shahat, M. F. Synthesis and Characterization of Nanosized Fe_2O_3 Pigments. *Int. J. Inorg. Chem.* **2012**, *2012*, 1–9.

(48)   Cao, M.; Li, Z.; Wang, J.; Ge, W.; Yue, T.; Li, R.; Colvin, V. L.; Yu, W. W. Food Related Applications of Magnetic Iron Oxide Nanoparticles: Enzyme Immobilization, Protein Purification, and Food Analysis. *Trends Food Sci. Technol.* **2012**, *27*, 47–56.

(49)   Liu, W.; Wang, L.; Jiang, R. Specific Enzyme Immobilization Approaches and Their Application with Nanomaterials. *Top. Catal.* **2012**, *55*, 1146–1156.

(50)   Kirk, O.; Borchert, T. V.; Fuglsang, C. C. Industrial Enzyme Applications. *Curr. Opin. Biotechnol.* **2002**, *13*, 345–351.

(51)   Madhavan, A.; Sindhu, R.; Binod, P.; Sukumaran, R. K.; Pandey, A. Strategies for Design of Improved Biocatalysts for Industrial Applications. *Bioresour. Technol.* **2017**.

(52)   Adrio, J. L.; Demain, A. L. Recombinant Organisms for Production of Industrial Products. *Bioeng. Bugs* **2010**, *1*, 116–131.

(53)   Vélez, A. M.; Horta, A. C. L.; Da Silva, A. J.; Iemma, M. R. D. C.; Giordano, R. D. L. C.; Zangirolami, T. C. Enhanced Production of Recombinant Thermo-Stable Lipase in Escherichia Coli at High Induction Temperature. *Protein Expr. Purif.* **2013**, *90*, 96–103.

(54)   Eş, I.; Vieira, J. D. G.; Amaral, A. C. Principles, Techniques, and Applications of Biocatalyst Immobilization for Industrial Application. *Appl. Microbiol. Biotechnol.* **2015**, *99*, 2065–2082.

(55)   Yiu, H. H. P.; Keane, M. A. Enzyme-Magnetic Nanoparticle Hybrids: New Effective Catalysts for the Production of High Value Chemicals. *J. Chem. Technol. Biotechnol.* **2012**, *87*, 583–594.

(56)   Suzuki, M.; Aki, A.; Mizuki, T.; Maekawa, T.; Usami, R.; Morimoto, H. Encouragement of Enzyme Reaction Utilizing Heat Generation from Ferromagnetic Particles Subjected to an AC Magnetic Field. *PLoS One* **2015**, *10*, 1–11.

(57)   Datta, S.; Christena, L. R.; Rajaram, Y. R. S. Enzyme Immobilization: An Overview on Techniques and Support Materials. *3 Biotech* **2013**, *3*, 1–9.

(58)   Dinçer, A.; Telefoncu, A. Improving the Stability of Cellulase by Immobilization on Modified Polyvinyl Alcohol Coated Chitosan Beads. *J. Mol. Catal. B Enzym.* **2007**, *45*, 10–14.

(59)   Elleuche, S.; Schrö Der, C.; Sahm, K.; Antranikian, G. Extremozymes — Biocatalysts with Unique Properties from Extremophilic Microorganisms. *Curr. Opin. Biotechnol.* **2014**, *29*, 116–123.

(60)   Sheldon, R. A.; van Pelt, S. Enzyme Immobilisation in Biocatalysis: Why, What and How. *Chem. Soc. Rev.* **2013**, *42*.

(61)   Liese, A.; Hilterhaus, L. Evaluation of Immobilized Enzymes for Industrial Applications Motivation and Recent Developments. *Chem. Soc. Rev. Chem. Soc. Rev* **2013**, *42*, 6236–6249.

(62) Dicosimo, R.; Mcauliffe, J.; Poulose, A. J.; Bohlmann, G. Industrial Use of Immobilized Enzymes. *Chem. Soc. Rev. Chem. Soc. Rev* **2013**, *42*, 6437–6474.

(63) Johnson, B. J.; Russ Algar, W.; Malanoski, A. P.; Ancona, M. G.; Medintz, I. L. Understanding Enzymatic Acceleration at Nanoparticle Interfaces: Approaches and Challenges. *Nano Today* **2014**, *9*, 102–131.

(64) Meridor, D.; Gedanken, A. Preparation of Enzyme Nanoparticles and Studying the Catalytic Activity of the Immobilized Nanoparticles on Polyethylene Films. *Ultrason. Sonochem.* **2013**, *20*, 425–431.

(65) Liu, Y.; Wang, S.; Zhang, C.; Su, X.; Huang, S.; Zhao, M. Enhancing the Selectivity of Enzyme Detection by Using Tailor-Made Nanoparticles. *Anal. Chem.* **2013**, *85*, 4853–4857.

(66) Wu, C.-S.; Lee, C.-C.; Wu, C.-T.; Yang, Y.-S.; Ko, F.-H. Size-Modulated Catalytic Activity of Enzyme-Nanoparticle Conjugates: A Combined Kinetic and Theoretical Study. *Chem. Commun. (Camb).* **2011**, *47*, 7446–7448.

(67) Wang, W.; Xu, Y.; Wang, D. I. C.; Li, Z. Recyclable Nanobiocatalyst for Enantioselective Sulfoxidation: Facile Fabrication and High Performance of Chloroperoxidase-Coated Magnetic Nanoparticles with Iron Oxide Core and Polymer Shell. *J. Am. Chem. Soc.* **2009**, *131*, 12892–12893.

(68) Yu, C.-C.; Kuo, Y.-Y.; Liang, C.-F.; Chien, W.-T.; Wu, H.-T.; Chang, T.-C.; Jan, F.-D.; Lin, C.-C. Site-Specific Immobilization of Enzymes on Magnetic Nanoparticles and Their Use in Organic Synthesis.

(69) Garcia, J.; Zhang, Y.; Taylor, H.; Cespedes, O.; Webb, M. E.; Zhou, D.; Schmid, A.; Dordick, J. S.; Hauer, B.; Kiener, A.; *et al.* Multilayer Enzyme-Coupled Magnetic Nanoparticles as Efficient, Reusable Biocatalysts and Biosensors. *Nanoscale* **2011**, *3*, 3721.

(70) Mukherjee, J.; Gupta, M. N. Lipase Coated Clusters of Iron Oxide Nanoparticles for Biodiesel Synthesis in a Solvent Free Medium. *Bioresour. Technol.* **2016**, *209*, 166–171.

(71) Shahrestani, H.; Taheri-Kafrani, A.; Soozanipour, A.; Tavakoli, O. Enzymatic Clarification of Fruit Juices Using Xylanase Immobilized on 1,3,5-Triazine-Functionalized Silica-Encapsulated Magnetic Nanoparticles. *Biochem. Eng. J.* **2016**, *109*, 51–58.

(72) Pollegioni, L.; Motta, P.; Molla, G. L-Amino Acid Oxidase as Biocatalyst: A Dream Too Far? *Appl. Microbiol. Biotechnol.* **2013**, *97*, 9323–9341.

(73) Sakuraba, H.; Yoneda, K.; Asai, I.; Tsuge, H.; Katunuma, N.; Ohshima, T. Structure of L-Aspartate Oxidase from the Hyperthermophilic Archaeon *Sulfolobus Tokodaii. Biochim. Biophys. Acta - Proteins Proteomics* **2008**, *1784*, 563–571.

(74) Bifulco, D.; Pollegioni, L.; Tessaro, D.; Servi, S.; Molla, G. A Thermostable L-Aspartate Oxidase: A New Tool for Biotechnological Applications. *Appl. Microbiol. Biotechnol.* **2013**, *97*, 7285–7295.

(75) D'Arrigo, P.; Allegretti, C.; Fiorati, A.; Piubelli, L.; Rosini, E.; Tessaro, D.; Valentino, M.; Pollegioni, L. Immobilization of l -Aspartate Oxidase from *Sulfolobus Tokodaii*

as a Biocatalyst for Resolution of Aspartate Solutions. *Catal. Sci. Technol.* **2015**, *5*, 1106–1114.

(76) Taniguchi, H.; Honnda, Y. *Encyclopedia of Microbiology*; Moselio Schaechter, Ed.; Third Edit.; Academic Press, 2009.

(77) Sundarram, A.; Murthy, T. P. K. α -Amylase Production and Applications : A Review. *J. Appl. Environ. Microbiol.* **2014**, *2*, 166–175.

(78) Gupta, R.; Gigras, P.; Mohapatra, H.; Goswami, V. K.; Chauhan, B. Microbial α-Amylases: A Biotechnological Perspective. *Process Biochem.* **2003**, *38*, 1599–1616.

(79) Tee, B. L.; Kaletunç, G. Immobilization of a Thermostable α-Amylase by Covalent Binding to an Alginate Matrix Increases High Temperature Usability. *Biotechnol. Prog.* **2009**, *25*, 436–445.

(80) Prakash, O.; Jaiswal, N. α-Amylase: An Ideal Representative of Thermostable Enzymes. *Appl. Biochem. Biotechnol.* **2010**, *160*, 2401–2414.

(81) Machius, M.; Declerck, N.; Huber, R.; Wiegand, G. Activation of Bacillus Licheniformis Alpha-Amylase through a Disorder→ Order Transition of the Substrate-Binding Site Mediated by a Calcium-Sodium-Calcium Metal Triad. *Structure* **1998**, *6*, 281–292.

(82) Morgan, F. J.; Morgan, F. J.; Priest, F. G.; Priest, F. G. Characterization of a Thermostable A-Amylase from *Bacillus Licheniformis* N CI B 6346. *J. Appl. Bacteriol.* **1981**, *50*, 107–114.

(83) Leila, S.; Mahmoud, H.; Khiabani, S.; Hamishehkar, H.; Salehi, R. Enhanced Stability and Catalytic Activity of Immobilized a -Amylase on Modified Fe_3O_4 Nanoparticles for Potential Application in Food Industries. *J. Nanoparticle Res.* **2015**.

(84) Knecht, L. D.; Ali, N.; Wei, Y.; Hilt, J. Z.; Daunert, S. Nanoparticle-Mediated Remote Control of Enzymatic Activity. *ACS Nano* **2012**, *6*, 9079–9086.

(85) Blankschien, M. D.; Pretzer, L. A.; Huschka, R.; Halas, N. J.; Gonzalez, R.; Wong, M. S. Light-Triggered Biocatalysis Using Thermophilic Enzyme - Gold Nanoparticle Complexes. *ACS Nano* **2013**, *7*, 654–663.

(86) Stehr, J.; Hrelescu, C.; Sperling, R. A.; Raschke, G.; Wunderlich, M.; Nichtl, A.; Heindl, D.; Kürzinger, K.; Parak, W. J.; Klar, T. A.; *et al.* Gold NanoStoves for Microsecond DNA Melting Analysis. *Nano Lett.* **2008**, *8*, 619–623.

(87) Richardson, H. H.; Carlson, M. T.; Tandler, P. J.; Hernandez, P.; Govorov, A. O. Experimental and Theoretical Studies of Light-to-Heat Conversion and Collective Heating Effects in Metal Nanoparticle Solutions. *Nano Lett.* **2009**, *9*, 1139–1146.

(88) Miyako, E.; Nagata, H.; Hirano, K.; Hirotsu, T. Laser-Triggered Carbon Nanotube Microdevice for Remote Control of Biocatalytic Reactions. *Lab Chip* **2009**, *9*, 788–794.

(89) Satarkar, N. S.; Biswal, D.; Hilt, J. Z. Hydrogel Nanocomposites: A Review of Applications as Remote Controlled Biomaterials. *Soft Matter* **2010**, *6*, 2364–2371.

(90) Hamad-schifferli, K.; Schwartz, J. J.; Santos, A. T.; Zhang, S.; Jacobson, J. M. Remote Electronic Control of DNA Hybridization through Inductive Coupling to an Attached

Metal Nanocrystal Antenna. *Nature* **2002**, *415*, 152–155.

(91)   Frimpong, R. A.; Fraser, S.; Hilt, J. Z. Synthesis and Temperature Response Analysis of Magnetic-Hydrogel Nanocomposites. *J. Biomed. Mater. Res. Part A An Off. J. Soc. Biomater.* **2007**, *1*, 1–6.

(92)   Mizuki, T.; Sawai;, M.; Nagaoka;, Y.; Morimoto;, H.; Maekawa;, T. Activity of Lipase and Chitinase Immobilized on Superparamagnetic Particles in a Rotational Magnetic Field. *PLoS One* **2013**, *8*.

(93)   Mizuki, T.; Watanabe, N.; Nagaoka, Y.; Fukushima, T.; Morimoto, H.; Usami, R.; Maekawa, T. Activity of an Enzyme Immobilized on Superparamagnetic Particles in a Rotational Magnetic Field. *Biochem. Biophys. Res. Commun.* **2010**, *393*, 779–782.

(94)   Klyachko, N. L.; Sokolsky-Papkov, M.; Pothayee, N.; Efremova, M. V.; Gulin, D. A.; Pothayee, N.; Kuznetsov, A. A.; Majouga, A. G.; Riffle, J. S.; Golovin, Y. I.; *et al.* Changing the Enzyme Reaction Rate in Magnetic Nanosuspensions by a Non-Heating Magnetic Field. *Angew. Chemie - Int. Ed.* **2012**, *51*, 12016–12019.

(95)   Zakharchenko, A.; Guz, N.; Laradji, A. M.; Katz, E.; Minko, S. Magnetic Field Remotely Controlled Selective Biocatalysis. *Nat. Catal.* **2017**, 1–9.

(96)   Kato, N.; Oishi, A.; Takahashi, F. Enzyme Reaction Controlled by Magnetic Heating Due to the Hysteresis Loss of γ-Fe_2O_3 in Thermosensitive Polymer Gels Immobilized β-Galactosidase. *Mater. Sci. Eng. C* **1998**, *6*, 291–296.

(97)   Takahashi, F.; Sakai, Y.; Mizutani, Y. Immobilized Enzyme Reaction Controlled by Magnetic Heating: γ-Fe_2O_3- Loaded Thermosensitive Polymer Gels Consisting of N-Isopropylacrylamide and Acrylamide. *J. Ferment. Bioeng.* **1997**, *83*, 152–156.

(98)   Suzuki, M.; Hayashi, H.; Mizuki, T.; Maekawa, T.; Morimoto, H. Efficient DNA Ligation by Selective Heating of DNA Ligase with a Radio Frequency Alternating Magnetic Field. *Biochem. Biophys. Reports* **2016**, *8*, 360–364.

(99)   Gupta, A. K.; Gupta, M. Synthesis and Surface Engineering of Iron Oxide Nanoparticles for Biomedical Applications. *Biomaterials* **2005**, *26*, 3995–4021.

(100)   Bobo, D.; Robinson, K. J.; Islam, J.; Thurecht, K. J.; Corrie, S. R. Nanoparticle-Based Medicines: A Review of FDA-Approved Materials and Clinical Trials to Date. *Pharm. Res.* **2016**, *33*, 2373–2387.

(101)   Mahmoudi, M.; Sant, S.; Wang, B.; Laurent, S.; Sen, T. Superparamagnetic Iron Oxide Nanoparticles (SPIONs): Development, Surface Modification and Applications in Chemotherapy. *Adv. Drug Deliv. Rev.* **2011**, *63*, 24–46.

(102)   Marcu, A.; Pop, S.; Dumitrache, F.; Mocanu, M.; Niculite, C. M.; Gherghiceanu, M.; Lungu, C. P.; Fleaca, C.; Ianchis, R.; Barbut, A.; *et al.* Magnetic Iron Oxide Nanoparticles as Drug Delivery System in Breast Cancer. *Appl. Surf. Sci.* **2013**, *281*, 60–65.

(103)   El-boubbou, K. Magnetic Iron Oxide Nanoparticles as Drug Carriers : Clinical Relevance. **2018**.

(104)   El-boubbou, K. Magnetic Iron Oxide Nanoparticles as Drug Carriers : Preparation, Conjugation and Delivery. *Nanomedicine (Lond.)* **2018**, *13*, 929–952.

(105)   Javed, Y.; Akhtar, K.; Anwar, H.; Jamil, Y. MRI Based on Iron Oxide Nanoparticles Contrast Agents: Effect of Oxidation State and Architecture. *J. Nanoparticle Res.* **2017**, *19*.

(106)   Banks, W. A.; Gray, A. M.; Erickson, M. A.; Salameh, T. S.; Damodarasamy, M.; Sheibani, N.; Meabon, J. S.; Wing, E. E.; Morofuji, Y.; Cook, D. G.; *et al.* Alternating Magnetic Field-Induced Hyperthermia Increases Iron Oxide Nanoparticle Cell Association/Uptake and Flux in Blood– Brain Barrier Models. *Pharm. Res.* **2015**, *32*, 229–262.

(107)   Maier-Hauff, K.; Ulrich, F.; Nestler, D.; Niehoff, H.; Wust, P.; Thiesen, B.; Orawa, H.; Budach, V.; Jordan, A. Efficacy and Safety of Intratumoral Thermotherapy Using Magnetic Iron-Oxide Nanoparticles Combined with External Beam Radiotherapy on Patients with Recurrent Glioblastoma Multiforme. *J. Neurooncol.* **2011**, *103*, 317–324.

(108)   World Health Organization. Antibacterial Agents in Clinical Development: An Analysis of the Antibacterial Clinical Development Pipeline, Including Tuberculosis. *Who/Emp/Iau/2017.12* **2017**.

(109)   Fedorenko, V.; Genilloud, O.; Horbal, L.; Marcone, G. L.; Marinelli, F.; Paitan, Y.; Ron, E. Z. Antibacterial Discovery and Development: From Gene to Product and Back. *Biomed Res. Int.* **2015**, *2015*.

(110)   Hackenberg, S.; Scherzed, A.; Kessler, M.; Hummel, S.; Technau, A.; Froelich, K.; Ginzkey, C.; Koehler, C.; Hagen, R.; Kleinsasser, N. Silver Nanoparticles: Evaluation of DNA Damage, Toxicity and Functional Impairment in Human Mesenchymal Stem Cells. *Toxicol. Lett.* **2011**, *201*, 27–33.

(111)   Sondi, I.; Salopek-Sondi, B. Silver Nanoparticles as Antimicrobial Agent: A Case Study on E. Coli as a Model for Gram-Negative Bacteria. *J. Colloid Interface Sci.* **2004**, *275*, 177–182.

(112)   Khan, S. T.; Musarrat, J.; Al-Khedhairy, A. A. Countering Drug Resistance, Infectious Diseases, and Sepsis Using Metal and Metal Oxides Nanoparticles: Current Status. *Colloids Surfaces B Biointerfaces* **2016**, *146*, 70–83.

(113)   Auffan, M.; Achouak, W.; Rose, J.; Roncato, M.; Chane, C.; Waite, D. T.; Masion, A.; Woicik, J. C.; Wiesner, M. R.; Bottero, J.; *et al.* Relation between the Redox State of Iron-Based Nanoparticles and Their Cytotoxicity toward *Escherichia Coli*. *Environ. Sci. Technol.* **2008**, *42*, 6730–6735.

(114)   Azam, A.; Ahmed, A. S.; Oves, M.; Khan, M. S.; Habib, S. S.; Memic, A. Antimicrobial Activity of Metal Oxide Nanoparticles against Gram-Positive and Gram-Negative Bacteria: A Comparative Study. *Int. J. Nanomedicine* **2012**, *7*, 6003–6009.

(115)   Arakha, M.; Pal, S.; Samantarrai, D.; Panigrahi, T. K.; Mallick, B. C.; Pramanik, K.; Mallick, B.; Jha, S. Antimicrobial Activity of Iron Oxide Nanoparticle upon Modulation of Nanoparticle-Bacteria Interface. *Sci. Rep.* **2015**, *5*, 14813.

(116)   Prabhu, Y. T.; Rao, K. V.; Kumari, B. S.; Sesha, V.; Kumar, S.; Pavani, T. Synthesis of Fe 3 O 4 Nanoparticles and Its Antibacterial Application. *Int. Nano Lett.* **2015**, 85–92.

(117) Tran, N.; Mir, A.; Mallik, D.; Sinha, A.; Nayar, S.; Webster, T. J. Bactericidal Effect of Iron Oxide Nanoparticles on *Staphylococcus Aureus*. *Int. J. Nanomedicine* **2010**, *5*, 277–283.

(118) Chifiriuc, M. C.; Grumezescu, A. M.; Andronescu, E.; Ficai, A.; Cotar, A. I.; Grumezescu, V.; Bezirtzoglou, E.; Lazar, V.; Radulescu, R. Water Dispersible Magnetite Nanoparticles Influence the Efficacy of Antibiotics against Planktonic and Biofilm Embedded *Enterococcus Faecalis* Cells. *Anaerobe* **2013**, *22*, 14–19.

(119) Grumezescu, A. M.; Gesta, M. C.; Holban, A. M.; Grumezescu, V.; Vasile, B. S.; Mogoanta, L.; Iordache, F.; Bleotu, C.; Dan Mogosanu, G. Biocompatible Fe3O4 Increases the Efficacy of Amoxicillin Delivery against Gram-Positive and Gram-Negative Bacteria. *Molecules* **2014**, *19*, 5013–5027.

(120) Hussein-Al-Ali, S. H.; El Zowalaty, M. E.; Hussein, M. Z.; Geilich, B. M.; Webster, T. J. Synthesis, Characterization, and Antimicrobial Activity of an Ampicillin-Conjugated Magnetic Nanoantibiotic for Medical Applications. *Int. J. Nanomedicine* **2014**, *9*, 3801–3814.

(121) El-Zowalaty, M. E.; Al-Ali, S. H. H.; Husseiny, M. I.; Geilich, B. M.; Webster, T. J.; Hussein, M. Z. The Ability of Streptomycin-Loaded Chitosan-Coated Magnetic Nanocomposites to Possess Antimicrobial and Antituberculosis Activities. *Int. J. Nanomedicine* **2015**, *10*, 3269–3274.

(122) Wang, C.; Zhang, K.; Zhou, Z.; Li, Q.; Shao, L.; Hao, R. Z.; Rui, X.; Wang1, S. Vancomycin-Modified Fe₃O₄ @SiO₂ @Ag Microflowers as Effective Antimicrobial Agents. *Int. J. Nanomedicine* **2017**, *12*, 3077–3094.

(123) Zhu, M.; Liu, W.; Liu, H.; Liao, Y.; Wei, J.; Zhou, X.; Xing, D. Construction of Fe₃O₄Vancomycin/PEG Magnetic Nanocarrier for Highly Efficient Pathogen Enrichment and Gene Sensing. *ACS Appl. Mater. Interfaces* **2015**, *7*, 12873–12881.

(124) Lin, Y. S.; Tsai, P. J.; Weng, M. F.; Chen, Y. C. Affinity Capture Using Vancomycin-Bound Magnetic Nanoparticles for the MALDI-MS Analysis of Bacteria. *Anal. Chem.* **2005**, *77*, 1753–1760.

(125) Gu, H.; Ho, P.; Tsang, K. W. T.; Wang, L.; Xu, B. Using Biofunctional Magnetic Nanoparticles to Capture Vancomycin-Resistant Enterococci and Other Gram-Positive Bacteria at Ultralow Concentration. *J. Am. Chem. Soc.* **2003**, *125*, 15702–15703.

(126) Kell, A. J.; Stewart, G.; Ryan, S.; Peytavi, R.; Boissinot, M.; Huletsky, A.; Bergeron, M. G.; Simard, B. Vancomycin-Modified Nanoparticles for Efficient Targeting and Preconcentration of Gram-Positive and Gram-Negative Bacteria. *ACS Nano* **2008**, *2*, 1777–1788.

(127) Butler, M. S.; Hansford, K. A.; Blaskovich, M. A. T.; Halai, R.; Cooper, M. A. Glycopeptide Antibiotics: Back to the Future. *J. Antibiot. (Tokyo).* **2014**, *67*, 631–644.

(128) Yim, G.; Thaker, M. N.; Koteva, K.; Wright, G. Glycopeptide Antibiotic Biosynthesis. *J. Antibiot. (Tokyo).* **2014**, *67*, 31–41.

(129) Kang, H. K.; Park, Y. Glycopeptide Antibiotics: Structure and Mechanisms of Action. *J. Bacteriol. Virol.* **2015**, *45*, 67–78.

(130) Pelaz, B.; Del Pino, P.; Maffre, P.; Hartmann, R.; Gallego, M.; Rivera-Fernandez, S.; de la Fuente, J. M.; Nienhaus, G. U.; Parak, W. J. Surface Functionalization of Nanoparticles with Polyethylene Glycol: Effects on Protein Adsorption and Cellular Uptake. *ACS Nano* **2015**, *9*, 6996–7008.

(131) Taurino, C.; Frattini, L.; Marcone, G. L.; Gastaldo, L.; Marinelli, F. Actinoplanes Teichomyceticus ATCC 31121 as a Cell Factory for Producing Teicoplanin. *Microb. Cell Fact.* **2011**, *10*.

(132) Jung, H.-M.; Jeya, M.; Kim, S.-Y.; Moon, H.-J.; Kumar Singh, R.; Zhang, Y.-W.; Lee, J.-K. Biosynthesis, Biotechnological Production, and Application of Teicoplanin: Current State and Perspectives. *Appl. Microbiol. Biotechnol.* **2009**, *84*, 417–428.

(133) Economou, N. J.; Zentner, I. J.; Lazo, E.; Jakoncic, J.; Stojanoff, V.; Weeks, S. D.; Grasty, K. C.; Cocklin, S.; Loll, P. J. Structure of the Complex between Teicoplanin and a Bacterial Cell-Wall Peptide: Use of a Carrier-Protein Approach. *Acta Crystallogr. Sect. D Biol. Crystallogr.* **2013**, *69*, 520–533.

(134) Bambeke, F. Van; Laethem, Y. Van; Courvalin, P.; Tulkens, P. M. Glycopeptide Antibiotics:From Conventional Molecules to New Derivatives. *Lead. Artic.* **2004**, *64*, 913–936.

(135) Lee, J. G.; Sagui, C.; Roland, C. Quantum Simulations of the Structure and Binding of Glycopeptide Antibiotic Aglycons to Cell Wall Analogues. *J. Phys. Chem. B* **2005**, *109*, 20588–20596.

(136) Arenal, R.; De Matteis, L.; Custardoy, L.; Mayoral, A.; Tence, M.; Grazu, V.; De La Fuente, J. M.; Marquina, C.; Ibarra, M. R. Spatially-Resolved EELS Analysis of Antibody Distribution on Biofunctionalized Magnetic Nanoparticles. *ACS Nano* **2013**, *7*, 4006–4013.

(137) Noel, S.; Liberelle, B.; Robitaille, L.; De Crescenzo, G. Quantification of Primary Amine Groups Available for Subsequent Biofunctionalization of Polymer Surfaces. *Bioconjug. Chem.* **2011**, *22*, 1690–1699.

(138) Miller, G. L. Use of Dinitrosalicylic Acid Reagent for Determination of Reducing Sugar. *Anal. Chem.* **1959**, *31*, 426–428.

(139) Finn, R. K. Theory of Agar Diffusion Methods for Bioassay. *Anal. Chem.* **1959**, *31*, 975–977.

(140) CLSI, C. and L. S. I. *Performance Standards for Antimicrobial Susceptibility Testing.*; 2017.

(141) May, J.; Shannon, K.; King, a; French, G. Glycopeptide Tolerance in Staphylococcus Aureus. *J. Antimicrob. Chemother.* **1998**, *42*, 189–197.

(142) Heo, D. N.; Min, K. H.; Choi, G. H.; Kwon, I. K.; Park, K.; Lee, S. C. Scale-Up Production of Theranostic Nanoparticles. In *Cancer Theranostics*; Elsevier Inc., 2014; pp. 457–470.

(143) Gonçalves, L. C.; Seabra, A. B.; Pelegrino, M. T.; de Araujo, D. R.; Bernardes, J. S.; Haddad, P. S. Superparamagnetic Iron Oxide Nanoparticles Dispersed in Pluronic F127 Hydrogel: Potential Uses in Topical Applications. *RSC Adv.* **2017**, *7*, 14496–14503.

(144) De Palma, R.; Peeters, S.; Van Bael, M. J.; Van Den Rul, H.; Bonroy, K.; Laureyn, W.; Mullens, J.; Borghs, G.; Maes, G. Silane Ligand Exchange to Make Hydrophobic Superparamagnetic Nanoparticles Water-Dispersible. *Chem. Mater.* **2007**, *19*, 1821–1831.

(145) Chen, M.; Zeng, G.; Xu, P.; Lai, C.; Tang, L. How Do Enzymes 'Meet' Nanoparticles and Nanomaterials? *Trends Biochem. Sci.* **2017**, 1–17.

(146) Secundo, F. Conformational Changes of Enzymes upon Immobilisation. *Chem. Soc. Rev.* **2013**, *42*, 6250.

(147) Sassolas, A.; Blum, L. J.; Leca-Bouvier, B. D. Immobilization Strategies to Develop Enzymatic Biosensors. *Biotechnol. Adv.* **2012**, *30*, 489–511.

(148) Knecht, S.; Ricklin, D.; Eberle, A. N.; Ernst, B. Oligohis-tags: Mechanisms of Binding to Ni^{2+}-NTA Surfaces. *J. Mol. Recognit.* **2009**, *22*, 270–279.

(149) Jurrus, E.; Engel, D.; Star, K.; Monson, K.; Brandi, J.; Felberg, L. E.; Brookes, D. H.; Wilson, L.; Chen, J.; Liles, K.; *et al.* Improvements to the APBS Biomolecular Solvation Software Suite. *Protein Sci.* **2018**, *27*, 112–128.

(150) Hermanson, G. T. *Bioconjugate Techniques*; third edit.; Academic Press, 2013.

(151) Getz, E. B.; Xiao, M.; Chakrabarty, T.; Cooke, R.; Selvin, P. R. A Comparison between the Sulfhydryl Reductants Tris (2-Carboxyethyl) Phosphine and Dithiothreitol for Use in Protein Biochemistry 1. *Anal. Biochem.* **1999**, *273*, 73–80.

(152) Nozaki, Y.; Tanford, C. Examination of Titration Behavior. In *Methods in Enzymology*; Academic Press, 1967; Vol. 11, pp. 715–734.

(153) Grimsley, G. R.; Scholtz, J. M.; Pace, C. N. A Summary of the Measured PK Values of the Ionizable Groups in Folded Proteins. *Protein Sci.* **2009**, *18*, 247–251.

(154) André, I.; Linse, S.; Mulder, F. A. A. Residue-Specific PKa Determination of Lysine and Arginine Side Chains by Indirect 15N and 13C NMR Spectroscopy: Application to Apo Calmodulin. *J. Am. Chem. Soc.* **2007**, *129*, 15805–15813.

(155) Jain, M.; Mariya Sebatini, A.; Radha, P.; Kiruthika, S.; Muthukumaran, C.; Tamilarasan, K. Synthesis, Characterization and Kinetic Analysis of Chitosan Coated Magnetic Nanobiocatalyst and Its Application on Glucose Oleate Ester Synthesis. *J. Mol. Catal. B Enzym.* **2016**, *128*, 1–9.

(156) Xu, J.; Sun, J.; Wang, Y.; Sheng, J.; Wang, F.; Sun, M. Application of Iron Magnetic Nanoparticles in Protein Immobilization. *Molecules* **2014**, *19*, 11465–11486.

(157) Wang, C.; Hsu, C. H.; Li, Z.; Hwang, L. P.; Lin, Y. C.; Chou, P. T.; Lin, Y. Y. Effective Heating of Magnetic Nanoparticle Aggregates for in Vivo Nano-Theranostic Hyperthermia. *Int. J. Nanomedicine* **2017**, *12*, 6273–6287.

(158) Marcone, G. L.; Binda, E.; Berini, F.; Marinelli, F. Old and New Glycopeptide Antibiotics: From Product to Gene and Back in the Post-Genomic Era. *Biotechnol. Adv.* **2018**, *36*, 534–554.